

# Long term dynamics and stabilization of nonlinear mechanical systems

#### Citation for published version (APA):

Vorst, van de, E. L. B. (1996). *Long term dynamics and stabilization of nonlinear mechanical systems*. [Phd Thesis 1 (Research TU/e / Graduation TU/e), Mechanical Engineering]. Technische Universiteit Eindhoven. https://doi.org/10.6100/IR455764

DOI: 10.6100/IR455764

#### Document status and date:

Published: 01/01/1996

#### Document Version:

Publisher's PDF, also known as Version of Record (includes final page, issue and volume numbers)

#### Please check the document version of this publication:

• A submitted manuscript is the version of the article upon submission and before peer-review. There can be important differences between the submitted version and the official published version of record. People interested in the research are advised to contact the author for the final version of the publication, or visit the DOI to the publisher's website.

• The final author version and the galley proof are versions of the publication after peer review.

• The final published version features the final layout of the paper including the volume, issue and page numbers.

Link to publication

#### General rights

Copyright and moral rights for the publications made accessible in the public portal are retained by the authors and/or other copyright owners and it is a condition of accessing publications that users recognise and abide by the legal requirements associated with these rights.

- · Users may download and print one copy of any publication from the public portal for the purpose of private study or research.
- You may not further distribute the material or use it for any profit-making activity or commercial gain
  You may freely distribute the URL identifying the publication in the public portal.

If the publication is distributed under the terms of Article 25fa of the Dutch Copyright Act, indicated by the "Taverne" license above, please follow below link for the End User Agreement:

www.tue.nl/taverne

#### Take down policy

If you believe that this document breaches copyright please contact us at:

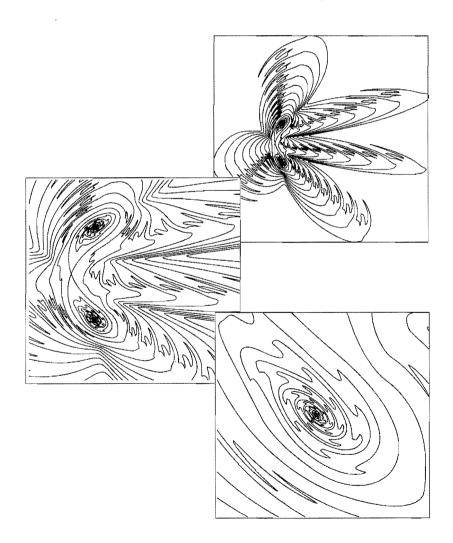
openaccess@tue.nl

providing details and we will investigate your claim.

# LONG TERM DYNAMICS AND STABILIZATION OF NONLINEAR MECHANICAL SYSTEMS.

# Edward L.B. van de Vorst

# LONG TERM DYNAMICS AND STABILIZATION OF NONLINEAR MECHANICAL SYSTEMS.



# LONG TERM DYNAMICS AND STABILIZATION OF NONLINEAR MECHANICAL SYSTEMS.

#### PROEFSCHRIFT

ter verkrijging van de graad van doctor aan de Technische Universiteit Eindhoven, op gezag van de Rector Magnificus, prof.dr. J.H. van Lint, voor een commissie aangewezen door het College van Dekanen in het openbaar te verdedigen op

vrijdag 1 maart 1996 om 14.00 uur

door

#### EDWARD LAURENTIUS BERNARDUS VAN DE VORST

geboren te Steensel (NBr)

Dit proefschrift is goedgekeurd door de promotoren:

prof.dr.ir. D.H. van Campen prof.dr.ir. J.J. Kok

Copromotor:

dr.ir. R.H.B. Fey

cover: Stable and unstable manifolds of a periodical excited bilinear single-DOF system.

#### CIP-DATA KONINKLIJKE BIBLIOTHEEK, DEN HAAG

Vorst, Edward Laurentius Bernardus van de

Long term dynamics and stabilization of nonlinear mechanical systems/ Edward Laurentius Bernardus van de Vorst. – [S.1. : s.n.] Thesis Technische Universiteit Eindhoven. – With summary in Dutch.

ISBN 90-386-0177-8

Subject headings: nonlinear dynamics / vibration control.

Printed by Febodruk – Enschede, The Netherlands

# CONTENTS

1	Intr	duction 1	
	1.1	Objective of this thesis	
	1.2	General introduction in nonlinear dynamics	
		1.2.1 Equations of motion and Poincaré section	
		1.2.2 Point, periodic and quasi-periodic attractors	
		1.2.3 Chaotic attractors and its identification	
		1.2.4 Saddles and repellors	
		1.2.5 Basins of attraction and their boundaries	
		1.2.6 Structural stability and bifurcations	
		1.2.7 Local bifurcations of fixed points and periodic orbits 10	
		1.2.8 Global Stability	
		1.2.9 Example	
	1.3	Numerical tools for analyzing long term dynamics	
		1.3.1 Reduction method	
		1.3.2 Periodic solution solvers and path-following	
		1.3.3 Local stability	
	1.4	Organization of this thesis	
I	Dis	continuous Systems 19	
2		s and Bifurcations in a Multi-DOF Beam System with Nonlinear Sup-	
	port	21	
	2.1	Introduction	
	2.2	Beam system supported by one-sided spring	
	2.3	Single-DOF model	
	2.4	Four-DOF model	

CONT	ENTS
------	------

	2.5	Experiments	31
	2.6	Conclusions	32
2	<b>F</b>	animental Vanification of the Standy State Debaniery of a Deam Custom	
3		erimental Verification of the Steady-State Behaviour of a Beam System Discontinuous Support	35
	3.1		35 35
	3.2	Experimental setup and numerical model.	33 37
	5.4	3.2.1 Beam supported by leaf springs.	37
			38
		3.2.2       Massless, one-sided spring.         3.2.3       Periodic excitation.	- 38 - 39
			39 40
		· · · · · · · · · · · · · · · · · · ·	
	~ ~	3.2.5 Numerical model.	40
	3.3	Experimental results.	41
	3.4	Conclusions.	44
4	Peri	odic Solutions of a Multi-DOF Beam System with Impact	49
	4.1	Introduction.	49
	4.2	Beam system with an elastic stop at its middle.	51
	4.3	Single-DOF model.	52
	4.4	Two-DOF model.	54
	4.5	Four-DOF model	59
	4.6	Conclusions	62
_	_		
5	-	erimental and Numerical Analysis of the Steady-State Behaviour of a	
		m System with Impact	65
	5.1	Introduction.	65
	5.2	Beam system with an elastic stop.	67
	5.3	Numerical analysis.	69
	5.4	Experimental analysis.	73
	5.5	Conclusions.	77
Π	M	anifolds (Global Stability)	83
		•	
6		nifolds of Nonlinear Dynamic Single-DOF Systems	85
	6.1	Introduction.	85
	6.2	Calculation of manifolds of single-DOF systems.	86
	6.3	Homoclinic and heteroclinic points.	88
	6.4	Homoclinic chaos.	88
	6.5	Fractal boundaries of basins of attraction.	89
	6.6	The creation of homoclinic and heteroclinic points.	93
	6.7	Conclusions	94

7	Determination of Global Stability of Steady-State Solutions of a Beam Sys-											
	tem with Discontinuous Support using Manifolds											
	7.1	Introduction	7									
	7.2	Calculation of manifolds	8									
	7.3	Beam system supported by one-sided spring	D									
	7.4	Single-DOF model	1									
	7.5	Experimental results	9									
	7.6	Conclusions	1									

# III Flexible Rotor-Bearing Systems

## 115

8	Stea	dy-State Behaviour of Flexible Rotor Dynamic Systems with Oil Journal
	Bear	ings 117
	8.1	Introduction
	8.2	Rotordynamic system supported by one oil journal bearing
	8.3	Rotor distance $L = 0.038$ m
		8.3.1 Static loads, $m_e = 0.0 \text{ g}$
		8.3.2 Static and dynamic loads, $m_e = 1.0 \text{ g}. \dots \dots$
		8.3.3 Static and dynamic loads, $m_e = 2.0 \text{ g} \dots $
	8.4	Rotor distance L = 0.133 m
		8.4.1 Static loads, $m_e = 0.0 g$
		8.4.2 Static and dynamic loads
	8.5	Rotor distance $L = 0.275$ m
		8.5.1 Static loads, $m_{e} = 0.0 \text{ g}$
		8.5.2 Static and dynamic loads, $m_{-}e = 2.0 \text{ g.} \dots \dots$
	8.6	Conclusions
	8.A	Finite-Length Bearing Theory
	8.B	Component mode synthesis and equations of motion
9	Stea	dy-State Behaviour of Nonlinear Flexible Rotor-Bearing Systems: Part
	II – .	Application: Influence of Cavitation Modelling 139
	9.1	Introduction
	9.2	Rotordynamic system supported by one oil journal bearing 141
	9.3	The short bearing theory
	9.4	Influence cavitation modelling on system responses
		9.4.1 Static loads, $m_e = 0.0$ g
		9.4.2 Static and dynamic loads, $m_e = 1.0 \text{ g}. \ldots \ldots \ldots \ldots 149$
		9.4.3 Static and dynamic loads, $m_e = 2.0 \text{ g}. \dots \text{ / } \dots \dots \dots 152$
	9.5	Conclusions
	9.A	Short Bearing Theory
		9.A.1 Short Bearing Theory using a cavitation region which depends
		on shaft velocity

159

	9.A.2	Short B	earing	Theory	y usir	ng a	cav	itati	on r	egi	on '	wh	icł	n is	iı	nde	e-		
		pendent	of sha	ft velo	city.						•	• •	•				•	•	155
9.B	Nomen	clature.				• •	• •	• •	• •		•	•			•		•	•	156

## **IV** Stabilization of Unstable Periodic Solutions

10	Vibration Control of Periodically Excited Nonlinear Dynamic Multi-DOF									
	Systems 161									
	10.1 Introduction	161								
	10.2 Control of multi-DOF nonlinear dynamic systems.	164								
	10.3 Reconstruction of the full state using Kalman filtering.									
	10.4 Computation of the desired trajectory.	168								
	10.5 Application: Beam supported by one-sided spring.	169								
	10.5.1 Preliminaries.	169								
	10.5.2 Control in case of exact system model.	171								
	10.5.3 Robustness of controller-observer.	174								
	10.5.4 Control of beam system for excitation frequency sweep.	177								
	10.5.5 Choice of control parameters.									
	10.6 Conclusions and recommendations.	179								
	10.A Equations of motion of beam system.	180								
11	Stabilization of Periodic Solutions of Nonlinear Mechanical Systems: Con-									
	trollability and Stability 11.1 Introduction.	183								
	11.2 Controllability: Can an unstable periodic solution be stabilized?									
	11.2.1 Theory									
	11.2.2 Simulations.									
	11.3 Sliding computed torque control: Stability analysis.									
	11.3.1 Filtering the control force.									
	11.3.2 Stability analysis.									
	11.3.3 Simulations									
	11.4 Conclusions.									
	11.A Stability analysis: Floquet theory	201								
12	Conclusions and Recommendations	203								
A	Component mode synthesis	209								
D										
B	Periodic Solution Solvers	215								
	B.1 Finite Difference Method.									
	B.2 Multiple Shooting Method.									
	B.3 Incremental Harmonic Balance method	219								
С	Path-following of Periodic Solutions	221								

C Path-following of Periodic Solutions

CONTENTS	XI
SUMMARY	223
SAMENVATTING	227
ACKNOWLEDGEMENTS	231
CURRICULUM VITAE	233



# **1** INTRODUCTION

## 1.1 Objective of this thesis.

In engineering practice, an increasing necessity can be observed for taking into account the influence of nonlinearities in the description of the dynamic behaviour of complex mechanical systems for several reasons. Firstly, quite often characteristic dynamic behaviour can be observed in complex mechanical systems which cannot be explained from analysis of linear models of such systems (often containing many degrees of freedom). Secondly, it appears that in a number of cases nonlinearities in a design effectively can be used for vibration control or vibration minimization (see part IV of this thesis). Besides the fundamental need for a better understanding of the dynamic behaviour, also the wide availability of digital computers with rapidly increasing powerfulness is a very stimulating factor for nonlinear analyses of dynamical systems.

Frequently, in mechanical systems from a spatial or geometrical point of view, nonlinearities have a local character. This means that from a spatial point of view, these local nonlinearities constitute only a restricted part of the mechanical system under consideration. However, their presence in general has important consequences for the overall dynamic behaviour. Important examples of local nonlinearities in mechanical systems are: fluid-film bearings in rotating machinery, dry friction and backlash phenomena in certain connections of mechanical systems, nonlinear spring and damper supports in piping or vehicle systems, etc.

A typical orbit of a dissipative linear or nonlinear mechanical system driven by a periodic excitation or by a constant force consists of a transient, whereafter the system will settle in a post-transient state, the long term or steady-state behaviour of the system. The long term behaviour of nonlinear systems is much more complex than the long term behaviour of linearized systems. Long term responses of linear systems will always have the same character as the excitation forces: if the excitation is sinusoidal, the long term behaviour will also be sinusoidal and will be unique. Also, the superposition

principle holds for linear systems. This is not the case for nonlinear systems, which makes the analysis of the long term behaviour of such systems much more complex and time consuming.

Long term solutions of the equations of motion of a nonlinear mechanical system can be computed in a direct way by solving two-point boundary value problems obtained by supplementing the equations of motion with periodicity conditions for the solutions. Often the (multiple) shooting method, which will be discussed later, is used for solving the two-point boundary value problem. Because this method is very expensive from a computational point of view for systems with many degrees of freedom (DOF's), in literature usually only very much schematized systems with one or two DOF's are investigated.

The research presented in this thesis is a continuation of the research carried out by Crooymans (1987) and Fey (1992). They investigated the periodic solutions of two-point boundary value problems using the finite difference method with an equidistant time discretization mesh, which will be discussed later. The finite difference method with an equidistant discretization mesh is generally less accurate than a (mulitple) shooting method (see section 1.3) but it is much more efficient, in particular for systems with many DOF's. However, the finite difference method with an equidistant discretization mesh does fail for some kinds of nonlinearities (see section 1.3).

Using finite differences, Crooymans (1987) investigated the long term behaviour of Laval-type rotor-bearing systems with rubbing. Fey (1992) analysed a class of Euler beam systems with local nonlinearities. As mentioned before, in mechanical systems frequently the nonlinearities have a local character but they can result in a dramatical change of the global dynamic behaviour. These localized nonlinearities can be advantageously taken into account by dividing the system into linear and nonlinear components, where the linear components generally have many DOF's. Then, the DOF's of the linear components can be reduced using a component mode synthesis method (Craig, 1985). The dynamic behaviour of a reduced linear component approximates that of the corresponding unreduced linear parts are coupled with the local nonlinearities, creating a reduced nonlinear system with a limited number of DOF's. The dynamic behaviour of the reduced nonlinear system approximates that of the unreduced nonlinear system approximates that of the unreduced nonlinear system approximates that of the reduced nonlinear system approximates that of the unreduced nonlinear system. Using the reduced system, periodic solutions can be calculated in a very efficient way.

In this thesis, we will also focus on nonlinear (mechanical) systems with local nonlinearities using a component mode synthesis method for the system reduction. Besides the finite difference method, two additional methods, the multiple shooting method and the incremental harmonic balance method (see section 1.3), have been developed to solve the two-point boundary value problems for the calculation of periodic solutions. The reason for this is that the finite difference method with equidistant time mesh shows convergence problems for systems with "hard" discontinuities, i.e. discontinuities like dry friction and rigid stops, which cause a large change of the state of the system in a small time interval. For this kind of nonlinearities, the multiple shooting method can be used as long as a time integration method with a variable time step size is

used. The multiple shooting method consumes more computational time than the finite difference method. It should be noticed that also the multiple shooting method is not suitable for all kinds of discontinuities. In this thesis only systems with discontinuities in the stiffness are investigated and for this kind of systems the multiple shooting method seems to be very useful. It is not investigated if the multiple shooting method is also useful for nonlinearities with discontinuities in the viscous damping coefficients which, for instance, is the case of dry friction. In comparison to the finite difference method, the incremental harmonic balance method is more efficient for weakly nonlinear systems and can also be used to get a quick global view of the response of a nonlinear system. The reduction method and the periodic solution solvers are implemented in the finite element package DIANA (1995). This package was used for all calculations in this thesis.

In contrast with linear dynamic systems, nonlinear dynamic systems can show different long term responses (attractors) for one set of system parameters. Which attractors will be approached by the system depends on the initial state of the system and the global stability of the coexisting attractors. If the global stability of a specific attractor is low, small perturbations on the system will easily result in a jump to another attractor. From a practical point of view, it is important to determine which attractor will show up, because the maximum response of the different attractors can be very different and also response spectra can be very different. Large amplitude responses may lead to large strains and stresses which can cause damage to the structure. In this thesis a method is developed to determine the global stability of attractors. This is done by calculating the boundaries of the basins of attraction of the attractors. The basins of attraction of an attractor are the set of initial states of orbits which approach the attractor if time proceeds. If the boundaries of the basins of attraction lie close to the attractor, often the global stability of this attractor will be low. The presented method is developed for single-DOF systems. However, it is shown that in some cases it can be used for multi-DOF systems. This is also demonstrated by experimental results (see chapter 7 of this thesis).

As an application, multi-DOF systems with discontinuities in the stiffness and rotorbearing systems are investigated and it is shown that generally models with much more than one DOF are necessary for a sufficiently accurate representation of the system behaviour.

Discontinuous systems are an important class of nonlinear mechanical systems. In many practical engineering applications, discontinuities occur. An example of a discontinuous system is a satellite with solar panels (Wijckmans, 1995). During the launching of a satellite, the solar panels are in a folded position. Because these solar panels are excited during the flight, vibrations can occur in the panels. In order to reduce the vibrations of the panels so-called one-sided snubbers are used. However, using the one-sided snubbers, the system becomes a discontinuous system. Such a discontinuous system is a typical example of a system with local nonlinearities. Although the nonlinearity is local, the overall dynamic response of the system can change drastically. A system with discontinuities cannot be linearized, so its is very difficult to approximate the system response through a linear analysis. Very often, such discontinuities cause much higher response frequencies, even in case the excitation frequency is low. Generally, this means that the higher eigenmodes of the linear parts of the system are excited. Then, these higher eigenmodes will strongly influence the low frequency response and multi-DOF systems will be necessary to calculate the system behaviour accurately. As mentioned earlier, only systems with discontinuities in the stiffness are investigated in this thesis. Experiments are carried out to support the validity of the numerical results.

Journal bearings are an essential feature of all rotating machinery and provide the vital load-carrying capacity to support rotors against static and dynamic loads. The standard practice for dynamic imbalance response and stability analysis of rotor-bearing systems is to determine the linearized bearing stiffness and damping coefficients about a stationary equilibrium position. In this mathematical assumption, the synchronous motion about the stationary equilibrium position is described by ellipses in case of low values of the unbalance. However, when the unbalance level becomes moderate to large, the rotor orbits are not necessarily elliptical, due to the nonlinear characteristics of the bearings. Furthermore, in a linear system, operating above the threshold angular rotor speed, the amplitude of motion grows exponentially with time and the orbits become unbounded. In an actual system this is not necessarily the case, because the nonlinear effects can cause the motion to be bounded by limit cycles. Moreover, under some circumstances a lower total response can be obtained by having a moderate level of rotor unbalance in the system.

Because rotor-bearing systems are typical examples of systems consisting of large linear parts (shaft and disks) and local nonlinearities (bearings), the models of these systems can be reduced considerably. Because of this, the long term dynamics of a rotor-bearing system can be analysed efficiently by calculating periodic solutions numerically by the methods outlined in this thesis. In this thesis some simple rotorbearing systems are investigated and it is shown that the eigenmodes of the shaft play an important role in the system response. Hence again multi-DOF models are necessary for a good prediction of the system behaviour. Furthermore, attention is paid to the bearing models which can be used to arrive at an adequate modelling of oil journal bearings in nonlinear dynamic analysis.

As stated earlier, local nonlinearities can change the system behaviour drastically. This results in system responses with undesirable frequencies and enlargement of the maximum system response by subharmonic resonance peaks. Generically, a low amplitude harmonic orbit coexists which may be unstable or may have a low global stability. In this thesis a control method is developed which provides that using one single control force in a certain position of the system, the system can be controlled to that low amplitude harmonic orbit, unstable or stable. Because the harmonic orbit is a natural solution of the system, the control force will become very small, theoretically even zero, if the system settles in the harmonic orbit.

Because only one control force is used to control the system, the difference between the number of inputs, which is one control force, and the number of outputs which must be controlled, which are all the degrees of freedom of the system, is very large. In standard control theory, the difference between the number of inputs and outputs of nonlinear controlled systems is much lower. Because of this, not a standard control method can be used to control the system to an unstable harmonic orbit. Furthermore, not every arbitrary nonlinear system will be controllable using one control force and not every unstable harmonic orbit can be stabilized. Because of this, methods are developed to determine the controllability of a system and to determine the stability of the controlled system.

In section 1.2, a short general introduction in nonlinear dynamics is given. Then in section 1.3 an overview is given of the numerical tools for analyzing the long term behaviour of nonlinear mechanical systems which are used in this thesis. In section 1.4 the organization of this thesis is explained.

#### **1.2** General introduction in nonlinear dynamics.

In this section some basic concepts and terminologies of nonlinear dynamics are given. For a more detailed introduction in nonlinear dynamics the reader is referred to Guckenheimer and Holmes (1983), Thompson and Stewart (1986), Parker and Chua (1989) and Thompson (1994).

#### 1.2.1 Equations of motion and Poincaré section.

The equations of motion of a nonlinear mechanical system can be written as

$$\boldsymbol{M}_{\boldsymbol{u}}(\boldsymbol{q}_{\boldsymbol{u}},t)\boldsymbol{\ddot{q}}_{\boldsymbol{u}} + \boldsymbol{f}_{\boldsymbol{i}\boldsymbol{n}}(\boldsymbol{\dot{q}}_{\boldsymbol{u}},\boldsymbol{q}_{\boldsymbol{u}},t) = \boldsymbol{f}_{\boldsymbol{e}\boldsymbol{x}_{\boldsymbol{u}}}(t) \tag{1.1}$$

where  $q_u$  is the  $n_{q_u}$ -column with the system DOF's, t is the time, a dot means a derivative with respect to time,  $M_u$  is the mass matrix,  $f_{in}$  is the  $n_{q_u}$ -column with internal forces and  $f_{ex_u}$  is the  $n_{q_u}$ -column with external loads. If equation (1.1) is not explicitly dependent of time, i.e.  $M_u(q_u, t) = M_u(q_u)$ ,  $f_{in}(\dot{q}_u, q_u, t) = f_{in}(\dot{q}_u, q_u)$  and  $f_{ex_u}(t) = f_{ex_u}$ , then the system is called *autonomous*, otherwise it is called *nonautonomous*. In this thesis, it is assumed that equation (1.1) can be rewritten as

$$\boldsymbol{M}_{\boldsymbol{u}}\ddot{\boldsymbol{q}}_{\boldsymbol{u}} + \boldsymbol{f}_{\boldsymbol{i}\boldsymbol{n}}(\dot{\boldsymbol{q}}_{\boldsymbol{u}}, \boldsymbol{q}_{\boldsymbol{u}}, t) = \boldsymbol{f}_{\boldsymbol{e}\boldsymbol{x}_{\boldsymbol{u}}}(t) \tag{1.2}$$

which means that the mass matrix is assumed to be independent of time and displacements. Furthermore, in this thesis it is assumed that the system has damping, so the system *dissipates* energy. Also, it is assumed that either the system is autonomous or that the terms in the internal forces  $f_{in}$  and external forces  $f_{exu}(t)$  which are an explicit function of time are periodic with period time  $T_e$  i.e.

$$f_{in}(\dot{q}_u, q_u, t + T_e) = f_{in}(\dot{q}_u, q_u, t) \quad \text{and} \quad f_{ex_u}(t + T_e) = f_{ex_u}(t) \quad (1.3)$$

A typical orbit of this kind of systems consists of a transient, whereafter the system will settle asymptotically onto a stable *long term* response, called an *attractor*. Such a post-transient orbit can be a point-attractor, a periodic attractor, a quasi-periodic attractor, or a chaotic attractor. Generically, each attractor is entirely surrounded in state space by its own basin of attraction. All transients starting in an infinitesimally small neighbourhood around the attractor return to it, making it *asymptotically stable* in the local sense of

Lyapunov. All the above types of recurrent motions can also appear as unstable long term responses giving saddles and repellors which will be discussed later.

A useful tool for visualizing the long term behaviour is the *Poincaré section*. For mechanical systems driven by a periodic excitation of period  $T_e$ , Poincaré sections can be defined by the state  $q_u$ ,  $\dot{q}_u$  at times  $t = iT_e$  where i = 1, 2, 3, ... This corresponds to a *stroboscopic sampling* of the state space with period time  $T_e$ .

#### 1.2.2 Point, periodic and quasi-periodic attractors.

A fixed point,  $q_f$ , of (1.2) is characterized by

$$\boldsymbol{f_{in}(q_f) = f_{ex_u}} \tag{1.4}$$

It can be stable or unstable. If it is asymptotically stable it is called a *point attractor*.

A local stability analysis of any fixed point starts with the linearized equations describing small variations around the point. For a fixed point, the stability depends on the signs of the real parts of the eigenvalues of  $\partial f_{in}/\partial q_u$  (i.e., the stiffness matrix). The necessary condition for stability is that all the real parts are negative; the necessary condition for instability is that at least one real part is positive.

A periodic orbit is a closed orbit in the state space satisfying that every response starting at the orbit returns precisely to its starting point after its period time T. Such a motion (not normally sinusoidal) is called a harmonic orbit if it has the same period as the excitation period. A 1/n subharmonic orbit is a periodic orbit with a period of ntimes the period of the excitation ( $n \in \mathbb{N}$ ). Besides the basis frequency, i.e. the lowest frequency occurring in the periodic orbit, in a harmonic orbit also frequencies occur which are a multiple of the basis frequency. In a (sub)harmonic orbit such a higher frequency may be dominant and may cause a resonance. This is called a superharmonic resonance. Notice that superharmonic solutions, i.e. a harmonic orbit with an basis frequency larger than the excitation frequency, normally cannot exist since an orbit of a system will normally contain its excitation frequency.

If a periodic orbit is asymptotically stable, it is called a *periodic attractor*, or *limit cycle*. In a Poincaré section a periodic orbit will appear as a finite number of *fixed points* (figure 1.1a–f). The local stability of a periodic orbit can be determined using Floquet theory. A short summary of the Floquet theory can be found in section 11.A. Application of the Floquet theory results in  $2n_{q_u}$  so-called *Floquet multipliers*. A periodic orbit is stable if all Floquet multipliers have a modulus less than unity. A periodic orbit is unstable if at least one of the moduli is larger than unity.

Consider a motion which has one periodic component of period  $T_1$  and a second of period  $T_2$ . The first component repeats after time  $t = nT_1$ , while the second repeats after  $t = mT_2$  where n and m are positive integers. If a (lowest) time can be found for which  $t = T = nT_1 = mT_2$ , then the motion is periodic with period T. If, however,  $T_1/T_2$  is irrational (that is to say  $T_1$  and  $T_2$  are *incommensurate*), then no such time can be found: the motion never precisely repeats itself, and is called *quasi-periodic*. Over a long time scale there will however be arbitrary close repetition. If the motion is asymptotically stable we have a *quasi-periodic attractor*. Quasi-periodic motions with

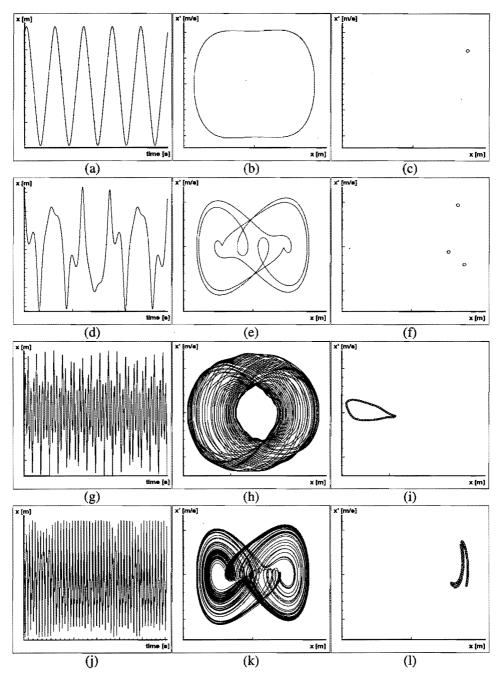


**Figure 1.1** Harmonic (a, b, c), 1/3 subharmonic (d, e, f), quasi-periodic (g, h, i) and chaotic (j, k,l) behaviour in the time-displacement domain (a, d, g, j), in the state space (b, e, h, k) and in a Poincaré section (c, f, i, l).

just two incommensurate periods will appear in a Poincaré section (with sampling period  $T_1$  or  $T_2$ ) as a closed curve (figure 1.1g-i).

#### 1.2.3 Chaotic attractors and its identification.

The last and most complex form of bounded post-transient behaviour is the *chaotic attractor*. The chaotic attractor exhibits an extremely sensitive dependence on initial conditions, and, despite the absence of any stochastic forcing of the deterministic system, a broad-band power spectrum. Two orbits in a chaotic attractor with almost the same initial states will diverge from each other and never cross each other although their maximum will be bounded. Because of this, the attractor has a bounded fractal structure and induces a complex mixing of orbits. The chaotic nature of an attractor can be established by examining the divergence of orbits, quantified by *Lyapunov exponents*. In a Poincaré section, a chaotic attractor will appear as a set of an infinite number of points; no point does return precisely to any of the points of the set (figure 1.1j–l).

Under a continuous slow variation of a system parameter, for example the excitation frequency, a common route to a chaotic attractor is a cascade of *period-doubling* bifurcations, each of which generates a stable oscillation with twice the period of its precursor. In this cascade the bifurcations become more and more closely spaced, the ratio of successive parameter intervals very often tending in the limit to the *Feigenbaum* number (Feigenbaum, 1983). This number is universal in the sense that it arises in a very wide class of problems.

Another common route to chaos is the quasi-periodic mode-locking route (Newhouse et al., 1978). Under slow variation of a system parameter, a quasi-periodic motion *locks* to subharmonic behaviour, i.e. the dominant frequencies in the quasi-periodic behaviour become rational. This is called *frequency locking* or *mode-locking*. Further variation of the system parameter results in the long term behaviour to become quasi-periodic; the dominant frequencies become irrational again. This is repeated if the system parameter is further varied where the quasi-periodic behaviour becomes more and more irregular until it changes into a chaotic attractor.

*Intermittency* is chaotic behaviour consisting of time intervals with almost periodic behaviour alternated by time intervals with highly irregular behaviour (Pomeau and Manneville, 1980). Under the variation of a system parameter the periodic intervals increase or decrease until the behaviour is entirely periodic or chaotic.

The Lyapunov exponents,  $\sigma_i$ , of an orbit measure the average long term exponential rate of divergence of all adjacent motions based on

$$\sigma_i = \lim_{t \to \infty} (1/t) \ln \left[ (\text{separation in direction } i \text{ at } t) / (\text{separation in direction } i \text{ at } 0) \right]$$
(1.5)

This limit has to be taken only amongst orbits whose final separation remains small. In a totally dissipative system, the sum of Lyapunov exponents of any orbit will be negative, with, however, no such restriction of any single exponent. If the maximum exponent,  $\sigma_1$ , is positive, then some adjacent orbits will diverge from the fundamental, and there will be a sensitive dependence on initial conditions; the orbit is unstable.

#### 1.2.4 Saddles and repellors.

A fixed point or motion is unstable if any single adjacent motion moves out of its immediate state space neighbourhood with exponential rate. The *index of instability* of a fixed point or periodic motion is based on the linear eigenvalues or Floquet multipliers. For a fixed point this index equals the number of eigenvalues with a positive real part. For a periodic orbit it is the number of Floquet multipliers with modulus larger than one.

If the index of instability is zero, the fixed point or motion is a stable attractor. If the index lies between zero and the phase dimension  $(2n_{q_u})$ , we have an unstable *saddle* orbit that repels in some directions but attracts in all the others. Saddles can be fixed, periodic, quasi-periodic or chaotic motions. Being unstable, they are not directly observable in a physical system, but they do play a key role in structuring the state space. In particular, saddles with index one, having a single unstable direction, frequently lie in and organize basin boundaries.

If the index is equal to the phase dimension, we have a *repellor*, corresponding to fixed, periodic, quasi-periodic or chaotic motions. These repel all adjacent motions.

#### 1.2.5 Basins of attraction and their boundaries.

For a nonlinear dynamic system simultaneously different attractors can coexist for one set of system parameters. In which attractor a orbit of a system will settle depends on the initial state of the system. The set of all initial states of orbits which approach a specific attractor is called the *basin of attraction* of the attractor. The basins of attraction in the  $\mathbb{R}^{2n_{q_u}}$ -1)-dimensional basin boundaries. Orbits initialized within a basin tend asymptotically, as  $t \to +\infty$ , to the attractor lying within the basin. Orbits starting precisely on a basin boundary (*separatrix*) often approach a saddle orbit which attracts within the boundary but repels across it.

The set of orbits that approach a saddle as  $t \to +\infty$ , approaching it tangentially along the stable incoming eigenvectors, are called *stable manifolds*. Similarly, the set of orbits asymptotic to a saddle as  $t \to -\infty$  are called *unstable manifolds*. The stable manifolds are particularly important in organizing a phase portrait. Generally, the stable form basin boundaries since the stable manifolds are the set of orbits which do not approach an attractor (they approach a saddle solution).

#### 1.2.6 Structural stability and bifurcations.

System parameters, r, of a dynamic system are understood to remain constant during the dynamical motions of the system. If one system parameter, r, changes, the long term orbits of the system also change. Typically, a small change in r produces small quantitative changes in a long term orbit. However, there is also a possibility that a small change in r can cause a long term orbit to undergo a qualitative change. Such a qualitative change is called a *bifurcation* and the value of  $r_c$  is called the *bifurcation* value. Examples of bifurcations are the disappearance or creation of a long term orbit and a change in the stability of a long term orbit. Informally, a dynamical system is *structurally stable* if there exists no infinitesimal perturbation of the system that results in a qualitative change of its long term orbits. (For a more thorough definition of structurally stability the reader is referred to Guckenheimer and Holmes (1983).) This means that a qualitative change of the long term orbit can occur only when the system is structurally unstable. Hence, the set of bifurcation values is the set of system parameter values at which the system is structurally unstable.

Local bifurcations, restricted to a small neighbourhood of the state space, involve the creation, destruction and splitting of attractors. Global bifurcations involve connections between the manifolds of saddles, often producing abrupt changes in the structure of the attractors and/or their basins.

Bifurcations, observed under the variation of one system parameter are called codimension one bifurcations. The co-dimension, c, is the number of real Floquet multipliers with modulus equal to one plus the number of conjugate pairs of Floquet multipliers with modulus equal to one. Generically, c system parameters have to be varied simultaneously to meet a co-dimension c bifurcation.

#### 1.2.7 Local bifurcations of fixed points and periodic orbits.

A system under *increasing* values of system parameter r can lose its stability at a local bifurcation when a fundamental primary path (of fixed points or motions) becomes unstable at  $r = r_c$ . When the path bifurcates and throws off a secondary path, the form and stability of the secondary path gives us the following three-fold classification. At a *super-critical* bifurcation the continuous fundamental path loses its stability as it intersects a stable secondary path that only exists for  $r > r_c$ . At a *sub-critical* bifurcation the fundamental path loses stability as it intersects an unstable secondary path that only exists for  $r > r_c$ . At a *sub-critical* bifurcation the fundamental path loses stability as it intersects an unstable secondary path that only exists for  $r < r_c$ . The third form, that arises in the paths of fixed points, is the *trans-critical* bifurcation. Here the fundamental path destabilizes as it intersects a continuous secondary path of fixed points which exists at sub- and super-critical values of r, being unstable for  $r < r_c$  and stable for  $r > r_c$ : the fundamental and secondary paths *exchange stability*. Of course, under decreasing values of system parameter the same bifurcations can be met at  $r = r_c$ .

A local bifurcation involving the loss of stability of an attractor will have one or more critical eigenvalues or Floquet multipliers with a corresponding mode for which the response is neither attracting nor repelling within the linear approximation.

A local bifurcation is observed on a path of fixed points as the real part of a linear eigenvalue passes through zero. If a real eigenvalue passes through zero, we have a *fold* or *saddle-node* bifurcation. As r is increased towards  $r_c$ , a saddle and a node merge; there is locally no fixed point for  $r > r_c$ , forcing the system to jump dynamically to a distant, unrelated attractor. The saddle-node can manifest itself as a sub-, super- or trans-critical bifurcation.

If the real part of a complex conjugate pair of eigenvalues passes through zero, we have the *primary Hopf* bifurcation in which a secondary path of limit cycles bifurcates from the monotonic path of fixed points as it loses stability. This secondary path can be stable with  $r > r_c$ , giving us the super-critical primary Hopf bifurcation: conversely, it

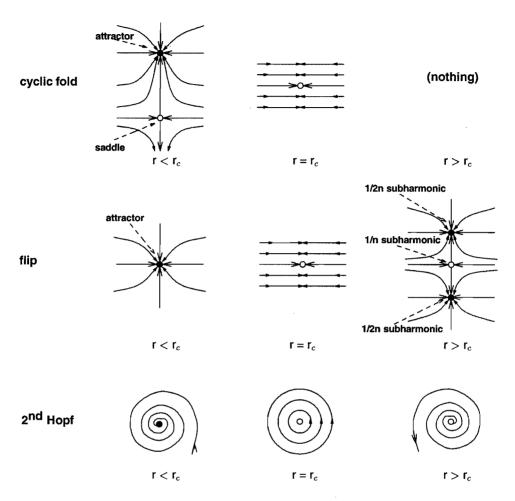


**Figure 1.2** Poincaré sections of periodic solutions near cylic fold, flip, and  $2^{nd}$  Hopf bifurcations.

can be unstable with  $r < r_c$ , giving the sub-critical form.

A local bifurcation can analogously be observed on a path of periodic orbits. A loss of stability will now correspond to a Floquet multiplier passing through the unit circle. If a single real Floquet multiplier passes through +1 we have a saddle-node, which typically manifests itself as a *cyclic fold* with c = 1 and features similarly to the fixed point saddle-node, generating in particular an inevitable dynamic jump to another attractor. If a real Floquet multiplier passes through -1 we have a c = 1 at which a secondary path of period-doubled periodic orbits bifurcates off the monotonic fundamental path as it loses its stability. This secondary path can be stable with  $r > r_c$ , giving us the super-critical flip: conversely, it can be unstable with  $r < r_c$ , giving the sub-critical form. A flip bifurcation generates a secondary path of periodic orbits with twice the period of the fundamental path. If a complex conjugate pair of eigenvalues crosses the

unit circle we have the *Neimark* or *secondary Hopf* bifurcation. Quasi-periodic motions on a torus typically bifurcate off the fundamental path of periodic orbits, in either superor sub-critical form. In figure 1.2 the Poincaré sections with periodic orbits are shown in the neighbourhood of the above described types of local bifurcations.

#### 1.2.8 Global Stability.

The adjective *global* is used to describe bifurcations and other phenomena that are not essentially described in a local region of the state space. The *global stability* of an attractor is determined by the structure of its basin boundaries. If the basin boundaries lie close to the attractor, perturbations of moderate level (not infinitesimal so that they cannot be described by the linearized system), will easily result in a jump to another attractor. In that case, the global stability of the attractor will be low, although it is locally stable. Global bifurcations occur if basin boundaries touch each other or touch attractors or saddles. They will not be discussed here.

#### 1.2.9 Example.

Figure 1.3 shows the maximum absolute displacements  $|y|_{max}$  occurring in the periodic solutions for varying excitation frequency for a beam system supported by a one-sided spring. In part I of this thesis this system is described in more detail. The figure shows branches with harmonic solutions, 1/2 subharmonic solutions, 1/3 subharmonic solutions and 1/5 subharmonic solutions.

On the branches, unstable parts occur (dotted lines). A branch with periodic solutions becomes unstable via a bifurcation. For instance, near 22 Hz an unstable part exists on the harmonic branch marked by two secondary Hopf bifurcations. For these excitation frequencies the system response is quasi-periodic. The harmonic and 1/2 subharmonic branches are connected and at the excitation frequency where these branches touch each other, flip bifurcations occur. Near these bifurcations, the harmonic solutions and 1/2 subharmonic solutions will be almost the same.

The branches with 1/3 subharmonic and 1/5 subharmonic solutions are closed and are not connected with other branches with periodic solutions. These branches consist of a stable part (upper part) and an unstable part (lower part). Two cyclic fold bifurcations connect the stable and unstable parts. Notice that these cyclic fold bifurcations occur at the lowest and highest excitation frequency for which the branches with 1/3 subharmonic and 1/5 subharmonic solutions exist.

The insets in figure 1.3 shows periodic solutions at some frequencies. Notice that in the frequency-response only the maximum absolute values of these periodic solutions are plotted and that generally in a periodic solution also other frequencies than the excitation frequency  $f_e$  are present. The insets with periodic solutions show that the shape of the harmonic and 1/2 subharmonic solutions change very much if the excitation frequency is varied.

Notice the superharmonic resonance peaks on the branch with harmonic solutions near 32.5 Hz and 42.8 Hz. These superharmonic resonance peaks are related to the second

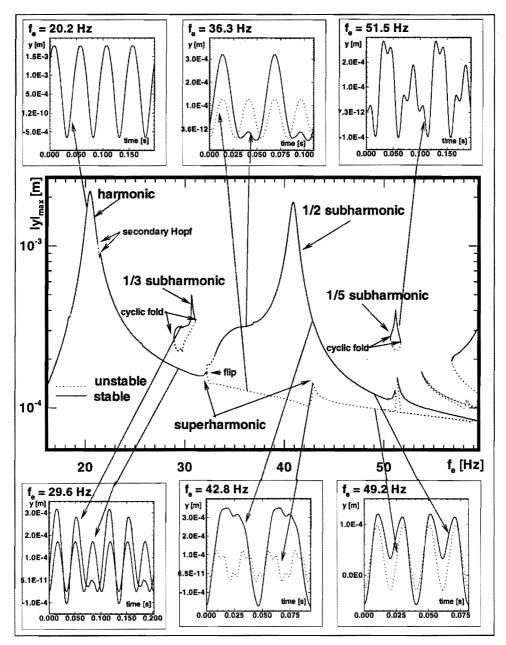


Figure 1.3 Maximum absolute displacements occurring in periodic solutions for varying excitation frequency and periodic solutions at some frequencies.

harmonic resonance peak at 128 Hz. Consequently, the harmonic solution at 42.8 Hz in figure 1.3 shows a high frequency which corresponds to the second eigenfrequency of the linear beam system.

## 1.3 Numerical tools for analyzing long term dynamics.

#### 1.3.1 Reduction method.

As mentioned in the introduction of this chapter, in many engineering applications of nonlinear systems the nonlinearities have a local character. The advantage of this kind of systems is that they can be divided into linear and nonlinear components where in general the linear components will have a large number of DOF's. The DOF's of the linear components can be reduced by applying a component mode synthesis method. The component mode synthesis method used in this thesis is based on residual flexibility modes and free interface eigenmodes. The residual flexibility modes provide unaffected (quasi-)static load behaviour of the linear components. For approximating the dynamic behaviour of the linear component, free-interface eigenmodes up to a certain cut-off frequency are used. After reduction the reduced linear and the nonlinear components are assembled, resulting in a reduced nonlinear system which is an approximation of the unreduced nonlinear system for dynamic problems; statically it is equivalent to the unreduced system. The behaviour of the reduced system will be accurate for frequencies lower than the cut-off frequency used in the reduction process. Because nonlinear systems generate higher frequencies than their excitation frequency, generically the cut-off frequency must be chosen considerably higher than the maximum excitation frequency (Aarts, 1993). In appendix A the component mode synthesis method used in this thesis is described from a computational point of view.

The equations of motion of the reduced nonlinear system can be written as

$$\boldsymbol{M}\ddot{\boldsymbol{q}} + \boldsymbol{f_{nl}}(\dot{\boldsymbol{q}}, \boldsymbol{q}, t) = \boldsymbol{f_{ex}}(t) \tag{1.6}$$

where q is the  $n_q$ -column with the reduced system DOF's, t is the time, a dot means a derivative with respect to time, M is the reduced mass matrix,  $f_{nl}$  is the  $n_q$ -column with reduced internal forces (containing the reduced stiffness and damping matrices) and  $f_{ex}$  is the  $n_q$ -column with reduced external loads. Notice that equation (1.6) has the same structure as equation (1.2), the equations of motion of the unreduced system.

#### 1.3.2 Periodic solution solvers and path-following.

For analyzing the long term behaviour of a nonlinear system, always numerical time integration of (1.6) can be carried out using for instance a Runge Kutta method or Adams method. As mentioned earlier, before a nonlinear dissipative system settles in a stable attractor, its orbit is transient. The time before settling in an attractor can be very long of duration, especially for weakly damped systems.

The long term behaviour can be analysed much more efficiently by calculating fixed points directly by solving equation (1.4) or by calculating periodic solutions by solving

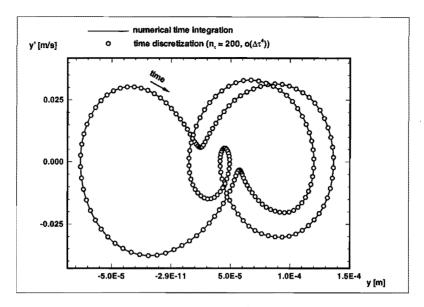


Figure 1.4 Phase portrait of periodic solution calculated by numerical time integration and finite difference method (time discretization with fourth order central difference scheme.)

a two-point boundary value problem of (1.6) with boundary condition

$$\begin{bmatrix} \boldsymbol{q}(t_0) \\ \dot{\boldsymbol{q}}(t_0) \end{bmatrix} = \begin{bmatrix} \boldsymbol{q}(t_0 + T_p) \\ \dot{\boldsymbol{q}}(t_0 + T_p) \end{bmatrix}$$
(1.7)

where  $T_p$  is the period time of the wanted periodic solution. In this way not only much computational time is saved but it is also possible to calculate unstable fixed points and unstable periodic solutions, like saddles and repellors. In the previous subsection it was already stated that saddles play an important role in structuring the phase portrait and the basin boundaries.

In this thesis three numerical methods are used for solving the two-point boundary value problems to determine periodic solutions. In the *finite difference method* the time is discretized, approximating the accelerations and velocities using the displacements at different time points (figure 1.4). In this thesis we use equidistant time steps making the method very efficient for systems with many degrees of freedom. However, because of the equidistant mesh, the method is not very useful for systems with "hard" discontinuities.

The (*multiple*) shooting method uses a time-integration method for solving the twopoint boundary value problem. The initial state of the system is iteratively changed until the boundary conditions are satisfied. The accuracy of this method depends on the time-integration method used. In this thesis a variable step/order Adams method is used for time-integration, so very accurate results can be obtained by the shooting method, even for systems with "hard" discontinuities. However, this makes the method more time consuming than the finite difference method. Furthermore, the computational time increases very much with the number of DOF's of the system and therefore at this moment the application of the method is only realistic for systems with approximately less than eight DOF's. It should be noticed that also the multiple shooting method in combination with a variable step/order Adams method for time-integration will not be suitable for all "hard" discontinuities. In this thesis, only systems with discontinuities in the stiffness are analysed and for this kind of systems, the multiple shooting method seems to work fine.

Finally, the *incremental harmonic balance method* approximates the periodic solution as a truncated Fourier series and applies a Galerkin method to calculate the coefficients in the Fourier series. The accuracy of this method depends on the number of Fourier terms and on the accuracy of the integrals in the Galerkin method. This makes the method less useful for systems with "hard" discontinuities, because for this kind of systems the number of Fourier terms should be large and the integrals in the Galerkin method should be accurate. The method is very useful for getting quickly a global view of the nonlinear behaviour of a system, especially for rotor-bearing systems. In the analysis of this type of systems the number of Fourier terms is low.

By applying a *path-following* method in combination with one of the periodic solution solvers, periodic solutions can be calculated efficiently for varying values of a system parameter. In this way paths of periodic solutions (or fixed points) can be calculated and co-dimension 1 local bifurcations can be found. If two system parameters are varied, also co-dimension 1 local bifurcations can be followed; in this way co-dimension 2 local bifurcations can be found.

In appendix B the above numerical solvers for periodic solutions are described in more detail. Path-following is described in appendix C.

#### 1.3.3 Local stability.

Using the fixed point or periodic solution solvers, stable and unstable fixed points as well as stable and unstable periodic solutions can be found. The local stability of a fixed point can be determined by the eigenvalues of the linearized system about the fixed point, as mentioned in the previous section.

The local stability of a periodic solution can be determined using *Floquet theory*. Floquet theory linearizes the system about the periodic solution and integrates small perturbations over the period time. If at least one perturbation grows the periodic solution is unstable. Applying Floquet theory results in  $2n_q$  Floquet multipliers. If the moduli of all Floquet multipliers are lower than one, the periodic solution is stable. If one of the moduli is larger than unity, then the periodic solution is unstable. Using the Floquet multipliers, also co-dimension 1 bifurcations can be determined (see previous section).

A short summary of the Floquet theory is given in section 11.A.

#### **1.4** Organization of this thesis.

This thesis contains a collection of papers, published in various journals and books and is organized as follows. In part I of this thesis discontinuous systems are investigated numerically and experimentally. The system which is investigated is a simply supported beam system which is periodically excited in the middle. In one case the beam is supported at its middle by a one-sided linear spring. This beam system was earlier investigated by Fey (1992) and is discontinuous in the stiffness. In another case the beam system has at its middle an elastic stop which is modelled using the nonlinear contact law of Hertz. In this way an impact problem is created. For both systems experiments are carried out to verify the numerical results.

In part II of this thesis a method for calculating manifolds is described and it is shown how the global stability of attractors can be determined using these manifolds. The method is developed for single-DOF systems but it is shown that in some cases it also can be used for multi-DOF systems. Experiments using the beam with at its middle a one-sided spring are carried out to verify the numerical results for the global stability of the attractors.

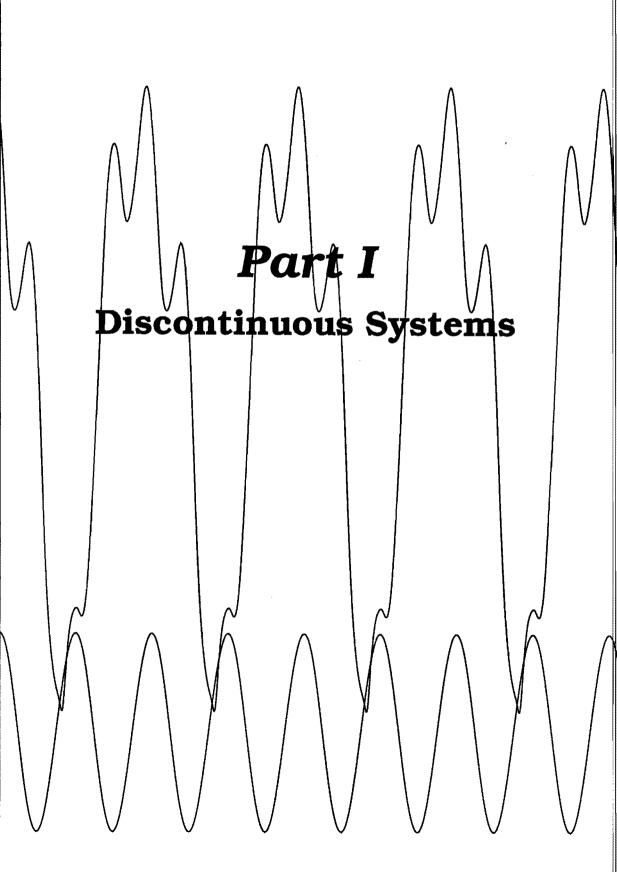
Part III is focussed on flexible rotor-bearing systems. A simple rotor-bearing system is investigated consisting of a flexible shaft with disk, supported on one side by an oil journal bearing and pinned on the other side. This system is analysed for different bearing models and imbalances. Special attention is given to the modelling of the oil journal bearings in nonlinear dynamic analysis.

In part IV of this thesis a control method is presented for stabilizing unstable harmonic orbits in order to reduce large system responses with low control effort. Applying this control method, the beam with one-sided spring of part I is controlled to unstable harmonic orbits using one single control force. Methods are presented to determine the stability of the controlled system and to determine the controllability of nonlinear systems.

#### References

- Aarts, J.W., 1993, "Component Mode Synthesis for Nonlinear Dynamical Systems," Master's thesis, WFW-report 93.048, TNO-report 93-CMC-R0546, Department of Mechanical Engineering, Eindhoven University of Technology, Eindhoven, The Netherlands (in Dutch).
- Craig Jr., R.R., 1985, "A Review of Time-Domain and Frequency-Domain Component Mode Synthesis Methods," *Combined Experimental/Analytical Modeling of Dynamic Structural Systems Using Substructure Synthesis*, D.R. Martinez and A.K. Miller, ed., ASME Applied Mechanics AMD-67, New York, pp. 1-31.
- Crooijmans, M.T.M, 1987, "On the Computation of Stationary Deterministic Behaviour of Non-Linear Dynamic Systems with Applications to Rotor-Bearing Structures," *PhD thesis*, Department of Mechanical Engineering, Eindhoven University of Technology, Eindhoven, The Netherlands, 1987.

- DIANA, 1995, *DIANA User's Manual 6.0 ed.*, TNO Building and Construction Research, Delft, The Netherlands.
- Feigenbaum., M.J., 1983, "Universal Behavior in Nonlinear Systems," *Physica*, Vol.7D, pp. 16–39.
- Fey, R.H.B., 1992, "Steady-State Behaviour of Reduced Dynamic Systems with Local Nonlinearities," *PhD thesis*, Department of Mechanical Engineering, Eindhoven University of Technology, Eindhoven, The Netherlands.
- Guckenheimer, J. and Holmes, P., 1983, "Nonlinear Oscillations, Dynamical Systems and Bifurcations of Vector Fields," *Applied Mathematical Sciences* 42, Springer-Verlag.
- Newhouse, S., Ruelle, D., and Takens, F., 1978, "Occurrence of Strange Axiom-a Attractors near Quasi-Periodic Flow on T<sup>m</sup>, m ≤ 3," Commun. Math Phys., Vol. 64, pp. 35-40.
- Parker, T.S. and Chua, L.O., 1989, "Practical Numerical Algorithms for Chaotic Systems," SpringerVerlag.
- Pomeau, Y. and Manneville, P., 1980, "Intermittent Transition to Turbulence in Dissipative Dynamical Systems," *Commun. Math. Phys*, Vol. 74, pp. 189-197.
- Thompson, J.M.T., 1994, "Basic Concepts of Nonlinear Dynamics," Nonlinearity and Chaos in Engineering Dynamics, Proceedings IUTAM Symposium, London, 19-23 July 1993, J.M.T. Thompson and S.R. Bishop, ed., John Wiley & Sons, pp. 1–21.
- Thompson, J.M.T. and Stewart, H.B., 1986, "Nonlinear Dynamics and Chaos," John Wiley & Sons Ltd.
- Wijckmans, M.W.J.E., 1995, "Dynamic Analyses of Idealised Solar Panels with a Bilinear Snubber," *Master's thesis*, WFW-report 95.071, Department of Mechanical Engineering, Eindhoven University of Technology, Eindhoven, The Netherlands.



# CHAOS AND BIFURCATIONS IN A MULTI-DOF BEAM SYSTEM WITH NONLINEAR SUPPORT.<sup>‡</sup>

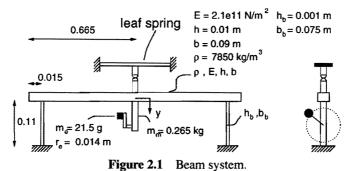
This paper deals with the long term behaviour of periodically excited mechanical systems consisting of linear components with many degrees of freedom and local nonlinearities. The system which is investigated is a 2D beam supported in the middle by a one-sided spring and excited by a periodic force. The linear part of this system is modelled using the finite element method and reduced using a component mode synthesis method. Models with 1 and 4 degrees of freedom are investigated. Branches of periodic solutions and branches of bifurcation points are calculated. Also stable and unstable manifolds are calculated. The system shows (sub)harmonic, quasi-periodic and chaotic behaviour. An intermittency route to chaos is investigated into detail. Experimental results of the beam system are compared with numerical results.

## 2.1 Introduction.

This paper deals with the long term behaviour of periodically excited mechanical systems, which consist of linear components with many degrees of freedom (DOF's) and local nonlinearities. As a practical example of such a system, one may think of a mooring-buoy which is connected by a cable to a ship and is excited by the waves of the sea, see Thompson & Stewart (1986). In this system the local nonlinearity is the cable (one-sided spring).

The linear components, which are supposed to be slightly or proportionally damped, are reduced using a component mode synthesis method based on free-interface eigenmodes and residual flexibility modes, Craig (1985). Only eigenmodes up to a cut-off frequency are kept in the reduced component. The residual flexibility modes guaran-

<sup>&</sup>lt;sup>‡</sup>Fey, R.H.B., Van de Vorst, E.L.B., Van Campen, D.H., De Kraker, A., Meijer, G.J., and Assinck, F.H., 1994, "Chaos and Bifurcations in a Multi-DOF Beam System with Nonlinear Support," *Nonlinearity and Chaos in Engineering Dynamics, Proceedings IUTAM Symposium, London, 19-23 July 1993*, J.M.T. Thompson and S.R. Bishop, ed., John Wiley & Sons, pp. 125–139 (updated, results published in Van Campen et al. (1995)).



tee unaffected (quasi-)static load behaviour of the reduced components. The highest kept eigenfrequency gives an indication for the highest frequency for which the reduced model is valid. The nonlinear components and the reduced linear components are coupled in order to approximate the unreduced system. The highest excitation frequency must be much lower than the cut-off frequency because the nonlinear system response contains higher frequencies than the excitation frequency. The choice of this cut-off frequency is not obvious. However, using this reduction method, it still remains possible to investigate efficiently the long term behaviour of systems with local nonlinearities, which are modelled using the finite element method, see Fey et al. (1992a).

In section 2.2 a periodically excited beam system with nonlinear support is introduced. The long term behaviour of two reduced models (1 and 4 DOF's) of this system is analysed. These models are derived using the reduction method mentioned above. In section 2.3 the single-DOF model is investigated. Periodic solutions are calculated by solving a two-point boundary value problem with the finite difference method, Fey (1992b). Branches of periodic solutions are followed using a path following technique. The local stability of these periodic solutions is investigated using Floquet theory. Basins of attraction of the single-DOF model are calculated using a method for calculating manifolds of unstable periodic solutions, Parker & Chua (1989). In section 2.4 the four-DOF model is investigated. Branches of bifurcation points are calculated using the shooting method in combination with path following, Meijaard (1991). Unstable manifolds are calculated for the four-DOF model. An experimental setup of the beam system has been constructed and experimental results are compared with numerical results in section 2.5. All calculations presented in this paper were carried out using a development release of the finite element package DIANA (1995).

## 2.2 Beam system supported by one-sided spring.

Figure 2.1 shows the beam system which is analysed both numerically and experimentally. The beam is supported at both ends by leaf springs, and supported in the middle by an one-sided leaf spring. The periodic force is realized by a rotating mass.

The beam and leaf springs are modelled using the finite element method and reduced using the component mode synthesis method mentioned above. The one-sided leaf spring is modelled by a linear one-sided massless spring. Because of symmetry only

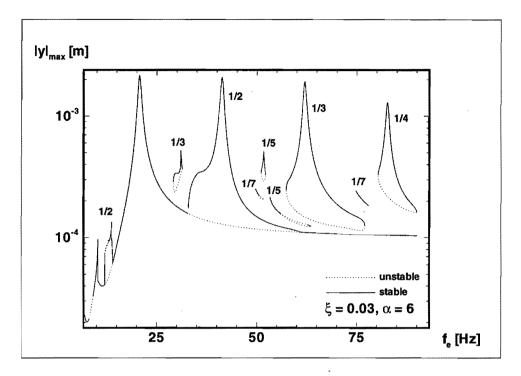


Figure 2.2 Maximum displacements of periodic solutions of single-DOF model. half the beam is modelled.

## 2.3 Single-DOF model.

The equation of motion for the single-DOF model is:

$$m\ddot{y} + b\dot{y} + k(\alpha_p + 1)y = m_e r_e \omega^2 \cos(\omega t)$$
(2.1)

Here  $\alpha_p = \begin{cases} \alpha, \ y < 0 \\ 0, \ y \ge 0 \end{cases}$  and  $\alpha = 6$ ,  $\omega = 2\pi f_e$ ,  $b = 2\xi\sqrt{mk}$ ,  $\xi = 0.03$ ,  $m = (\varphi_1^T M \varphi_1)/\varphi_{1y}^2 = 2.37$  kg,  $k = (\varphi_1^T K \varphi_1)/\varphi_{1y}^2 = 18960$  N/m,  $m_e = 10.75$  g,  $r_e = 0.014$  m. M and K are the mass and the stiffness matrix of the linear part of the system, i.e. the beam without the one-sided spring.  $\varphi_1$  is the first eigenmode of the linear system with an eigenfrequency of 14.2 Hz.  $\varphi_{1y}$  is the element of  $\varphi_1$  corresponding with the displacement of the middle of the beam y. Branches of periodic solutions of this system are calculated for varying excitation frequency  $f_e$ . The maximum displacements of these periodic solutions are given in figure 2.2. Besides the harmonic peak near 20.8 Hz also 1/2, 1/3, 1/4, 1/5 and 1/7 subharmonic resonances are found.

The highest 1/2, 1/3 and 1/4 subharmonic resonance peaks are related to the first harmonic resonance peak near 20.8 Hz. The 1/3 subharmonic near 31 Hz, the two 1/5

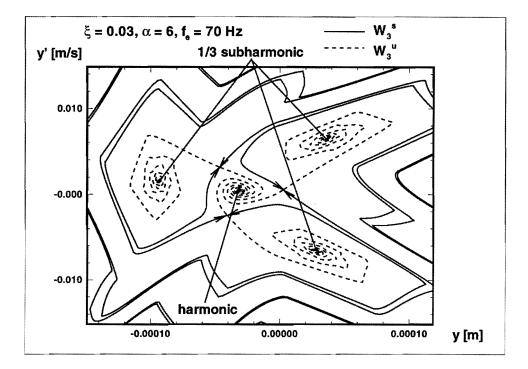


**Figure 2.3** Poincaré section with stable and unstable manifolds ( $W_3^s$  and  $W_3^u$ ) of single-DOF system at  $f_e = 70$  Hz.

subharmonics near 55 Hz and the 1/7 subharmonic near 75 Hz are related to the 2nd superharmonic resonance peak near 10 Hz. The 1/2 subharmonic near 13.8 Hz and the 1/7 subharmonic near 50 Hz are related to the 3rd superharmonic resonance peak near 7 Hz.

The stable and unstable manifolds ( $W_3^s$  and  $W_3^u$ ) of the unstable 1/3 subharmonic which exists at  $f_e = 70$  Hz, are shown in figure 2.3. This figure shows that one half of  $W_3^u$  goes to the stable 1/3 subharmonic attractor and the other half of  $W_3^u$  goes to the stable harmonic attractor.  $W_3^s$  represent the boundaries of the basins of attraction of these attractors.

Figure 2.4 shows the unstable and stable manifolds of the unstable harmonic and unstable 1/7 subharmonic saddle solution at  $f_e = 50.5$  Hz. Homoclinic and heteroclinic intersections of the stable and unstable manifolds exist. If a stable and an unstable manifold intersect, an infinitely number of other intersections of the two manifolds *must exist*. Because of this the manifolds get a chaotic structure. In this area of the Poincaré section no chaotic attractor could be found, only one 1/2 subharmonic and one 1/7 subharmonic attractor exist. Because of the homoclinic and heteroclinic intersections the boundaries of the basins of attraction of these attractors are fractal. The dimension of the boundaries of the basins of attraction is calculated to be 1.85, Grebogi et al. (1983).

Note, that the distance between the stable manifolds and the 1/7 subharmonic attractor

#### 2.4. FOUR-DOF MODEL.

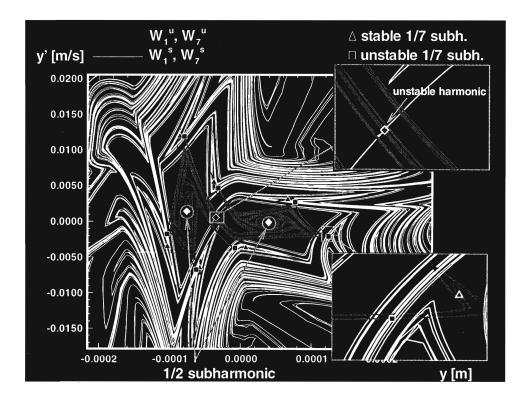


Figure 2.4 Poincaré section with stable and unstable manifolds of single-DOF system at  $f_e = 50.5$  Hz.

is very small; a little disturbance on the system vibrating in this attractor can easily result in a jump to the 1/2 subharmonic attractor, Soliman & Thompson (1990).

#### 2.4 Four-DOF model.

If the linear system is reduced with the component mode synthesis method to 4 degrees of freedom (3 eigenmodes with eigenfrequencies  $f_1 = 14.2$  Hz,  $f_2 = 127.3$  Hz,  $f_3 = 352.8$ Hz and one residual flexibility mode), the linear model is valid up to a frequency of 350 Hz. Earlier investigation of a similar system showed that the four-DOF model including the one-sided spring with  $\alpha = 6$  is a good approximation of the unreduced system for excitation frequencies  $f_e$  lower than 80 Hz, Fey (1992b). Again branches of periodic solutions are calculated for this four-DOF model for varying excitation frequency  $f_e$ . The maximum displacements of the periodic solutions for the middle of the beam are given in figure 2.5.

Figure 2.5 shows that the response of the four-DOF model is very similar to the response of the single-DOF model (figure 2.2). At the harmonic branch now extra superharmonic resonance peaks are found caused by the second eigenfrequency of the

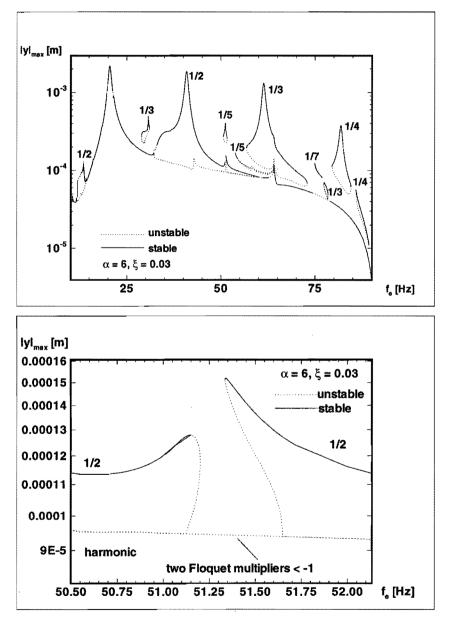


Figure 2.5 Maximum displacements of periodic solutions of the four-DOF model. y is the displacement of the middle of the beam.

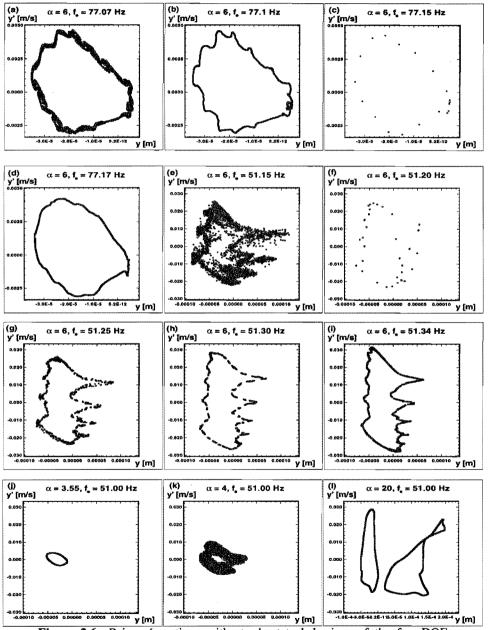


Figure 2.6 Poincaré sections with steady-state behaviour of the four-DOF model.

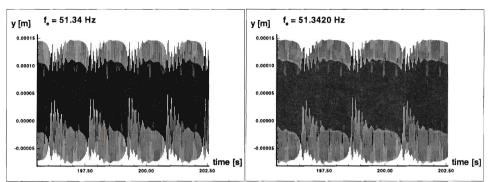
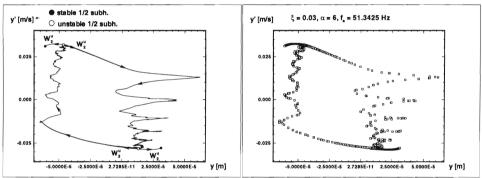


Figure 2.7 Steady-state behaviour of the four-DOF model: intermittency.



**Figure 2.8** (a) Unstable manifolds of unstable 1/2 subharmonic. (b) Transient of four-DOF model.

model. Near 64 Hz, 42 Hz, 32 Hz, 25 Hz, the 2nd, 3rd, 4th and 5th superharmonic resonance peaks of the second harmonic resonance peak exist, respectively.

At the right-hand side of the 1/3 subharmonic branch the harmonic branch is now unstable marked by two secondary Hopf bifurcations. In this frequency interval quasiperiodic behaviour and mode-locking leading to chaos is found, Newhouse et al. (1978) (figures 2.6a-2.6d). The quasi-periodic and chaotic behaviour in this frequency range is dominated by a frequency of about 25 Hz. Near 25 Hz the 5th superharmonic resonance peak exists which is related to the second harmonic resonance peak (near 127.3 Hz). Also an extra 1/3 subharmonic branch was found near 78 Hz. Both the quasi-periodic mode-locking route leading to chaos and the extra 1/3 subharmonic branch are related to the 5th superharmonic resonance peak near 25 Hz.

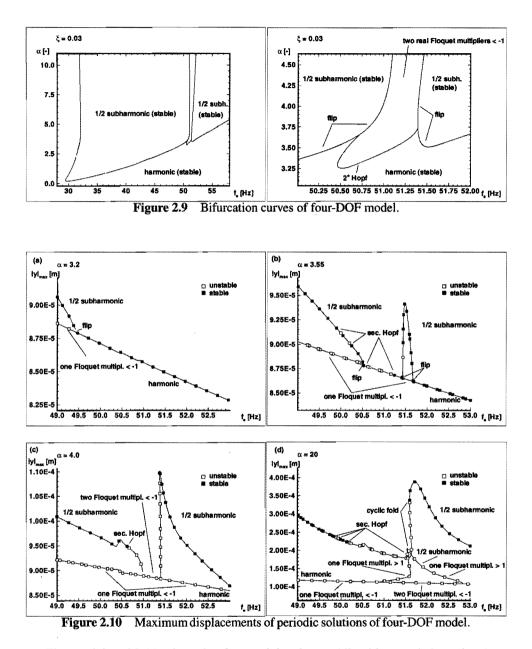
This 5th superharmonic resonance peak is also responsible for the fact that the 1/2 subharmonic branch is divided into two parts now in the frequency range near 50 Hz. Between the two 1/2 subharmonic branches only an unstable harmonic branch exists, which has *two* real Floquet multipliers lower than -1. The steady-state behaviour of the four-DOF model in the frequency range near 50 Hz is shown in figures 2.6e-2.6i and figure 2.7. Figure 2.7 shows that if the excitation frequency  $f_e$  is near 51.34 Hz the

steady-state behaviour seems to be periodic over a long time but then suddenly shows a small burst, after which the almost periodic behaviour recovers again. This kind of chaotic behaviour is called intermittency, see Pomeau & Manneville (1980). If the excitation frequency is decreased the periodic behaviour intervals become smaller until the behaviour is entirely chaotic. Like in the frequency range 77-78 Hz, the chaotic behaviour is again dominated by a frequency of about 25 Hz; the intermittency interval is related to the 5th superharmonic resonance peak of the second harmonic resonance peak.

At  $f_e = 51.3425$  Hz besides the unstable harmonic with two Floquet multipliers lower than -1, also a stable and an unstable 1/2 subharmonic and a stable and an unstable 1/5 subharmonic exist (figure 2.5). The unstable manifolds  $W_2^u$  of the unstable 1/2 subharmonic saddle solutions are shown in figure 2.8a. In this figure, the crosssections of the manifolds are not homoclinic points because these are manifolds of a multi-DOF model (unstable manifolds do not intersect one another of course). The figure shows that one half of  $W_2^u$  goes to the 1/2 subharmonic attractor. The other half of  $W_2^u$  almost returns to the unstable 1/2 subharmonic saddle solution and almost creates a homoclinic connection. A homoclinic connection exists when the unstable manifold returns to its unstable periodic saddle solution: simultaneously it is the stable manifold of that unstable periodic saddle solution. This is not the case here, because  $W_2^u$  has a chaotic structure in the neighbourhood of the unstable 1/2 subharmonic saddle solution, which indicates that here an infinitely number of intersections exist of  $W_2^u$ and the stable manifold  $W_2^s$  of the unstable 1/2 subharmonic saddle solution. In figure 2.8b a transient is shown, which has the same structure as  $W_2^u$ . Because  $W_2^u$  finally approaches the unstable 1/2 subharmonic\*, this transient finally ends in the stable 1/2subharmonic. The unstable manifolds of the harmonic  $W_1^u$  solutions are planes in the Poincaré section, spanned by the two eigenmodes corresponding with the two Floquet multipliers which are lower than -1. These manifolds finally approach a curve which has the same structure as  $W_2^u$ . One half of the unstable manifolds of the unstable 1/5 subharmonic also approaches a curve with the same structure as  $W_2^u$ , whereas the other half ends in the stable 1/5 subharmonic. If  $f_e$  is decreased the stable 1/2 subharmonic and unstable 1/2 subharmonic saddle solution disappear via a cyclic fold bifurcation. Because of this the transient behaviour in figure 2.8b becomes stable resulting in the steady-state behaviour becoming chaotic with almost the same structure as  $W_2^u$  at  $f_e =$ 54.3425 Hz; this behaviour is called intermittency (figure 2.6i).

The bifurcation points (one real Floquet multiplier lower than -1, and one Floquet multiplier equal to -1), which mark out the intermittency interval are followed. Here, two system parameters must be varied which are chosen to be the excitation frequency  $f_e$  and the relative stiffness of the one-sided spring  $\alpha$ . The branches of bifurcation points are given in figure 2.9. In figure 2.10 the response is given in the frequency range near 50 Hz for different values of the relative stiffness of the one-sided spring  $\alpha$ .

<sup>\*</sup>Because in the neighbourhood of the 1/2 subharmonic saddle solution  $W_2^u$  intersects with  $W_2^s$ , an infinitely number of intersections must exist and because  $W_2^s$  goes to the 1/2 subharmonic saddle solution,  $W_2^u$  must also approach the unstable 1/2 subharmonic saddle solution.



Figures 2.9 and 2.10a show that for  $\alpha = 3.2$  only one 1/2 subharmonic branch exists, next to the harmonic branch, which becomes unstable via a flip bifurcation. If  $\alpha$  is increased a small part of the stable harmonic branch becomes unstable via two secondary Hopf bifurcations at the right-hand side of the 1/2 subharmonic branch. Quasi-periodic behaviour was found in this frequency interval (figure 2.6j). Further increasing  $\alpha$  to 3.55 (figure 2.10b) results in a second 1/2 subharmonic branch. If  $\alpha$  is increased once again

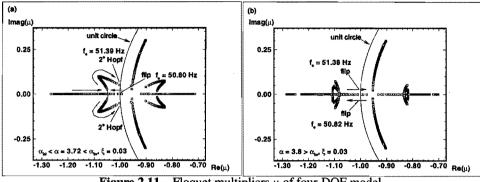


Figure 2.11 Floquet multipliers  $\mu$  of four-DOF model.

the flip bifurcation, which marks the left 1/2 subharmonic branch, approaches the left secondary Hopf bifurcation. At the point where they merge,  $\alpha = \alpha_{bl}$ , a co-dimension 2 bifurcation exists. Here, three Floquet multipliers are equal to -1. If  $\alpha$  is increased again to  $\alpha_{br}$ , another co-dimension 2 bifurcation is created, when the right secondary Hopf bifurcation touches the left flip bifurcation of the right 1/2 subharmonic branch. The middle part of the harmonic branch is unstable with two Floquet multipliers lower than -1 (figure 2.10c). Chaotic behaviour was found in this frequency interval (figure 2.6k).

Note, that the two co-dimension-2 bifurcations do not exist for the same value of  $\alpha$ . If  $\alpha$  is between  $\alpha_{bl}$  and  $\alpha_{br}$  the middle unstable part of the harmonic branch is marked at the left-hand side by one Floquet multiplier equal to -1 and one real Floquet multiplier lower than -1, while at the right-hand side a secondary Hopf bifurcation exists. At the left-hand side of the middle unstable part of the harmonic branch *two* real Floquet multipliers are lower than -1 and at the right-hand side two complex Floquet multipliers have a modulus larger than 1. In figure 2.11a the Floquet multipliers are shown as a function of the excitation frequency  $f_e$ . The two real Floquet multipliers lower than -1 become equal at some point and subsequently they become conjugate complex; at the secondary Hopf bifurcation their modulus has been decreased to 1. Figure 2.11b shows that if  $\alpha$  is larger than  $\alpha_{br}$  the Floquet multipliers still become complex in this frequency range but do not pass the unit circle any more.

Figure 2.10d shows the response of the system in the frequency area around 50 Hz for  $\alpha = 20$ . The left-hand and right-hand 1/2 subharmonic branches have been connected resulting in an upper and a lower 1/2 subharmonic branch. An unstable part exists at the upper 1/2 subharmonic branch marked by two secondary Hopf bifurcations. Here, stable quasi-periodic behaviour exists with a base frequency which is half the excitation frequency. In the Poincaré section this is represented by two closed curves (figure 2.6l).

### 2.5 Experiments.

An experimental setup of the beam system presented in figure 2.1 has been constructed with  $m_e = 46.86$  g,  $\alpha = 6.49$  and  $\xi = 0.015$ . In figure 2.12 numerical and experimental

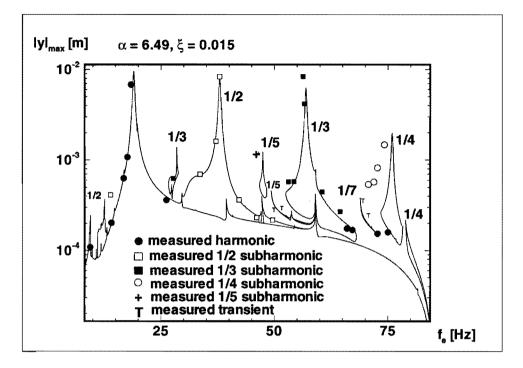


Figure 2.12 Experimental results.

results are compared. The experimental results correspond very well with the numerical results (four-DOF model) represented by the solid lines; almost all subharmonics are observed in the experiments.

No periodic behaviour was found in the experiment in the frequency range near 50 Hz (T symbols). The numerical results predict two unstable 1/5 subharmonics and one stable 1/2 subharmonic. In section 2.3 fractal boundaries of basins of attraction were found for the single-DOF system in this frequency range. Earlier investigation of a similar system showed that the 1/2 subharmonic attractor has a low global stability in this frequency range, Van de Vorst et al.(1993). This explains why in the experiment no periodic behaviour is found in this frequency range because system parameters will not be time-invariant exactly, in particular the excitation frequency  $f_e$ .

#### 2.6 Conclusions.

In this paper a nonlinearly supported beam system was investigated. The beam was modelled using the finite element method. This model was reduced using a component mode synthesis method. In this system the first few eigenfrequencies cover a broad frequency range. This is the reason why the single-DOF model shows almost the same frequency response as the four-DOF model in the low frequency range. The

#### 2.6. CONCLUSIONS.

experimental results confirm this. Sometimes it is insufficient to investigate only local stability using Floquet theory. This theory does not detect fractal boundaries of basins of attraction which may cause attractors to have a low global stability. In the experiment no periodic behaviour could be found in frequency intervals where the numerical results predicted periodic attractors with a low global stability. The general conclusion is that it is possible to investigate complicated systems with local nonlinearities both efficiently and accurately by using the reduction method.

The results show that by adding a relatively weak discontinuous support, the dynamics of the beam system become dramatically more complicated. As stated above, the first few eigenfrequencies cover a broad frequency range and for systems for which this does not hold, the dynamics will be more complicated. However, the investigated system has a very low damping level. Increasing of the damping suppresses the nonlinear phenomena like the higher order subharmonics and fractal boundaries of basins of attraction. Furthermore, a higher damping level will decrease the influence of the higher eigenmodes of the system on lower excitation frequencies. Nevertheless, if the stiffness of the one-sided spring is increased and if the system has more eigenfrequencies in the investigated frequency domain, the damping level has to be very high for suppressing all nonlinear phenomena.

#### References

- Van Campen, D.H., Van de Vorst, E.L.B., Van der Spek, J.A.W., and De Kraker, A., 1995, "Dynamics of a Multi-DOF Beam System with Discontinuous Support," *Nonlinear Dynamics*, Vol. 8, pp. 453–466.
- Craig Jr., R.R., 1985, "A Review of Time-Domain and Frequency-Domain Component Mode Synthesis Methods," *Combined Experimental/Analytical Modeling of Dynamic Structural Systems Using Substructure Synthesis*, D.R. Martinez and A.K. Miller, ed., ASME Applied Mechanics AMD-67, New York, pp. 1-31.
- DIANA, 1995, *DIANA User's Manual 6.0 ed.*, TNO Building and Construction Research, Delft, The Netherlands.
- Grebogi, C., McDonald, S.W., Ott, E., Yorke, Y.A., 1983, "Final State Sensitivity: An Obstruction to Predictability," *Physics Letters*, Vol. 99A, pp. 415-418.
- Fey, R.H.B., Van Campen, D.H. and De Kraker, A., 1992a, "Long Term Structural Dynamics of Mechanical Systems With Local Nonlinearities," *Nonlinear Vibrations*, Vol. DE-50, AMD-144, WAM of the ASME, Anaheim CA. Also published in ASME *Journal of Vibration and Acoustics*, April 1996 (in press).
- Fey, R.H.B., 1992b, "Steady-State Behaviour of Reduced Dynamic Systems with Local Nonlinearities," *PhD thesis*, Department of Mechanical Engineering, Eindhoven University of Technology, Eindhoven, The Netherlands.
- Meijaard, J.P., 1991, "Dynamics of Mechanical Systems, Algorithms for a Numerical Investigation of the Behaviour of Non-Linear Discrete Models," *PhD thesis*, Delft University of Technology, Delft, The Netherlands.

#### 34 CHAPTER 2. CHAOS AND BIFURCATIONS IN A MULTI-DOF BEAM SYSTEM...

- Newhouse, S., Ruelle, D., and Takens, F., 1978, "Occurrence of Strange Axiom-a Attractors near Quasi-Periodic Flow on T<sup>m</sup>, m ≤ 3," Commun. Math Phys., Vol. 64, pp. 35-40.
- Parker, T.S. and Chua, L.O., 1989, "Practical Numerical Algorithms for Chaotic Systems," Springer-Verlag.
- Pomeau, Y. and Manneville, P., 1980, "Intermittent Transition to Turbulence in Dissipative Dynamical Systems," *Commun. Math. Phys*, Vol. 74, pp. 189-197.
- Soliman, S.M. and Thompson, J.M.T., 1990, "Stochastic Penetration of Smooth and Fractal Basin Boundaries under Noise Excitation," *Dynamics and Stability Systems*, Vol. 5, pp. 281-298.
- Thompson, J.M.T. and Stewart, H.B., 1986, "Nonlinear Dynamics and Chaos," John Wiley & Sons Ltd.
- Van de Vorst, E.L.B., Fey, R.H.B., Van Campen, D.H., and De Kraker, A., 1993, "Manifolds of Nonlinear Dynamic Single-DOF Systems," *Topics in Applied Mechanics, Integration of Theory & Applications in Applied Mechanics*, J.F. Dijksman and F.T.M. Nieuwstadt, ed., Kluwer Academic Publishers, pp. 293-303.

# 3

# EXPERIMENTAL VERIFICATION OF THE STEADY-STATE BEHAVIOUR OF A BEAM SYSTEM WITH DISCONTINUOUS SUPPORT.<sup>‡</sup>

This paper deals with the experimental verification of the long term behaviour of a periodically excited linear beam supported by a one-sided spring. Numerical analysis of the beam showed subharmonic, quasi-periodic and chaotic behaviour. Furthermore three different routes leading to chaos were found. Because of the relative simplicity of the beam system and the variety of calculated nonlinear phenomena, an experimental setup is made of this beam system to verify the numerical results. The experimental results correspond very well with the numerical results as far as the subharmonic behaviour is concerned. Measured chaotic behaviour is proved to be chaotic by calculating Lyapunov exponents of experimental data.

# 3.1 Introduction.

Mechanical systems consisting of linear components with many degrees of freedom (DOF's) and local nonlinearities are frequently met in engineering practice. Examples of such systems are: rotating mechanical systems with nonlinear bearings, mechanical systems with dry friction and backlash phenomena in certain connections, etc.. From a spatial point of view the local nonlinearities constitute only a small part of the mechanical system. However, their presence generally will have important consequences for the overall dynamic behaviour.

Analyzing the long term behaviour of nonlinear systems is generally very expensive from a computational point of view and therefore it is important to keep the number of DOF's low. The long term behaviour of systems with local nonlinearities can be analysed efficiently if the number of DOF's of the linear parts is reduced using a component mode synthesis method (Craig, 1985, Fey, 1992). The component mode synthesis method used in this research is based on residual flexibility modes and free-interface eigenmodes up

<sup>&</sup>lt;sup>‡</sup>Van de Vorst, E.L.B, Assinck, F.H., De Kraker, A., Fey, R.H.B, and Van Campen, D.H., 1995, "Experimental Verification of the Steady-State Behaviour of a Beam System with Discontinuous Support," *Experimental Mechanics*, accepted for publication.

to a cut-off frequency. The residual flexibility modes guarantee unaffected (quasi-)static behaviour. The reduced linear parts are coupled with the local nonlinearities and this results in a reduced nonlinear system which is an approximation of the unreduced system. The reduced nonlinear system can be used up to the cut-off frequency. Because nonlinear systems can generate higher frequencies than the excitation frequency, in general the cut-off frequency has to be chosen much higher than the maximum excitation frequency.

In recent years, nonlinear dynamical systems have been studied by many people. For a general introduction in nonlinear dynamics the reader is referred to Guckenheimer and Holmes (1983), Thompson and Stuart (1986), Parker and Chua (1989) and Thompson (1994). The long term behaviour of a nonlinear system, which is excited by a periodic external load, can be periodic, quasi-periodic, or chaotic. The period of a periodic attractor may be equal to the excitation period (harmonic), but may also be a multiple of the excitation period (subharmonic). As an example, a 1/2 subharmonic attractor has a period, which is twice the excitation period. A quasi-periodic attractor is a function of two or more signals, which have incommensurate frequencies. A chaotic attractor is characterized by a broad band spectrum and by an extreme sensitivity for initial conditions.

Different attractors can coexist for one set of system parameters, i.e. the parameters which describe the system. Which attractor a trajectory will approach asymptotically when time proceeds, depends on the initial conditions of the system. Every attractor has its own basin of attraction, i.e. the set of initial conditions of trajectories which asymptotically approach the attractor. If only one attractor exists, the basin of attraction may be formed by all possible initial conditions.

Fey et al. (1992) investigated a 2-D pinned-pinned beam system with periodic excitation and supported by a one-sided spring and a linear damper in its point of symmetry. This system with a local nonlinearity was modelled using finite elements and reduced using the reduction method mentioned above. Subsequently periodic solutions of the reduced system were calculated for varying excitation frequency by solving a two-point boundary value problem using the finite difference method in combination with a path-following method (Fey, 1992). Figure 3.1 shows the maximum displacement y of the middle of the beam occurring in the periodic solutions for varying excitation frequency  $f_{\rm e}$ . The figure shows besides the first harmonic resonance peak also stable 1/2, 1/3, 1/5, 1/7 and 1/9 subharmonic resonance peaks. A quasi-periodic, mode-locking route leading to chaos was found in the frequency region  $f_e = 47-49$  Hz (Newhouse et al., 1978). Furthermore a period doubling cascade leading to chaos was found in the frequency region  $f_e = 8-9$  Hz. The stable 1/2 subharmonic branch is divided into two branches near  $f_e = 32$  Hz. In this frequency region except for a stable 1/7 subharmonic solution also stable intermitting behaviour was found (Pomeau & Manneville, 1980). This means that intervals with periodic behaviour are alternated with intervals with chaotic behaviour.

This paper deals with the experimental verification of the calculated nonlinear phenomena in the above beam system. Therefore an experimental setup is designed which corresponds as closely as possible to the numerical beam model. In section 3.2 the experimental setup is described and some remarks are made on the measuring equipment.

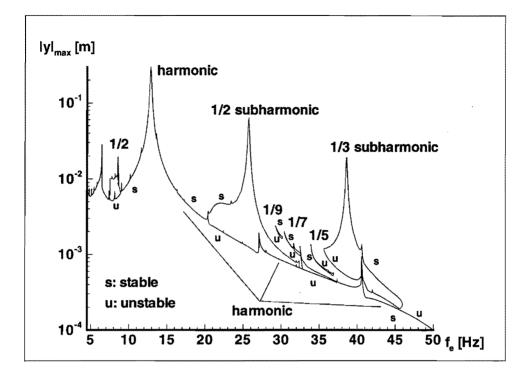


Figure 3.1 Maximum displacements of periodic solutions of a beam system supported in the middle by a one-sided spring. y is the displacement of the middle of the beam.

In section 3.3 the experimental results are compared with the numerical results, followed by some conclusions in section 3.4. All calculations presented in this paper were carried out using a development release of the finite element package DIANA (1995).

# 3.2 Experimental setup and numerical model.

Figure 3.2 shows the beam system which is analysed both numerically and experimentally. In the following subsections the experimental setup will be described in more detail.

#### 3.2.1 Beam supported by leaf springs.

The beam investigated by Fey (1992) was pinned at both ends. In the experiment the pinned-pinned beam is realized by a beam supported at both ends by leaf springs. The two leaf springs are dimensioned in such a way that the lowest three eigenfrequencies of the beam system do not differ too much compared to those of the pinned-pinned beam.

No extra damping was added because the system is already damped by air and material damping and too much damping would suppress the nonlinear phenomena.

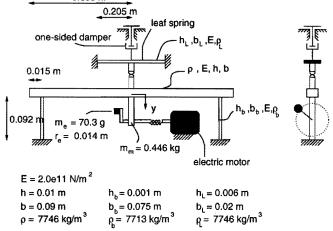


Figure 3.2 Experimental setup of beam system.

#### 3.2.2 Massless, one-sided spring.

The most critical point in the experimental setup is the local nonlinearity, the massless one-sided spring. In the experiment two options were investigated for modeling the one-sided spring.

In the first option the one-sided spring is realized using a thin long steel wire which is connected squared at the middle of the beam. Because of the very small buckling load of the wire, it will only generate tension loads behaving like a linear spring, so theoretically the wire acts as a one-sided spring. However, in the experiment the wire started vibrating in transversal direction which caused a disturbance on the beam. To suppress the transversal vibration of the wire, it was packed in foamed plastic. Because of this extra damping is added to the system.

Another problem was that the wire in tension did not behave like a *linear* spring due to stretching of the connection. Because of this in the experiment the derivative of the force to the displacement generated by the wire was continuous. Theoretically a one-sided spring implies that this derivative is discontinuous if the displacement is zero. Because the displacement range for which the wire behaves like a nonlinear spring was relatively large compared to the maximum displacements of the beam, a second option was investigated.

In the second option the one-sided spring is realized using a leaf spring which is placed parallel to the beam. Using a pin the beam and the one-sided spring can make contact (figure 3.2). An advantage of this option is that now the derivative of the force to the displacement generated by the one-sided leaf spring is discontinuous. A disadvantage of this option is that the leaf spring is not massless. To suppress the influences of the mass of the leaf spring, its dimensions are chosen such that its first eigenfrequency is much higher than the maximum excitation frequency. Furthermore, in the experiment the one-sided linear leaf spring is damped using a one-sided damper to achieve an uniform collision between the beam and the one-sided leaf spring. Because

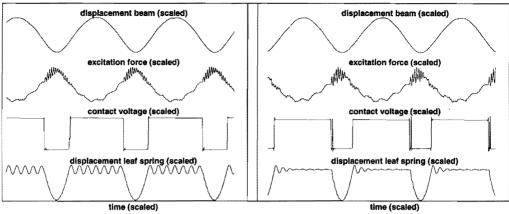


Figure 3.3 Experimental data for system without (left) and with (right) onesided damper ( $f_e = 18$  Hz).

a one-sided damper is used no extra damping is added to the system.

By adding a voltage difference between the beam and the one-sided leaf spring, the existence of contact between the beam and the one-sided leaf spring can be determined. Figure 3.3 shows the contact voltage, the measured excitation force and the measured displacements of the beam and the one-sided spring if the excitation frequency is  $f_e = 18$  Hz for the system with and without the one-sided damper. The figure shows that the one-sided leaf spring vibrates if the beam and the one-sided spring do not make contact (contact voltage high). If the one-sided damper is added to the leaf spring, it is damped out before the beam hits again the one-sided leaf spring. However, for higher excitation frequencies the available time for damping the leaf spring is reduced and for these excitation frequencies the leaf spring is not fully damped out before the beam hits it again. Notice that in figure 3.3 obviously the one-sided damper has a negative influence on the disturbances of the excitation force (see also section 3.2.4). Coincidentally for this frequency the undamped one-sided leaf spring and the beam move in the same direction as they make contact, which results in smaller disturbances on the measured excitation force.

Because the one-sided leaf spring yielded the best comparison of experimental and numerical results, the results presented in the next sections are based on this set-up.

#### 3.2.3 Periodic excitation.

It is important that during the experiment the periodic excitation is sinusoidal. In the first experiments an electric exciter was used for realizing the periodic excitation. This exciter worked very well for the linear beam but when the one-sided leaf spring was added, the generated excitation force was not sinusoidal any more. The excitation force lowered very much if the one-sided spring made contact with the beam. Because of this another exciter was used.

Another way to generate a sinusoidally excitation force is an electric motor driven, rotating mass at the middle of the beam. To prevent a force in y-perpendicular direction,

firstly two gear wheels with the same mass unbalance rotating in opposite direction were used for the periodic excitation. However, measurements of the excitation force showed that a lot of high frequencies were generated, probably caused by the teeth frequency. Because of this only one gear wheel with an unbalance was used. Using one gear wheel the high frequencies disappeared but a disadvantage of this approach is that the rotating mass also causes a force in y-perpendicular direction. The rotating mass was placed on the beam so that this extra force acts transversally on the beam. Acceleration measurements at both sides at the middle of the beam showed that the torsion of the beam generated by this force is very small and can be neglected.

The mass unbalance is driven by an electric motor. Because of the high weight of the motor, the motor is not connected to the beam and a flexible coupling is needed for coupling the mass unbalance with the rotor. For this flexible coupling two options were used: a rubber hose coupling and an aluminium coupling.

The rubber hose coupling has a very low bending and tension stiffness. A disadvantage of this coupling is that it has also a very low torsion stiffness which can lead to a rotation frequency modulation. The system with the rubber hose coupling showed in some frequency regions an extra 'strange' frequency in the response (see also section 3.3). Because it was assumed that this might be caused by the low torsion stiffness of the rubber coupling another coupling was tested. This cardan-type coupling consists of an aluminium pipe with at both ends a small stainless steel bellows. A disadvantage of this coupling is its rather high tension stiffness which causes an extra bending moment on the beam if the displacement of the middle of the beam is high.

The experimental results presented in the next section are done using both the rubber hose and aluminium coupling.

#### 3.2.4 Measurement set-up.

The displacements of the middle of the beam and the one-sided leaf spring are measured using contactless LVDT's. A force transducer between the beam and the exciter gives an indication of the acting excitation force. Notice that this force transducer also measures the mass influences of the exciter so the measured excitation force does not exactly equal the generated excitation force. This is one of the reasons for the disturbances on the measured excitation force in figure 3.3. The excitation frequency, which can be varied by the power supplied to the electric motor, is measured with an optical device.

#### 3.2.5 Numerical model.

In the numerical analysis the beam and leaf springs are modelled using finite elements and subsequently reduced with the component mode synthesis method (mentioned in section 3.1) to four DOF's (three eigenmodes with eigenfrequencies  $f_1 = 13.1$  Hz,  $f_2 = 117.2$  Hz,  $f_3 = 352.9$  Hz and one residual flexibility mode). The reduced model is assumed to be valid up to a frequency of 350 Hz. Earlier investigation of a similar system showed that the 4-DOF model including the one-sided spring is a good approximation of the unreduced system for excitation frequencies  $f_e$  lower than 80 Hz (Fey, 1992).

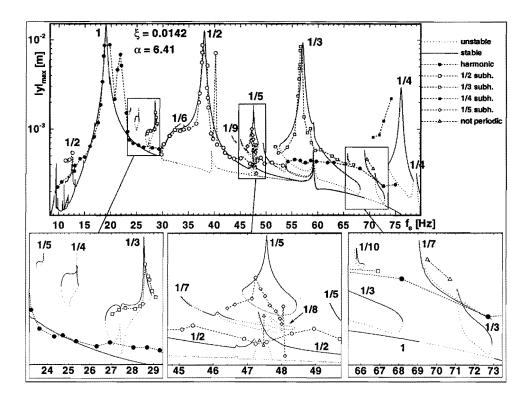


Figure 3.4 Numerical and experimental results (points) for beam system with rubber coupling.

The one-sided leaf spring is modelled by a one-sided linear spring, so mass influences and the one-sided damper are neglected. The stiffness of the one-sided spring is  $\alpha k$  with  $\alpha = 6.41$  and  $k = (\varphi_1^T K \varphi_1) / \varphi_{1y}^2 = 33754$  N/m. K is the stiffness matrix of the linear part of the system, i.e. the beam without the one-sided spring.  $\varphi_1$  is the first eigenmode of the linear system with an eigenfrequency of 13.1 Hz.  $\varphi_{1y}$  is the element of  $\varphi_1$  corresponding with the displacement y of the middle of the beam. So  $\alpha$  is approximately the scale factor of the one-sided spring stiffness with respect to the beam stiffness.

The damping in the system is estimated experimentally using logarithmic decrement evaluation and added to the model. In the model the beam is damped by a linear damper at the middle of the beam with damping constant  $b = 820\xi$  Ns/m, where  $\xi = 0.0142$ . Because of symmetry only half the beam is modelled.

#### 3.3 Experimental results.

In figure 3.4 the calculated and the measured maximum displacements occurring in the steady-state behaviour are shown for the system with the rubber hose coupling. The experimental points above 70 Hz were measured using another electric motor

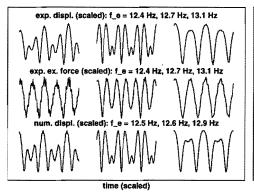


Figure 3.5 Numerical and experimental transients (1/2 subharmonic).

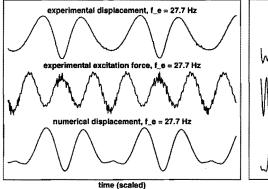


Figure 3.7 Numerical and experimen-

tal transients (1/3 subharmonic).

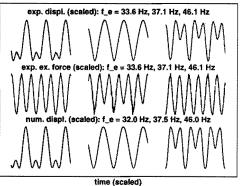


Figure 3.6 Numerical and experimental transients (1/2 subharmonic).

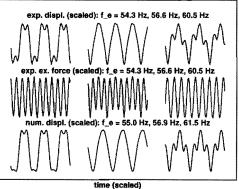


Figure 3.8 Numerical and experimental transients (1/3 subharmonic).

with less power but with a higher maximum angular speed. The experimental results correspond surprisingly well with the numerical results. Almost all subharmonics are observed in the experiments and they match very well both in frequency and maximum displacements. In figures 3.5–3.10 some experimental and numerical transients of subharmonics are compared. The results in these figures indicate that also in the time domain the subharmonics resemble. The 1/3-subharmonic around 28 Hz and the 1/4 subharmonics around 74 Hz were even observed experimentally first and found numerically afterwards.

The results depicted in figure 3.4 indicate that extra peaks occur right behind the harmonic, 1/2 subharmonic and 1/3 subharmonic resonance peaks. In these peaks the behaviour of the system is not periodic but a small extra ('strange') frequency occurs in the response. Assumed was that this frequency is caused by the low torsional stiffness of the rubber hose coupling resulting in a nonuniform rotational excitation frequency.

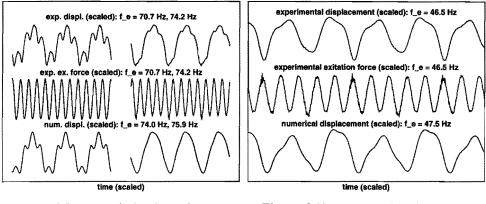


Figure 3.9 Numerical and experimental transients (1/4 subharmonic).

Figure 3.10 Numerical and experimental transients (1/5 subharmonic).

New experiments showed that the extra peaks disappear for these frequency intervals if the aluminium coupling mentioned in section 3.2.3 is used. However, the small extra 'strange' frequency still occurred in the 1/2 subharmonic and 1/3 subharmonic solutions without influencing the maximum displacement. Probably the reason for the extra frequency is the interaction between the vibrating beam and the rotating mass which makes it difficult to control the rotational frequency without adding a large flywheel effect to the exciter.

In the frequency regions around 28 Hz, 47 Hz, 52-63 Hz, and 70-75 Hz coexistence of stable solutions is met. The 1/3 and 1/5 subharmonics in the frequency regions around 28 Hz and 47 Hz can be initiated experimentally by hitting the harmonically vibrating beam. In the frequency region 52-63 Hz it was very difficult to find the (stable) harmonic and 1/2 subharmonic solution due to the dominant 1/3 subharmonic attractor. A normal excitation frequency change and allowing only little disturbances on the system when vibrating in the harmonic or 1/2 subharmonic solution directly resulted in a jump to the stable 1/3 subharmonic attractor. Only by very slowly varying the excitation frequency starting with an excitation frequency for which the stable 1/3 subharmonic attractor does not exist and some patience, the harmonic and 1/2 subharmonic solutions could be found. This is caused by the fact that the stable harmonic and 1/2 subharmonic attractors under the 1/3 subharmonic branch have a low global stability, i.e. the boundaries of the basins of attraction lie very close to the stable and 1/2 subharmonic solutions (Van de Vorst et al., 1993, Fey et al., 1994, Soliman & Thompson, 1990). Because of this the harmonic solution underneath the 1/3 subharmonics in the frequency region 63-68 Hz could not be found experimentally.

Notice that in figure 3.4 the measured 1/2 subharmonics and harmonics underneath the 1/3 subharmonics have higher maximum displacements than the numerically calculated 1/2 subharmonic and harmonic solutions. Because of this these displacements were measured again now using the aluminium coupling. In the new experiments however it was much more difficult to find the 1/2 subharmonics and harmonics but the few measured solutions have maximum displacements which are now very similar to the

#### 44 CHAPTER 3. EXPERIMENTAL VERIFICATION OF THE STEADY-STATE BEHAVIOUR...

numerical solutions. This is probably caused by the higher axial and bending stiffness of the aluminium coupling which increases both the stiffness in horizontal and vertical direction of the system. Using the rubber hose coupling the stiffness in horizontal direction of the system is very low because of the two leaf springs at both ends of the beam. This easily results in vibrations in the horizontal direction, increasing apparently the maximum displacements of the beam for high excitation frequencies.

Numerically, quasi-periodic and chaotic behaviour was found in small frequency ranges (0.1 Hz) around 12 Hz and 47 Hz and in the frequency range 69-71 Hz. Experimentally no chaotic behaviour was found around 12 Hz, probably because the frequency range for which chaotic behaviour exists numerically is very small. Although the frequency range for which chaotic behaviour exists around 47 Hz is also very small, still aperiodic signals could be measured in this frequency interval.

Numerically in the frequency region 69-71 Hz a quasi-periodic mode-locking leading to chaos route was found. Experimentally some aperiodic signals were found in this frequency interval. However, the measured behaviour showed to be very similar to the coexisting numerical 1/7 subharmonic solutions. So obviously the aperiodic behaviour is caused by system disturbances.

Also in the frequency range around 53.5 Hz besides the 1/3 subharmonics, aperiodic behaviour was measured if the aluminium coupling was used (not visible in figure 3.4). In the numerical investigation of this frequency region stable 1/2 and 1/3 subharmonics, an unstable 1/3 subharmonic, an unstable harmonic and two unstable 1/5 subharmonics were found but no chaotic behaviour. Earlier numerical investigation by Van de Vorst et al. (1993) showed that in this frequency region fractal boundaries of basins of attraction are present. The fractal basin boundaries and the mass influences of the one-sided leaf spring probably are the reason for the measured aperiodic signals.

The aperiodic signals measured in the frequency range around 53.5 Hz using the aluminium coupling are additionally investigated using time-delay coordinates and by calculation of the highest Lyapunov exponents. Figure 3.11 shows the reconstructed phase space using time-delay coordinates (Packard et al., 1980) for the measured aperiodic behaviour at  $f_e = 53.5$  Hz and the measured 1/3 subharmonic behaviour at  $f_e = 54.2$  Hz. For the reconstruction 8192 measured displacement points are used with time increment 0.005 s. The embedding dimension m = 3 and delay time  $\tau = 0.01$  s. The figure clearly shows the difference between the aperiodic behaviour and the 1/3 subharmonic behaviour. Figure 3.12 shows the highest Lyapunov exponents of these signals calculated using the method of Wolf et al. (1985). The highest Lyapunov exponent of the aperiodic behaviour converges to 17. This supports the opinion that the behaviour at  $f_e = 53.5$  Hz is chaotic.

#### **3.4 Conclusions.**

In this paper an experimental verification of the steady-state behaviour of a periodically driven linear beam supported by a one-sided spring has been presented. The numerical

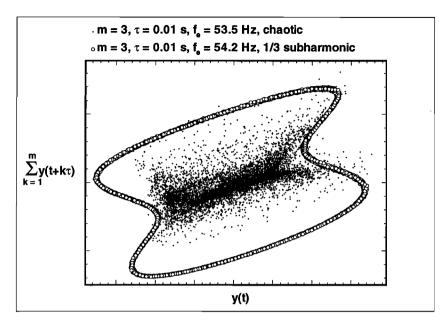


Figure 3.11 Reconstruction of phase space of experimental displacement of beam using time-delay coordinates.

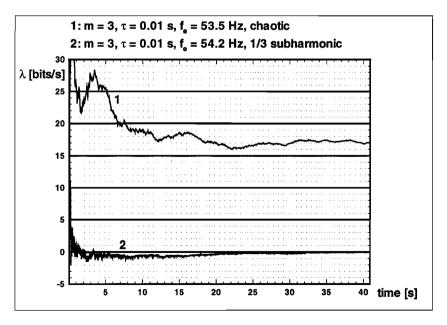


Figure 3.12 Highest Lyapunov exponents of experimental displacement of beam.

and experimental results match very well as far as the subharmonic behaviour is concerned. Also the existence of attractors with a low global stability and the coexistence of attractors is met in the experiments.

Measured aperiodic behaviour is proved to be chaotic by calculating the highest Lyapunov exponent of experimental data. The frequency regions for which chaotic behaviour was found are very small and also chaotic behaviour was found in frequency ranges for which numerically the existence of attractors with a low global stability is predicted. Because in the beam system which is investigated, the frequency regions for which numerically chaotic behaviour is found are very small, the system is not very suitable for investigating chaotic behaviour. However, in future experiments these frequency regions can be enlarged by increasing the stiffness of the one-sided spring.

Quasi-periodic behaviour was not found in the experiments probably because again this behaviour is found numerically in very small frequency intervals in the investigated system. Numerical calculations showed that for higher excitation frequencies the frequency intervals for which quasi-periodic behaviour exists are larger. For investigation of these intervals another electric motor will be needed with a higher maximum angular speed. It is also important in the near future to create a set-up for a more uniform rotational speed of the exciter device.

This paper shows that despite of the fact that it is very difficult to realize a periodic sinusoidal excitation force and a one-sided spring in an experiment, the most important nonlinear phenomena could be measured experimentally. Apparently, the mass-influences of the one-sided leaf spring and the disturbances on the sinusoidal excitation force do not affect the nonlinear phenomena.

The general conclusion is that it is possible to model and to investigate complicated dynamic systems with local nonlinearities both efficiently and accurately by using finite elements in combination with a reduction method and a nonlinear dynamics toolbox.

#### References

- Craig Jr., R.R., 1985, "A Review of Time-Domain and Frequency-Domain Component Mode Synthesis Methods," *Combined Experimental/Analytical Modeling of Dynamic Structural Systems Using Substructure Synthesis*, D.R. Martinez and A.K. Miller, ed., ASME Applied Mechanics AMD-67, New York, pp. 1-31.
- DIANA, 1995, *DIANA User's Manual 6.0 ed.*, TNO Building and Construction Research, Delft, The Netherlands.
- Fey, R.H.B., 1992, "Steady-State Behaviour of Reduced Dynamic Systems with Local Nonlinearities," *PhD thesis*, Department of Mechanical Engineering, Eindhoven University of Technology, Eindhoven, The Netherlands.
- Fey, R.H.B., Van Campen, D.H. and De Kraker, A., 1992, "Long Term Structural Dynamics of Mechanical Systems With Local Nonlinearities," *Nonlinear Vibrations*, Vol. DE-50, AMD-144, WAM of the ASME, Anaheim CA. Also published in ASME *Journal of Vibration and Acoustics*, April 1996 (in press).

#### 3.4. CONCLUSIONS.

- Fey, R.H.B., Van de Vorst, E.L.B., Van Campen, D.H., De Kraker, A., Meijer, G.J., and Assinck, F.H., 1994, "Chaos and Bifurcations in a Multi-DOF Beam System with Nonlinear Support," *Nonlinearity and Chaos in Engineering Dynamics, Proceedings IUTAM Symposium, London, 19-23 July 1993*, J.M.T. Thompson and S.R. Bishop, ed., John Wiley & Sons, pp. 125–139.
- Guckenheimer, J. and Holmes, P., 1983, "Nonlinear Oscillations, Dynamical Systems and Bifurcations of Vector Fields," *Applied Mathematical Sciences* 42, Springer-Verlag.
- Newhouse, S., Ruelle, D., and Takens, F., 1978, "Occurrence of Strange Axiom-a Attractors near Quasi-Periodic Flow on T<sup>m</sup>, m ≤ 3," Commun. Math Phys., Vol. 64, pp. 35-40.
- Packard, N.H., Crutchfield, J.P., Farmer, J.D., and Shaw, R.S., 1980, "Geometry from a Time Series," *Physical Review Letters*, Vol 45, pp. 712–716.
- Parker, T.S. and Chua, L.O., 1989, "Practical Numerical Algorithms for Chaotic Systems," SpringerVerlag.
- Pomeau, Y. and Manneville, P., 1980, "Intermittent Transition to Turbulence in Dissipative Dynamical Systems," *Commun. Math. Phys*, Vol. 74, pp. 189-197.
- Soliman, S.M. and Thompson, J.M.T, 1990, "Stochastic Penetration of Smooth and Fractal Basin Boundaries under Noise Excitation," *Dynamics and Stability Systems*, Vol. 5, pp. 281-298.
- Thompson, J.M.T., 1994, "Basic Concepts of Nonlinear Dynamics," Nonlinearity and Chaos in Engineering Dynamics, Proceedings IUTAM Symposium, London, 19-23 July 1993, J.M.T Thompson and S.R. Bishop, ed., John Wiley & Sons, pp. 1–21.
- Thompson, J.M.T. and Stewart, H.B., 1986, "Nonlinear Dynamics and Chaos," John Wiley & Sons Ltd.
- Van de Vorst, E.L.B., Fey, R.H.B., Van Campen, D.H., and De Kraker, A., 1993, "Manifolds of Nonlinear Dynamic Single-DOF systems," *Topics in Applied Mechanics, Integration of Theory & Applications in Applied Mechanics*, J.F. Dijksman and F.T.M. Nieuwstadt, ed., Kluwer Academic Publishers, pp. 293–303.
- Wolf, A., Swift, J.B., Swinney, H.L., and Vastano, J.A., 1985, "Determining Lyapunov Exponents from a Time Series," *Physica*, Vol. 16D, pp. 285–317.

### 48 CHAPTER 3. EXPERIMENTAL VERIFICATION OF THE STEADY-STATE BEHAVIOUR...

# PERIODIC SOLUTIONS OF A MULTI-DOF BEAM SYSTEM WITH IMPACT<sup> $\ddagger$ </sup>

In this paper the steady-state behaviour is analysed of a periodically driven multi-DOF beam system which has an elastic stop at its middle. The elastic stop is modelled in a continuous way using the contact law of Hertz. The beam is modelled using finite elements and subsequently reduced using a component mode synthesis method. The steady-state behaviour of the system reduced to one, two, and four DOF's is investigated by calculating periodic solutions at varying excitation frequency. Periodic solutions are calculated by solving two-point boundary value problems using the multiple shooting method in combination with a path-following technique. It is shown that models with more than one DOF are required for a good assessment of the long term behaviour of the system.

# 4.1 Introduction.

In many practical engineering applications of mechanical systems, impacts at stops occur. It is important to carry out a dynamical analysis of such systems, to identify and subsequently reduce the noise and wear caused by repeated unacceptably large impacts. Examples of systems with impacts are gear rattle, heat exchanger tube wear in nuclear power stations and ships colliding against fenders. Systems with stops are typical examples of systems with strong local nonlinearities. Although the nonlinearity is local, the overall dynamic response of the system may change drastically. A system with stops cannot be linearized, so it is very difficult to predict the system response without a nonlinear analysis.

In general, two different approaches are possible for analysis of the impact in the systems outlined above. One approach is to assume that the impact occurs instantaneously. The analysis is thus divided into two intervals: before and after the impact. The interconnection between the two intervals is made by a momentum balance and a

<sup>&</sup>lt;sup>‡</sup>Van de Vorst, E.L.B., Van Campen, D.H., Fey, R.H.B., and De Kraker, A., 1995, "Periodic Solutions of a Multi-DOF Beam System with Impact," *Journal of Sound and Vibration*, accepted for publication.

parameter representing the amount of energy dissipation in the impact, called the coefficient of restitution. This approach is used in many analyses of impact oscillators and has led to the identification of bifurcational behaviour which is not found in smooth dynamical systems. Impact rules which assume instantaneous reversal of velocity induce discontinuities in the derivatives of maps defined by taking a section through the full phase space. In fact, these discontinuities yield the 'new' bifurcational behaviour, called grazing or border-collision bifurcations (Nordmark, 1991, Nusse et al. 1994, Chin et al., 1994).

The other approach is to let the collision forces act in a continuous matter. The impact analysis of a system of colliding bodies is hence performed simply by including the collision of the contact forces in the system equations of motion during the contact period. A suitable model for the contact forces during the contact period is the nonlinear Hertzian force-displacement law (Hertz, 1895). This model itself does not represent the energy dissipation process. Although the theory of Hertz is based on elasticity, some studies have been performed to extend the theory to include energy dissipation (Goldsmith, 1960, Lankarani and Nikravesh, 1994). In Foale and Bishop (1994) bifurcations occurring in single-DOF impact oscillators in which the impact is modelled using the Hertzian contact law are compared with 'grazing' bifurcations which occur in impact oscillators where the impact is modelled in a discontinuous way.

The main focus of research into impact oscillators in recent years has been into single-degree-of-freedom systems. In this paper we will focus on the influence on the system response of adding more degrees of freedom (DOF's). A beam system is investigated which has an elastic stop at its middle and is periodically excited in the middle. A less complicated version of this beam system, supported in the middle by a massless one-sided linear spring, was investigated earlier by Fey (1992), Fey et al. (1994) and Van de Vorst et al. (1995). The beam system can be divided into a linear and a nonlinear component. The linear component (the beam) is modelled by means of the finite element method and consequently has much more DOF's than the nonlinear one. Because the numerical analysis of the resulting nonlinear system is very expensive from a computational point of view, in particular for increasing number of DOF's, it is worthwhile to keep the number of DOF's as low as possible. This can be achieved by applying a reduction method to the finite element model of the linear component (the beam). The particular reduction method applied is the component mode synthesis method (Craig, 1985, Fey, 1992) and offers the possibility for a considerable reduction of the DOF's and for a systematic investigation of the influence of adding or deleting DOF's. Moreover, the component mode synthesis method can easily be used for more complex systems. The component mode synthesis method utilized in this paper uses free interface eigenmodes up to a cut-off frequency and residual flexibility modes to approximate the dynamic and static behaviour of the linear component. After reduction of the linear component, the nonlinearity is added, resulting in a reduced nonlinear system which will be valid for frequencies up to the cut-off frequency used in the reduction procedure. Because generically nonlinear systems generate higher frequencies than their excitation frequency, the cut-off frequency has to be chosen must higher than the maximum excitation frequency.

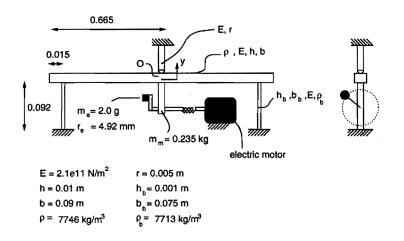


Figure 4.1 Beam system.

The elastic stop is modelled using the contact law of Hertz without energy dissipation mentioned earlier. Hence, the collision forces act in a continuous way. Periodic solutions of the reduced system are calculated for varying excitation frequency by solving two-point boundary value problems using the multiple shooting method (Ascher et al., 1988) in combination with a path-following method (Fey, 1992). The response of the system is investigated using models with 1, 2 and 4 DOF's. Also, different modal damping levels are applied. All calculations presented in this paper were carried out using a development release of the finite element package DIANA (1995).

#### 4.2 Beam system with an elastic stop at its middle.

Figure 4.1 shows the beam system which is analysed numerically. The beam is supported at both ends by leaf springs. If the displacement y of the middle of the beam is positive, the beam hits a spherical elastic contact with radius r = 0.005 m, which is connected rigidly to the world. In the middle of the beam also a rotating mass is present generating a periodic force. Energy dissipation is established by a linear damper (not shown in figure 4.1) at the middle of the beam (see also section 4.3).

The beam and leaf springs are modelled using the finite element method and reduced using the component mode synthesis method mentioned in section 4.1. Because of symmetry only half the beam is modelled. (The elastic stop and the excitation force are positioned exactly at the middle of the beam. Hence the asymmetric model is linear, which means that symmetry breaking bifurcations cannot occur.) As mentioned in section 4.1, the contact force  $F_s$  between the beam and the spherical elastic contact is modelled using the Hertz's law (Hertz, 1895, Goldsmith 1960) that is

$$F_s(y) = \begin{cases} k_s y^{3/2}, & y \ge 0\\ 0, & y < 0 \end{cases}$$
(4.1)

In (4.1) the parameter  $k_s$  is taken 1.034 10<sup>10</sup> Nm<sup>2/3</sup> for a contact radius of r = 5 mm and

 $E = 2.1 \ 10^{11} \text{ N/m}^2$  of the spherical contact.

#### 4.3 Single-DOF model.

After reduction of the finite element model, the equation of motion for the single-DOF model may be obtained as

$$m\ddot{y} + b\dot{y} + ky + k_{p}y^{3/2} = m_{e}r_{e}\omega^{2}cos(\omega t)$$
(4.2)

Here  $k_p = \begin{cases} k_s, & y \ge 0\\ 0, & y < 0 \end{cases}$  and  $k_s = 5.17 \ 10^9 \ \text{Nm}^{2/3}, \omega = 2\pi f_e, b = 2\xi \sqrt{mk}, \xi = 0.0142,$  $m = (\varphi_1^T M \varphi_1) / \varphi_{1y}^2 = 2.48 \ \text{kg}, \ k = (\varphi_1^T K \varphi_1) / \varphi_{1y}^2 = 16877 \ \text{N/m}, \ m_e = 1.0 \ \text{g}, \ r_e = 4.92 \ \text{mm}.$  *M* and *K* are the mass and the stiffness matrix of the linear part of the system, i.e. the beam without the one-sided spring.  $\varphi_1$  is the first eigenmode of the linear system with an eigenfrequency of 13.1 Hz.  $\varphi_{1y}$  is the element of  $\varphi_1$  corresponding to the displacement of the middle of the beam y.

Branches of periodic solutions of this system are calculated for varying excitation frequency  $f_e$ . The maximum absolute displacements  $|y|_{\text{max}}$  occurring in these periodic solutions are shown in figure 4.2. The figure shows besides the harmonic resonance peak near 25.3 Hz also subharmonic resonance peaks. In figure 4.3 the periodic solution at  $f_e = 25.3$  Hz is shown.

Notice that compared to the linear system the first harmonic resonance peak has increased from 13.1 Hz to 25.3 Hz. In Shaw and Holmes (1983) an expression is given for the bilinear eigenfrequency  $f_b$  of an undamped bilinear single-DOF system:

$$f_b = \frac{2\sqrt{1+\alpha}}{1+\sqrt{1+\alpha}} f_1 \tag{4.3}$$

where  $\alpha = k_b/k$  with  $k_b$  the stiffness of the bilinear spring. In our system the contact forces are nonlinear. If, however,  $\alpha$  is calculated from equation (4.3) using  $f_b = 25.3$  Hz and  $f_1 = 13.1$  Hz, this results in  $\alpha \approx 790$  and using this  $\alpha$  the contact forces resulting from Hertz's law and from the bilinear system can be compared. In the bilinear case the contact force is  $F_{s_b}(y) = \alpha ky = 790 \times 16877y = 1.33 \ 10^7 y$  N. In the Hertz's law the contact force is  $F_{s_H}(y) = k_s y^{3/2} = 5.17 \ 10^9 y^{3/2}$  N. This means that  $F_{s_b} > F_{s_H}$ for  $0 < y < 6.6 \ 10^{-6}$  and  $F_{s_b} < F_{s_H}$  for  $y > 6.6 \ 10^{-6}$ . In our case (figure 4.2) the penetration of the contact in the beam is  $y < 4.5 \ 10^{-6}$ .

Figure 4.2 shows that the influence of the stiffening character of Hertz's contact law is small because the high resonance peaks do not bend off much. Only in the top of the 1/3 subharmonic resonance peak near 76 Hz a little part of the 1/3 subharmonic branch is unstable caused by the stiffening effect. The influence of the stiffening character of the contact law is low because the maximum penetration of the elastic contact in the beam does not vary very much compared to the maximum amplitude of the system, and the contact time of the beam and the elastic contact is low compared to the period time of the period time of the periodic solutions.

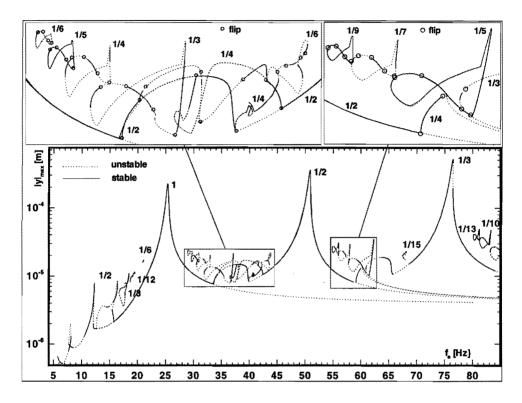


Figure 4.2 Maximum displacements of periodic solutions of 1-DOF model.

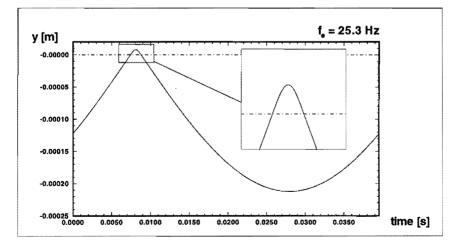


Figure 4.3 Periodic solution of 1-DOF model at  $f_e = 25.3$  Hz.

The highest 1/2 and 1/3 subharmonic resonance peaks in figure 4.2 are related to the harmonic resonance peak. The lower 1/3 (near 37.1 Hz) and 1/5 (near 62.2 Hz) subharmonic solutions are related to the second superharmonic resonance peak near 12.4 Hz. The 1/2 (near 16.1 Hz), 1/4 (near 33 Hz), 1/7 (near 58 Hz), and 1/10 (near 83 Hz) subharmonic solutions are related to the third superharmonic resonance peak near 8.1 Hz. The 1/3 (near 18.4 Hz), 1/5 (near 31 Hz), 1/9 (near 56 Hz), and 1/13 (near 81 Hz) subharmonic solutions are related to the fourth superharmonic resonance peak near 6.0 Hz (not visible in figure 4.2).

On the harmonic branch and every subharmonic branch one or more periodic doubling routes leading to chaos exist. (These are not shown in figure 4.2, the periodic doubling routes exist at the unstable parts of the branches marked by two flip bifurcations.) On the 1/2 subharmonic branch the qualitative dynamics change very much for small frequency variations near 40 Hz. This is caused by the fact that near 40 Hz grazing impact occurs: the beam just touches the elastic contact. For frequencies lower than 40 Hz in the 1/2 subharmonic solutions the beam hits the contact twice per period, whereas for frequencies larger than 40 Hz in the 1/2 subharmonic solutions the beam hits the contact once per period. Because the contact law is continuous, the system response does not change dramatically at grazing impact; no grazing bifurcations can be found in this system. However, similar to discontinuous impacts, one would expect that the system response changes very much in the neighbourhood of grazing impact, i.e. at increasing penetration. Because of the grazing impact near 40 Hz, the maximum displacements of the system increase and two periodic doubling routes leading to chaos where found in that frequency area. Only the 1/4 subharmonic solutions of these period doubling routes are shown in figure 4.2. Grazing impact also occurs at the 1/3 subharmonic resonance peak near 66 Hz.

#### 4.4 Two-DOF model.

Using the component mode synthesis method, the system can be reduced to two DOF's. Then, in the model one residual flexibility mode and one free-interface eigenmode ( $f_1 = 13.1 \text{ Hz}$ ) are included. The two-DOF model has two eigenfrequencies:  $f_1 = 13.1 \text{ Hz}$  and  $f_2 = 125.1 \text{ Hz}$ . Notice that because only one free-interface eigenmode is included, the second eigenfrequency is inaccurate. Because the second eigenfrequency of the beam,  $f_2 = 117.2 \text{ Hz}$ , lies close to the second eigenfrequency of the two-DOF model, still this model is suitable to show the effect of adding one DOF to the system on the system response. In the two-DOF model, besides the linear damper in the middle, extra damping is added by means of modal damping of the two eigenmodes with modal damping coefficient  $\xi_m = 0.01$ . Extra modal damping is added because it is impossible to calculate periodic solutions without modal damping due to the low damping level of the system (without modal damping all periodic solutions are numerically unstable) and in practice also modal damping is present.

Figure 4.4 shows the maximum absolute displacements  $|y|_{\text{max}}$  of the middle of the beam, occurring in the periodic solutions for varying excitation frequency of the

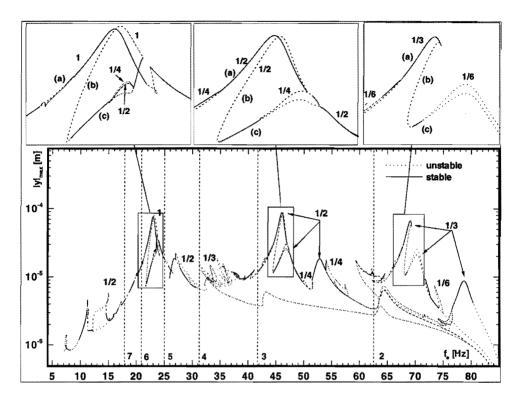


Figure 4.4 Maximum displacements of periodic solutions of 2-DOF model ( $\xi_m = 0.01$ ).

two-DOF model. The figure shows again the harmonic, 1/2 subharmonic and 1/3 subharmonic solutions, now with extra resonance peaks. The extra resonance peaks on the harmonic branch are superharmonic resonance peaks of the second eigenfrequency of the model: a 5th superharmonic resonance peak (near 26 Hz), a 4th superharmonic resonance peak (near 44 Hz) and a 2nd superharmonic resonance peak (near 64 Hz). These superharmonic resonance peaks cause an additional resonance peak on the 1/2 subharmonic and 1/3 subharmonic branches. These subharmonic branches have three peaks, where the third peak is related to the 5th superharmonic resonance peak (near 26 Hz) of the second eigenfrequency of the model.

The vertical dashed lines in figure 4.4 show the frequency where the superharmonic resonance peaks of the second eigenmode are expected (using  $f_2 = 125.1$  Hz). These dashed lines show that the 5th, 4th, 3rd and 2nd superharmonic resonances occur at a higher frequency than expected. The second harmonic resonance peak (not visible in figure 4.4) occurs near 126.5 Hz, so the second 'eigenfrequency'\* increases from 125.1

<sup>\*</sup>Because the model is nonlinear, one cannot speak of the *eigenfrequencies* of the model. Here, 'eigenfrequency' is used for the frequency at which the model resonates.

Hz to 126.5 Hz. This does not explain the higher frequencies for which superharmonic resonances occur; the 5th superharmonic resonance peak occurs near 26.5 Hz and 26.5  $\times$  5 = 132.5 Hz > 126.5 Hz. In a bilinear system with  $\alpha$  = 790, which shows a similar shift of the harmonic resonance peaks as in our system (see section 4.3), the superharmonic resonances occur at the same higher frequencies. This means that the higher superharmonic resonance frequencies are not caused by the stiffening character of the contact law of Hertz. Investigation of the periodic solutions in the superharmonic resonance peaks shows that the closer the superharmonic resonance peak lies to the first harmonic resonance peak, the larger the penetration of the elastic contact is 'connected' to the beam. Furthermore, the superharmonic resonance peaks which lie close to the first harmonic resonance peak are not only dominated by the second 'eigenfrequency' but also by the first 'eigenfrequency'. This means that the closer a *n*th superharmonic resonance peak lies to the first harmonic resonance peak lies to the first 'eigenfrequency'. This means that the closer a *n*th superharmonic resonance peak lies to the first harmonic resonance peak lies to the first 'eigenfrequency'. This means that the closer a *n*th superharmonic resonance peak lies to the first harmonic resonance peak lies to the first harmonic resonance peak, the more the *n*th superharmonic resonance frequency will be increased from  $f_2/n$  to  $(f_1 + f_2)/n$ .

Near the first harmonic resonance peak (23 Hz) two separated harmonic branches coexist ((a) and (b)). Both branches have a harmonic resonance peak. One branch (b) is unstable at the top. The unstable part on this branch is marked by two cyclic fold bifurcations and underneath the unstable part a stable branch (c) exists with a period doubling route to chaos. Investigation of the periodic solutions shows that in the upper (unstable) part of the branch (b) the beam hits the contact twice per period and in the lower (stable) part of the branch (c) the beam hits the contact once per period (see also figure 4.6). Near the two cyclic fold bifurcations grazing impact occurs. At the top of the other (stable) harmonic branch (a) the beam hits the contact twice per period. Furthermore, the periodic solutions of the upper unstable part (b) are dominated by only the first 'eigenfrequency' of the system, where the periodic solutions of the other branches (a) and (c) are dominated by both the first and the second 'eigenfrequency'. Apparently, because of the larger velocity of the beam at impact, the higher modes of the system are excited. As mentioned before, the superharmonic resonances near the first harmonic resonance peak occur at a higher frequency than expected. Because of this, also the 6th superharmonic resonance peak occurs at a higher frequency than expected. Since branch (b) is dominated by the first 'eigenfrequency' only and branch (a) is dominated by both the first and the second 'eigenfrequency', it can be concluded that the resonance peak on the stable branch (a) near 23 Hz is the 6th superharmonic resonance peak  $((f_1 + f_2)/n = (13.1 + 125.1)/6 = 23 \text{ Hz})$  and the resonance peak on the unstable branch (b) is the first harmonic resonance peak.

In the 1/2 and 1/3 subharmonic resonance peaks the beam hits the contact also twice per period, whereas in the single-DOF model the beam hits the contact once per period near the harmonic, 1/2 subharmonic and 1/3 subharmonic resonance peaks. Figure 4.4 shows that near the 1/2 subharmonic and 1/3 subharmonic resonance peaks no separated branches coexist like near the harmonic resonance peak. However, near these subharmonic peaks similar behaviour is found as near the harmonic resonance peak. Increasing the frequency from 45 Hz to 47 Hz on the 1/2 subharmonic branch (a), the maximum displacement increases until the top whereafter it decreases until

the branch becomes unstable via a cyclic fold bifurcation. The branch (b) turns back and simultaneously the maximum displacement increases again. Near the cyclic fold bifurcation grazing impact occurs, however again in both the stable (a) and the unstable (b) branch the beam hits the contact twice per period. Further decreasing of the frequency results in a decrease of amplitude of the unstable branch which then becomes stable via a cyclic fold bifurcation at 44.5 Hz and turns back again to increasing frequencies. In this stable branch (c) the beam hits the contact once per period (near 44.5 Hz grazing impact occurs). Further increasing the frequency leads to a resonance peak where the branch is unstable marked by two flip bifurcations. Here a period doubling route leading to chaos exists. Only the 1/4 subharmonic solutions of this period doubling route are shown in figure 4.4. At the top of the 1/2 harmonic branch (c) at 47 Hz again grazing impact occurs, although for decreasing and increasing frequency in the 1/2 subharmonic solutions the beams hits the contact once per period.

The 1/2 subharmonic resonance peak near 47 Hz on branch (c) cannot be related directly to a superharmonic resonance peak. Investigation of the periodic solutions shows that again the stable 1/2 subharmonic branches (a) and (c) are dominated by both the first and the second 'eigenfrequencies' while the unstable branch (b) (marked by two cyclic fold bifurcations) is dominated by the first 'eigenfrequency' only. Near the 1/3 subharmonic resonance peak similar behaviour was found.

The subharmonic solutions related to the superharmonic resonance peaks of the first resonance peak, which dominated the response of the single-DOF model between the highest harmonic, 1/2 and 1/3 subharmonic peaks, could not be found in the two-DOF model. Only the 1/3 subharmonic solution related to the 2nd superharmonic resonance peak of the first eigenmode could be found near 33 Hz and this branch is fully unstable now. Furthermore, now more period doubling routes leading to chaos are found on the harmonic and subharmonic branches, and in the frequency ranges 30–37 Hz and 59–66 Hz chaotic behaviour was found.

Notice that in contrast to the frequency response of the single-DOF model now the 1/2 subharmonic and 1/3 subharmonic resonance peaks are lower than the harmonic resonance peak. This is caused by the anti-resonance near 85 Hz. Furthermore, the frequency where the harmonic and subharmonic resonance peaks occur are decreased with 2 Hz. The reason for this is that now the beam hits the contact twice per period in the peaks, whereas the response at the peaks is dominated by the first two 'eigenfrequencies'. In comparison with the linear system, the first eigenfrequency is moved from 13.1 Hz to 23.1 Hz. The second eigenfrequency has not changed very much (125.1 Hz  $\rightarrow$  126.5 Hz).

Figure 4.5 shows the maximum displacements occurring in the periodic solutions if the modal damping coefficient is decreased to  $\xi_m = 0.001$ . The response of the system is similar to the response for  $\xi_m = 0.01$ . However, now the resonance peaks are higher. Nevertheless, still in the highest resonance peaks the beam hits the contact twice per period. Furthermore, the unstable parts on the branches (most of them with period doubling routes) have become larger. Again, the subharmonic solutions caused by superharmonic resonance peaks of the first harmonic resonance peak could not be found. One additional 1/14 unstable subharmonic branch was found near 57 Hz.

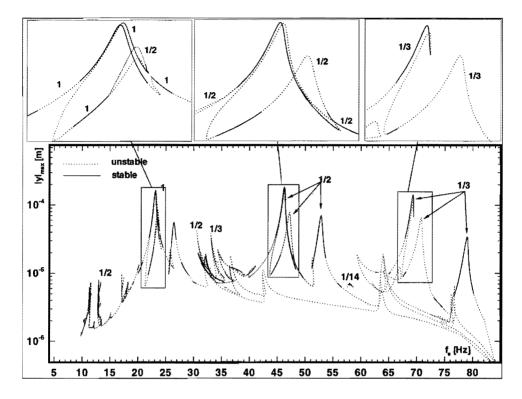


**Figure 4.5** Maximum displacements of periodic solutions of 2-DOF model ( $\xi_m = 0.001$ ).

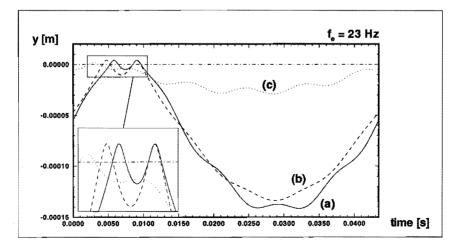


**Figure 4.6** Periodic solutions of 2-DOF model at  $f_e = 23.0$  Hz ( $\xi_m = 0.001$ ).

#### 4.5. FOUR-DOF MODEL

Figure 4.6 shows the periodic solutions of the two-DOF model at  $f_e = 23.0$  Hz. The figure shows that the periodic solutions of branches (a) and (b) hit the contact twice, whereas in comparison to the periodic solution of the single-DOF model (Figure 4.3), in the periodic solutions of the two-DOF model higher frequencies are present.

#### 4.5 Four-DOF model

In this section the system is reduced to four DOF's. Simulations with the system reduced to five DOF's showed no major differences, so it may be concluded that the four-DOF model is a good approximation for the unreduced system in the frequency range under investigation. In the four-DOF model three free-interface eigenmodes are included ( $f_1 = 13.1 \text{ Hz}$ ,  $f_2 = 117.5 \text{ Hz}$ ,  $f_3 = 326.5 \text{ Hz}$ ) and one residual flexibility mode. The model is approximately valid up to 500 Hz. The eigenfrequencies of the four-DOF model are  $f_1 = 13.1 \text{ Hz}$ ,  $f_2 = 117.5 \text{ Hz}$ ,  $f_3 = 326.5 \text{ Hz}$ ,  $f_4 = 749.5 \text{ Hz}$ , where the last frequency is caused by the residual flexibility mode and is not accurate. Again in the four-DOF model, besides the linear damper in the middle, extra damping is added by means of modal damping of the four eigenmodes with modal damping coefficient  $\xi_m$ .

Figure 4.7 shows the maximum absolute displacements  $|y|_{max}$  of the middle of the beam occurring in the periodic solutions for varying excitation frequency of the four-DOF model with  $\xi_m = 0.01$ . Again the response is dominated by the harmonic resonance peak and 1/2 and 1/3 subharmonic resonance peaks which are related to the first harmonic resonance peak. Also again superharmonic resonances exist at the harmonic branch which are related to the 2nd and 3rd 'eigenfrequency' of the system and again these superharmonic resonance peaks occur at a higher frequency than expected just as in the two-DOF model. These superharmonic resonance peaks result in additional resonance peaks on the 1/2 and 1/3 subharmonic solutions. The first (highest) peak on the branches with subharmonics is related to the first harmonic resonance peak. The other two peaks on the 1/2 and 1/3 subharmonic branches are dominated by both the 2nd and 3rd 'eigenfrequency'. In the previous section we saw that every resonance peak near the first harmonic resonance peak is projected on the 1/2 and 1/3 subharmonic branches. If the extra two peaks on the 1/2 and 1/3 subharmonic branches are projected back near the first harmonic resonance peak, these two peaks have to be caused by the 5th superharmonic resonance peak near 27 Hz of the 2nd 'eigenfrequency' (see inset figure 4.7). Because of superharmonic resonances of the 3rd 'eigenfrequency', the 5th superharmonic resonance peak is divided into two peaks: one peak is high and one peak is much lower (with two peaks on it). Because the 5th superharmonic resonance peak is divided into two peaks, also two extra peaks occur on the 1/2 and 1/3 subharmonic branches.

In contrast to the two-DOF model, in the four-DOF model no second harmonic branch was found near the first harmonic resonance peak. Still, there might be a second harmonic branch but the 1/2 and 1/3 subharmonic resonance peaks do not indicate that there exists one. Also, because in the four-DOF model the second eigenfrequency is moved from 125.1 Hz to 117.5 Hz in comparison with the two-DOF model, now the

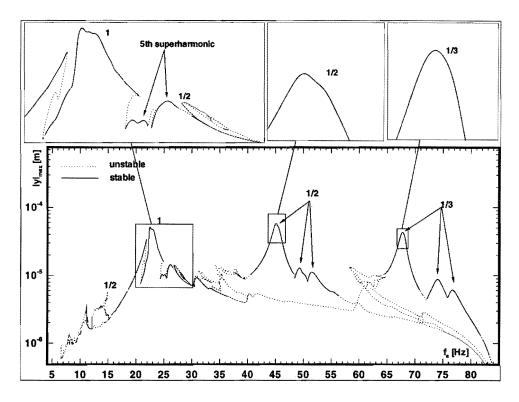


Figure 4.7 Maximum displacements of periodic solutions of 4-DOF model ( $\xi_m = 0.01$ ).

frequency for which the 6th superharmonic resonance peak occurs has also decreased. In the two-DOF model the 6th superharmonic resonance peak was responsible for the existence of the second harmonic branch. The harmonic, 1/2 and 1/3 subharmonic resonance peaks are stable and the beam hits the contact twice per period. In the two extra peaks on the 1/2 and 1/3 subharmonic solutions the beam hits the contact once per period.

Figure 4.7 shows that less period doubling routes on the harmonic, 1/2 and 1/3 subharmonic branches exist than in the two-DOF model with  $\xi_m = 0.01$ . This is caused by the fact that because now four eigenmodes are damped with modal damping coefficient  $\xi_m = 0.01$ , the amount of damping in the system is increased which results in less nonlinear phenomena. Nevertheless, in the frequency areas 30-38 Hz and 58-63 Hz chaotic behaviour was found.

Figure 4.8 shows the response of the system if the modal damping coefficient is decreased to  $\xi_m = 0.001$ . Compared to figure 4.7, now all sub- and super-harmonic resonance peaks increase and in the frequency domain where the harmonic resonance peak exists many superharmonic resonance peaks can be seen. These superharmonic resonance peaks are not related to one 'eigenfrequency' of the model. The superharmonic

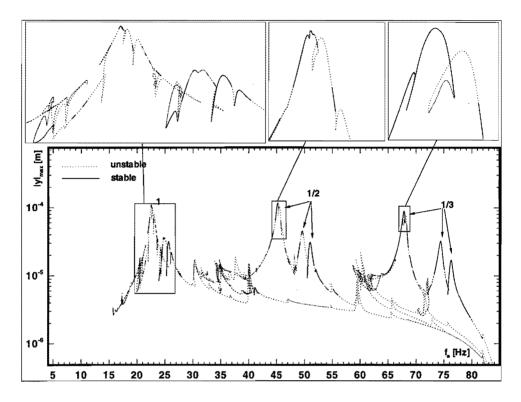


Figure 4.8 Maximum displacements of periodic solutions of 4-DOF model  $(\xi_m=0.001)$ .

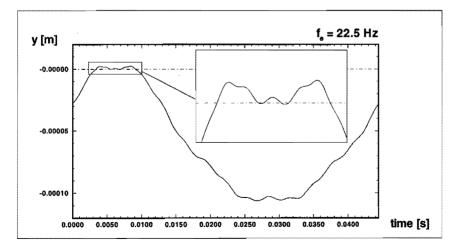


Figure 4.9 Periodic solution of 4-DOF model at  $f_e = 22.5$  Hz ( $\xi_m = 0.001$ ).

resonance peaks in the frequency domain 24-26 Hz are dominated again by the 2nd and 3rd 'eigenfrequency' of the model and they are responsible for the two extra resonance peaks on the 1/2 and 1/3 subharmonic branches. Again in these peaks the beam hits the contact once per period. The higher peaks in the frequency domain 22-23 Hz are dominated by the 1st and 2nd 'eigenfrequency' of the model. Some peaks are unstable and here period doubling routes leading to chaos exist. In the stable peaks the beam hits the contact once per period, in the unstable peaks the beam hits the contact three times per period (figure 4.9). Also on other parts of the branches additional period doubling routes leading to chaos exist compared to  $\xi_m = 0.01$ .

#### 4.6 Conclusions.

In this paper periodic solutions are calculated for a multi-DOF beam system with an elastic stop at its middle for varying excitation frequency. The linear beam is modelled using finite elements and reduced using component mode synthesis. The elastic contact is modelled using the contact law of Hertz and the periodic solutions are calculated by solving two-point boundary value problems using the multiple shooting method. Using this method it is possible to calculate stable and (very) unstable periodic solutions and in combination with a path-following method very complex branches of periodic solutions can be calculated.

The results show that the mean resonance peaks of the single-DOF system can be globally predicted in advance if the frequency for which the harmonic resonance peak occurs is known. All the superharmonic and subharmonic resonance peaks can be predicted using the harmonic resonance frequency. However, because on every harmonic and subharmonic branch period doubling routes leading to chaos exist, the behaviour of the single-DOF system is dominated by chaotic behaviour between the highest harmonic, 1/2 and 1/3 subharmonic resonance peaks.

The two-DOF model shows globally the same maximum amplitudes as the single-DOF system. However, because of the second eigenmode an additional peak is found on the 1/2 and 1/3 subharmonic branches. In contrast to the single-DOF model, where the beam hits the elastic contact once per period in the highest resonance peaks, now the beam hits the elastic contact twice per period in these peaks. This means that the periodic solutions near the resonance peaks are very different compared to those of the single-DOF model. Between the highest harmonic, 1/2 and 1/3 subharmonic resonance peaks the behaviour is again dominated by chaotic behaviour, which is now caused by additional period doubling routes on the harmonic, 1/2 and 1/3 subharmonic resonance branches. The subharmonics caused by superharmonic resonances of the first 'eigenfrequency', which dominated the response of the single-DOF system, have disappeared.

The response of the four-DOF model shows that although the third linear eigenfrequency of the beam is four times the highest excitation frequency under investigation, this 'eigenfrequency' still has a large influence on the system behaviour. The results show that the amount of damping in the model has a large influence on the frequency responses. Increasing the modal damping leads to less period doubling routes and smaller frequency intervals with chaotic behaviour. However, also at higher damping levels 1/2 and 1/3 subharmonics dominate the frequency response and the influence of the third linear eigenfrequency is still large.

Because in this paper the impact contact is modelled using a continuous contact law, no grazing bifurcations can be found. In the neighbourhood of grazing impact, i.e. the beam just touches the elastic contact, in many cases period doubling routes occur. However, this is not always the case and not every period doubling route is in the neighbourhood of a frequency for which grazing impact occurs.

#### Acknowledgement.

This work was supported by the Centre for Mechanical Engineering of TNO Building and Construction Research, Delft, The Netherlands.

#### References

- Ascher, U.M., Mattheij, R.M.M., and Russell, R.D., 1988, "Numerical Solution of Boundary Value Problems for Ordinary Differential Equations," Prentice-Hall Inc..
- Chin, W., Ott, E., Nusse, H.E., and Grebogi, C., 1994, "Grazing Bifurcations in Impact Oscillators," *Physical Review E*, Vol. 50, pp. 4427-4444.
- Craig Jr., R.R., 1985, "A Review of Time-Domain and Frequency-Domain Component Mode Synthesis Methods," *Combined Experimental/Analytical Modeling of Dynamic Structural Systems Using Substructure Synthesis*, D.R. Martinez and A.K. Miller, ed., ASME Applied Mechanics AMD-67, New York, pp. 1-31.
- DIANA, 1995, *DIANA User's Manual 6.0 ed.*, TNO Building and Construction Research, Delft, The Netherlands.
- Fey, R.H.B., 1992, "Steady-State Behaviour of Reduced Dynamic Systems with Local Nonlinearities," *PhD thesis*, Department of Mechanical Engineering, Eindhoven University of Technology, Eindhoven, The Netherlands.
- Fey, R.H.B., Van de Vorst, E.L.B., Van Campen, D.H., De Kraker, A., Meijer, G.J., and Assinck, F.H., 1994a, "Chaos and Bifurcations in a Multi-DOF Beam System with Nonlinear Support," *Nonlinearity and Chaos in Engineering Dynamics, Proceedings IUTAM Symposium, London, 19-23 July 1993*, J.M.T. Thompson and S.R. Bishop, ed., John Wiley & Sons, pp. 125–139.
- Foale, S. and Bishop, S.R., 1994, "Bifurcations in Impact Oscillations," Nonlinear Dynamics, Vol. 6, pp. 285–299.
- Goldsmith, W., 1960, "Impact: The Theory and Physical Behaviour of Colliding Solids," E. Arnold Ltd., London.

- 64 CHAPTER 4. PERIODIC SOLUTIONS OF A MULTI-DOF BEAM SYSTEM WITH IMPACT
  - Hertz, H., 1895, "Gesammelte Werke, vol. 1: Schriften Vermischten Inhalts," Leipzig, Germany.
  - Lankarani H.M., and Nikravesh, P.E., 1994, "Continuous Contact Force Models for Impact Analysis in Multibody Systems," *Nonlinear Dynamics*, Vol. 5, pp. 193–207.
  - Nordmark, A.B., 1991, "Non-periodic Motion Caused by Grazing Incidence in an Impact Oscillator," *Journal of Sound and Vibration*, Vol. 145, pp. 279–297.
  - Nusse, H.E., Ott, E. and Yorke, J.A., 1994, "Border-Collision Bifurcations: An Explanation for Observed Bifurcation Phenomena," *Physical Review E*, Vol. 49, pp. 1073–1076.
  - Shaw, S.W. and Holmes, P.J., 1983, "A Periodically Forced Piecewise Linear Oscillator," *Journal of Sound and Vibration*, Vol. 90, no. 1, pp. 129–155.
  - Van de Vorst, E.L.B, Assinck, F.H., De Kraker, A., Fey, R.H.B, and Van Campen, D.H., 1995, "Experimental Verification of the Steady-State Behaviour of a Beam System with Discontinuous Support," *Experimental Mechanics*, accepted for publication.

# EXPERIMENTAL AND NUMERICAL ANALYSIS OF THE STEADY-STATE BEHAVIOUR OF A BEAM SYSTEM WITH $IMPACT^{\ddagger}$

In this paper the steady-state behaviour of a beam system with a periodically moving support and an elastic stop is analysed both numerically and experimentally. In the numerical analysis a continuous model for the elastic stop is used based on the contact force law of Hertz. The beam is modelled using finite elements and subsequently reduced using a component mode synthesis method leading to a nonlinear six degree of freedom model. The steady-state behaviour of this model is investigated by calculating periodic solutions at varying excitation frequency. This is done by solving two-point boundary value problems using the multiple shooting method in combination with a path-following method. Experimental research concerning periodic solutions is carried out to verify the numerical results. The experimental results correspond very well with the numerical results. It appears that the high eigenfrequencies of the linear beam system strongly influence the low frequency nonlinear steady-state response. This means that multi-degree-of-freedom systems are essential for an accurate representation of the actual system behaviour.

# 5.1 Introduction.

In many practical engineering applications of mechanical systems, impacts at stops occur. It is important to carry out a dynamical analysis of such systems, to identify and subsequently reduce the noise and wear caused by repeated unacceptably large impacts. Examples of such systems are gear rattle, heat exchanger tube wear in nuclear power stations and ships colliding against fenders. Systems with stops are typical examples of systems with local nonlinearities. Although the nonlinearity is local, the overall dynamic response of the system in general changes drastically. A system with stops cannot be linearized, so it is very difficult to predict the system response without a

<sup>&</sup>lt;sup>‡</sup>Van de Vorst, E.L.B., Heertjes, M.F., De Kraker, A., Fey, R.H.B., and Van Campen, D.H., 1995, "Experimental and Numerical Analysis of the Steady-State Behaviour of a Beam System with Impact," *Experimental Mechanics*, submitted.

nonlinear analysis.

In recent years, nonlinear dynamical systems have been studied by many researchers. For a general introduction in nonlinear dynamics the reader is referred to Guckenheimer and Holmes (1983), Thompson and Stuart (1986), Parker and Chua (1989) and Thompson (1994). The long term behaviour of a nonlinear system, which is excited by a periodic external load, can be periodic, quasi-periodic, or chaotic. The period of a periodic attractor may be equal to the excitation period (harmonic), but may also be a multiple of the excitation period (subharmonic). As an example, a 1/2 subharmonic attractor has a period, which is twice the excitation period. If in a (sub)harmonic solution another frequency than the ground frequency (the lowest frequency occuring in the solution) or the excitation frequency is dominant, the (sub)harmonic solution occurs near a superharmonic resonance peak. A quasi-periodic attractor is a function of two or more signals, which have incommensurate frequencies. A chaotic attractor is characterized by a broad band spectrum and by an extreme sensitivity for initial conditions.

Most of the recent research concerning impact oscillators is based on single-degreeof-freedom (DOF) systems. In Van de Vorst et al. (1995) the need of adding more DOF's (higher eigenmodes) for an accurate low frequency response is investigated by analyzing a periodically driven beam system with an elastic stop at its middle. They concluded that the eigenmodes corresponding to high eigenfrequencies have a large influence on the low frequency steady-state response. In comparison to the response of a single-DOF system, the higher eigenmodes cause extra (superharmonic) resonance peaks and disappearance of subharmonic solutions.

The objective of this paper is to investigate experimentally the influence of higher eigenmodes on the low frequency system response of a system with an elastic stop. Furthermore it is investigated whether an elastic stop can be modelled using the contact force law of Hertz (Hertz, 1895, Goldsmith, 1960). The verification is mainly focussed on comparing periodic responses. Experiments are done using a clamped steel beam with a spherical aluminum contact hitting a second aluminum contact if the relative displacement at the contact point is negative. The whole system is base excited by a moving support.

As mentioned earlier, in the numerical analysis the elastic stop is modelled using Hertz's contact force law. Hence, the collision forces act in a continuous way. The beam system can be divided into a linear and a nonlinear component. The linear component (the beam) is modelled by means of the finite element method and consequently has much more DOF's than the nonlinear one. Because the numerical analysis of the resulting nonlinear system is very expensive from a computational point of view, in particular for increasing number of DOF's, it is worthwhile to keep the number of DOF's as low as possible. This can be achieved by applying a reduction method to the finite element model of the linear component. The particular reduction method applied is the component mode synthesis method (Craig, 1985, Fey, 1992) and offers the possibility for a considerable reduction of the DOF's. Moreover, the component mode synthesis method can easily be used for geometrically more complex linear components. The component mode synthesis method used in this paper is based upon free-interface eigenmodes up to a cut-off frequency and residual flexibility modes to approximate the dynamic behaviour

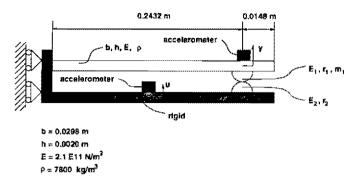


Figure 5.1 Experimental setup of beam system.

of the linear component. After reduction of the linear component the nonlinear elements are added, resulting in a reduced nonlinear system which will be valid for frequencies up to the cut-off frequency used in the reduction procedure. Because generically in nonlinear responses higher frequencies are present than the excitation frequency, the cut-off frequency has to be chosen much higher than the maximum excitation frequency. Periodic solutions of the reduced system are calculated for varying excitation frequency by solving two-point boundary value problems using the multiple shooting method (Ascher et al., 1988) in combination with a path-following method (Fey, 1992).

In section 5.2 the experimental setup of the beam system is given. In section 5.3 the steady-state behaviour of the beam system is investigated numerically by calculating periodic solutions. In section 5.4 the experimental results for the beam system are compared with the numerical results. Finally in section 5.5 some conclusions are drawn.

#### 5.2 Beam system with an elastic stop.

Figure 5.1 shows the beam system which is analysed both numerically and experimentally. The beam is clamped on one side to a vibrating table and has a spherical elastic contact on the other side. If the relative displacement (y - u) of the right-hand side of the beam is negative, it hits another spherical elastic contact which is also connected to the vibrating table. Using the vibrating table, which is driven by an electric motor, this spherical contact and the left-hand side of the beam are base excited with a prescribed vertical displacement  $u(t) = 0.5015 \cos(2\pi f_e t)$  mm.

As mentioned in section 5.1, in the numerical analysis the system is divided into two components: a linear component (the linear beam with periodically driven frictionless sliding support in y-direction on the left-hand side) and a nonlinear component (the elastic contact). The linear component is modelled using finite elements and subsequently reduced. In the reduction two residual flexibility modes (one for the left end base excitation and one for the elastic stop), one rigid body mode and four free-interface eigenmodes ( $f_1 = 30.51$  Hz,  $f_2 = 192.68$  Hz,  $f_3 = 507.26$  Hz and  $f_4 = 973.45$  Hz) are included. This results in a six DOF-model for the *reduced* clamped beam with eigenfrequencies:  $f_1 = 17.495$  Hz,  $f_2 = 137.28$  Hz,  $f_3 = 414.33$  Hz,  $f_4 = 843.26$  Hz,  $f_5 = 137.28$  Hz,  $f_5 = 112.495$  Hz,  $f_5 = 112.495$  Hz,  $f_7 = 112.495$  Hz,  $f_8 = 112.495$  Hz,  $f_$ 

1538.8 Hz and  $f_6 = 3940.9$  Hz. The first six eigenfrequencies of the *unreduced* clamped linear beam are  $f_1 = 17.495$  Hz,  $f_2 = 137.28$  Hz,  $f_3 = 414.33$  Hz,  $f_4 = 842.91$  Hz,  $f_5 = 1419.7$  Hz and  $f_6 = 2136.1$  Hz, so the last three eigenfrequencies of the reduced system are 0.04 %, 8 % and 84 % inaccurate, respectively, and the reduced model is accurate up to approximately 1000 Hz.

As mentioned in section 5.1, the contact force  $F_s$  between two equal spherical elastic contacts is modelled using Hertz's law (Hertz, 1895, Goldsmith, 1960), that is

$$F_s(y,u) = \begin{cases} k_s(y-u)^{3/2}, & (y-u) \ge 0\\ 0, & (y-u) < 0 \end{cases}$$
(5.1)

In (5.1) the parameter  $k_s$  is taken 4.5 10<sup>9</sup> Nm<sup>2/3</sup> for contact radii  $r_1 = r_2 = 15$  mm and Young's moduli  $E_1 = E_2 = 7.0 \ 10^{10} \text{ N/m}^2$  of the aluminum spherical contacts. The mass of the spherical contact (including the accelerometer) is  $m_1 = 37.56$  g.

The damping in the system without elastic contact is estimated experimentally using logarithmic decrement evaluation. According to this estimation, the damping in the model can be taken into account by adding modal damping with a modal damping coefficient of  $\xi_m = 0.003$  for each eigenmode. Calculations using this damping level showed in some frequency ranges such a complex path with periodic solutions that a very large number of periodic solutions has to be calculated to follow the path. Furthermore almost all calculated periodic solutions appeared to be unstable. In the real system, also damping is present during the impact time. This is not modelled in the numerical analysis. Because of this, branches of periodic solutions have also been calculated using a modal damping coefficient of  $\xi_m = 0.015$ . Using this modal damping coefficient, all the branches can be followed with a limited number of periodic solutions.

In the experiments two accelerometers are used. One is placed at the position of the elastic contact on the beam measuring  $\ddot{y}$ . The other one is placed at the vibrating table measuring  $\ddot{u}$ .

Because of the limited power of the electric motor, the maximum excitation frequency which can be used in the experiment is 70 Hz. Acceleration measurements showed that the prescribed displacement is practically sinusoidal between 20 Hz and 70 Hz. For frequencies lower than 20 Hz, high frequencies occur on top of the sinusoidal signal due to the eigenfrequencies of the driving mechanism. As mentioned in section 5.2 the amplitude of the prescribed displacement of the vibrating table is 0.5015 mm. Figure 5.2 shows the amplitudes of the measured and numerical accelerations  $(0.5015(2\pi f_e)^2)$ of the vibrating table for varying excitation frequency. The results in the figure indicate that the difference between calculated and measured amplitudes increases for increasing excitation frequency to about 23 % for  $f_e = 70$  Hz. This is due to the mass of the vibrating table and the flexibility of the drive.

In the acceleration measurements of  $\ddot{y}$  many high frequencies are present due to the low damping in the system. In order to be able to assess the measured accelerations, the measurement data is filtered by a low pass filter with a bandwidth of 850 Hz.

The elastic contacts did not show any plastic deformation after the experiments. This is important because plastic deformation will result in a change of the contact radius

#### 5.3. NUMERICAL ANALYSIS.

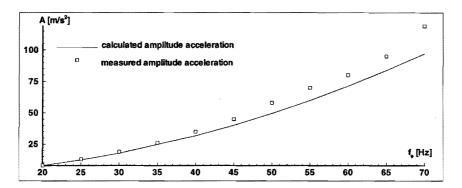


Figure 5.2 Calculated and measured amplitudes of prescribed acceleration of vibrating table for varying excitation frequency  $f_e$ .

of the spherical contacts and hence also in a change of the Hertzian constant. It was observed that the surface at the area of elastic contacts became black after carrying out some experiments probably due to oxidation of the aluminum. The measurements in the frequency range 20–70 Hz were carried out twice. In both measurements, the same results were obtained and this also indicates the absence of plastic deformation in the contact area and also that the oxidation of the aluminum does not affect the experimental results.

#### 5.3 Numerical analysis.

Figure 5.3 shows the maximum absolute displacements y (the position of the elastic contact on the beam) occurring in the calculated periodic solutions for varying excitation frequency  $f_e$  for  $\xi_m = 0.015$ . For calculating figure 5.3 42000 periodic solutions were calculated.

Figure 5.3 shows a harmonic branch with periodic solutions and also a 1/2 and a 1/3 subharmonic branch with periodic solutions. Near 34 Hz two harmonic resonance peaks occur on the harmonic branch. These two harmonic resonance peaks are related to the first eigenmode of the linear system ( $f_1 = 17.495$  Hz) and the second eigenmode of the linear system ( $f_2 = 137.28$  Hz). Due to the very stiff elastic contact the first 'eigenfrequency'\* increases to approximately 34 Hz. The fourth superharmonic resonance peak of the second 'eigenfrequency' of the system exists in the same frequency range. Apparently, the fourth superharmonic resonance peak causes an anti-resonance splitting the first harmonic resonance peak into two peaks.

Furthermore, on the harmonic branch superharmonic resonance peaks occur. Figure 5.3 shows a 2nd (near 70 Hz), a 3rd (near 47 Hz), a 5th (near 29 Hz), a 6th (near 24 Hz) and a 7th (near 20 Hz) superharmonic resonance peak related to the second 'eigenfrequency' of the system. The superharmonic resonance peaks related to the third

<sup>\*</sup>Because the model is nonlinear, one cannot speak of the *eigenfrequencies* of the model. Here, 'eigenfrequency' is used for the frequency at which the model resonates harmonically.

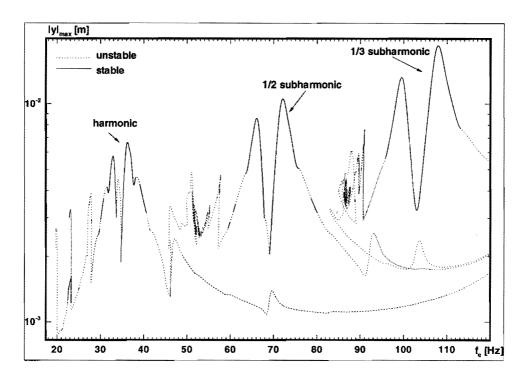


Figure 5.3 Maximum displacements of periodic solutions of 6-DOF model with  $\xi_m = 0.015$ .

'eigenfrequency' of the system are much smaller but can still be seen on the harmonic branch in figure 5.3 (for instance the 10th superharmonic resonance peak occurs near 41 Hz).

The 1/2 subharmonic and 1/3 subharmonic branches shown in figure 5.3 are related to the first 'eigenfrequency' of the system. Just like the first resonance peak on the harmonic branch, the resonance peaks on the 1/2 subharmonic branch and 1/3 subharmonic branch are split into two peaks. It seems that the harmonic branch is projected on the 1/2 subharmonic and 1/3 subharmonic branches. Near 93 Hz on the 1/2 subharmonic branch a superharmonic resonance peak occurs which is related to the 3th superharmonic resonance peak related to the second 'eigenfrequency' of the system on the harmonic branch.

In the frequency ranges 41–65 Hz and 78–95 Hz only few stable periodic solutions were found. In these frequency ranges mainly chaotic behaviour was found. Also between the highest resonance peaks on the harmonic and 1/2 subharmonic branches chaotic behaviour was found.

Figures 5.4 and 5.5 show the maximum absolute accelerations  $|\ddot{y}|_{\text{max}}$  of the beam at the elastic contact occurring in the periodic solutions for varying excitation frequency for the model with  $\xi_m = 0.015$  and  $\xi_m = 0.003$ . A part of the 1/2 subharmonic branch of the model with  $\xi_m = 0.003$  was not calculated near 53 Hz due to the complexity of

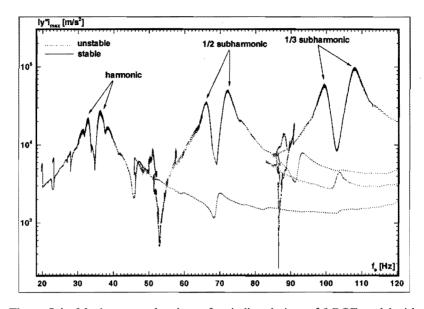


Figure 5.4 Maximum accelerations of periodic solutions of 6-DOF model with  $\xi_m = 0.015$ .

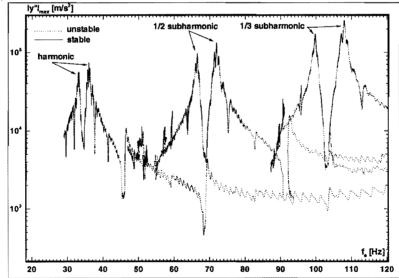


Figure 5.5 Maximum accelerations of periodic solutions of 6-DOF model with  $\xi_m = 0.003$ .

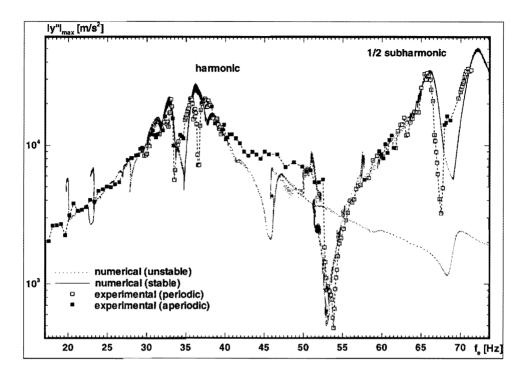


Figure 5.6 Numerical and *shifted* experimental maximum accelerations of periodic solutions of 6-DOF model with  $\xi_m = 0.015$ .

the branch (see also earlier discussion in section 5.2). For the same reason a part of the (unstable) 1/3 subharmonic branch was not calculated in the frequency range 85–104 Hz. For calculating the response of the system with  $\xi_m = 0.003$ , 71000 periodic solutions were calculated.

Figure 5.5 indicates that the model with  $\xi_m = 0.003$  shows much more superharmonic resonance peaks related to high 'eigenfrequencies' on the harmonic branch. Due to the low modal damping of these 'eigenfrequencies', the corresponding eigenmodes are more strongly excited. Furthermore, the model with  $\xi_m = 0.003$  shows higher harmonic, 1/2 subharmonic and 1/3 subharmonic resonance peaks in comparison to the model with  $\xi_m = 0.015$ . Also more superharmonic resonance peaks occur on top of these resonance peaks in case  $\xi_m = 0.003$ . Calculations using a model reduced to eight DOF's instead of six and  $\xi_m = 0.003$  showed that adding more DOF's results in more (small) superharmonic resonance peaks on top of the harmonic, 1/2 subharmonic and 1/3 subharmonic resonance peaks. Apparently numerous eigenmodes are excited near these resonance peaks. Apart from the resonance peaks, the branches of the models with  $\xi_m = 0.003$  and  $\xi_m = 0.015$  have the same level. Notice that near 53 Hz the maximum acceleration of the model with  $\xi_m = 0.015$  is very low. This is described in more detail in the next section.

#### 5.4 Experimental analysis.

Measurements using the linear beam system without elastic contact showed that the first three eigenfrequencies of the linear beam are 17.2 Hz, 128.9 Hz and 378.9 Hz which are approximately 2 %, 6 % and 9% lower than the calculated eigenfrequencies  $f_1 = 17.495$  Hz,  $f_2 = 137.28$  Hz,  $f_3 = 414.33$  Hz. Apparently, the system parameter values in the experimental setup (E,  $\rho$ , mass of elastic contact, etc.) differ from the system parameter values in the numerical model. Because of this the experimental results of the nonlinear system are shifted to a lower frequency.

As mentioned in section 5.2 the measured accelerations are filtered by a low pass filter with a bandwidth of 850 Hz. Some experiments were carried out without a low pass filter. The maximum accelerations obtained without a low pass filter showed a shift compared to the experimental results obtained using the filter. Without a low pass filter, the experimental maximum accelerations and the numerical maximum accelerations resemble. Hence, the low pass filter causes a maximum acceleration shift. The highest accelerations occur at the moment when the beam hits the elastic contact. At that moment in a very small time interval the accelerations are much larger than the accelerations of the beam if it does not make contact with the elastic stop. Because of this, the low pass filter reduces the maximum accelerations.

Figure 5.6 shows the measured maximum absolute acceleration occurring in the signals for varying excitation frequency (symbols) together with the calculated branches for  $\xi_m = 0.015$  (lines). In order to compare the experimental and numerical results, the experimental maximum accelerations are shifted in the positive frequency direction a 6% and are shifted in the positive maximum acceleration direction a 600%. Apart from a frequency shift and a maximum acceleration reduction, the experimental and numerical results for the beam system with elastic contact correspond very well.

The measured accelerations are divided into two categories, namely periodic signals and aperiodic signals. As far as the aperiodic signals are concerned, in figure 5.6 the maximum absolute accelerations are plotted. Notice that because of this the experimental and numerical results cannot be compared entirely, since in the calculated response only periodic signals (stable and unstable) are used. Most of the aperiodic signals are chaotic signals. This can be checked by calculating Lyapunov exponents of these signals (Wolf et al., 1985, Van de Vorst et al., 1995). This paper is focused on the measured periodic signals since these can be easier compared to numerically obtained periodic signals.

In figure 5.6 the experimental results correspond very well with the numerical results. Just like in the numerical results, near 34 Hz two harmonic resonance peaks occur in the experiments. However, in the experiment the right harmonic resonance peak has a dip and this was not found in the numerical results. Due to the limited power of the electric motor, it could not be investigated whether the right 1/2 subharmonic resonance peak on the 1/2 subharmonic branch has also a dip. As mentioned in the previous section, all peaks on top of the harmonic resonance peaks are projected to the 1/2 subharmonic resonance peaks. In the numerical response a dip exists for  $f_e = 37.65$  Hz. However, this dip does not exist on top of the right harmonic resonance peak like in the experimental results.

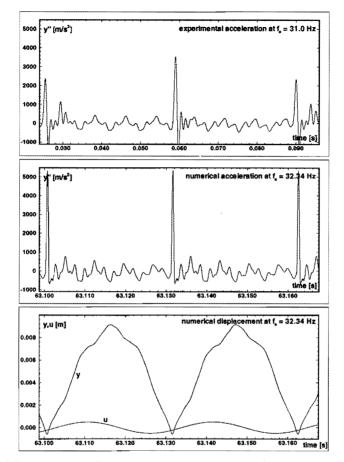


**Figure 5.7** Numerical ( $f_e = 32.34 \text{ Hz}$ ) and experimental ( $f_e = 31.0 \text{ Hz}$ ) harmonic signals.

In figures 5.7–5.10 some experimental and numerical periodic signals are shown which occur near the first harmonic resonance peak. In the figures the measured and numerical contact point acceleration, the numerical contact displacement and the prescribed foundation displacement are shown. Because of the earlier mentioned frequency shift between the numerical and experimental results, the periodic signals are compared for different frequencies for which the signals show the best correspondence. The measured accelerations which are shown in the figures, are filtered by the earlier mentioned low pass filter with a bandwidth of 850 Hz. In figures 5.7–5.9 the experimental and numerical results correspond well. Notice that in the figures the maximum acceleration in the numerical signals is lower than can be expected from figure 5.6 (figure 5.6 gives the maximum absolute acceleration occurs in a very small time interval and because of time discretization in figures 5.7–5.9, the maximum acceleration occurring in the plotted calculated signals is lower.

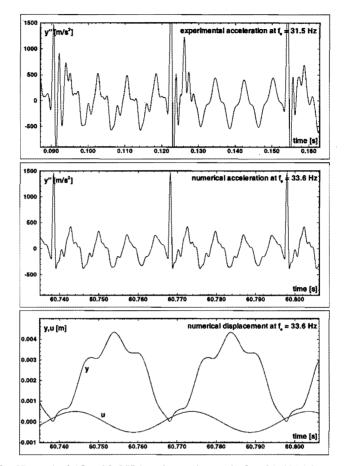


**Figure 5.8** Numerical ( $f_e = 33.6 \text{ Hz}$ ) and experimental ( $f_e = 31.5 \text{ Hz}$ ) harmonic signals

In figure 5.10 the experimental and numerical acceleration signals are compared for  $f_e = 34.5$  Hz and  $f_e = 37.64$  Hz, respectively. At  $f_e = 34.5$  Hz the experimental results show a dip (figure 5.6) in the right first harmonic resonance peak. As mentioned earlier, in the numerical results a dip exists for  $f_e = 37.64$  Hz, which value is 2 Hz higher than expected if the experimental results have a 6 % frequency shift. Figure 5.10 shows that apart from the largest acceleration, the experimental and numerical signals correspond well. The acceleration dip in the numerical results is related to the 11th superharmonic resonance peak of the third 'eigenfrequency' of the nonlinear system ( $11 \times 37.64 = 414$  Hz  $\approx f_3$ ). Apparently, the third eigenfrequency in the experiment is about  $11 \times 34.5 = 379.5$  Hz. As mentioned earlier the third eigenfrequency of the linear beam was experimentally determined to be 378.9 Hz, so this confirms that the acceleration dip is caused by the 11th superharmonic of the third eigenfrequency. Because the third eigenfrequency of the numerical linear model differs approximately 9 % from the eigenfrequency of the experimental linear beam, in the numerical analysis the dip related

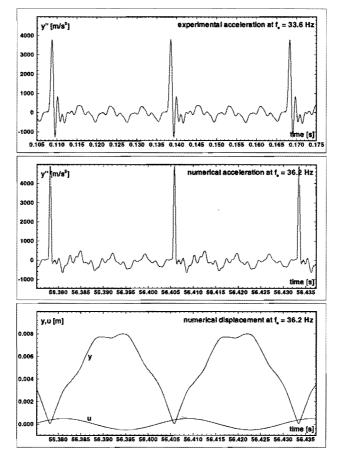


**Figure 5.9** Numerical ( $f_e = 36.2 \text{ Hz}$ ) and experimental ( $f_e = 33.6 \text{ Hz}$ ) harmonic signals.

to the third eigenfrequency does not occur on top of the right harmonic resonance peak but at  $f_e = 37.64$  Hz.

Near  $f_e = 53.0$  Hz the maximum acceleration in both the numerical and experimental results is very low. Figure 5.11 shows the experimental and numerical periodic signals for  $f_e = 50.8$  Hz and  $f_e = 53$  Hz, respectively. Both signals correspond very well and the numerical time-displacement plot shows why the acceleration is so small in this frequency range: if the elastic stop hits the beam, both the elastic stop and beam have approximately the same velocity and this holds for the entire contact time. In the experiment, for this frequency range the noise produced by the experimental setup was surprisingly low.

In figures 5.12–5.14 some experimental and numerical periodic signals are shown which occur near the 1/2 subharmonic resonance peak. Again the experimental and numerical results correspond very well. Notice that for  $f_e = 67.8$  Hz also a considerable high frequency component is present in the time-displacement plot. This high frequency

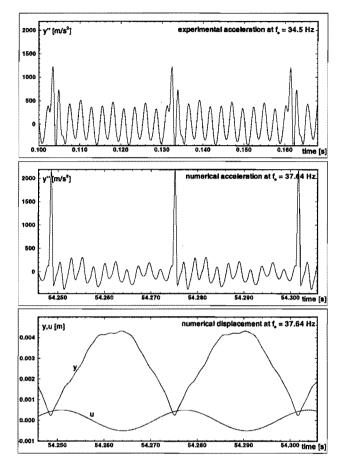


**Figure 5.10** Numerical ( $f_e = 37.64$  Hz) and experimental ( $f_e = 34.5$  Hz) harmonic signals.

component  $f_h$  has four periods per two excitation periods:  $f_h = (67.8/2) \times 4 = 135.6$  Hz  $\approx f_2 = 137.28$  Hz. This confirms that the dip between the two harmonic and 1/2 subharmonic resonance peaks is related to the 4th superharmonic resonance peak of the second 'eigenfrequency' of the system. Notice also the similarity of the periodic solutions near the first harmonic resonance peak (figures 5.7–5.9) and the 1/2 subharmonic resonance peak (figures 5.12–5.14).

#### 5.5 Conclusions.

In this paper, a periodically driven beam system with an elastic contact was investigated both experimentally and numerically. Apart from a frequency shift and a maximum acceleration reduction, the experimental and numerical results correspond very well. The results indicate that higher eigenmodes of the beam play an important role in the low frequency response of the system. Especially near the harmonic and 1/2 subharmonic

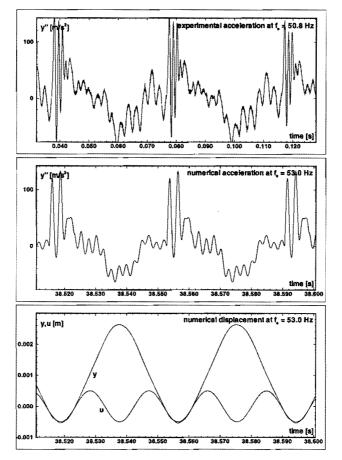


**Figure 5.11** Numerical ( $f_e = 53.0$  Hz) and experimental ( $f_e = 50.8$  Hz) 1/2 subharmonic signals.

resonance peaks, many high frequency eigenmodes are excited. The experimental results indicate that the elastic contact can be modelled using the contact force law of Hertz.

The damping in the *linear* system was experimentally determined to be approximately  $\xi_m = 0.003$ . However, section 5.4 shows that the results obtained using a modal damping coefficient of  $\xi_m = 0.015$  correspond much better. Apparently, the dissipation in the *nonlinear* system is much higher due to the elastic contact. This energy dissipation was not modelled in the numerical model. One has to take into account that by increasing the modal damping coefficient, the damping of all eigenmodes is increased. In the actual system, the energy dissipation caused by the elastic contact is concentrated on one position of the beam (at the contact area). At this point the numerical model can be improved by using a hysterestic damping model in Hertz's law, for instance the model of Lankarani and Nikravesh (1994).

In the experiments a low pass filter was used in order to get a better comparison between experimental and numerical results. A disadvantage of this filter is that the

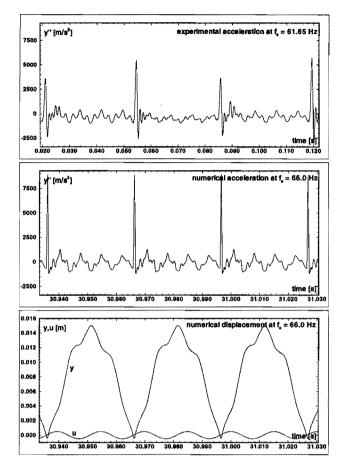


**Figure 5.12** Numerical ( $f_e = 66.0$  Hz) and experimental ( $f_e = 61.65$  Hz) 1/2 subharmonic signals.

maximum accelerations which occur in the measured signals are reduced considerably. As mentioned before, near the resonance peaks, the numerical model which is valid up to 1000 Hz is not accurate enough for approximating the actual system. For these frequency ranges, also a filter bandwidth of above the 1000 Hz should be used instead of the filter bandwidth of 850 Hz used in this paper. Also it would be preferable to measure displacements instead of accelerations in future experiments, since displacement signals do not show as many high frequencies as acceleration measurements. Because of this, the experimental and numerical displacement signals can be compared easier and probably even without using a low pass filter.

#### Acknowledgement.

This work was supported by the Centre for Mechanical Engineering of TNO Building and Construction Research, Delft, The Netherlands. All calculations presented in this

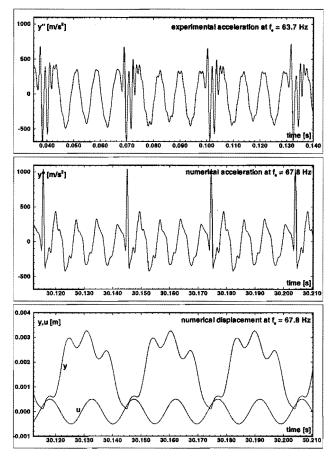


**Figure 5.13** Numerical ( $f_e = 67.8$  Hz) and experimental ( $f_e = 63.7$  Hz) 1/2 subharmonic signals.

paper were carried out using a development release of the finite element package DIANA (1995).

# References

- Ascher, U.M., Mattheij, R.M.M., and Russell, R.D., 1988, "Numerical Solution of Boundary Value Problems for Ordinary Differential Equations," Prentice-Hall, Inc..
- Craig Jr., R.R., 1985, "A Review of Time-Domain and Frequency-Domain Component Mode Synthesis Methods," *Combined Experimental/Analytical Modeling of Dynamic Structural Systems Using Substructure Synthesis*, D.R. Martinez and A.K. Miller, ed., ASME Applied Mechanics AMD-67, New York, pp. 1-31.
- DIANA, 1995, *DIANA User's Manual 6.0 ed.*, TNO Building and Construction Research, Delft, The Netherlands.

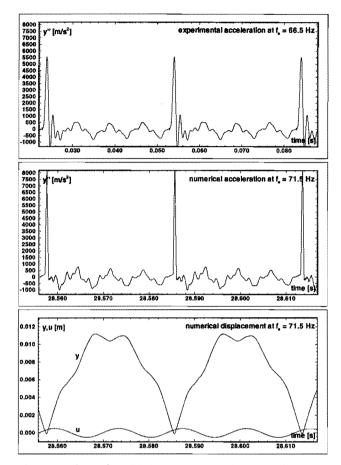
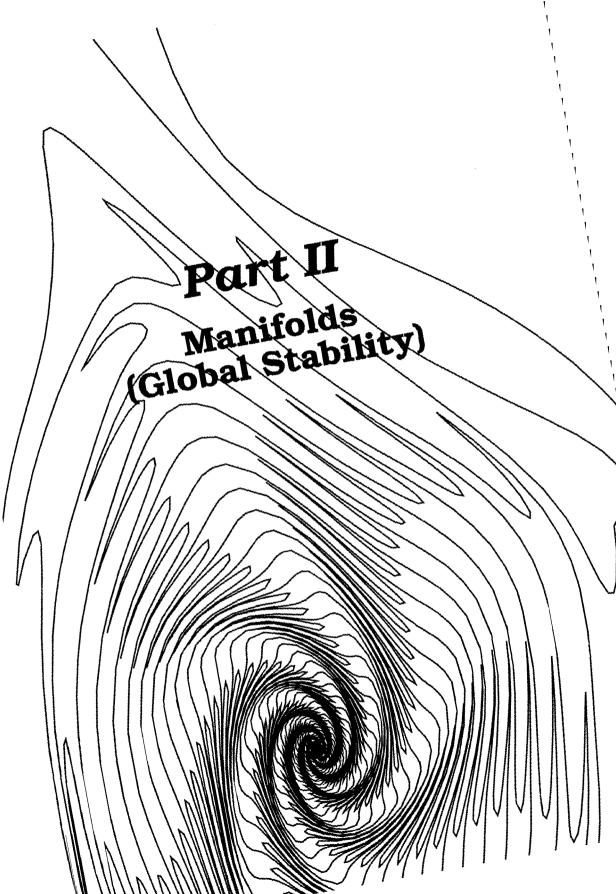


**Figure 5.14** Numerical ( $f_e = 71.5$  Hz) and experimental ( $f_e = 66.5$  Hz) 1/2 subharmonic signals.

- Fey, R.H.B., 1992, "Steady-State Behaviour of Reduced Dynamic Systems with Local Nonlinearities," *PhD thesis*, Department of Mechanical Engineering, Eindhoven University of Technology, Eindhoven, The Netherlands.
- Goldsmith, W., 1960, "Impact: The Theory and Physical Behaviour of Colliding Solids," E. Arnold Ltd., London.
- Guckenheimer, J. and Holmes, P., 1983, "Nonlinear Oscillations, Dynamical Systems and Bifurcations of Vector Fields," *Applied Mathematical Sciences* 42, Springer-Verlag.
- Hertz, H., 1895, "Gesammelte Werke, vol. 1: Schriften Vermischten Inhalts," Leipzig, Germany.
- Lankarani H.M., and Nikravesh, P.E., 1994, "Continuous Contact Force Models for Impact Analysis in Multibody Systems," *Nonlinear Dynamics*, Vol. 5, pp. 19 3–207.
- Parker, T.S. and Chua, L.O., 1989, "Practical Numerical Algorithms for Chaotic Systems," SpringerVerlag.

#### 82CHAPTER 5. EXPERIMENTAL AND NUMERICAL ANALYSIS OF THE STEADY-STATE BEHAVIOUR ...

- Thompson, J.M.T., 1994, "Basic Concepts of Nonlinear Dynamics," Nonlinearity and Chaos in Engineering Dynamics, Proceedings IUTAM Symposium, London, 19-23 July 1993, J.M.T Thompson and S.R. Bishop, ed., John Wiley & Sons, pp. 1–21.
- Thompson, J.M.T. and Stewart, H.B., 1986, "Nonlinear Dynamics and Chaos," John Wiley & Sons Ltd.
- Van de Vorst, E.L.B, Assinck, F.H., De Kraker, A., Fey, R.H.B, and Van Campen, D.H., 1995, "Experimental Verification of the Steady-State Behaviour of a Beam System with Discontinuous Support," *Experimental Mechanics*, accepted for publication.
- Van de Vorst, E.L.B., Van Campen, D.H., Fey, R.H.B., and De Kraker, A., 1995, "Periodic Solutions of a Multi-DOF Beam System with Impact," *Journal of Sound and Vibration*, accepted for publication.
- Wolf, A., Swift, J.B., Swinney, H.L., and Vastano, J.A., 1985, "Determining Lyapunov Exponents from a Time Series," *Physica*, Vol. 16D, pp. 285–317.



.



# 6

# MANIFOLDS OF NONLINEAR DYNAMIC SINGLE-DOF SYSTEMS.<sup>‡</sup>

This paper deals with the long term behaviour (attractors) of nonlinear dynamic single degree of freedom (DOF) systems, excited by a periodic external load. In nonlinear systems, different attractors can coexist for one set of system parameters. The set of initial conditions of trajectories which approach one attractor is called the basin of attraction of the attractor. The boundaries of the basins of attraction are formed by the stable manifolds of unstable periodic solutions. These stable manifolds are the set of initial conditions of trajectories which approach an unstable periodic solution (saddle). Because these are the only trajectories which do not approach an attractor, in general the stable manifolds are the boundaries of the basins of attraction. When stable and unstable manifolds intersect, a chaotic attractor or fractal boundaries of basins of attraction are created. These phenomena are demonstrated by calculating the manifolds of two single-DOF systems, one with a cubic stiffening spring and one with an one-sided spring.

# 6.1 Introduction.

The long term behaviour of a nonlinear system, which is excited by a periodic external load, can yield a periodic, quasi-periodic, or chaotic attractor. The period of a periodic attractor may be equal to the excitation period (harmonic attractor), but may also be a multiple of the excitation period (subharmonic attractors). As an example, a 1/2 subharmonic attractor has a period, which is twice the excitation period. A quasi-periodic attractor is a function of two or more signals, which have incommensurate frequencies. A chaotic attractor is characterized by a broad band spectrum and by an extreme sensitivity for initial conditions.

In a nonlinear system, different attractors can coexist for one set of system parameters,

<sup>&</sup>lt;sup>‡</sup>Van de Vorst, E.L.B., Fey, R.H.B., Van Campen, D.H., and De Kraker, A., 1993, "Manifolds of Nonlinear Dynamic Single-DOF Systems," *Topics in Applied Mechanics, Integration of Theory & Applications in Applied Mechanics*, J.F. Dijksman and F.T.M. Nieuwstadt, ed., Kluwer Academic Publishers, pp. 293–303 (updated).

i.e. the parameters which describe the system. Which attractor a trajectory will approach asymptotically when time proceeds depends on the initial conditions of the system. Every attractor has its own basin of attraction, i.e. the set of initial conditions of trajectories which asymptotically approach the attractor. If only one attractor exists, the basin of attraction may be formed by all possible initial conditions.

There are several ways to calculate the basins of attraction of a system. We mention for instance the cell-mapping method (Hsu, 1980, Hsu, 1987, Van der Spek et al., 1993). In this paper we determine these basins by calculating the so-called stable and unstable manifolds of unstable periodic solutions of the saddle type. The stable (unstable) manifolds of a saddle is the set of initial conditions of trajectories which approach asymptotically the saddle when time is increased (decreased). Because the points on the stable manifolds are the only initial conditions for which the trajectories do not approach an attractor, in general the stable manifolds are the boundaries or separatrices of the basins of attraction.

In section 6.2 a method for calculating stable and unstable manifolds is shortly described. This method is only useful for single degree of freedom (DOF) systems. In section 6.3 homoclinic and heteroclinic points, which are intersections of stable and unstable manifolds, are described. In section 6.4 homoclinic chaos is illustrated by means of a numerical example of a system with a cubic stiffening spring (Duffing spring). In section 6.5 fractal boundaries of basins of attraction are illustrated by a system with an one-sided spring. In section 6.6 it is explained how heteroclinic points can be created.

The basins of attraction will be presented in a so-called Poincaré section. The Poincaré section is defined as the  $2n_q$  dimensional state space, stroboscopically enlightened at times  $t = (\Phi_p/2\pi f_e) + i/f_e$ , where *i* is an arbitrary integer,  $\Phi_p$  is the phase angle,  $n_q$  the number of degrees of freedom and  $f_e$  the excitation-frequency. In this paper  $\Phi_p$  is chosen zero. The Poincaré section of a subharmonic solution of order (1/n) (*n* integer) will contain *n* points. In case of a single-DOF system the manifolds will appear as lines in the Poincaré section.

#### 6.2 Calculation of manifolds of single-DOF systems.

The method used for the calculation of manifolds was developed in Parker and Chua (1989). We will describe this method shortly. Periodic solutions of a nonlinear system can be calculated by solving a two-point boundary value problem with the finite difference method (Fey, 1992) or with the shooting method (Meijaard, 1991). The stability of these periodic solutions can be investigated using Floquet theory (Parker and Chua, 1989). Application of Floquet theory results in eigenvalues, the so-called Floquet multipliers, and corresponding eigenvectors: The Floquet multipliers quantify the extent of (in)stability of a periodic solution. When the calculated solution is stable the modulus of all the Floquet multipliers will be smaller than one. The solution is unstable if the modulus of one or more Floquet multipliers is larger than one. The solution is marginally stable if the largest modulus of the Floquet multipliers equals one. The

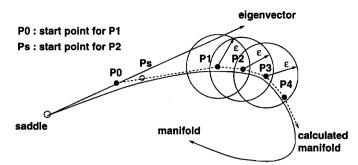


Figure 6.1 Calculation of stable manifold.

number of Floquet multipliers is twice the number of degrees of freedom of the system.

In case of a single-DOF system two Floquet multipliers are found. A so-called saddle of a single-DOF system is an unstable periodic solution with one real Floquet multiplier with a modulus larger than one, and one real Floquet multiplier with a modulus smaller than one. The two eigenvectors give the stable and unstable directions of the saddle in the Poincaré section. In the stable direction the saddle attracts trajectories; in the unstable direction it repels trajectories. Using these directions the initial conditions on the stable and unstable manifolds in the immediate neighbourhood of the saddle in the Poincaré section are determined and are used to calculate the manifolds.

The stable (unstable) manifolds of a saddle are all the initial conditions of trajectories, which approach asymptotically the saddle when time is increased (decreased). As stated before, the manifolds of a saddle of a single-DOF system are lines in a Poincaré section. If one integrates over the period of a saddle, every point on its manifold is mapped to a point on the same manifold.

For the calculation of the stable manifold a start point  $P_0$  is chosen in the Poincaré section on the line through the saddle point in the direction of the stable eigenvector, resulting from the stability analysis which, after integration backwards in time over the period of the saddle, has a return point  $P_1$ , which lies within a small relative distance  $\epsilon$  of the eigenvector (figure 6.1).  $P_0$  can be found by choosing optional start points closer to the saddle until the return point  $P_1$  lies within the relative distance  $\epsilon$  of the eigenvector. The next point on the stable manifold is the return point  $P_2$  of a start point which lies on the line between the points  $P_0$  and  $P_1$  and is chosen so that the return point  $P_2$  lies within the relative distance  $\epsilon$  of point  $P_1$  on the stable manifold. In practice this start point is found by calculating return points of several start points. Firstly the return point of  $P_1$  is calculated. If this return point does not lie within the relative distance  $\epsilon$  of  $P_1$ , the return point is calculated of a start point which lies halfway  $P_0$  and  $P_1$ . If this return point still lies not close enough to  $P_1$ , a new start point is chosen halfway  $P_0$  and the last start point. This process is continued until the return point lies within the distance  $\epsilon$  of  $P_1$ .

All the return points which are calculated to achieve this are stored because they are all points of the stable manifold; every return point of a start point on a manifold lies also on the manifold. The other points on the stable manifold  $P_3$ ,  $P_4$ , etc. are calculated in the same way; a start point is chosen between the already calculated points of the

manifold so that the return point lies within the distance  $\epsilon$  of the last calculated point of the manifold. However, sometimes this calculation can be avoided because the point was already calculated and stored in an earlier stadium but did not lie within the relative distance  $\epsilon$  of the last calculated point then.

The unstable manifold can be calculated using the same procedure, although now a start point is chosen on the unstable eigenvector resulting from the stability analysis and return points are calculated by integrating forward in time. The accuracy of the calculated manifolds depends on the relative distance  $\epsilon$ . Unfortunately, the accuracy of a calculation can only be checked by recalculating the manifold with a smaller relative distance  $\epsilon$ .

#### 6.3 Homoclinic and heteroclinic points.

If an intersection of a stable and unstable manifold exists, there has to be an infinite number of other intersections of these two manifolds, because every return point of a start point on a manifold must lie also on this manifold. If an intersection of the stable and unstable manifolds occurs, its return point must lie also on both manifolds and is also an intersection-point.

The intersections of a stable and an unstable manifold of the same saddle are called homoclinic points. Intersections of stable and unstable manifolds of different saddles are called heteroclinic points. Because of these homoclinic and heteroclinic points, the stable and/or unstable manifolds get a 'chaotic' structure when they cross each other.

Stable manifolds can never intersect other stable manifolds. Trajectories of initialpoints, which lie on a stable manifold, approach asymptotically the saddle. If two stable manifolds of different saddles would intersect, this would imply an infinite number of intersections, so the saddles would also be intersection points, which they are not. For unstable manifolds this is also the case.

#### 6.4 Homoclinic chaos.

It is well known that homoclinic points of manifolds can result in a chaotic attractor, which will appear on the unstable manifolds (Parker and Chua, 1989). These unstable manifolds get a chaotic structure because of the homoclinic points. In figure 6.2a the manifolds of the following system are shown:

$$\ddot{x} + 0.25\dot{x} + 0.02x + x^3 = 8.5\cos(t) \tag{6.1}$$

Figure 6.2a shows the existence of a harmonic saddle, a 1/3 subharmonic saddle, and a 1/3 subharmonic attractor. The stable manifolds  $W_1^s$  of the harmonic saddle intersect with the unstable manifolds  $W_1^u$  and one half of the unstable manifolds  $W_3^u$  of the 1/3 subharmonic saddle. Because of the fact that most homoclinic points lie close to the harmonic saddle,  $W_1^u$  gets a chaotic structure.  $W_1^u$  is leaded back to the saddle because of the homoclinic points, and this saddle is unstable so trajectories in this area will stay

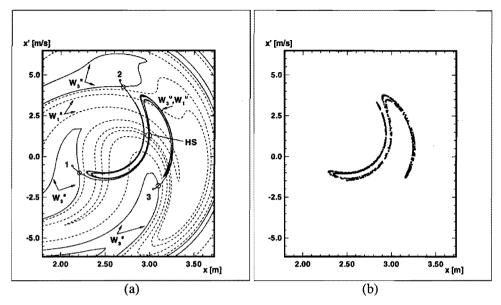


**Figure 6.2** (a) Stable and unstable manifolds. The numbers 1-3 represent the 1/3 subharmonic attractor. The saddles are in the circles with HS=harmonic saddle.  $W_1^s$  is the dashed line. (b) Chaotic attractor.

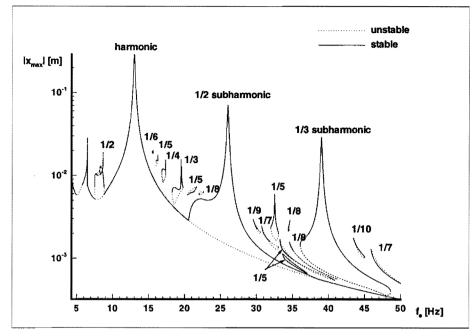
on  $W_1^u$ . Here a chaotic attractor exists, plotted in figure 6.2b, which will appear on  $W_1^u$ .  $W_1^s$  is not a boundary of basins of attraction because the harmonic saddle lies in a chaotic attractor. This is one way how chaos is created and it is called homoclinic chaos, because it is created by the homoclinic points.

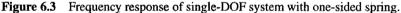
One half of  $W_3^u$  is also attracted by this chaotic attractor, but does not intersect with  $W_1^u$ . Because of this heteroclinic points are created of  $W_3^u$  and  $W_1^s$ , and  $W_3^u$  gets the same 'chaotic' structure as  $W_1^u$ . Because of the infinite number of heteroclinic intersections in the neighbourhood of the harmonic saddle, trajectories started on  $W_3^u$ will finally approach the saddle and go further on  $W_1^u$ .

The stable manifolds  $W_3^s$  of the 1/3 subharmonic saddle are the boundaries of basins of attraction of the 1/3 subharmonic attractor and the chaotic attractor. Notice that the basin of attraction of the 1/3 subharmonic attractor is separated into three parts. There exist three 1/3 subharmonic attractors, which are the same, except for a phase-difference of one excitation period. The other half of  $W_3^u$  ends in these 1/3 subharmonic attractors.

#### 6.5 Fractal boundaries of basins of attraction.

Homoclinic points and heteroclinic points can also result in fractal boundaries of basins of attraction. Grebogi et al. (1986) proved that fractal boundaries of basins of attraction are caused by homoclinic and heteroclinic points, and they showed that this is a common phenomenon in nonlinear dynamics. To investigate fractal boundaries of attraction the





following system is considered:

$$m\ddot{x} + b\dot{x} + k(1+\alpha)x = F\cos(2\pi f_e t) \tag{6.2}$$

with m = 1.0358 kg, b = 1.166 Ns/m, k = 3282.2 N/m, F = 19.69 N and  $\alpha = 6$  if x < 0 and  $\alpha = 0$  if  $x \ge 0$ . This system was investigated earlier by Fey (1992) and by Thompson and Stewart (1986).

In figure 6.3 the maximum displacements x occurring in the periodic solutions are shown for varying excitation frequency. Besides a harmonic resonance peak near 13 Hz a lot of subharmonic resonance peaks exist. The highest 1/2 and 1/3 subharmonic solutions are related to the harmonic resonance peak. The 1/3 subharmonic near 20 Hz, the 1/5 subharmonics near 32.5 Hz and the 1/7 subharmonic near 46 Hz are related to the 2nd superharmonic resonance peaks. The other subharmonic solutions are also related to higher order superharmonic resonance peaks of the first harmonic resonance peak.

In figure 6.4-6.6 the manifolds of this system are shown of this system for  $f_e = 20.5$ , 21.5 and 21.85 Hz, respectively. At 20.5 Hz two attractors exist; a harmonic and a 1/5 subharmonic. Also a 1/5 subharmonic saddle exists and  $W_5^s$  is the boundary of the basins of attraction.

At 21.5 Hz the harmonic attractor has been replaced by two 1/2 subharmonic attractors and a harmonic saddle via a flip bifurcation (Fey, 1992). Heteroclinic points of  $W_1^s$  and  $W_5^u$  exist and because most heteroclinic points lie close to the 1/5 subharmonic saddle,  $W_1^s$  gets a chaotic structure in that area. The boundaries of the basins of attraction are not smooth any more but fractal. At 21.85 Hz the 1/5 subharmonic attractors and

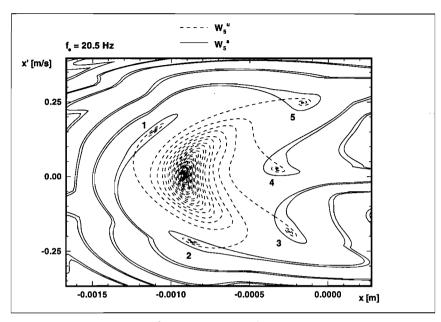


**Figure 6.4** Manifolds at  $f_e = 20.5$  Hz. Numbers 1-5 represent the 1/5 subharmonic attractor.

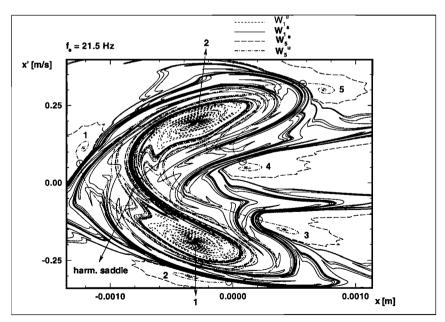


**Figure 6.5** Manifolds at  $f_e = 21.5$  Hz. Numbers 1-5 represent the 1/5 subharmonic attractor. Numbers 1-2 represent the 1/2 subharmonic attractor. Saddles are in the circles.

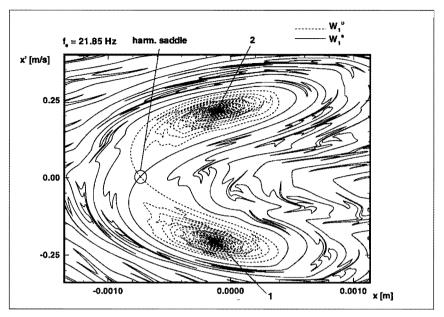


Figure 6.6 Manifolds at  $f_e = 21.85$  Hz. Numbers 1-2 represent the 1/2 subharmonic attractor.

saddles have disappeared and the boundaries of the basins of attraction are smooth again. Sudden changes of basins of attraction are called metamorphoses (Grebogi et al., 1986).

Fractal boundaries of basins of attraction were investigated earlier by Grebogi et al. (1983) and they presented a method for calculating the dimension of the basins of attraction. They calculate the trajectories of initial conditions  $(x, \dot{x}), (x + \epsilon, \dot{x})$  and  $(x - \epsilon, \dot{x})$ . If one or two of these trajectories approach a different attractor they call  $(x, \dot{x})$ uncertain. If f is the fraction of uncertain points of a subspace of a Poincaré section, then  $f = \epsilon^{D-d}$ . D is the dimension of the Poincaré section (D = 2 in case of a single-DOFsystem), and d is the dimension of the basin of attraction. If the basin boundaries are smooth, d is equal to one; if the basin boundaries are fractal, d is a non-integer.

This dimension was calculated for the basins of attraction of the above mentioned system for  $f_e = 37$  Hz. Figure 6.7 shows the manifolds for this case. 1/2 and 1/3 subharmonic attractors exist and harmonic and 1/3 and 1/5 subharmonic saddles. Heteroclinic and homoclinic points cause fractal boundaries of basins of attraction in the neighbourhood of the 1/2 subharmonic attractors. The dimension d was calculated 1.92 for the subsection of the Poincaré section with boundaries  $-0.0004 \le x \le 0.0004$  [m] and  $-0.015 \le x \le 0.015$  [m/s].

The distance between the 1/2 subharmonic attractors and the stable manifolds is very small. This means that a little disturbance on one 1/2 subharmonic attractor can result in a phase-jump or a jump to one of the three 1/3 subharmonic attractors. The 1/3 subharmonic attractors (which are not shown in figure 6.7) are much more stable than the 1/2 subharmonic attractors. In Soliman and Thompson (1990) the influence of adding noise to the excitation force was investigated. They showed that especially

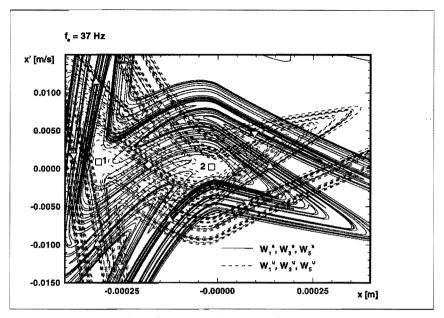


Figure 6.7 Manifolds at  $f_e = 37$  Hz. The symbols represent the harmonic and two 1/5 subharmonic saddles. The numbers 1-2 represent the 1/2 subharmonic attractor. The 1/3 subharmonic saddle and 1/3 subharmonic attractor are not shown.

in case of fractal basin boundaries, the sensitivity for noise on the excitation force of attractors can be very high, and these attractors become unstable.

A periodic attractor can turn into a virtual chaotic attractor because of noise (Soliman and Thompson, 1990, Iansiti et al., 1985). In figure 6.5 the unstable manifolds have a chaotic structure around the 1/2 subharmonic attractors. Because of this, noise on the excitation force may change the 1/2 subharmonic attractors into a virtual chaotic attractor, and this virtual chaotic attractor will have the same structure as the unstable manifolds. Notice that the unstable manifolds get a chaotic structure because of the fact that  $W_5^u$  does not cross  $W_1^u$  and because of the infinite intersections of  $W_5^u$  and  $W_1^s$ . This explains why attractors with a low global stability are especially found in systems with fractal basin boundaries.

#### 6.6 The creation of homoclinic and heteroclinic points.

The question why stable and unstable manifolds intersect was investigated by several researchers. In Yamaguchi and Tanikawa (1992) the manifolds of saddles of a period-doubling-cascade which results in chaos are investigated. They proved that  $W_{2n}^u$  always intersects with  $W_{2m}^s$ , with n, m integers and n < m and  $W_{2n}^s$  and  $W_{2m}^u$  do not intersect. In Grebogi et al. (1987) another criterion was found for Henon's map. They proved that in Henon's map  $W_n^u$  always intersects with  $W_m^s$ , with n < m.

Looking at figure 6.5, a harmonic saddle and a 1/5 subharmonic saddle exist. One

half of  $W_5^u$  leads to the 1/5 subharmonic attractor. The other half of  $W_5^u$ , which are five manifolds, must approach two attractors, the 1/2 subharmonic attractors. If one 1/2 subharmonic attractor point is integrated over one *excitation* period, it will lie in the other point of 1/2 subharmonic attractor. This means that every point in the neighbourhood of one point of the 1/2 subharmonic attractor must have a return point, after integration over one *excitation* period, which lies in the neighbourhood of the other point of the 1/2 subharmonic attractor. Points on an unstable manifold, which approach one point of the 1/2 subharmonic attractor must have return points, which lie on an unstable manifold which approaches the other point of the 1/2 subharmonic attractor. Because of this the number of unstable manifolds which approach the 1/2 subharmonic attractors must be a multiple of two: each point of the 1/2 subharmonic attractors in the Poincaré section must be approached by an equal number of manifolds.

The five unstable manifolds of  $\mathcal{W}_5^u$  are not a multiple of two. Because of this the manifolds circle around the 1/2 subharmonic attractors and must cross  $\mathcal{W}_1^s$ ; heteroclinic points are created.

In figure 6.7 the same happens with the unstable manifolds of the 1/3 and 1/5 subharmonic saddles which approach the 1/2 subharmonic attractors. Three and five are also not multiples of two and  $W_3^u$  and  $W_5^u$  cross  $W_1^s$ . Here, also homoclinic points of  $W_1^u$  and  $W_3^u$ ,  $W_3^u$  and  $W_3^s$ ,  $W_5^u$  and  $W_5^s$  exist.

The conclusion is that heteroclinic points are created when a 1/n subharmonic saddle, a 1/m subharmonic attractor and a 1/m (or 2/m) subharmonic saddle coexist, with n > m, and n is not equal to 2km with k integer. Notice that this is only valid if the unstable manifolds of the 1/n subharmonic saddle are attracted by the 1/m subharmonic attractor.

#### 6.7 Conclusions.

A method for calculating manifolds of single-DOF systems has been presented. The stable manifolds of an unstable periodic solution may determine the domains of attraction of the attractors. The unstable manifolds of an unstable periodic solution give information about the existing attractors and their stability. A chaotic attractor will in most cases appear on unstable manifolds. Using manifolds, the existence of homoclinic chaos and fractal boundaries of basins of attraction has been shown. An explanation has been given for how heteroclinic points can be created.

The method is not practical for systems with more than one degree of freedom. The basins of attraction of multi-DOF systems cannot be represented by one 2D-Poincaré section. The basins of attraction are (hyper) planes, and calculating them using stable manifolds is very expensive. Unstable manifolds can be calculated for multi-DOF systems in case the Floquet multipliers are real.

#### 6.7. CONCLUSIONS.

#### Note

All calculations in this paper were done using a development-release of the finite element package DIANA (1995) (module *STRDYN* for nonlinear dynamic analysis). For numerical integration, the Adams method (NAG, 1991) was used (accuracy of 9 significant digits).

# Acknowledgements

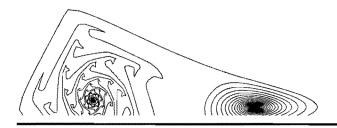
We would like to thank W. van de Water of the Department of Physics of Eindhoven University of Technology for bringing additional papers to our attention. This work was supported by TNO Building and Construction Research.

## References

- DIANA, 1995, *DIANA User's Manual 6.0 ed.*, TNO Building and Construction Research, Delft, The Netherlands.
- Fey, R.H.B., 1992, "Steady-State Behaviour of Reduced Dynamic Systems with Local Nonlinearities," *PhD thesis*, Department of Mechanical Engineering, Eindhoven University of Technology, Eindhoven, The Netherlands.
- Grebogi, C., McDonald, S.W., Ott, E., Yorke, Y.A., 1983, "Final State Sensitivity: An Obstruction to Predictability," *Physics Letters*, Vol. 99A, pp. 415-418.
- Grebogi, C., Ott, E. and Yorke, Y.A., 1986, "Metamorphoses of Basin Boundaries in Nonlinear Dynamical Systems," *Physical Review Letters*, Vol. 56, pp. 1011–1014.
- Grebogi, C., Ott, E., and Yorke, Y.A., 1987, "Basin Boundary Metamorphoses: Changes in Accessible Boundary Orbits," *Physica*, Vol. 24D, pp. 243–262.
- Hsu, C.S., 1980, "A Theory of Cell-to-Cell Mapping Dynamical Systems," *Journal of Applied Mechanics*, Vol. 47, pp. 931–939.
- Hsu, C.S., 1987, "Cell to Cell Mapping; A Method of Global Analysis for Nonlinear Systems," Springer-Verslag of Applied Mechanics.
- Iansiti, M., Hu, Q., Westervelt, R.M., and Tinkham, M., 1985, "Noise and Chaos in a Fractal Basin Boundary Regime of a Josephson Junction," *Physical Review Letters*, Vol. 55, pp. 746–749.
- Meijaard, J.P., 1991, "Dynamics of Mechanical Systems, Algorithms for a Numerical Investigation of the Behaviour of Non-linear Discrete Models," *PhD thesis*, Department of Mechanical Engineering, Delft University of Technology, Delft, The Netherlands.
- NAG Fortran Library, 1991, mark 15 edition.
- Parker, T.S. and Chua, L.O., 1989, "Practical Numerical Algorithms for Chaotic Systems," Springer-Verlag.

#### 96 CHAPTER 6. MANIFOLDS OF NONLINEAR DYNAMIC SINGLE-DOF SYSTEMS

- Soliman, S.M. and Thompson, J.M.T., 1990, "Stochastic Penetration of Smooth and Fractal Basin Boundaries under Noise Excitation," *Dynamics and Stability Systems*, Vol. 5, pp. 281-298.
- Van der Spek, J.A.W., Van Campen, D.H., and De Kraker, A., 1993, "Application of Cell Mapping Methods to Nonlinear Dynamic Systems," *Topics in Applied Mechanics, Integration of Theory & Applications in Applied Mechanics*, J.F. Dijksman and F.T.M. Nieuwstadt, ed., Kluwer Academic Publishers, pp. 293–303.
- Thompson, J.M.T. and Stewart, H.B., 1986, "Nonlinear Dynamics and Chaos," John Wiley & Sons Ltd.
- Yamaguchi, Y. and Tanikawa, K., 1992, "Structure Change of Stable and Unstable Manifolds in Two-Dimensional Maps: Period-Doubling Bifurcation," *Chaos, Solitons & Fractals*, Vol. 2, pp. 139–146.



7

# DETERMINATION OF GLOBAL STABILITY OF STEADY-STATE SOLUTIONS OF A BEAM SYSTEM WITH DISCONTINUOUS SUPPORT USING MANIFOLDS.<sup>‡</sup>

This paper deals with the global stability of the long term dynamics of nonlinear mechanical systems under periodic excitation. Generally, the boundaries of the basins of attraction are formed by the stable manifolds of unstable periodic solutions. These stable manifolds are the set of initial conditions of trajectories which approach an unstable periodic saddle solution. Because these are the only trajectories which do not approach an attractor, in general the stable manifolds are the boundaries of the basins of attraction. In this paper manifolds are calculated of a beam system supported by a one-sided spring in order to identify the global stability of the coexisting attractors. The numerical results are compared with experimental results.

## 7.1 Introduction.

Generally, the long term behaviour of periodically excited nonlinear mechanical systems is much more complex than the steady-state behaviour of linear systems. The long term behaviour can be periodic, quasi-periodic or chaotic. Furthermore, the long term behaviour may depend on the initial state of the system. The system behaviour can also be very sensitive to its system parameters and/or to disturbances on the system in some frequency ranges.

The long term behaviour of a nonlinear system can be determined by calculating periodic solutions by solving a two-point boundary value problem with the finite difference method (Fey, 1992), alternatively by using the shooting method (Ascher et al., 1988) or the incremental harmonic balance method (Lau and Yuen, 1991). The first method is most efficient from a computational point of view for systems with many degrees of freedom (DOF's). If one periodic solution has been calculated, branches of periodic solutions can be followed using a path following technique. The *local* stability of these

<sup>&</sup>lt;sup>‡</sup>Van de Vorst, E.L.B., Van Campen, D.H., Fey, R.H.B., and De Kraker, A., 1995, "Determination of Global Stability of Steady-State Solutions of a Beam System with Discontinuous Support using Manifolds," *Chaos, Solitons, & Fractals*, accepted invited paper.

#### 98CHAPTER 7. DETERMINATION OF GLOBAL STABILITY OF STEADY-STATE SOLUTIONS ...

periodic solutions is investigated using Floquet theory. A periodic solution is locally stable if any infinitesimal disturbance on the system vibrating in that solution yields the system to return to that periodic solution.

If two or more attractors coexist, the basins of attraction, i.e. the set of initial states for which the corresponding trajectories approach the attractor, determine the *global* stability of the attractors. If, for instance, a locally stable attractor is lying close to the boundary of its basin of attraction, a little disturbance on the system vibrating in that attractor can result in a jump to another attractor. So a locally stable attractor may have a low global stability.

For determining the global stability of attractors, the boundaries of the basins of attraction should be known. Generally, the boundaries of the basins of attraction are the stable manifolds of unstable periodic saddle solutions. The stable (unstable) manifolds of an unstable periodic solution are the set of initial states for which the corresponding trajectories approach the unstable periodic solution if the time is increased (decreased). So by calculating the stable manifolds of unstable periodic solutions, the global stability of stable attractors can be determined. Parker and Chua (1989) developed a method for calculating stable and unstable manifolds of single-DOF systems. Generally, for multi-DOF systems, stable manifolds become planes in the Poincaré section. Therefore, it becomes very expensive to calculate these manifolds. However, often the unstable manifolds are still one-dimensional and can be calculated using the Parker and Chua method. Nevertheless, it generally is not possible to determine efficiently the global stability of multi-DOF systems using manifolds.

In this paper the stable and unstable manifolds of a 2D-beam system supported by a one-sided spring are calculated in order to determine the global stability of the attractors of the system. This system was earlier investigated by Fey et al. (1994) and showed complex nonlinear behaviour. Fey et al. (1994) showed that the single-DOF model is to some extend already a good approximation for the beam system in the low frequency range.

In section 7.2 the Parker and Chua method for calculating manifolds of unstable periodic solutions is described shortly. In section 7.3 the periodically excited beam system with nonlinear support, which will be analysed, is described. In section 7.4 the long term behaviour and global stability of the single-DOF model is analysed by calculating the manifolds for different excitation frequencies. In order to check the numerical results obtained in section 7.4, in section 7.5 the global stability of the attractors in an experimental set-up of the beam system is determined. All calculations presented in this paper were carried out using a development release of the finite element package DIANA (1995).

#### 7.2 Calculation of manifolds.

The method used for the calculation of manifolds was developed by Parker and Chua (1989). In this section we will describe this method shortly. As mentioned in section 7.1 the local stability of a periodic solution can be investigated using Floquet theory.

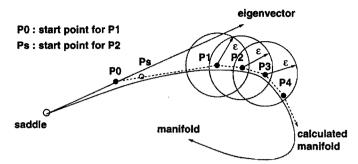


Figure 7.1 Calculation of manifold.

Application of Floquet theory results in eigenvalues, the so-called Floquet multipliers, and corresponding eigenvectors. The Floquet multipliers quantify the extent of local (in)stability of a periodic solution. If the calculated solution is stable, the modulus of all the Floquet multipliers will be smaller than one. The solution is unstable if the modulus of one or more Floquet multipliers is larger than one. The solution is marginally stable if the largest modulus of the Floquet multipliers equals one.

In case of a so-called unstable periodic saddle solution, one or more Floquet multipliers exist with a modulus larger than one, and one or more Floquet multipliers exist with a modulus smaller than one. The eigenvectors corresponding to the Floquet multipliers are the stable and unstable directions of the saddle in the Poincaré section. In the stable directions the saddle attracts trajectories; in the unstable directions it repels trajectories. In this way, the initial directions of the stable and unstable manifolds in the immediate neighbourhood of the saddle in the Poincaré section are determined.

The stable (unstable) manifolds of an unstable periodic saddle solution is the set of all initial conditions corresponding to trajectories, which approach asymptotically the saddle when time is increased (decreased). This implies that if one integrates over the period of a saddle, every point on its manifold is mapped to a point on the same manifold.

Using the Parker and Chua method, only manifolds which are one-dimensional in the Poincaré section can be calculated. This implies that the corresponding Floquet multiplier and eigenvector of the saddle solution is real. For the calculation of a manifold a start point  $P_0$  is chosen in the Poincaré section on the line through the saddle point in the direction of the stable eigenvector, resulting from the local stability analysis which, after integration backwards (in case of a stable manifold) or forwards (in case of an unstable manifold) in time over the period of the saddle, has a return point  $P_1$ , which lies within a small relative distance  $\epsilon$  of the eigenvector (figure 7.1).  $P_0$  can be found by choosing optional start points closer to the saddle until the return point  $P_1$  lies within the relative distance  $\epsilon$  of the eigenvector.

The next point on the stable manifold is the return point  $P_2$  of a start point  $P_s$  which lies on the line between the points  $P_0$  and  $P_1$  and is chosen in such way that the return point  $P_2$  lies within the relative distance  $\epsilon$  of point  $P_1$  on the stable manifold. In practice this start point is found by calculating return points of several start points. Firstly the return point of  $P_1$  is calculated. If this return point does not lie within the relative distance  $\epsilon$  of  $P_1$ , the return point is calculated of a start point which lies halfway  $P_0$ 

100CHAPTER 7. DETERMINATION OF GLOBAL STABILITY OF STEADY-STATE SOLUTIONS...

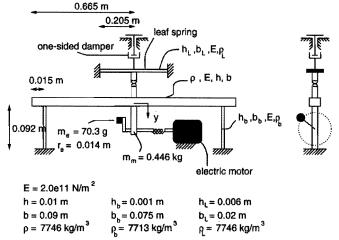


Figure 7.2 Experimental setup of beam system.

and  $P_1$ . If this return point still lies not close enough to  $P_1$ , a new start point is chosen halfway  $P_0$  and the last start point. This process is continued until the return point lies within the distance  $\epsilon$  of  $P_1$ .

All the return points which are calculated to achieve this are stored because they are all points of the stable manifold; every return point of a start point on a manifold lies also on the manifold. The other points on the stable manifold  $P_3$ ,  $P_4$ , etc. are calculated in the same way; a start point is chosen between the already calculated points of the manifold in such way that the return point lies within the relative distance  $\epsilon$  of the last calculated point of the manifold. However, sometimes this calculation can be avoided because the point was already calculated and stored in an earlier stadium, but did not lie within the relative distance  $\epsilon$  of the last calculated point the neutron of the last calculated point the statement.

The accuracy of the calculated manifolds depends on the relative distance  $\epsilon$ . Unfortunately, the accuracy of a calculation can only be checked by recalculating the manifold with a smaller distance  $\epsilon$ .

# 7.3 Beam system supported by one-sided spring.

Figure 7.2 shows the beam system which is analysed both numerically and experimentally. The beam is supported at both ends by leaf springs, and supported in the middle by a one-sided leaf spring. The one-sided leaf spring is damped one-sided for reducing its vibrations if it does not make contact with the beam. The periodic forcing is realized by a rotating mass which is driven by an electric motor. For coupling the rotating mass with the electric motor a rubber hose is used. For a more detailed description of the experiment the reader is referred to (Van de Vorst et al., 1995).

The beam and leaf springs are modelled using the finite element method. The onesided leaf spring is modelled by a one-sided spring, so mass influences are neglected. Because of symmetry only half the beam is modelled.

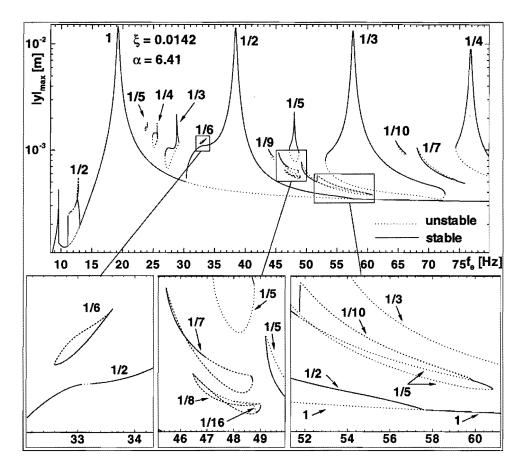


Figure 7.3 Maximum displacements of periodic solutions of single DOF model.

## 7.4 Single-DOF model.

As mentioned in section 7.1, Fey et al. (1994) showed that the system reduced to one DOF is to some extend already a good approximation for the beam system (see also section 7.5). After reduction of the finite element model, the equation of motion for the single-DOF model can be obtained as

$$m\ddot{y} + b\dot{y} + k(\alpha_p + 1)y = m_e r_e \omega^2 cos(\omega t)$$
(7.1)

Here  $\alpha_p = \begin{cases} \alpha, \ y < 0 \\ 0, \ y \ge 0 \end{cases}$  and  $\alpha = 6.41$ ,  $\omega = 2\pi f_e$ ,  $b = 2\xi\sqrt{mk}$ ,  $\xi = 0.009$ ,  $m = (\varphi_1^T M \varphi_1)/\varphi_{1y}^2 = 2.48$  kg,  $k = (\varphi_1^T K \varphi_1)/\varphi_{1y}^2 = 16877$  N/m,  $m_e = 35.15$  g,  $r_e = 0.014$  m. M and K are the mass and the stiffness matrix of the linear part of the system, i.e. the beam without the one-sided spring.  $\varphi_1$  is the first eigenmode of the linear system with an eigenfrequency of 13.1 Hz.  $\varphi_{1y}$  is the element of  $\varphi_1$  corresponding to the displacement

of the middle of the beam y. Branches of periodic solutions of this system are calculated for varying excitation frequency  $f_e$ . The maximum absolute displacements of these periodic solutions are given in figure 7.3. Besides the harmonic peak near 19.2 Hz also 1/2, 1/3, 1/4, 1/5, 1/6, 1/7, 1/8, 1/9, 1/10, and 1/16 subharmonic resonances are found.

The highest 1/2, 1/3, 1/4 subharmonic resonance peaks are related to the harmonic resonance peak. The lower 1/3 (near 28 Hz), 1/5 (near 48 Hz) and 1/7 (near 70 Hz) subharmonic solutions are related to the second superharmonic resonance peak near 9.6 Hz. The 1/2 (near 13 Hz), 1/4 (near 25 Hz), 1/7 (near 46 Hz), 1/8 (near 48 Hz), and 1/10 (near 65 Hz) subharmonic solutions are related to the third superharmonic resonance peak near 6.4 Hz (not visible in figure 7.3). Near 12 Hz, 48 Hz and 55 Hz, periodic doubling cascades exist, which start with a 1/2, 1/8 and 1/5 subharmonic solutions exist, also a stable harmonic or stable 1/2 subharmonic solution coexists. It is important to determine the global stability of the stable harmonic and 1/2 subharmonic solutions because if this stability is low, the maximum response of the system will increase considerably due to the high resonance peaks of the subharmonic solutions.

Figure 7.4 shows Poincaré sections with the stable and unstable manifolds  $W_5^s$ ,  $W_5^u$  of the unstable 1/5 subharmonic saddle solution for the single-DOF system for  $f_e = 24$  Hz. This figure also shows the stable and unstable manifolds  $W_4^s$ ,  $W_4^u$  of the unstable 1/4 subharmonic saddle solution for  $f_e = 25.4$  Hz and the stable and unstable manifolds  $W_3^s$ ,  $W_3^u$  of the unstable 1/3 subharmonic saddle solution for  $f_e = 28$  Hz. The 1/5, 1/4 and 1/3 subharmonic solutions are related to the fourth, third and second superharmonic resonance peaks respectively. In the figure the cross points of the stable and unstable manifolds are the unstable subharmonic saddle solutions. The stable manifolds are the other half approaches the stable subharmonic solutions. The stable manifolds are the boundaries of the basins of attraction. Notice that if a 1/n subharmonic solution exists, n equal 1/n subharmonic attractors have their own basin of attraction.

Figure 7.4 shows that the harmonic solution has the lowest global stability in the frequency range where the 1/3 subharmonic solutions exist (27-30 Hz) compared to the frequency ranges where the 1/5 and 1/4 subharmonic solutions exist. For  $f_e = 28$  Hz the boundaries of the basins of attraction are closest to the harmonic solution. Furthermore, the total basin of attraction of the harmonic solution is small for  $f_e = 28$  Hz in comparison to the attraction basin for  $f_e = 24$  Hz and  $f_e = 25.4$  Hz. The local stability of the harmonic solutions for  $f_e = 24$  Hz, 25.4 Hz and 28 Hz are almost equal; the modulus of the corresponding Floquet multipliers are 0.952, 0.954, 0.958 respectively. It can be concluded from this figure that subharmonic solutions related to lower order superharmonic resonances have the largest influence on the global stability of coexisting attractors.

Figure 7.6 shows the Poincaré sections with manifolds for  $f_e = 32$  Hz and 33 Hz. For  $f_e = 32$  Hz only a stable 1/2 subharmonic solution and an unstable harmonic solution exist. The stable manifolds  $W_1^s$  of the unstable harmonic solution are the boundaries of the basins of attraction of two 1/2 subharmonic solutions with a phase difference of

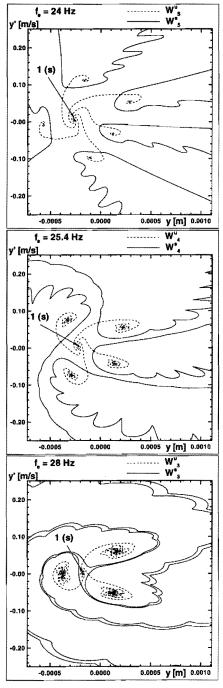


**Figure 7.4** Manifolds for single DOF system for  $f_e = 24$  Hz,  $f_e = 25.4$  Hz and  $f_e = 28$  Hz.

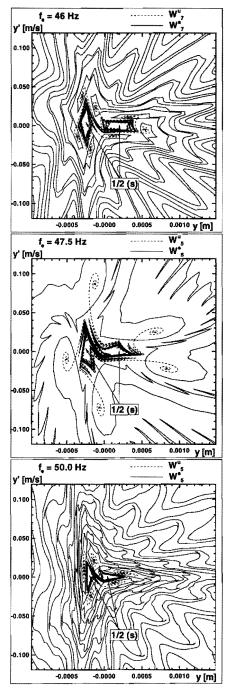
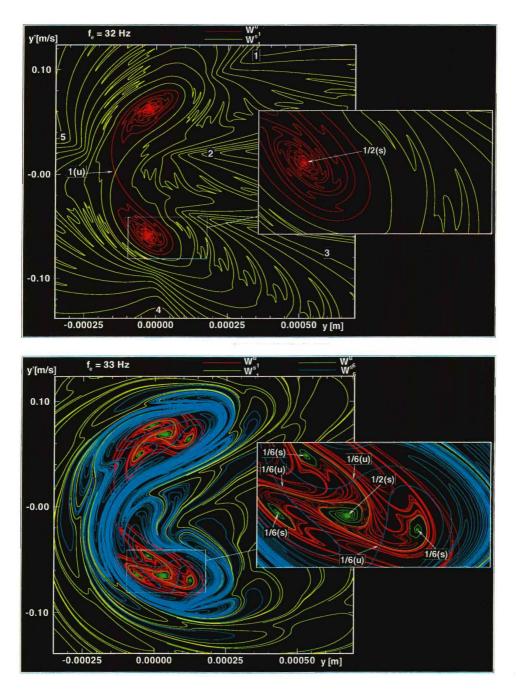


Figure 7.5 Manifolds for single DOF system for  $f_e = 46$  Hz,  $f_e = 47.5$  Hz and  $f_e = 50$  Hz.

104CHAPTER 7. DETERMINATION OF GLOBAL STABILITY OF STEADY-STATE SOLUTIONS...



**Figure 7.6** Manifolds for single DOF system for  $f_e = 32$  Hz and  $f_e = 33$  Hz.

one excitation period. The third superharmonic resonance peak near 6.4 Hz indicates that there might be a 1/5 subharmonic solution for this frequency (5 × 6.4 = 32 Hz). However, the 1/5 subharmonic solution does not exist but the structure of the stable manifolds  $W_1^s$  indicates that for other system parameters (a lower damping level) the 1/5 subharmonic solution does exist;  $W_1^s$  has 5 V-forms (the numbers 1-5 in figure 7.6) where the 1/5 subharmonic solution is created if, for instance, the damping level is decreased.

For  $f_e = 33$  Hz also stable and unstable 1/6 subharmonic solutions exist. Figure 7.6 shows that the stable manifolds  $\mathcal{W}_6^s$  of the unstable 1/6 subharmonic solution intersect with the unstable manifolds  $W_1^u$  of the unstable harmonic solution. If a stable and unstable manifold intersect, simultaneously another infinite number of intersections of the two manifolds has to exist because every start point on a manifold is mapped on the same manifold if one integrates over one excitation period. This means that an intersection point is mapped on both the stable and unstable manifold, so an intersection point is mapped on an intersection point. Intersections of stable manifolds and unstable manifolds of the same unstable saddle solution are called homoclinic points. Intersections of stable and unstable manifolds of different unstable saddle solutions are called heteroclinic points. Hence, figure 7.6 shows an infinite number of heteroclinic points of  $\mathcal{W}_1^u$  and  $\mathcal{W}_6^s$ . Because of this  $\mathcal{W}_6^s$  gets a fractal structure; the boundaries of the basins of attraction of the stable 1/6 subharmonic solutions become fractal. Notice that  $\mathcal{W}_1^u$  also gets a fractal structure due to the infinite heteroclinic intersections and because it can not intersect with the unstable manifolds  $\mathcal{W}_{6}^{u}$  ((un)stable manifolds do not intersect one another). Actually, the 1/6 subharmonic solution was identified by looking at the special structure of  $\mathcal{W}_1^u$ . The global stability of the 1/2 subharmonic attractor is decreased considerably by the creation of the 1/6 subharmonic solution.

Figure 7.7 shows the stable and unstable manifolds  $\mathcal{W}_1^s$ ,  $\mathcal{W}_1^u$  of the unstable harmonic solution for  $f_e = 43.0$  Hz. Again, only a 1/2 subharmonic solution coexists with an unstable harmonic solution. In figure 7.8 the frequency is increased to  $f_e = 44$  Hz. Now in addition a stable and an unstable 1/9 subharmonic solution coexist (which are related to the fourth superharmonic resonance peak). Besides  $W_1^s$ ,  $W_1^u$  now also the stable and unstable manifolds  $W_{9}^{s}$ ,  $W_{4}^{u}$  of the unstable 1/9 subharmonic saddle solution are shown in figure 7.8. The figure shows that one half of  $\mathcal{W}_9^u$  approaches the stable 1/9 subharmonic solution and that  $W_9^s$  are the boundaries of the basins of attraction of the 1/9 subharmonic solutions. The other half of  $\mathcal{W}_9^u$  approaches the unstable harmonic solution and the stable 1/2 subharmonic solutions. An infinite number of heteroclinic points exist near the unstable 1/9 subharmonic saddle solution because here  $\mathcal{W}_9^u$  intersects with  $\mathcal{W}_1^s$ . Due to the infinite number of heteroclinic intersections the boundaries of the basins of attraction of the two 1/2 subharmonic solutions get a fractal structure and approach  $W_{s}^{s}$ and therefore it is difficult to see  $\mathcal{W}_9^s$  in figure 7.8. The basins of attraction of the 1/9 subharmonic attractors are small and also the global stability is low for these attractors, because  $W_9^s$  lies close to the stable 1/9 subharmonic attractors. Notice that compared to figure 7.6 now the global stability of the 1/2 subharmonic solution is less reduced by the creation of extra subharmonic solutions.

In figure 7.5 the stable and unstable manifolds are shown of the 1/7 and 1/5 subhar-

106CHAPTER 7. DETERMINATION OF GLOBAL STABILITY OF STEADY-STATE SOLUTIONS...

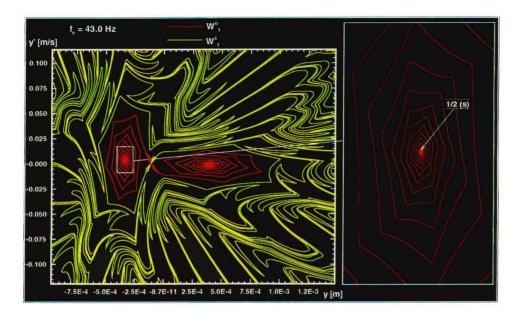


**Figure 7.7** Manifolds for single DOF system for  $f_e = 43.0$  Hz.

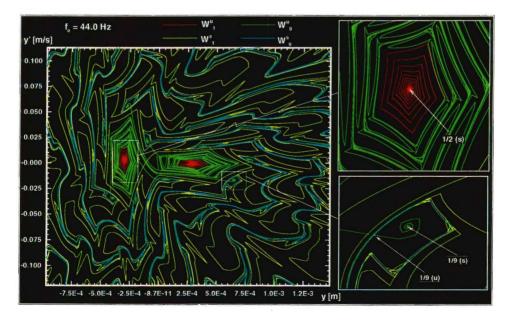


**Figure 7.8** Manifolds for single DOF system for  $f_e = 44.0$  Hz.

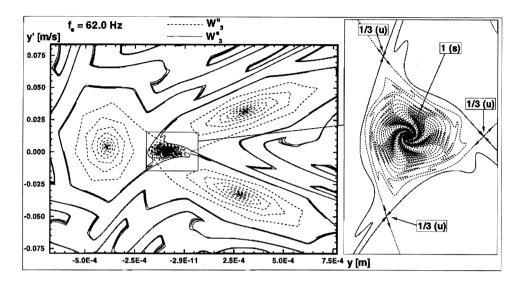


Figure 7.9 Manifolds for single DOF system for  $f_e = 62.0$  Hz.

monic solutions at  $f_e = 46$  Hz,  $f_e = 47.5$  Hz and  $f_e = 50$  Hz. The manifolds  $\mathcal{W}_1^u, \mathcal{W}_1^s$ of the unstable harmonic solutions are not shown but  $W_1^s$  has a fractal structure due to the infinite heteroclinic intersections with  $W_7^u$  and  $W_5^u$ . The 1/7 subharmonic solutions at  $f_e = 46$  Hz are related to the third superharmonic, whereas the 1/5 subharmonic solutions at  $f_e = 47.5$  Hz and  $f_e = 50$  Hz are related to the second superharmonic resonance peak. One half of the unstable manifolds of the unstable subharmonic solutions approaches the stable subharmonic attractors, whereas the other half intersects with  $\mathcal{W}_{1}^{s}$ and approaches the unstable harmonic and stable 1/2 subharmonic solutions. The stable manifolds of the unstable subharmonic saddle solutions are the boundaries of the basins of attraction of the stable subharmonic attractors. Figure 7.5 shows that only the 1/5 subharmonic solutions at  $f_e = 47.5$  Hz which are related to the second superharmonic resonance peak have a large global stability and have a large basin of attraction. Only the 1/5 subharmonic solutions at  $f_e = 50$  Hz reduce the global stability of the stable 1/2 subharmonic attractors considerably, although the global stability of the stable 1/5 subharmonic solutions itself is not very large. From this it can be concluded that the subharmonic solutions related to the lower order superharmonic resonance peaks have a larger global stability, but these subharmonic solutions will not always reduce the global stability of coexisting attractors. Furthermore, other subharmonic attractors with a low global stability can reduce the global stability of coexisting attractors considerably.

Figure 7.9 shows the stable and unstable manifolds  $W_3^s$  and  $W_3^u$  of the unstable 1/3 subharmonic saddle solution at  $f_e = 62.0$  Hz. For this frequency a stable harmonic and 1/3 subharmonic solution coexist. The figure shows that the basin of attraction of the harmonic solution is very small. In practice, the harmonic solution will be difficult to find. The global stability of the stable 1/3 subharmonic solutions is large. Figure 7.10 has the same scalings as figure 7.9 and shows again  $W_3^s$  and  $W_3^u$  for an increased excitation

108CHAPTER 7. DETERMINATION OF GLOBAL STABILITY OF STEADY-STATE SOLUTIONS...

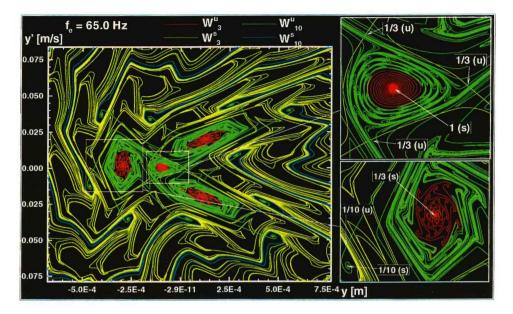


Figure 7.10 Manifolds for single DOF system for  $f_e = 65.0$  Hz.

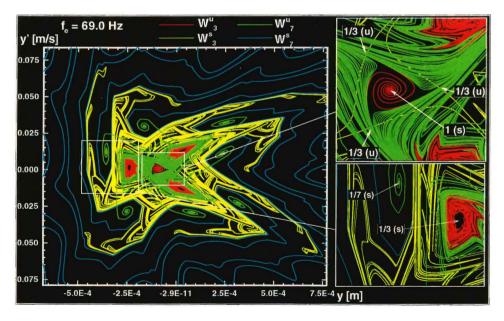


Figure 7.11 Manifolds for single DOF system for  $f_e = 69.0$  Hz.

frequency of  $f_e = 65.0$  Hz. Now also stable and unstable 1/10 subharmonic solutions exist which are related to the third superharmonic resonance peak. Heteroclinic intersections exist of  $W_3^s$  and  $W_{10}^u$  and because of this  $W_3^s$  gets a fractal structure near  $W_{10}^s$  and  $W_{10}^u$ gets a fractal structure near  $W_3^u$ . The basin of attraction of the harmonic solution is again very small and the global stability of the stable 1/3 subharmonic solutions is still large. The global stability of the stable 1/10 subharmonic solutions is low and their basins of attraction are small.

Figure 7.11 shows the stable and unstable manifolds,  $W_3^s$ ,  $W_3^u$ ,  $W_7^s$  and  $W_7^u$  of the unstable 1/3 subharmonic saddle solution and the unstable 1/7 subharmonic saddle solution respectively at  $f_e = 69.0$  Hz. The 1/7 subharmonic solutions are related to the second superharmonic resonance peak, and their basins of attraction are larger than the basins of attraction of the 1/10 subharmonic solutions in figure 7.10. This confirms that the basin of attraction of subharmonic resonance peaks. Notice that now the global stability of the 1/3 subharmonic solution is also reduced. In figure 7.11 only a part of  $W_3^s$  is shown, otherwise  $W_3^s$  would cover the whole figure, excluded the basins of attraction of the 1/7 subharmonic solutions.

# 7.5 Experimental results.

In order to check the numerical results of section 7.4, an experimental set-up of the beam system is used to determine the global stability of the attractors in the experiment.

Figure 7.12 shows the maximum displacements occurring in the periodic solutions as function of the excitation frequency for the four-DOF model and the experimental results (symbols). The four-DOF model is established by modelling the beam and leaf springs using finite elements and subsequently reducing the model with a component mode synthesis method (Craig, 1985, Fey et al. 1996) to four DOF's (three eigenmodes with eigenfrequencies  $f_1 = 13.1$  Hz,  $f_2 = 117.5$  Hz,  $f_3 = 326.5$  Hz and one residual flexibility mode).

Figure 7.12 shows that the four-DOF model, which is proven to be a good approximation for the unreduced model in the investigated frequency range (Fey et al., 1996), has almost a similar response as the single-DOF model in figure 7.3. All subharmonic solutions of the single-DOF model are found in the four-DOF model also. Extra superharmonics resonance peaks are visible in figure 7.12. The superharmonic resonance peaks at  $f_e = 30$  Hz,  $f_e = 40$  Hz and  $f_e = 59$  Hz are related to the second eigenfrequency of the beam. Another difference is that the 1/2 subharmonic, the 1/3 subharmonic and 1/4 subharmonic solutions which are related to the second superharmonic resonance peak of the first harmonic resonance peak are divided into two branches near  $f_e = 47.5$ Hz,  $f_e = 70$  Hz and  $f_e = 79$  Hz respectively. Near  $f_e = 47.5$  Hz, intermittency behaviour was found and this frequency range was further investigated in (Fey et al., 1994). In the frequency range  $f_e = 69-73$  Hz the harmonic solution is unstable marked by two secondary Hopf bifurcations. Here, a stable 1/7 subharmonic attractor exists and in the frequency range  $f_e = 71-73$  Hz also a stable 1/3 subharmonic attractor exists.

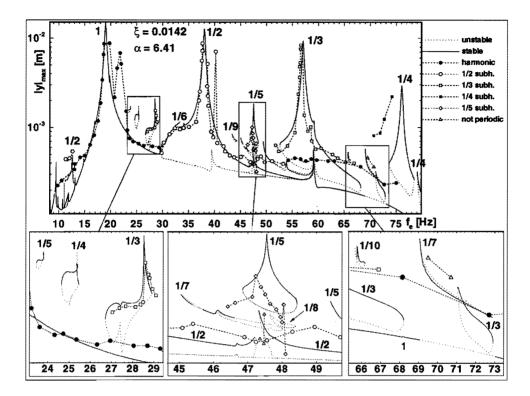


Figure 7.12 Maximum displacements of periodic solutions of four DOF model and experimental results.

In the experiments all subharmonic solutions which are related to the harmonic resonance peak and second superharmonic resonance peak are found. In the experiments extra peaks are found right behind the first harmonic resonance peak and the 1/2 subharmonic and 1/3 subharmonic peaks which are related to the first harmonic resonance peak. In these frequency intervals, in the experiments a small extra frequency in the response occurred, which caused the enlargement of the maximum displacements (the signals are not periodic). This frequency is caused by the flexible rubber hose coupling, which couples the electric motor with the rotating mass (Van de Vorst et al., 1995).

The 1/3 subharmonic solutions near 28 Hz were found by fastly varying the excitation frequency or by hitting the beam if it was vibrating in the coexisting harmonic solution. Only one 1/4 subharmonic solution near 24 Hz was found, again by hitting the beam. Slowly varying the excitation frequency while the beam is vibrating in the 1/4 subharmonic solution directly resulted in a jump to the harmonic solution. This means that the global stability of the 1/4 subharmonic solution is very low. The 1/5 subharmonic solution near 24 Hz was not found in the experiment. In section 7.4 it was shown that the 1/3 subharmonic solution has the largest basin of attraction in comparison to the 1/5 and 1/4 subharmonic solutions near 24 and 25 Hz. Furthermore, the harmonic solution has the lowest global stability in the frequency range underneath the 1/3 subharmonic solutions. The experimental results confirm this but one has to take into account that the frequency ranges for which the 1/4 and 1/5 subharmonic attractors exist are much smaller than the frequency range for which the 1/3 subharmonic solutions exist. This implies that in the experiment it is more difficult to find the 1/4 and 1/5 subharmonic solutions.

The 1/6 subharmonic solutions near 33 Hz were not found in the experiment although in section 7.4 it was concluded that the 1/6 subharmonic solution decreases the global stability of the 1/2 subharmonic solution considerably. The reason for this may be that the 1/6 subharmonic solutions exist in a small frequency range and their maximum displacements are almost equal to the maximum displacements for the 1/2 subharmonic solution. Furthermore, the 1/6 subharmonic solutions are very similar to the coexisting 1/2 subharmonic solutions.

In the frequency range near 47.5 Hz, the 1/5 subharmonic solution was measured in the experiment, again by hitting the beam if it vibrates in the 1/2 subharmonic solution. Here, the 1/9 and 1/7 subharmonic solutions could not be found. In section 7.4 it was concluded that the 1/9 and 1/7 subharmonic attractors have a small basin of attraction compared to the 1/5 subharmonic solution. In this frequency range also chaotic behaviour was found experimentally. The 1/5 subharmonic solution near 50 Hz was also not found.

In the frequency range  $f_e = 54-68$  Hz where the 1/3 subharmonic solutions exist, in the experiment it was very difficult to find the coexisting harmonic solutions. Only by starting outside this frequency range and subsequently slowly varying the frequency, it was possible to measure the harmonic solution. Little disturbances on the beam directly resulted in a jump to the 1/3 subharmonic solution. Notice that these harmonic solutions have a larger maximum amplitude than the numerically calculated solutions. This is due to the low tension stiffness of the rubber hose coupling, see (Van de Vorst et al., 1995). In section 7.4 it was shown that the harmonic solutions underneath the 1/3 subharmonic solutions have a much lower global stability than the stable 1/3 subharmonic solutions. Furthermore the basin of attraction of the harmonic solution is much smaller. This was observed in the experiments.

The 1/10 subharmonic solutions above the 1/3 subharmonic solutions were not found in the experiments. In section 7.4 it was shown that this 1/10 subharmonic attractor has a small basin of attraction and that its global stability is low. Furthermore, the frequency range for which the 1/10 subharmonic solution exists is small. Near 72 Hz an aperiodic signal was measured in the experiment. Comparison of the signal with the 1/7 subharmonic solutions showed that these two signals are very similar. The 1/4 subharmonic solutions near 75 Hz were again found by hitting the beam if it is vibrating in the harmonic solution.

# 7.6 Conclusions.

In this paper, the manifolds of a single-DOF model of a beam system, supported in the middle by a one-sided spring, were calculated in order to determine the global stability

#### 112CHAPTER 7. DETERMINATION OF GLOBAL STABILITY OF STEADY-STATE SOLUTIONS ...

of coexisting attractors. Because the beam system has eigenfrequencies which lie in a large frequency range, the single-DOF model is a good approximation of the beam system in the frequency range under investigation. The experimental results show that it is possible to determine the global stability of attractors using the manifolds of the single-DOF model.

An advantage of calculating basins of attraction using manifolds is that it is very easy to detect if fractal boundaries of basins of attraction exist, because in that case the stable and unstable manifolds intersect. A disadvantage is that this method can not be used for multi-DOF systems since the stable manifolds become planes in the Poincaré section. However, for multi-DOF systems it is possible to calculate the unstable manifolds and often the structure of these manifolds will inform if homoclinic or heteroclinic points exist. Hence it still can be determined whether the boundaries of the basins of attraction are fractal. Nevertheless, manifolds can not be used to determine the global stability of steady-state attractors of multi-DOF systems.

The results show that subharmonic solutions related to higher order superharmonic resonance peaks often have a low global stability and a small basin of attraction. However, these subharmonic solutions can have a large influence on the basins of attraction of other attractors (their boundaries may become fractal) and thus on the global stability of these attractors.

# Acknowledgement.

This work was supported by the Centre for Mechanical Engineering of TNO Building and Construction Research, Delft, The Netherlands.

# References

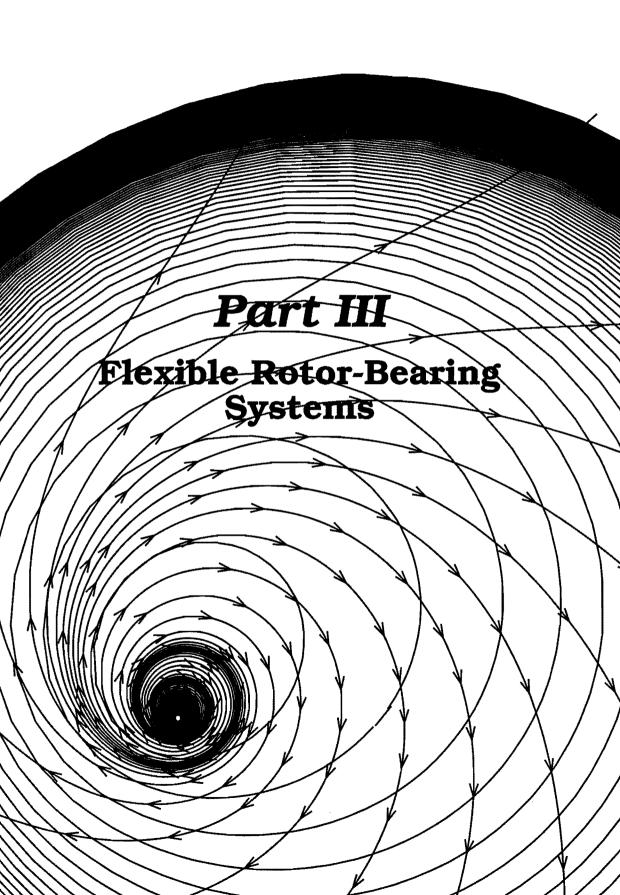
- Ascher, U.M., Mattheij, R.M.M., and Russell, R.D., 1988, "Numerical Solution of Boundary Value Problems for Ordinary Differential Equations," Prentice-Hall Inc..
- Craig Jr., R.R., 1985, "A Review of Time-Domain and Frequency-Domain Component Mode Synthesis Methods," *Combined Experimental/Analytical Modeling of Dynamic Structural Systems Using Substructure Synthesis*, D.R. Martinez and A.K. Miller, ed., ASME Applied Mechanics AMD-67, New York, pp. 1-31.
- DIANA, 1995, *DIANA User's Manual 6.0 ed.*, TNO Building and Construction Research, Delft, The Netherlands.
- Fey, R.H.B., 1992, "Steady-State Behaviour of Reduced Dynamic Systems with Local Nonlinearities," *PhD thesis*, Department of Mechanical Engineering, Eindhoven University of Technology, Eindhoven, The Netherlands.
- Fey, R.H.B., Van de Vorst, E.L.B., Van Campen, D.H., De Kraker, A., Meijer, G.J., and Assinck, F.H., 1994, "Chaos and Bifurcations in a Multi-DOF Beam System with Nonlinear

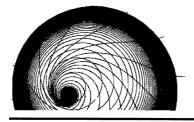
#### 7.6. CONCLUSIONS.

Support," Nonlinearity and Chaos in Engineering Dynamics, Proceedings IUTAM Symposium, London, 19-23 July 1993, J.M.T. Thompson and S.R. Bishop, ed., John Wiley & Sons, pp. 125–139.

- Fey, R.H.B., Van Campen, D.H., and De Kraker, A., April 1996, "Long Term Structural Dynamics of Mechanical Systems with Local Nonlinearities," ASME *Journal of Vibration and Acoustics*, (in press).
- Lau, S.L. and Yuen, S.W., 1991, "The Hopf Bifurcation and Limit Cycle by the Incremental Harmonic Balance Method," *Computer Methods in Applied Mechanics and Engineering*, Vol. 91, pp. 1109–1121.
- Parker, T.S. and Chua, L.O., 1989, "Practical Numerical Algorithms for Chaotic Systems," Springer-Verlag.
- Van de Vorst, E.L.B, Assinck, F.H., De Kraker, A., Fey, R.H.B, and Van Campen, D.H., 1995, "Experimental Verification of the Steady-State Behaviour of a Beam System with Discontinuous Support," *Experimental Mechanics*, accepted for publication.

114CHAPTER 7. DETERMINATION OF GLOBAL STABILITY OF STEADY-STATE SOLUTIONS...





8

# STEADY-STATE BEHAVIOUR OF FLEXIBLE ROTOR DYNAMIC SYSTEMS WITH OIL JOURNAL BEARINGS.<sup>‡</sup>

This paper deals with the long term behaviour of flexible rotor systems, which are supported by nonlinear bearings. A system consisting of a rotor and a shaft which is supported by one oil journal bearing is investigated numerically. The shaft is modelled using finite elements and reduced using a component mode synthesis method. The bearings are modelled using the finite-length bearing theory. Branches of periodic solutions are calculated for three models of the system with an unbalance at the rotor. Also self-excited oscillations are calculated for the three models if no mass unbalance is present. The results show that a mass unbalance can stabilize rotor systems and that the first eigenfrequency has a large influence on the self-excited oscillations.

# 8.1 Introduction.

It is a well-known phenomenon that the periodic solutions of periodically excited rotor systems can become unstable in certain intervals of the angular rotor speed. This instability is caused by the nonlinear characteristics of the bearings. For practical applications it is important to determine the unstable intervals and to calculate which kind of behaviour results in these intervals: periodic, quasi-periodic or chaotic. Generally in the unstable intervals the maximum response of the system will increase and also extra frequencies can occur in the response. This may lead to shaft rubbing which is undesirable in practice. For the same reason it is important to detect for which angular rotor speeds resonances may occur.

The standard practice for dynamic imbalance response and stability analysis of rotor-bearing systems is to determine the linearized bearing stiffness and damping co-

<sup>&</sup>lt;sup>‡</sup>Van de Vorst, E.L.B., Fey, R.H.B., De Kraker, A., and Van Campen, D.H., 1994, "Steady-State Behaviour of Flexible Rotor Dynamic Systems with Oil Journal Bearings," *Proceedings of the WAM of the ASME, Symposium on Nonlinear and Stochastic Dynamics*, A.K. Bajaj, N.S. Namachchivaya, R.A. Ibrahim, ed., AMD-Vol. 192, DE-Vol 78, New York, pp. 107-114. Updated version accepted for publication in *Nonlinear Dynamics*, 1996.

#### 118CHAPTER 8. STEADY-STATE BEHAVIOUR OF FLEXIBLE ROTOR DYNAMIC SYSTEMS ...

efficients about a stationary equilibrium position. In this mathematical assumption, the synchronous motion about the stationary equilibrium position is described by ellipses in case of low values of the unbalance. However, when the unbalance level becomes moderate to large, the rotor orbits are not necessarily elliptical, due to the nonlinear characteristics of the bearings. Furthermore, in a linear system, operating above the threshold angular rotor speed, the amplitude of motion grows exponentially with time and the orbits become unbounded. In an actual system this is not necessarily the case because the nonlinear effects can cause the motion to be bounded by limit cycles. Moreover, under some circumstances a lower total response can be obtained by having a moderate level of rotor unbalance in the system.

The analysis of the nonlinear effects in rotor-bearing systems is extremely difficult. The most commonly accepted method for nonlinear dynamic analysis is to perform a time-transient integration method for the complete set of equations of motion. Therefore, even for relatively simple systems this becomes a formidable task since the Reynolds' equation for the bearings has to be evaluated at each time step (Gunter et al., 1983).

In this paper the finite-length impedance bearing theory (Childs et al., 1977) is used for modelling the bearings. In this way rotor-bearing systems can be analysed efficiently because the current bearing forces in the equations of motion for the complete rotor system are calculated using analytical expressions. The finite-length bearing theory is accurate but only useful for plain cylindrical journal bearings.

An additional reduction of computational time can be achieved because rotor systems are typical examples of nonlinear dynamic systems consisting of large linear parts (shaft, disks) and local nonlinearities (bearings). This kind of systems can be analysed efficiently if the number of degrees of freedom of the linear parts are reduced using a component mode synthesis method (Craig, 1985, Fey, 1992, Fey et al., 1996). The use of component mode synthesis methods for reducing rotor systems is common practice, see for example Li and Gunter (1981), Nelson and Meacham (1981) and Nelson et al. (1982). The component mode synthesis method used in this research is based on residual flexibility modes and free-interface eigenmodes up to a cut-off frequency The residual flexibility modes guarantee unaffected (quasi-)static behaviour. The reduced linear parts are coupled with the local nonlinearities and this results in a reduced nonlinear system which is an approximation of the unreduced system. The reduced nonlinear system can be used up to the cut-off frequency. Because nonlinear systems can generate higher frequencies than the excitation frequency, in general the cut-off frequency has to be chosen much higher than the maximum excitation frequency.

In section 8.2 the rotor system which is investigated is introduced. The long term behaviour for three models of this system is investigated. In section 8.3 a model with the rotor close to the oil journal bearing is evaluated. Periodic solutions of this model are calculated for different mass eccentricities by solving two-point boundary value problems using the finite difference method (Fey, 1992, Fey et al., 1996, Fey et al., 1994) or the incremental harmonic balance method (Lau and Yuen, 1991). By means of a path-following technique (Fey, 1992, Fey et al., 1996) changes of these periodic solutions are calculated efficiently if a system parameter (for example the angular rotor speed) is varied. The local stability of the periodic solutions is determined using

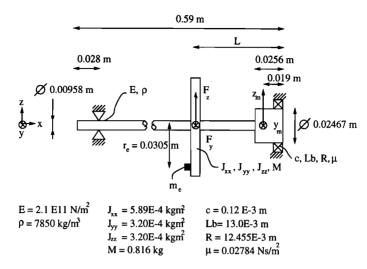


Figure 8.1 Rotordynamic system.

Floquet multipliers. These Floquet multipliers are also used to detect co-dimension one bifurcation points on the branches with periodic solutions. In sections 8.4 and 8.5 the distance between the rotor and oil journal bearing is increased. All calculations in this paper were carried out using a development release of the finite element package DIANA (1995).

# 8.2 Rotordynamic system supported by one oil journal bearing.

Figure 8.1 shows the rotor system which is analysed numerically. The system consists of a rotor and a flexible shaft supported on one side by an oil journal bearing and pinned on the other side. As mentioned in section 8.1, the oil journal bearing is modelled using the finite-length bearing theory. This theory is based on the impedance method (Childs et al., 1977). In the long bearing theory and short bearing theory used for instance by Myers (1984) and Khonsari and Chang (1993), it is assumed that the half of the bearing for which cavitation exists depends only on the minimum oil film thickness. However, this assumption is only valid for low shaft velocities. The impedance method uses the shaft velocity also for calculating the cavitation region in the bearing which implies that this method is also valid for high shaft velocities. In Van de Vorst et al. (1995) it has been shown that the influence of the velocity on the cavitation region cannot be neglected in nonlinear analysis of rotor-bearing systems. In appendix 8.A the formulae are given for the finite-length bearing theory.

The Sommerfeld number  $\sigma$  of the bearing is defined as

$$\sigma = \frac{L_b R^3 \mu}{c^2} \frac{\omega}{F}$$

with  $L_b$  the bearing length, R the bearing radius,  $\mu$  the lubricant viscosity, c the bearing

	1	
unreduced	reduced	
202 DOF	14 DOF	diff
[rad/s]	[rad/s]	[%]
484.71	484.71	0.00
484.71	484.71	0.00
1230.6	1230.6	0.00
1230.6	1230.6	0.00
2892.8	2940.7	1.66
2892.8	2940.7	1.66

Table 8.1 Eigenfrequencies linear undamped shaft without the bearing, L = 0.133 m.

unreduced	reduced	
202 DOF	14 DOF	diff
[rad/s]	[rad/s]	[%]
232.12	232.12	0.00
232.12	232.12	0.00
948.38	948.38	0.00
948.38	948.38	0.00
2808.58	2848.04	1.40
2808.58	2848.04	1.40

**Table 8.2** Eigenfrequencies pinnedpinned linear undamped shaft, L = 0.133 m.

clearance,  $\omega$  the angular rotor speed and F the static external load force acting on the bearing. The system is investigated in the frequency range  $\omega = 0-1050$  rad/s and if the static force is taken as F = 8 N (which is approximately the weight of the rotor), the Sommerfeld number of the bearing varies from 0-6.4.

Only the gyroscopic effects of the rotor are taken into account; the gyroscopic effects of the shaft are neglected. The distance between the oil journal bearing and the rotor is L. The system is analysed for three values of L: 0.038 m, 0.133 m, 0.275 m. The system is externally loaded by gravity and a mass unbalance of the rotor, so the dynamic loads can be written as

$$F_y = r_e m_e \omega^2 \cos(\omega t)$$
;  $F_z = r_e m_e \omega^2 \sin(\omega t)$ 

with  $r_e = 0.0305$  m and  $m_e$  is the mass unbalance.

The shaft is assumed to be modally damped with modal damping coefficients  $\xi = 0.01$  for all eigenmodes. The shaft is modelled using the finite element method and subsequently reduced using the component mode synthesis method mentioned in section 8.1. In the reduction two rigid body modes, eight residual flexibility modes (two for the bearing, two for the outputs  $y_m$  and  $z_m$  and four for the rotor) and four free-interface eigenmodes are used, so the model has 14 degrees of freedom (DOF's). Notice that the system could be further reduced to 12 DOF's if the output points are chosen at the rotor or at the bearing. However, this reduction is not carried through because in the future the system will be investigated experimentally. In the experiments, the displacements at the positions  $y_m$  and  $z_m$  will be measured. In appendix 8.B the component mode synthesis method is described and the equations of motion are given for the investigated system.

Table 8.1 shows the eigenfrequencies of the free undamped shaft without the oil journal bearing for L = 0.133 m. The results for the reduced model are compared to those for the unreduced model. In table 8.2 the eigenfrequencies of the undamped shaft pinned (simply supported) at the bearing position are shown for L = 0.133 m. The tables show that the reduced model yields accurate eigenfrequencies up to about 2000 rad/s. For other values of the rotor distance L similar results for the eigenfrequencies can be obtained.

### 8.3 Rotor distance L = 0.038 m.

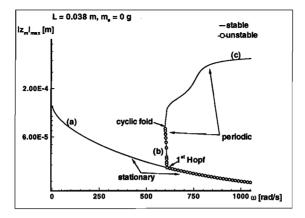
In this section the distance between the rotor and the oil journal bearing L = 0.038 m. The rotor is very close to the oil journal bearing so the bearing is heavily loaded. The model is analysed for different values of the mass unbalance  $m_e$ .

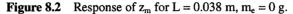
#### 8.3.1 Static loads, $m_e = 0.0 g$ .

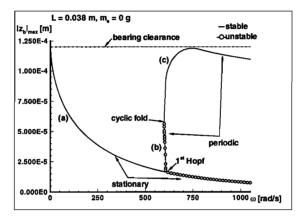
In this subsection no mass unbalance is present ( $m_e = 0$  g). Figures 8.2 and 8.3 show the maximum absolute displacements of the measurement point  $z_m$  and bearing position  $z_b$  respectively as function of the angular rotor speed  $\omega$ . For low angular rotor speeds  $\omega < 590$  rad/s only stationary ('static') solutions are found (branch (a)). At  $\omega \approx 610$ rad/s these stationary solutions become unstable via a primary Hopf bifurcation. Further increasing the angular rotor speed leads to the occurrence of self-excited oscillations, normally referred to as  $1/2 \omega$  whirl or oil whirl in rotordynamics (Myers, 1984). These self-excited oscillations are calculated for varying angular rotor speed by solving twopoint boundary problems using the finite difference method in combination with a path-following method (Fey, 1992, Fey et al. 1995, Fey et al., 1994).

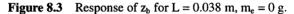
In figures 8.2 and 8.3 also the maximum absolute displacements of the measurement point  $z_m$  and bearing position  $z_b$  occurring in the self-excited oscillations are shown. An unstable  $1/2 \omega$  whirl branch (b) starts at the primary Hopf bifurcation and exists for somewhat lower angular rotor speeds than the threshold angular rotor speed for which the primary Hopf bifurcation exists. The branch becomes stable by a cyclic fold bifurcation and bends off to higher angular rotor speeds (branch (c)). Notice that stable and unstable periodic solutions exist for angular rotor speeds lower than the threshold speed. Figure 8.5a shows the shaft positions in the bearing for the stable and unstable  $1/2 \omega$  whirl at  $\omega = 600$  rad/s.

The solid line in figure 8.4 shows the frequencies  $\Omega$  of the periodic solutions. At the dotted line the frequency  $\Omega$  is half the angular rotor speed  $\omega$ . As expected, the stable and unstable branches (b) and (c), have frequencies which are almost half the angular rotor speed. However, for high angular rotor speeds  $\omega > 750$  rad/s, the frequencies  $\Omega$  of the self-excited oscillations of branch (c) are much lower than half the angular rotor speed. The frequency goes to  $\Omega \approx 400$  rad/s. It is known that the frequency  $\Omega$  of self-excited oscillations can move to the first eigenfrequency of the model (Gunter et al., 1983). The three branches of symbols in figure 8.4 represent the three lowest eigenfrequencies of the model linearized around the stationary solutions for varying angular rotor speed. The eigenfrequencies corresponding to the two lowest flexible eigenmodes of the shaft vary between 300-350 rad/s and are much lower than the frequencies of the self-excited oscillations. However, the eigenfrequencies plotted in figure 8.4 belong to the stationary solutions and the amplitude of the shaft motion in the bearing has large influence on the eigenfrequencies of the model, because the rotor is close to the bearing. In the self-excited oscillations the shaft curve is far away from the stationary points (figure 8.5a). Because of this the amplitude of the shaft motion in the bearing is high which will









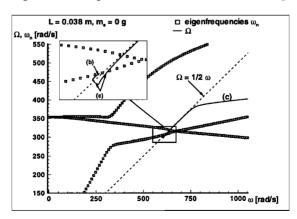
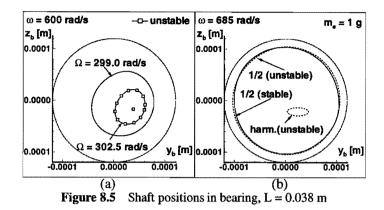


Figure 8.4 Frequencies of self-excited oscillations and eigenfrequencies of linearized system for L = 0.038 m,  $m_e = 0$  g.



result in an increase of the 'eigenfrequencies'\* of the shaft. So in the periodic solutions the increased first flexible 'eigenfrequency' of the shaft can be expected to be very close to the frequencies of the self-excited oscillations.

Notice that the primary Hopf bifurcation occurs if the angular rotor speed is nearly two times the first eigenfrequency of the linearized model (this eigenfrequency will be equal to the 'eigenfrequency' of the nonlinear model because the shaft motion is zero). Furthermore, the unstable branch of periodic solutions (b) starts with a free frequency  $\Omega$  which is almost equal to the first eigenfrequency of the linearized model which could be expected (figure 8.4).

In the periodic solutions the shaft motion in the bearing is large. As mentioned above, the shaft motion strongly influences the 'eigenfrequencies' of the nonlinear model and the growth of the shaft motion increases the 'eigenfrequencies'. If the angular rotor speed is increased to two times the increased first 'eigenfrequency' of the shaft, the free frequencies  $\Omega$  of the periodic solutions are close to the increased first 'eigenfrequency'. Because of this the maximum response at the measurement point increases (figure 8.2) and because the free frequency is not near half the angular rotor speed the shaft eccentricities in the bearing decrease (figure 8.3).

#### 8.3.2 Static and dynamic loads, $m_e = 1.0 g$ .

In this subsection a mass unbalance is added of  $m_e = 1.0$  g. Periodic solutions of the model are calculated for varying angular rotor speed. Figures 8.6 and 8.7 show the maximum absolute displacements of  $z_m$  and  $z_b$  occurring in the periodic solutions as function of the angular rotor speed.

The dotted lines in figures 8.6 and 8.7 represent the dynamic response of the model linearized around the stationary solutions. Taking into account that the stability of the linearized model equals the stability of the stationary solutions in figures 8.6 and 8.7, it can be concluded that the linearized model is only valid for low angular rotor speeds. This is because for low angular rotor speeds the dynamic loads are small, which results

<sup>\*</sup>Because the model is nonlinear, one cannot speak of the *eigenfrequencies* of the model. Here, 'eigenfrequency' is used for the frequency at which the model resonates.

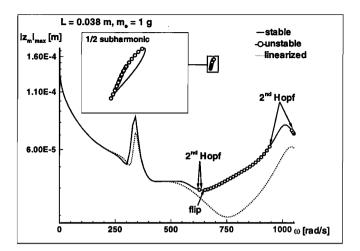
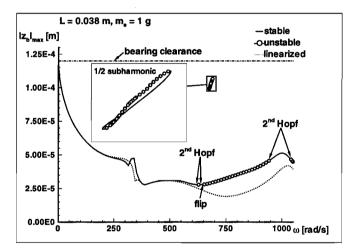


Figure 8.6 Imbalance response of  $z_m$  for L = 0.038 m,  $m_e = 1.0$  g.



**Figure 8.7** Imbalance response of  $z_b$  for L = 0.038 m,  $m_e = 1.0$  g.

in dynamic solutions close to the stationary solutions.

The dynamic response shows that at almost the same angular rotor speed for which in figure 8.2 the primary Hopf bifurcation occurred, now the harmonic solution becomes unstable via a secondary Hopf bifurcation. If the angular rotor speed is further increased the harmonic solution becomes again stable via a second secondary Hopf bifurcation. In this small unstable frequency range quasi-periodic behaviour was found. Further increasing the angular rotor speed leads to a flip bifurcation. Here again quasi-periodic behaviour was found which locks to 1/2 subharmonic behaviour if the angular rotor speed is further increased to 675 rad/s (see insets of figures 8.2 and 8.3). If the angular rotor speed is increased to  $\omega > 690$  rad/s the 1/2 subharmonic behaviour changes again into quasi-periodic behaviour. In the frequency range  $\omega \approx 950-1020$  rad/s the harmonic

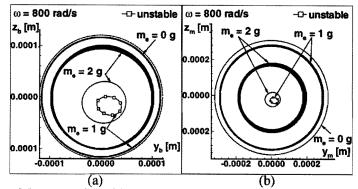


Figure 8.8 (a) Shaft positions in bearing, (b) Shaft positions at measurement point, L = 0.038 m.

solution is stable again, and for  $\omega > 1020$  rad/s quasi-periodic behaviour was found.

Figure 8.5b shows the positions of the shaft in the bearing of the 1/2 subharmonic and harmonic solutions for  $\omega = 685$  rad/s. Notice the large difference of amplitude size between the 1/2 subharmonic solutions and the unstable harmonic solution.

#### 8.3.3 Static and dynamic loads, $m_e = 2.0 g$ .

In this subsection the mass unbalance is increased to  $m_e = 2.0$  g. Figures 8.9 and 8.10 show the maximum displacements of  $z_m$  and  $z_b$  occurring in the periodic solutions for varying angular rotor speed. Now the whole branch of harmonic solutions is stable so by adding mass unbalance the model can be stabilized (Gunter et al., 1983), although the harmonic resonance peaks increase compared to figures 8.9 and 8.10.

Furthermore, in the frequency range  $\omega \approx 710-900$  rad/s besides the stable harmonic solution another (quasi-periodic) attractor coexists with large shaft eccentricities in the bearing. The quasi-periodic attractor locks to 1/2 subharmonic behaviour near 725 rad/s. Only the 1/2 subharmonic attractor is shown in figures 8.9 and 8.10. So by adding mass unbalance rotor systems can be stabilized but other attracors may coexist and the initial conditions of the model determine which attractor will be approached by the model if time proceeds.

Figure 8.8 shows the shaft positions in the bearing and at the measurement point for different mass unbalances at  $\omega = 800$  rad/s. This figure shows that the shaft eccentricities occurring in the periodic solution for  $m_e = 0$  g (with free frequency  $\Omega = 385$  rad/s) and in the quasi-periodic solution for  $m_e = 1$  g (with free frequency  $\Omega \approx 383$  rad/s) and  $m_e = 2$  g (with free frequency  $\Omega \approx 377$  rad/s) are much higher than the eccentricities occurring in the unstable and stable periodic solutions for  $m_e = 1$  g and  $m_e = 2$  g, respectively. Also the maximum response at the measurement point is much higher for these attractors. This is due to the free frequencies, which are near the first flexible 'eigenfrequency' of the shaft. This is in contrast with the unstable periodic solution for  $m_e = 1$  g and the stable periodic solution for  $m_e = 2$  g, which have much lower maximum responses because these solutions do not have free frequencies since all the frequencies occurring

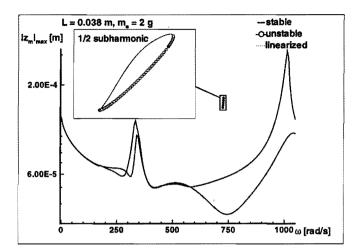


Figure 8.9 Imbalance response of  $z_m$  for L = 0.038 m,  $m_e = 2.0$  g.

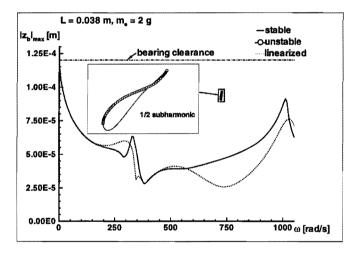


Figure 8.10 Imbalance response of  $z_b$  for L = 0.038 m,  $m_e = 2.0$  g.

in these periodic solutions are related to the excitation frequency.

# 8.4 Rotor distance L = 0.133 m.

In this section the distance between the rotor and the oil journal bearing L is 0.133 m. This means that the oil journal bearing is less loaded than in section 8.3. Again the model is analysed for different values of the mass unbalance  $m_e$ .

### 8.4.1 Static loads, $m_e = 0.0 g$ .

Figures 8.11 and 8.12 show the response of the model for varying angular rotor speed if no dynamic loads are present. The figures show a similar response as figures 8.2

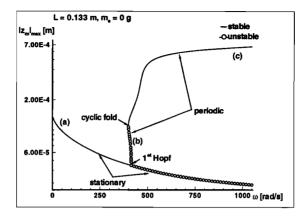
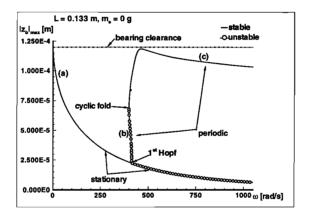
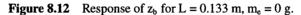


Figure 8.11 Response of  $z_m$  for L = 0.133 m,  $m_e = 0$  g.





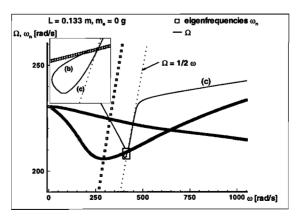
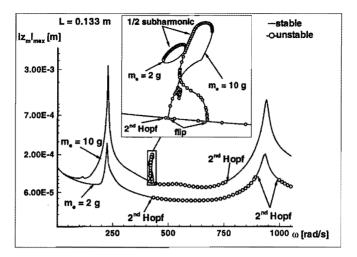


Figure 8.13 Frequencies of self-excited oscillations and eigenfrequencies of linearized system for L = 0.133 m,  $m_e = 0.9$ .



**Figure 8.14** Imbalance response of  $z_m$  for L = 0.133 m.

and 8.3. Because the bearing is less loaded, the threshold angular rotor speed for which the primary Hopf bifurcation occurs is decreased. Now for lower angular rotor speeds the shaft comes close to the centre point of the bearing (the central equilibrium position implies implicitly unstable for oil journal bearings). Furthermore, the first eigenfrequency of the system is decreased.

Again the unstable branch (b) with periodic solutions, which occurs near the threshold angular rotor speed, bends off and becomes stable (branch (c)). Also the unstable branch (b) starts with a free frequency equal to the first eigenfrequency of the linearized model (figure 8.13).

Notice that again the free frequency of branch (c) approaches the increased first flexible 'eigenfrequency' of the nonlinear model if the angular rotor speed is higher than two times this 'eigenfrequency'. Because the shaft motion in the bearing has less influence on the 'eigenfrequencies' of the nonlinear model (the distance between the rotor and bearing is increased), this 'eigenfrequency' will be closer to the first eigenfrequency of the linearized model (compared to the system with L = 0.038 m) and this results in a smaller angular rotor speed range for which the free frequency is near half the angular rotor speed.

#### 8.4.2 Static and dynamic loads.

Figure 8.14 shows the maximum absolute displacement of  $z_m$  occurring in the periodic solutions for varying angular rotor speed for mass unbalances  $m_e = 2$  g and 10 g. For  $m_e$ = 2 g a stable and unstable 1/2 subharmonic solution coexist but only for a very small angular rotor speed range. For high angular rotor speeds the harmonic solution is only stable near the second harmonic resonance peak. Because now the oil journal bearing is less loaded (static and dynamic) than in section 8.3, the mass unbalance needed for stabilizing the model has to be much higher than  $m_e = 2.0$  g. The figure shows that the

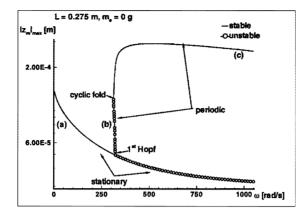


Figure 8.15 Response of  $z_m$  for L = 0.275 m,  $m_e = 0 \text{ g}$ .

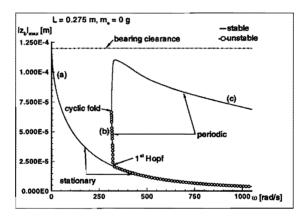


Figure 8.16 Response of  $z_m$  for L = 0.275 m,  $m_e = 0$  g.

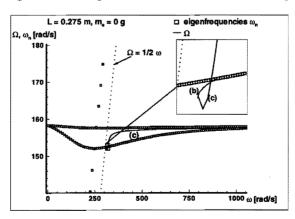


Figure 8.17 Frequencies of self-excited oscillations and eigenfrequencies of linearized system for L = 0.275 m,  $m_e = 0$  g.

130CHAPTER 8. STEADY-STATE BEHAVIOUR OF FLEXIBLE ROTOR DYNAMIC SYSTEMS ...

1/2 subharmonic still exist even if the mass unbalance is increased to  $m_e = 10$  g and a part of the harmonic branch is unstable marked by two secondary Hopf bifurcations. This implies that if the mass unbalance is not close to the bearing which causes the instability, the mass unbalance for stabilizing the model has to be very high.

# 8.5 Rotor distance L = 0.275 m.

In this section the distance between the rotor and the oil journal bearing is increased to L = 0.275 m. Now the rotor is at the middle of the shaft.

# 8.5.1 Static loads, $m_e = 0.0 g$ .

Figures 8.15 and 8.16 show the response of the model if only static loads are included in the model. The figures show again similar responses as the models with L = 0.038m and L = 0.133 m. The threshold speed is further decreased because the bearing is less loaded and the first eigenfrequency is lower. Again the threshold speed is close to two times the first eigenfrequency of the linearized model and the unstable branch (b) starts with a free frequency equal to this first eigenfrequency. Because the shaft motion in the bearing has now very little influence on the 'eigenfrequencies' of the nonlinear model, the free frequency of branch (c) goes almost directly to the first 'eigenfrequency' of the nonlinear model.

## 8.5.2 Static and dynamic loads, $m_c = 2.0 g$ .

Figure 8.18 shows the maximum absolute displacement of  $z_m$  occurring in the periodic solutions for varying angular rotor speed with mass unbalance  $m_e = 2$  g. Now the response calculated using the linearized model is almost the same as the response calculated using periodic solutions of the nonlinear model. Because the rotor is far away from the nonlinear bearing, this bearing is not heavily dynamically loaded so the linearized model is valid for high angular rotor speeds. The harmonic branch becomes unstable via a flip bifurcation at the same frequency where in figure 8.15 the primary Hopf bifurcation occurred. Via a second flip bifurcation this branch is stabilized again and after a small stable part it becomes unstable again via a secondary Hopf bifurcation. Quasi-periodic behaviour was found in the unstable frequency ranges.

# 8.6 Conclusions.

In this paper several flexible rotor systems with one oil journal bearing were investigated numerically. The linear part of the system, the shaft and rotor, was reduced using a component mode synthesis method. Using this method systems with local nonlinearities can be analysed very efficiently.

The results show that calculating the response of the systems linearized around the stationary solutions is only accurate for small bearing loads. Even in case of static

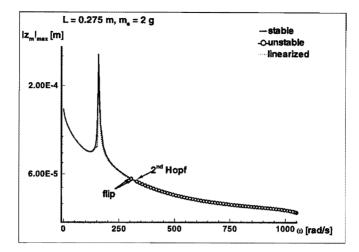


Figure 8.18 Imbalance response of  $z_m$  for L = 0.275 m,  $m_e = 2.0$  g.

loads only, the stability of the systems cannot be determined using the linearized system because the results show that even for angular rotor speeds lower than the threshold angular rotor speed for which the primary Hopf bifurcation occurs, periodic solutions (stable or unstable) can coexist with the stable stationary solutions and the initial state of the system will determine which attractor will be approached if time proceeds. Because of the existence of the unstable branch the system response will immediately show a large increase if the angular rotor speed is increased beyond the threshold rotor speed.

Furthermore the results show that the eigenfrequencies of the system have a large influence on the self-excited oscillations. In all cases the threshold angular rotor speed is almost two times the first eigenfrequency of the linearized system. For angular rotor speeds lower than the threshold speed an unstable  $1/2\omega$  whirl branch of periodic solutions exists, which starts at the primary Hopf bifurcation and becomes stable via a cyclic fold bifurcation and bends off to higher angular rotor speeds. Meanwhile the shaft eccentricities in the bearing show a large increase.

The 'eigenfrequencies' of the nonlinear model depend on the amplitude of the shaft motion in the bearing. For high shaft eccentricities the 'eigenfrequencies' will be larger. If the angular rotor speed is increased beyond the threshold rotor speed the shaft eccentricities grow and the 'eigenfrequencies' of the nonlinear model increase. If the angular rotor speed is increased to almost two times the increased first 'eigenfrequency' of the nonlinear model, the free frequency of the periodic solutions approaches the increased first 'eigenfrequency'. Because of this, the maximum response of the system increases very much. The frequency range for which solutions exist with free frequencies near  $1/2\omega$  will be larger for systems for which the amplitude of the shaft motion in the bearing has a large influence on the 'eigenfrequencies' of the system, since the difference between the first 'eigenfrequency' of the linearized model and the increased first 'eigenfrequency' will be larger. Generally, in this frequency range the maximum response will be smaller.

#### 132CHAPTER 8. STEADY-STATE BEHAVIOUR OF FLEXIBLE ROTOR DYNAMIC SYSTEMS ...

Adding mass unbalance can stabilize the system but the results show that other attractors with large shaft eccentricities in the bearing may coexist, so the steady-state behaviour of the system depends on the initial conditions of the system. Furthermore adding mass unbalance has only a large influence if the mass unbalance is added close to the bearing which causes the instability. Stabilization of the system results in much lower imbalance response of the system because generally in the unstable frequency ranges quasi-periodic behaviour exists with a free frequency which is near the first 'eigenfrequency' of the system. However, the resonance peaks increase.

Notice that, in contrast with recent investigations, no chaotic behaviour has been identified for the system under investigation. In Brown et al. (1994) chaotic behaviour was found in a simple model of a rigid rotor, supported hydrodynamically using a short bearing theory. They concluded that if the dynamic loads exceed the gravitational load chaotic behaviour occurs. However, because they use a rigid shaft, the system does not have eigenfrequencies which dominate in our results. Apparently, the eigenfrequencies of the shaft transform the chaotic behaviour to quasi-periodic behaviour. Another possible explanation is that the Sommerfeld number which they use is much lower than in our analysis, meaning that the eccentricity ratio for static loads only is much higher in their case.

Of course the accuracy of the results presented in this paper will depend on the accuracy of the bearing model which has been constructed. As mentioned in section 8.2, in future work the system which is investigated in this paper will be investigated experimentally and using the experimental results, the accuracy of the bearing model can be determined.

## Acknowledgement.

This work was supported by the Centre for Mechanical Engineering of TNO Building and Construction Research, Delft, The Netherlands.

#### 8.A Finite-Length Bearing Theory.

The pure-squeeze-velocity vector is defined by

$$\boldsymbol{v}_{\boldsymbol{s}} = \boldsymbol{v} - \bar{\boldsymbol{\omega}} \times c\boldsymbol{\epsilon} \tag{8.1}$$

where  $\epsilon$  is the eccentricity ratio vector, v the velocity vector of the shaft in the bearing and the *zero-load whirl*  $\bar{\omega}$  represents the angular velocity of the convecting system relative to the system of reference. Thus  $\bar{\omega}$  is defined by

$$\bar{\omega} = 0.5(\omega_j + \omega_b) \tag{8.2}$$

where  $\omega_j$  and  $\omega_b$  represent the observed mean angular velocity of the journal and the sleeve, respectively.

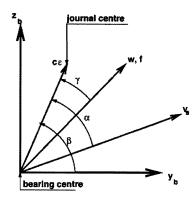


Figure 8.19 Kinematic variables.

Using the pure-squeeze-velocity vector and an impedance vector w, the equations for the bearing load force can be written as

$$\boldsymbol{f} = \left(\frac{R}{c}\right)^3 2\mu L_b \boldsymbol{v}_s \boldsymbol{w} \tag{8.3}$$

with  $v_s$  the modulus of  $v_s$ .

In case of  $\pi$  finite-length bearings the modulus of the impedance vector w can be expressed as (Childs et al., 1977)

$$w = \left\{ 0.15(E^2 + G^2)^{1/2} (1 - \xi)^{3/2} \right\}^{-1}$$
(8.4)

with

$$E = 1 + 2.12Q,$$
  

$$G = 3\eta (1 + 3.60Q)/4(1 - \xi)$$
  

$$Q = (1 - \xi)(L_b/2R)^{-2}$$
(8.5)

In (8.4) and (8.5)  $\xi$  and  $\eta$  are defined as

$$\xi = \epsilon \cos(\gamma), \quad \eta = \epsilon \cos(\gamma)$$
 (8.6)

where  $\epsilon$  is the modulus of the eccentricity ratio vector ( $\epsilon < 1$ ).  $\gamma$  is the attitude angle of  $\epsilon$  relative to **f** (figure 8.19) and can be calculated by means of

$$\gamma = \left\{ 1 - \xi' (1 - {\eta'}^2)^{-1/2} \right\}$$

$$\left[ \arctan\left\{ \frac{4(1+2.12B)(1-{\eta'}^2)^{1/2}}{3(1+3.60B){\eta'}} \right\} - \frac{\pi}{2}{\eta'}/|\eta'| + \arcsin(\eta') \right]$$

$$+\alpha - \arcsin(\eta')$$
(8.7)

with

$$B = (1 - \epsilon^2)(L_b/2R)^{-2}$$
(8.8)

and

$$\xi' = \epsilon \cos(\alpha), \quad \eta' = \epsilon \cos(\alpha)$$
 (8.9)

where  $\alpha$  is the attitude angle of  $\epsilon$  relative to  $v_s$  (figure 8.19).

# 8.B Component mode synthesis and equations of motion.

We consider the rotor system in figure 8.1. Firstly, the system is divided into linear components and nonlinear components. The linear components are supposed to be slightly damped or proportionally damped. This implies that the rotor with gyroscopy has to be added to the reduced linear component (the shaft without rotor and oil journal bearing) after the reduction. The  $n_x$ -column of degrees of freedom (DOF's)  $\boldsymbol{x} = \begin{bmatrix} \boldsymbol{x_b}^T & \boldsymbol{x_i}^T \end{bmatrix}^T$  of the linear component is divided into a  $n_b$ -column  $\boldsymbol{x_b}$  with interface DOF's (i.e. externally loaded DOF's and DOF's loaded by adjacent linear components or local nonlinearities), and a  $n_i$ -column  $\boldsymbol{x_i}$  ( $n_i = n_x - n_b$ ) with unloaded internal DOF's. The eight interface DOF's of the linear component are two displacements and two rotations for coupling the disk to the shaft (DOF's  $y_r, z_r, \phi_{y_r}, \phi_{z_r}$ ), the displacements for coupling the oil journal bearing (DOF's  $y_b, z_b$ ) and the displacements at the measurement point (DOF's  $y_m, z_m$ ).

The equations of motions of the linear component are

$$\boldsymbol{M_c} \ddot{\boldsymbol{x}} + \boldsymbol{C_c} \dot{\boldsymbol{x}} + \boldsymbol{K_c} \boldsymbol{x} = \boldsymbol{f_c} \tag{8.10}$$

where  $M_c$ ,  $C_c$  and  $K_c$  are the mass matrix, the damping matrix and the stiffness matrix, respectively, all of size  $(n_x, n_x)$ . For reducing the DOF's of the linear component x is written as a linear combination of  $n_c$  columns:

$$\boldsymbol{x} = \boldsymbol{T}_1 \boldsymbol{p}' \tag{8.11}$$

where

$$\boldsymbol{T_1} = \left[ \begin{array}{cc} \boldsymbol{\Phi_b} & \boldsymbol{U_r} & \boldsymbol{U_e} \end{array} \right] \tag{8.12}$$

 $U_r = \begin{bmatrix} u_1 & u_2 \end{bmatrix}$  are the two rigid body modes of the component.  $U_e = \begin{bmatrix} u_3 & \dots & u_6 \end{bmatrix}$  are the eigenvectors corresponding to the lowest four eigenvalues of the linear component.  $\Phi_b$  are the eight so-called residual flexibility modes and are calculated as follows

$$\boldsymbol{\Phi}_{\boldsymbol{b}} = \left(\boldsymbol{G}_{\boldsymbol{e}} - \sum_{k=3}^{6} \frac{\boldsymbol{u}_{\boldsymbol{k}} \boldsymbol{u}_{\boldsymbol{k}}^{T}}{(\omega_{\boldsymbol{k}}^{2})}\right) \left[\begin{array}{c} \boldsymbol{I}_{\boldsymbol{b}\boldsymbol{b}} \\ \boldsymbol{0}_{\boldsymbol{i}\boldsymbol{b}} \end{array}\right]$$
(8.13)

where  $G_e$  is the elastic flexibility matrix:

$$\boldsymbol{G}_{\boldsymbol{e}} = \sum_{k=3}^{n_{\boldsymbol{x}}} \frac{\boldsymbol{u}_{\boldsymbol{k}} \boldsymbol{u}_{\boldsymbol{k}}^{T}}{(\omega_{\boldsymbol{k}}^{2})} = \boldsymbol{P}^{T} \boldsymbol{G} \boldsymbol{P}$$
(8.14)

In (8.14) the matrix  $\boldsymbol{P}$  is defined by:

$$\boldsymbol{P} = \boldsymbol{I} - \boldsymbol{M_c} \boldsymbol{U_r} \boldsymbol{U_r}^T \tag{8.15}$$

while the matrix G is defined by:

$$\boldsymbol{G} = \begin{bmatrix} \boldsymbol{K}^{\star^{-1}} & \boldsymbol{0} \\ \boldsymbol{0} & \boldsymbol{0} \end{bmatrix}$$
(8.16)

where  $K^{\star}$  is the  $(n_x - 2, n_x - 2)$ -stiffness matrix of the reduced component if two DOF's are supported in such way that  $K^{\star-1}$  exists (thus the two rigid body modes are supported). For the proof of the correctness of this algorithm the reader is referred to Craig (1985).

Using the  $n_k = 2 + 4$  columns of  $U_k = \begin{bmatrix} U_r & U_e \end{bmatrix}$  and the  $n_b = 8$  columns of  $\Phi_b$  in the reduction matrix  $T_1 = \begin{bmatrix} \Phi_b & U_k \end{bmatrix}$ , the following Ritz approximation of the component displacement field can now be applied:

$$\boldsymbol{x} = \boldsymbol{T}_{1} \boldsymbol{p}' \rightarrow \begin{bmatrix} \boldsymbol{x}_{b} \\ \boldsymbol{x}_{i} \end{bmatrix} = \begin{bmatrix} \boldsymbol{\Phi}_{bb} & \boldsymbol{U}_{bk} \\ \boldsymbol{\Phi}_{ib} & \boldsymbol{U}_{ik} \end{bmatrix} \begin{bmatrix} \boldsymbol{p}_{b} \\ \boldsymbol{p}_{k} \end{bmatrix}$$
(8.17)

Starting from (8.17), the DOF's  $p_b$  are replaced by the interface DOF  $x_b$  using a coordinate transformation matrix  $T_2$  to permit simple coupling of the reduced component equations:

$$\begin{bmatrix} p_b \\ p_k \end{bmatrix} = \begin{bmatrix} \Phi_{bb}^{-1} & -\Phi_{bb}^{-1}U_{bk} \\ 0_{kb} & I_{kk} \end{bmatrix} \begin{bmatrix} x_b \\ p_k \end{bmatrix}$$

$$\rightarrow p' = T_2 p$$
(8.18)

This results in the following total transformation:

$$\boldsymbol{x} = \boldsymbol{T}\boldsymbol{p}, \quad \boldsymbol{T} = \boldsymbol{T}_1 \boldsymbol{T}_2 \tag{8.19}$$

Applying the transformation (8.19) to the unreduced equations of motion (8.10), the  $(n_c=n_k+n_b=14)$  reduced component equations become:

$$\boldsymbol{T}^{T}\boldsymbol{M}_{\boldsymbol{c}}\boldsymbol{T}\boldsymbol{\ddot{\boldsymbol{p}}} + \boldsymbol{T}^{T}\boldsymbol{C}_{\boldsymbol{c}}\boldsymbol{T}\boldsymbol{\dot{\boldsymbol{p}}} + \boldsymbol{T}^{T}\boldsymbol{K}_{\boldsymbol{c}}\boldsymbol{T}\boldsymbol{\boldsymbol{p}} = \boldsymbol{T}^{T}\boldsymbol{f}_{\boldsymbol{c}}$$
(8.20)

After reduction the local nonlinearities (the bearing) and the rotor are added to the reduced linear component. This can be done easily since the interface DOF's are available in the reduced component.

The equations of motion of the reduced system can now be written as

$$\boldsymbol{M}\ddot{\boldsymbol{q}} + \boldsymbol{f}_{nl}(\dot{\boldsymbol{q}}, \boldsymbol{q}, t) = \boldsymbol{f}_{ex}(t) \tag{8.21}$$

where

$$\boldsymbol{M} = \boldsymbol{T}^T \boldsymbol{M}_c \boldsymbol{T} + \boldsymbol{M}_r \tag{8.22}$$

where  $M_r$  is the mass matrix of the rotor,

$$\boldsymbol{q} = \left[ \begin{array}{cc} \boldsymbol{x_b}^T & \boldsymbol{p_k}^T \end{array} \right]^T \tag{8.23}$$

$$\boldsymbol{x}_{\boldsymbol{b}} = \left[ \begin{array}{cccc} y_{r} & z_{r} & \phi_{y_{r}} & \phi_{z_{r}} & y_{b} & z_{b} & y_{m} & z_{m} \end{array} \right]^{T}$$
(8.24)

$$\boldsymbol{f}_{nl} = \boldsymbol{C}\boldsymbol{\dot{q}} + \boldsymbol{K}\boldsymbol{q} + \begin{bmatrix} \boldsymbol{f}_{nx}^{T}(\boldsymbol{\dot{x}_{c}},\boldsymbol{x}_{c}) & \boldsymbol{0}_{\boldsymbol{k}}^{T} \end{bmatrix}^{T}$$
(8.25)

$$\boldsymbol{C} = \boldsymbol{T}^T \boldsymbol{C}_c \boldsymbol{T} + \boldsymbol{C}_r \tag{8.26}$$

where  $C_r$  is the gyroscopic matrix of the rotor,

$$\boldsymbol{K} = \boldsymbol{T}^T \boldsymbol{K}_{\boldsymbol{c}} \boldsymbol{T} \tag{8.27}$$

$$\boldsymbol{f}_{nx} = \begin{bmatrix} 0 & 0 & 0 & f_y & f_z & 0 & 0 \end{bmatrix}^T$$
(8.28)

where  $f_y = f \cos(\beta - \gamma)$ ,  $f_z = f \sin(\beta - \gamma)$  with f is the modulus of the bearing force f (equation 8.3), and  $\beta$  as defined in figure 8.19,

where  $F_y$  and  $F_z$  are the mass unbalance forces.

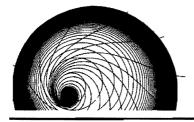
The eigenfrequencies  $\omega \leq \omega_{n_k}$   $(n_k=6)$  of (8.21) for the case  $f_{nx} = f_{ex} = 0$  are very accurate, with  $\omega_{n_k}$  the highest kept eigenfrequency in the reduction. In general, higher eigenfrequencies will be inaccurate. Because nonlinear systems can generate higher frequencies than their excitation frequency, in general  $\omega_{n_k}$  has to be chosen higher than the maximum excitation frequency.

## References

- Brown, R.D., Addison, P., and Chan, H.C., 1994, "Chaos in the Unbalance Response of Journal Bearings," *Nonlinear Dynamics*, Vol. 5, pp. 421-432.
- Childs, D., Moes, H., and Van Leeuwen, H., 1977, "Journal Bearing Impedance Descriptions for Rotordynamic Applications," ASME *Journal of Lubrication Technology*, Vol. 99, pp. 198–210.
- Craig Jr., R.R., 1985, "A Review of Time-Domain and Frequency-Domain Component Mode Synthesis Methods," Combined Experimental/Analytical Modeling of Dynamic Structural Systems Using Substructure Synthesis, D.R. Martinez and A.K. Miller, ed., ASME Applied Mechanics AMD-67, New York, pp. 1-31.

- DIANA, 1995, *DIANA User's Manual 6.0 ed.*, TNO Building and Construction Research, Delft, The Netherlands.
- Fey, R.H.B., 1992, "Steady-State Behaviour of Reduced Dynamic Systems with Local Nonlinearities," *Ph.D. Thesis*, Department of Mechanical Engineering, Eindhoven University of Technology, Eindhoven, The Netherlands.
- Fey, R.H.B., Van Campen, D.H., and De Kraker, A., April 1996, "Long Term Structural Dynamics of Mechanical Systems with Local Nonlinearities," ASME *Journal of Vibration and Acoustics*, (in press).
- Fey, R.H.B., Van de Vorst, E.L.B., Van Campen, D.H., De Kraker, A., Meijer, G.J., and Assinck, F.H., 1994, "Chaos and Bifurcations in a Multi-DOF Beam System with Nonlinear Support," Nonlinearity and Chaos in Engineering Dynamics, Proceedings IUTAM Symposium, London, 19-23 July 1993, J.M.T. Thompson and S.R. Bishop, ed., John Wiley & Sons, pp. 125-139.
- Gunter, E.J., Humphris, R.H. and Springer, H., 1983, "Influence of Unbalance on the Nonlinear Dynamical Response and Stability of Flexible Rotor-Bearing Systems," *Rotor Dynamical Instability*, M. L. Adams, ed., Kluwer Academic Publishers, pp. 37–58.
- Khonsari, M.M., and Chang, Y.J., 1993, "Stability Boundary of Non-Linear Orbits Within Clearance Circle of Journal Bearings," ASME *Journal of Vibration and Acoustics*, Vol. 115, pp. 303–307.
- Lau, S.L. and Yuen, S.W., 1991, "The Hopf Bifurcation and Limit Cycle by the Incremental Harmonic Balance Method," *Computer Methods in Applied Mechanics and Engineering*, Vol. 91, pp. 1109–1121.
- Li, D.F. and Gunter, E.J., 1981, "Component Mode Synthesis of Large Rotor Systems," ASME Paper 81-GT-147, ASME Gas Turbine Conference, ASME *Journal of Engineering* for Power.
- Myers, C.J., 1984, "Bifurcation Theory Applied to Oil Whirl in Plain Cylindrical Journal Bearings," ASME *Journal of Applied Mechanics*, Vol. 51, pp. 244–250.
- Nelson, H.D. and Meacham, W.L., 1981, "Transient Analysis of Rotor-Bearing Systems using Component Mode Synthesis," ASME Paper 81-GT-110, ASME Gas Turbine Conference.
- Nelson, H.D., Meacham, W.L., Fleming, D.P. and Kascak, A.F., 1982, "Nonlinear Analysis of Rotor-Bearing Systems using Component Mode Synthesis," ASME Paper 82-GT-303, ASME Gas Turbine Conference.
- Van de Vorst, E.L.B., Fey, R.H.B., De Kraker, A., and Van Campen, D.H., 1995, "Steady-State Behaviour of Nonlinear Flexible Rotor-Bearing Systems: Part II – Application: Influence of Cavitation Modelling," *Machine Vibration*, Vol 3 pp. 146-155.

138CHAPTER 8. STEADY-STATE BEHAVIOUR OF FLEXIBLE ROTOR DYNAMIC SYSTEMS ...



9

## STEADY-STATE BEHAVIOUR OF NONLINEAR FLEXIBLE ROTOR-BEARING SYSTEMS: PART II – APPLICATION: INFLUENCE OF CAVITATION MODELLING.<sup>‡</sup>

In this paper the long term behaviour is investigated of a rotor-bearing system, consisting of a disk and flexible shaft supported on one side by an oil journal bearing and pinned on the other side. Periodic solutions of this system with and without mass unbalance are calculated. In rotordynamic analysis, it is often assumed that the cavitation region in the bearings is only marginally influenced by the shaft velocity in the bearing, so the cavitation region is chosen to depend on the shaft eccentricity alone. In this paper the influence of this assumption on the responses of the rotor-bearing system is investigated for the short bearing theory. The results show that the type of cavitation model has a large influence on the response of the rotor-bearing model and that the assumption mentioned above is not valid for the system investigated.

## 9.1 Introduction.

Journal bearings are an essential feature of all rotating machinery and provide the vital load-carrying capacity to support rotors against static and dynamic loads. The analysis of the nonlinear effects in rotor-bearing systems is extremely difficult. The most commonly accepted method for nonlinear analysis is to perform a time-transient numerical integration method for the complete equations of motion. Therefore, even for relatively simple systems this becomes a formidable task since the Reynolds' equation has to be evaluated at each time step (Gunter et al., 1983).

In the companion paper (part I, Van de Vorst, et al. 1995) a method is presented for an efficient analysis of the long term behaviour of rotor-bearing systems. In general these systems consist of large linear parts (shaft, disks) and local nonlinearities (bearings). The linear parts can be reduced using a component mode synthesis method (Craig, 1985, Fey, 1992, Fey et al., 1996). The reduced linear parts are coupled with the local

<sup>&</sup>lt;sup>‡</sup>Van de Vorst, E.L.B., Fey, R.H.B., De Kraker, A., and Van Campen, D.H., 1995, "Steady-State Behaviour of Nonlinear Flexible Rotor-Bearing Systems: Part II – Application: Influence of Cavitation Modelling," *Machine Vibration*, Vol 3 pp. 146-155.

### 140CHAPTER 9. STEADY-STATE BEHAVIOUR OF NONLINEAR FLEXIBLE ROTOR-BEARING ...

nonlinearities. This results in a reduced nonlinear system which is an approximation of the unreduced rotor-bearing system and is valid in a certain frequency domain. Using the reduced rotor-bearing system now branches of periodic solutions (and their stability) can be calculated efficiently as function of some system parameter (for instance the angular rotor speed) by solving two-point boundary value problems using finite differences in combination with a path-following method (Fey, 1992, Fey et al., 1996).

To avoid that the Reynolds' equation has to be evaluated at each time step, for some types of bearings closed-form solutions can be generated to approximate the bearing forces. In these solutions the current bearing forces are given as algebraic expressions of the position and velocity of the shaft in the bearing. The most well-known theories which use this approach are the short (Ocvirk) bearing theory (Holmes and Sykes, 1989, Khonsari and Chang, 1993, Brown et al., 1994) and the long (Sommmerfeld) bearing theory (Myers, 1984). In the short bearing theory, the Reynolds' equation is solved assuming that the length of the bearing  $L_b$  is small compared to the radius of the bearing R (typically  $L_b/R < 1/2$ ). In the long bearing theory it is assumed that the length of the bearing is large compared to the radius of the bearing (typically  $L_b/R > 1$ ). Because in general these assumptions are not valid in practice, Childs et al. (1977) developed a finite length bearing theory using a combination of the short and long bearing theory.

A disadvantage of the bearing theories is that they are only valid for plain cylindrical bearings and not for say partial bearings. Another method which avoids that the Reynolds' equation has to be evaluated at each time step solves the Reynolds' equation on forehand for a grid of shaft eccentricities in the bearing. During the analysis the current bearing forces can be calculated using interpolation of the bearing forces at the grid points. In this way a lot of computation time is saved and also bearings which are not plain cylindrical can be analysed efficiently.

In general cavitation will occur in oil journal bearings. Usually, cavitation effects are taken into account by calculating the current bearing forces using the positive fluid pressures only. For the above mentioned bearing theories this means that only half the oil film in the bearing contributes to the bearing forces. Generally, this cavitation region will depend on both the shaft eccentricity and the shaft velocity in the bearing. However, in theories used for instance by Holmes and Sykes (1989), Khonsari and Chang (1993) and Myers (1984) it is assumed that the influence of the shaft velocity on this region is very small. In the short, long and finite-length theory used by Childs et al. (1977) and Brown et al. (1994) this assumption is not made. In Brown et al. (1994) in addition it is attempted to include inertial effects by reducing the influence of the shaft velocity on the cavitation region. The reason for assuming the cavitation region to be constant is that the resulting algebraic equations for the bearing forces will be much less complex. Because of this, these theories are attractive for making analytical calculations for rotor-bearing systems.

In this paper the influence of the cavitation modelling on the nonlinear response of a flexible rotor-bearing system is investigated. The rotor-bearing system consists of a disk and a flexible shaft supported on one side by an oil journal bearing and pinned (simply supported) on the other side (section 9.2). For modelling of the bearing the above mentioned short bearing theory is used. Two short bearing models are considered,

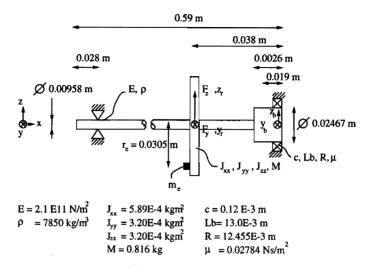


Figure 9.1 Rotordynamic system.

viz. one which has a cavitation region depending on the shaft eccentricity only and one for which the cavitation region depends on both the shaft eccentricity and shaft velocity. In section 9.3 the bearing forces generated by these two bearing models are compared for different values of the shaft velocity and angular shaft speed. In section 9.4 the influence of the cavitation modelling on the system without and with mass unbalance is analysed. All calculations in this paper were carried out using a development release of the finite element package DIANA (1995).

## 9.2 Rotordynamic system supported by one oil journal bearing.

Figure 9.1 shows the rotordynamic system which is analysed numerically. The Sommerfeld number  $\sigma$  of the bearing is defined as

$$\sigma = \frac{L_b R^3 \mu}{c^2} \frac{\omega}{f_s}$$

with  $L_b$  the bearing length, R the bearing radius,  $\mu$  the lubricant viscosity, c the bearing clearance,  $\omega$  the angular rotor speed and  $f_s$  the static external load force acting on the bearing. The system is investigated in the frequency range  $\omega = 0-1050$  rad/s and if the static force is taken  $f_s = 8$  N (which is approximately the weight of the rotor), the Sommerfeld number of the bearing varies from 0–6.4.

Only the gyroscopic effects of the rotor are taken into account; the gyroscopic effects of the shaft are neglected. The system is statically loaded by gravity and dynamically by a mass unbalance at the rotor. The unbalance loads can be written as

$$F_y = r_e m_e \omega^2 \cos(\omega t)$$
 ;  $F_z = r_e m_e \omega^2 \sin(\omega t)$ 

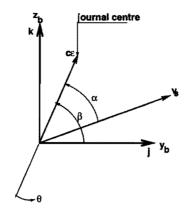


Figure 9.2 Kinematic variables.

with eccentricity radius  $r_e = 0.0305$  m while  $m_e$  is the unbalance mass.

The shaft is assumed to be modally damped with modal damping coefficients  $\xi = 0.01$  for all eigenmodes. The shaft is modelled using the finite element method and subsequently reduced using the component mode synthesis method mentioned in section 9.1. In the reduction process two rigid body modes, six residual flexibility modes (two for the bearing and four for the rotor) and four free-interface eigenmodes are used, so the model has 12 degrees of freedom (DOF's) (see also the companion paper (part I, Van de Vorst et al., 1995)).

## 9.3 The short bearing theory.

As mentioned in section 9.1, two different short bearing models are compared in this paper. The Reynolds' equation for a constant-viscosity incompressible fluid can be stated in polar coordinates as

$$\frac{\partial}{\partial\theta} \left( h^3 \frac{\partial p}{\partial\theta} \right) + R^2 \frac{\partial}{\partial x_b} \left( h^3 \frac{\partial p}{\partial x_b} \right) = \frac{12\mu R^2}{c^3} \left[ c\dot{\epsilon}\cos(\theta) + c\epsilon(\dot{\beta} - \bar{\omega})\sin(\theta) \right]$$
(9.1)

where  $h = 1 + \epsilon \cos(\theta)$  is the normalized film thickness,  $\theta$  is the bearing polar cylindrical coordinate with respect to the eccentricity ratio  $\epsilon$ ,  $x_b$  is the axial position variable,  $\epsilon$  is the modulus of  $\epsilon$ , and p is the fluid pressure. Further,  $\beta$  is the attitude angle of  $\epsilon$  relative to the stationary coordinate system  $x_b, y_b, z_b$  (figure 9.2), and the zero-load whirl  $\bar{\omega}$  represents the angular velocity of the convecting system relative to the system of reference. Thus  $\bar{\omega}$  is defined by

$$\bar{\omega} = 1/2(\omega_j + \omega_b) \tag{9.2}$$

where  $\omega_j$  and  $\omega_b$  represent the observed mean angular velocity of the journal and the sleeve, respectively.

In Childs et al. (1977) the pure-squeeze-velocity vector is defined by

$$\boldsymbol{v}_{\boldsymbol{s}} = \boldsymbol{v} - \bar{\omega} \times c\boldsymbol{\epsilon} = \boldsymbol{j}(\dot{y}_{b} + \bar{\omega}z_{b}) + \boldsymbol{k}(\dot{z}_{b} - \bar{\omega}y_{b})$$
(9.3)

where v is the velocity vector of the shaft in the bearing and i, j, k are the unit vectors in the stationary  $x_b, y_b, z_b$  system (figure 9.2). Using the pure-squeeze-velocity vector yields the following restatement of the Reynolds' equation (9.1)

$$\frac{\partial}{\partial \theta} \left( h^3 \frac{\partial p}{\partial \theta} \right) + R^2 \frac{\partial}{\partial x_b} \left( h^3 \frac{\partial p}{\partial x_b} \right) = \frac{12\mu R^2 v_s}{c^3} \cos(\alpha + \theta) \tag{9.4}$$

with  $v_s$  the modulus of  $v_s$  and  $\alpha$  the attitude angle of  $\epsilon$  relative to  $v_s$  (figure 9.2).

In the short bearing solution the first term on the left-hand side of equation (9.4) is neglected. Using the boundary conditions  $p(\theta, L_b/2) = p(\theta, -L_b/2) = 0$ , the following average pressure definition can be obtained

$$\bar{p}(\theta) = -\mu L_b^2 v_s \cos(\alpha + \theta) / c^3 h^3$$
(9.5)

The pressure is seen to be positive between the angles  $\theta_1$ ,  $\theta_2$  defined by

$$\theta_1 = \frac{\pi}{2} - \alpha, \qquad \theta_2 = \frac{3\pi}{2} - \alpha \tag{9.6}$$

In words, the pressure is positive over a region of  $\pi$  radians centered about  $v_s$ .

From equation (9.3) the attitude angle  $\alpha$  relative to  $\epsilon$  is defined by

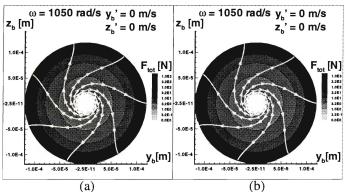
$$\alpha = \beta - \arctan\left(\frac{\dot{z}_b - \bar{\omega}y_b}{\dot{y}_b + \bar{\omega}z_b}\right) \tag{9.7}$$

Since  $\beta = \arctan(z_b/y_b)$ , it is easy to see that if the shaft velocity v is zero then  $\alpha = \frac{\pi}{2}$  and this yields  $\theta_1 = 0$  and  $\theta_2 = \pi$ . In words, the pressure is positive over a region of  $\pi$  radians starting at the maximal film thickness  $\beta - \pi$  and ending at the minimal film thickness  $\beta$ .

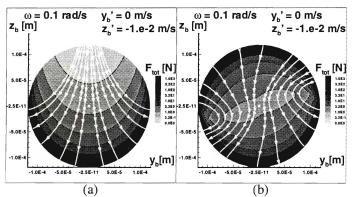
In this paper two short bearing models are used for calculating the bearing forces. One model calculates the bearing forces by integration of equation (9.5) using only the positive pressures (equation (9.6)). The other model assumes the cavitation region to be independent of the shaft velocity so equation (9.5) is integrated over  $\theta_1 = 0$ ,  $\theta_2 = \pi$ . In appendix A the algebraic formulas for the bearing forces are given.

Figure 9.3 shows the bearing forces as function of the shaft eccentricity if the shaftvelocity in the bearing is zero and the angular shaft speed  $\omega = 1050$  rad/s for both short bearing models. The lines with arrows give the directions of the bearing forces and the gray shades indicate the magnitude of the bearing forces. In figure 9.3a the cavitation region depends on the shaft velocity, whereas in figure 9.3b the cavitation region is independent of the shaft velocity. As could be expected, since the shaft velocity is zero, both bearing models give exactly the same results.

Figure 9.4 shows the bearing forces as function of the shaft eccentricity if the shaft velocity is not zero; the shaft moves in the negative z-direction. The angular shaft speed is very small:  $\omega = 0.1$  rad/s. Because of this the velocity has a large influence on the cavitation region in the bearing and the two bearing theories give very different results. The bearing forces calculated using the velocity dependent cavitation region is



**Figure 9.3** Bearing forces as function of shaft eccentricities,  $\dot{y}_b = \dot{z}_b = 0$  m/s,  $\omega = 1050$  rad/s, Short bearing theory with cavitation region which (a) depends on velocity (b) is independent of velocity.



**Figure 9.4** Bearing forces as function of shaft eccentricities,  $\dot{y}_b = 0$  m/s,  $\dot{z}_b = -10^{-2}$  m/s,  $\omega = 0.1$  rad/s, Short bearing theory with cavitation region which (a) depends on velocity (b) is independent of velocity.

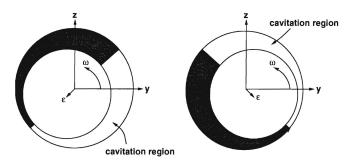
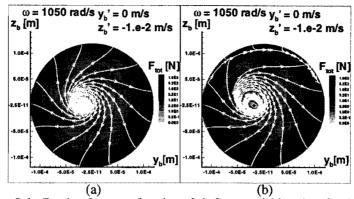


Figure 9.5 Cavitation region for velocity independent bearing model.



**Figure 9.6** Bearing forces as function of shaft eccentricities,  $\dot{y}_b = 0$  m/s,  $\dot{z}_b = -10^{-2}$  m/s,  $\omega = 1050$  rad/s, Short bearing theory with cavitation region which (a) depends on velocity (b) is independent of velocity.

almost symmetrical around the z-axis (figure 9.4a) (if the angular shaft speed is zero the bearing forces are symmetrical around the z-axis because the cavitation region is the upper half of the bearing). The velocity independent model gives bearing forces which are not symmetrical around z-axis because the cavitation region depends on the shaft eccentricity only. This means that if the angular shaft speed is counterclockwise and the minimal film thickness is in the lower right quadrant, the cavitation region is above the shaft. If the minimal film thickness is in the lower left quadrant, the cavitation region is beneath the shaft (figure 9.5). Because of this the bearing forces are not symmetrical.

Figure 9.6 shows the bearing forces as function of the shaft eccentricity if the angular rotor speed is increased to 1050 rad/s and the shaft velocity is again in the negative z-direction. The shaft velocity is  $10^{-2}$  m/s which corresponds with a situation where the shaft makes a circular orbit around the centre of the bearing with an angular speed of 1050 rad/s and an eccentricity ratio  $\epsilon \approx 0.08$ . The directions of the bearing forces calculated using velocity independent cavitation model differ for high shaft eccentricities (figure 9.6b). Notice that this occurs only in the upper half of the bearing where the shaft moves away from the bearing forces in figure 9.6a. In figure 9.4 in this area also the largest differences occurred. Furthermore, differences occur near the centre of the bearing where the total bearing forces are minimal.

# 9.4 Influence cavitation modelling on system responses.

#### 9.4.1 Static loads, $m_e = 0.0 g$ .

In this subsection the rotor-bearing model mentioned in section 9.2 without mass unbalance is investigated. Figure 9.7 shows the maximum absolute displacements at the bearing position  $z_b$  as function of the angular rotor speed  $\omega$  if the bearing is modelled using the short bearing theory with a velocity independent cavitation region. The figure

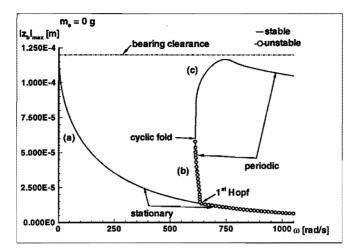


Figure 9.7 Response of  $z_b$  for  $m_e = 0$  g and cavitation depends on velocity.

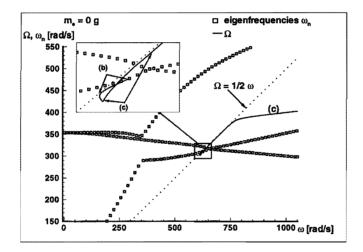


Figure 9.8 Frequencies of self-excited oscillations and eigenfrequencies of linearized system for  $m_e = 0$  g and cavitation depends on velocity.

shows a similar result as the response calculated using the finite length bearing theory (Van de Vorst et al., 1995), which means that the short bearing theory can be used in this case to a good approximation. For low angular rotor speeds  $\omega < 600$  rad/s only stationary ('static') solutions are found (branch (a)). At  $\omega \approx 630$  rad/s the stationary solutions become unstable via a primary Hopf bifurcation. Further increasing of the angular rotor speed leads to the occurrence of self-excited oscillations (1/2  $\omega$  whirl). These self-excited oscillations are calculated for varying angular rotor speed by solving two-point boundary problems using the finite difference method in combination with a path-following method.

In figure 9.7 also the maximum absolute displacements at the bearing position  $z_b$ 

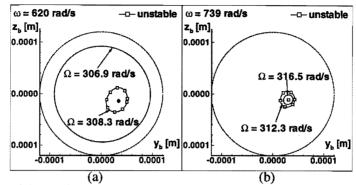


Figure 9.9 Shaft positions in bearing,  $m_e = 0$  g, cavitation (a) depends on velocity, (b) is independent of velocity.

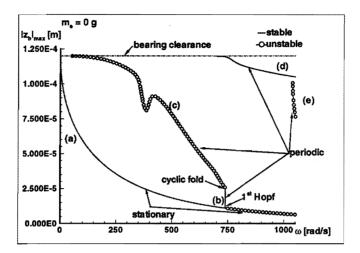
occurring in the self-excited oscillations are shown. An unstable  $1/2 \omega$  whirl branch (b) occurs which starts at the primary Hopf bifurcation and exists for lower angular rotor speeds than the threshold angular rotor speed for which the primary Hopf bifurcation exists. The branch becomes stable via a cyclic fold bifurcation and bends off to higher angular rotor speeds (branch (c)). Notice that stable and unstable periodic solutions exist for angular rotor speeds lower than the threshold speed. Figure 9.9a shows the shaft positions in the bearing for the stable and unstable  $1/2 \omega$  whirl at  $\omega = 620$  rad/s.

Figure 9.8 shows the frequencies  $\Omega$  of the periodic solutions. At the dotted line the frequency  $\Omega$  is half the angular rotor speed  $\omega$ . As expected, the stable and unstable branches (b) and (c) have frequencies which are almost half the angular rotor speed. For high angular rotor speeds  $\omega > 750$  rad/s, the frequencies  $\Omega$  of the self-excited oscillations of branch (c) are much lower than half the angular rotor speed. The frequency goes to  $\Omega \approx 400$  rad/s which is near the first 'eigenfrequency'\* of the system (see also the companion paper (Van de Vorst et al., 1995)).

Figure 9.10 shows the maximum absolute displacement at the bearing position  $z_b$  as function of the angular rotor speed  $\omega$  if the short bearing theory with a velocity independent cavitation region is used. The stationary solutions are exactly the same solutions as in figure 9.7, but for this cavitation model the threshold speed is increased to  $\omega \approx 735$  rad/s. The damping constants of the two cavitation models, which are used for calculating the stability of the solutions, are the derivatives of the mentioned algebraic equations in Appendix 9.A with respect to the velocity. The difference in the threshold speed indicates that apparently these damping constants are different even if the shaft velocity is zero. This means that already for very low velocities the cavitation region in the bearing differs very much for the two models.

In figure 9.10 after the primary Hopf bifurcation a stable  $1/2 \omega$  whirl occurs (b),

<sup>\*</sup>Because the model is nonlinear, one cannot speak of the *eigenfrequencies* of the model. Here, 'eigenfrequency' is used for the frequency for which the model resonates. The three branches of symbols in figure 9.8 represent the lowest three eigenfrequencies of the model *linearized* around the stationary solutions for varying angular rotor speed. These frequencies differ from the 'eigenfrequencies' if the shaft motion in the bearing is high (Van de Vorst et al., 1995).



**Figure 9.10** Response of  $z_b$  for  $m_e = 0$  g and cavitation is independent of velocity.

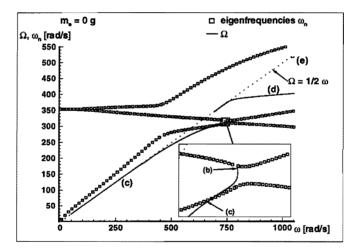


Figure 9.11 Frequencies of self-excited oscillations and eigenfrequencies of linearized system for  $m_e = 0$  g and cavitation independent of velocity.

which becomes unstable by a cyclic fold bifurcation. Then the branch bends off to lower angular rotor speeds until very high shaft eccentricities occur in the bearing (c)(the shaft runs against the bearing side). Figure 9.9b shows the shaft positions in the bearing for the stable and unstable  $1/2 \omega$  whirl at  $\omega = 739$  rad/s. The existence of the unstable branch (c) of self-excited oscillations indicates that here two stable attractors coexist. One solution is the stable stationary solution or stable  $1/2 \omega$  whirl. Numerical simulation showed that the other solution has very large shaft eccentricities in the bearing. This solution could not be calculated by means of the numerical periodic solvers mentioned earlier due to the fact that the equations of motion become very stiff for high shaft eccentricities. Notice that this solution also exists for angular rotor speeds much lower

than the threshold angular rotor speed for which the primary Hopf bifurcation occurs.

The behaviour with very large shaft eccentricities exists in the angular rotor speed range  $\omega = 25-700$  rad/s. Further increasing of the angular rotor speed leads to a decrease of the shaft eccentricities and for  $\omega \approx 700$  rad/s the self-excited oscillations could be calculated again (d).

Figure 9.11 shows the frequencies  $\Omega$  of the periodic solutions. At the dotted line the frequency  $\Omega$  is half the angular rotor speed  $\omega$ . For low angular rotor speeds branch (c) has a free frequency which is almost half the angular rotor speed. However, for angular rotor speeds  $\omega > 500$  rad/s, the frequencies  $\Omega$  of the branches (b) and (c) are much lower than  $1/2\omega$ . The free frequencies go to the first 'eigenfrequency' of the system and because the dampings constants are different for this cavitation model also the 'eigenfrequencies' will be different. The frequency  $\Omega$  of the self-excited oscillations for  $\omega > 750$  rad/s (d) again is much lower than half the angular rotor speed, again due to the fact that the free frequency goes to the first 'eigenfrequency' of the model.

For angular rotor speeds  $\omega > 1040$  rad/s a second self-excited oscillation was found using this bearing model. This self-excited oscillation (e) is unstable and has one real Floquet multiplier larger than 1 and two complex Floquet multipliers with modulus larger than 1. This self-excited oscillation has a frequency which is very close to the  $\Omega = 1/2\omega$ -line.

Comparison of the responses of the two bearing models shows that the cavitation modelling has a large influence on the self-excited oscillations. In section 9.3 it was concluded that the velocity independent short bearing model is only valid for low shaft velocities and high angular rotor speeds. The results show that already the threshold speed differs. Only branch (d) in figure 9.10 is similar to a part of branch (c) in figure 9.7. Because the free frequency at these branches is lower than half the angular rotor speed, lower shaft velocities occur and because also the angular rotor speed is high, the velocity independent cavitation model is valid.

### 9.4.2 Static and dynamic loads, $m_e = 1.0 g$ .

In this subsection a mass unbalance is added of  $m_e = 1.0$  g. Periodic solutions of the model are calculated for varying angular rotor speed. Figure 9.12 shows the maximum absolute displacement of  $z_b$  occurring in the periodic solutions as function of the angular rotor speed for the velocity dependent cavitation region.

The dotted line in figure 9.12 represents the dynamic response of the model linearized around the stationary solutions. Taking into account that the stability of the linearized model equals the stability of the stationary solutions in figure 9.7, it can be concluded that the linearized model is only valid for low angular rotor speeds. This is because for low angular rotor speeds the dynamic loads are small which results in dynamic solutions close to the stationary solutions.

The dynamic response shows that at almost the same angular rotor speed for which in figure 9.7 the primary Hopf bifurcation occurred, now the harmonic solution becomes unstable via a secondary Hopf bifurcation. If the angular rotor speed is increased further, the harmonic solution again becomes stable via a second secondary Hopf bifurcation.

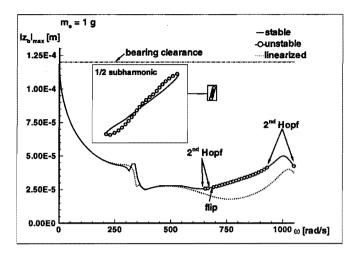


Figure 9.12 Imbalance response of  $z_b$  for  $m_e = 1.0$  g and cavitation region depends on velocity.

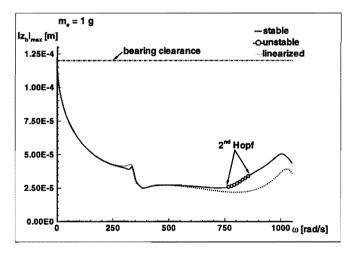


Figure 9.13 Imbalance response of  $z_b$  for  $m_e = 1.0$  g, and cavitation region is independent of velocity.

In this small unstable frequency range quasi-periodic behaviour was found. Further increasing of the angular rotor speed leads to a flip bifurcation. Here again quasi-periodic behaviour was found which locks to 1/2 subharmonic behaviour if the angular rotor speed is further increased to 675 rad/s. If the angular rotor speed is increased to  $\omega > 690$  rad/s, the 1/2 subharmonic behaviour changes again into quasi-periodic behaviour. In the frequency range  $\omega \approx 950$ -1020 rad/s the harmonic is stable again, and for  $\omega > 1020$  rad/s quasi-periodic behaviour was found.

Figure 9.14a shows the shaft positions in the bearing of the 1/2 subharmonic and harmonic solutions for  $\omega = 685$  rad/s. Notice the large difference in amplitude of the 1/2

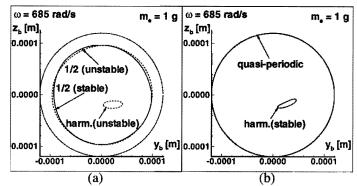


Figure 9.14 Shaft positions in bearing,  $m_e = 1$  g, cavitation region (a) depends on velocity, (b) is independent of velocity.

subharmonic solutions and the unstable harmonic solution.

Figure 9.13 shows the maximum absolute displacement of  $z_b$  occurring in the periodic solutions as function of the angular rotor speed if the cavitation region is independent of the shaft velocity and the mass unbalance  $m_e = 1$  g.

Again the dotted lines in figure 9.13 represent the dynamic response of the model linearized around the stationary solutions. The linearized response differs for high angular rotor speeds  $\omega > 690$  rad/s from the linearized response in figure 9.12. The nonlinear response shows that now only one unstable part exists in the harmonic branch marked by two secondary Hopf bifurcations. The unstable part is much smaller than in figure 9.12. However, besides the stable harmonic solution a stable quasi-periodic attractor with very high shaft eccentricities in the bearing was found for the whole frequency range (not visible in figure 9.13). Figure 9.14b shows the quasi-periodic attractor and the stable harmonic solution for  $\omega = 685$  rad/s. The free frequency of the quasi-periodic attractor is close to  $1/2\omega$  but because of the high shaft eccentricities no 1/2 subharmonic solution could be calculated. The quasi-periodic behaviour has much higher shaft eccentricities than the 1/2 subharmonic behaviour in figure 9.14a.

Comparison of the responses calculated using the two short bearing models learns that apparently for low angular rotor speeds similar results are obtained. Only near the first resonance peak ( $\omega \approx 350$  rad/s) small differences occur. For these angular rotor speeds also the linearized response is accurate. Also for high angular rotor speeds the harmonic solutions are very similar although differences occur in their stability. However, in the whole frequency range also a quasi-periodic attractor with very high shaft eccentricities has been found for the velocity independent cavitation region and this attractor exists only for a small frequency range for the velocity dependent cavitation region. This quasi-periodic solution has much higher shaft eccentricities for the velocity independent cavitation region.

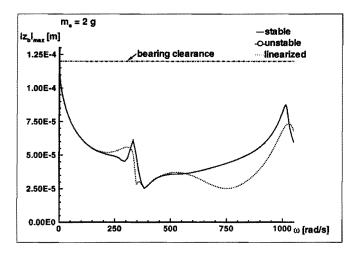


Figure 9.15 Imbalance response of  $z_b$  for  $m_e = 2.0$  g and cavitation region depends on velocity.

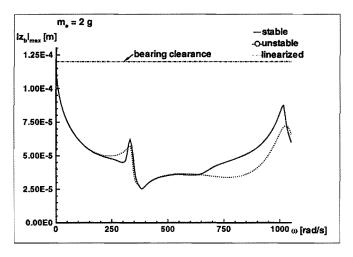


Figure 9.16 Imbalance response of  $z_b$  for  $m_e = 2.0$  g and cavitation region is independent of velocity.

## 9.4.3 Static and dynamic loads, $m_e = 2.0 g$ .

In figure 9.15 the mass unbalance is increased to  $m_e = 2.0$  g and the cavitation region depends on both the shaft eccentricity and the shaft velocity. Now the harmonic solutions is always stable so by adding mass unbalance the model can be stabilized (Gunter et al., 1983).

However, in the frequency range  $\omega \approx 710-900$  rad/s a quasi-periodic attractor coexists with large shaft eccentricities in the bearing. This attractor is not visible in figure 9.15. The existence of this attractor, which was found by numerical time integration, indicates

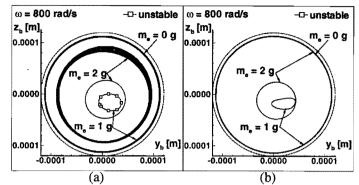


Figure 9.17 Shaft positions in bearing for cavitation (a) depends on velocity, (b) is independent of velocity.

that there might be other unstable (sub)harmonic solutions. These solutions however could not be found using finite differences. So by adding mass unbalance rotordynamic systems can be stabilized but here the initial conditions of the model will determine which attractor will be approached by the model if time proceeds due to the coexistence of the quasi-periodic attractor.

In figure 9.16 the cavitation region is independent of the shaft velocity. Now again all harmonic solutions are stable. Again, in the frequency range between the two resonance peaks a quasi-periodic attractor coexists with large shaft eccentricities in the bearing.

Figure 9.17 shows the shaft motions in the bearing for different mass unbalances at  $\omega = 800$  rad/s for the two short bearing models. The figure shows that the stable and unstable harmonic solutions for  $m_e = 1$  g and  $m_e = 2$  g with small shaft eccentricities are very similar, although the stability of the solutions for  $m_e = 1$  g is different. However the self-excited solutions for  $m_e = 0$  g, and the quasi-periodic solutions for  $m_e = 1$  g and  $m_e = 2$  g have much higher shaft eccentricities in the bearing if the cavitation region is independent of the shaft velocity.

The free frequencies of the self-excited oscillation and the quasi-periodic solution in figure 9.17a are  $\Omega = 386$  rad/s ( $m_e = 0$  g),  $\Omega \approx 384$  rad/s ( $m_e = 1$  g) and  $\Omega \approx 376$  rad/s ( $m_e = 2$  g). The free frequencies of the self-excited oscillation and the quasi-periodic solution in figure 9.17b are all near  $\Omega \approx 386$  rad/s.

Comparison of the results shows that apparently the influence of the shaft velocity on the cavitation region is low if the response has a moderate level of shaft eccentricities in the bearing (harmonic solutions for  $m_e = 2$  g). If the shaft eccentricities are small or very high, large differences occur in the responses. Section 3 showed that the bearing forces differ for high shaft eccentricities and for small eccentricities (for which the bearing forces are low), if the angular rotor speed is high and the shaft velocity is high. This confirms that the velocity dependent and independent cavitation models will give almost the same response for a moderate level of shaft eccentricity. 154CHAPTER 9. STEADY-STATE BEHAVIOUR OF NONLINEAR FLEXIBLE ROTOR-BEARING ...

## 9.5 Conclusions.

In this paper a flexible rotordynamic system with one oil journal bearing was investigated numerically for different mass unbalances and for two different cavitation models in the bearing. The linear part of the system, the shaft and rotor, was reduced using a component mode synthesis method. Using this method systems with local nonlinearities can be analysed very efficiently.

The results show that bearing theories with a cavitation region in the bearing which depends on the shaft eccentricity only, are only valid for systems with a moderate level of shaft eccentricities in the bearings. For these systems one can assume the cavitation region to be independent of the shaft velocity. Systems with high shaft eccentricities or low eccentricities should be calculated using a theory based on a cavitation region which depends on the shaft velocity also. The results show that even for calculation of the stability of the stationary solutions the cavitation region cannot be expected to depend on the shaft eccentricity alone, because the damping constants differ too much. This indicates that the cavitation region already changes for very low shaft velocities.

## Acknowledgement.

This work was supported by the Centre for Mechanical Engineering of TNO Building and Construction Research, Delft, The Netherlands.

## 9.A Short Bearing Theory.

## 9.A.1 Short Bearing Theory using a cavitation region which depends on shaft velocity.

In Moes and Bosma (1981) the bearing forces of the short bearing theory which assumes the cavitation region to depend on the shaft velocity are given in terms of the impedance method. Using the pure-squeeze-velocity vector and a well chosen dimensionless bearing load force vector, also called impedance vector w, the equations for the bearing load force can be written as

$$\boldsymbol{f} = \left(\frac{R}{c}\right)^3 2\mu L_b \boldsymbol{v}_s \boldsymbol{w} \tag{9.8}$$

In case of  $\pi$  short bearings the components of the impedance vector w can be expressed as

$$w_{\xi} = \left(\frac{L_b}{R}\right)^2 \frac{6(1+2\xi^2-\zeta^2)T+\xi}{4(1-\epsilon^2)^2}$$
(9.9)

$$w_{\zeta} = \left(\frac{L_b}{R}\right)^2 \frac{6\zeta(\xi T + 1 - E/3)}{4(1 - \epsilon^2)^2}$$
(9.10)

with

$$T = \frac{2 \arctan\left(\left(\sqrt{(1-\epsilon^2)}\right)/(\sqrt{1-\zeta^2}-\xi)\right)}{\sqrt{(1-\epsilon^2)}},$$
  

$$E = \frac{(1-\epsilon^2)}{(1-\zeta^2)}$$
(9.11)

and  $\xi$  and  $\zeta$  stand for a coordinate system, where  $\xi$  coincides with the direction of the pure-squeeze-velocity vector which implies that

$$\xi = c\epsilon \cos(\alpha), \quad \zeta = c\epsilon \sin(\alpha)$$
 (9.12)

## 9.A.2 Short Bearing Theory using a cavitation region which is independent of shaft velocity.

In Khonsari and Chang (1993) the following algebraic equations for the short bearing theory are given if the cavitation region is independent of the shaft velocity.

$$f_{\epsilon} = -\left(\frac{\mu L_b R^3}{2c^2}\right) \left(\frac{L_b}{R}\right)^2 \left[\frac{4\epsilon^2(\bar{\omega}-\dot{\beta})}{(1-\epsilon^2)^2} + \frac{\pi(1+2\epsilon)}{(1-\epsilon^2)^{5/2}}\right]$$
(9.13)

$$f_{\beta} = \left(\frac{\mu L_b R^3}{2c^2}\right) \left(\frac{L_b}{R}\right)^2 \left[\frac{\pi(\bar{\omega}-\dot{\beta})\epsilon}{(1-\epsilon^2)^{3/2}} + \frac{4\epsilon\dot{\epsilon}}{(1-\epsilon^2)^2}\right]$$
(9.14)

## 9.B Nomenclature.

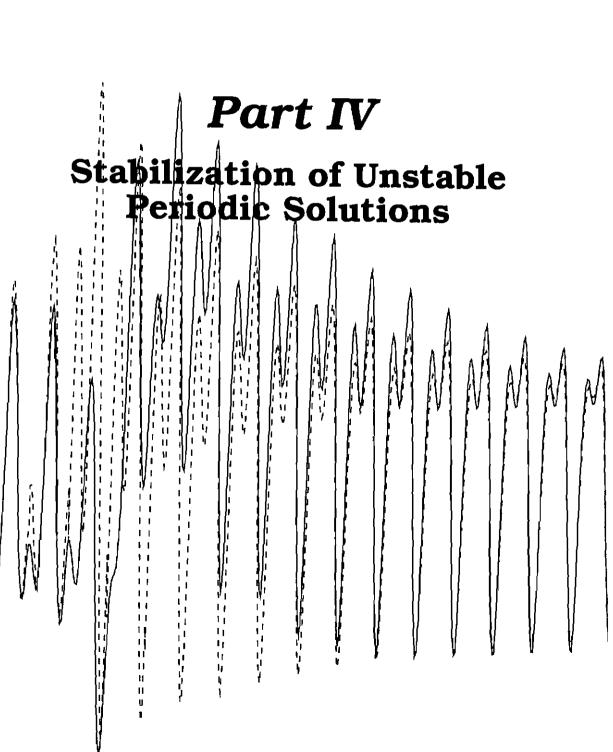
σ	Sommerfeld number
$L_b$	bearing length
Ŕ	bearing radius
μ	lubricant viscosity
с	bearing clearance
$\omega$	angular rotor speed
$m_e$	mass unbalance
re	radius of mass unbalance
p	fluid pressure
$x_b, y_b, z_b$	stationary coordinate system
ε	eccentricity ratio vector
$\beta$	attitude angle of $\epsilon$ relative to the stationary $x_b, y_b, z_b$ -system
h	normalized film thickness
θ	bearing polar cylindrical coordinate with respect to $\epsilon$
$v_s$	pure-squeeze-velocity vector
v	velocity vector
$\bar{\omega}$	zero-load whirl
$\omega_j$	observed mean angular velocity of the journal
$\omega_b$	observed mean angular velocity of the sleeve
i, j, k	unit vectors in the stationary $x_b, y_b, z_b$ -system
α	attitude angle of $\epsilon$ relative to $v_s$
w	impedance vector

## References

- Brown, R.D., Addison, P., and Chan, H.C., 1994, "Chaos in the Unbalance Response of Journal Bearings," *Nonlinear Dynamics*, Vol. 5, pp. 421-432.
- Childs, D., Moes, H., and Van Leeuwen, H., 1977, "Journal Bearing Impedance Descriptions for Rotordynamic Applications," ASME *Journal of Lubrication Technology*, Vol. 99, pp. 198–210.
- Craig Jr., R.R., 1985, "A Review of Time-Domain and Frequency-Domain Component Mode Synthesis Methods," *Combined Experimental/Analytical Modeling of Dynamic Structural Systems Using Substructure Synthesis*, D.R. Martinez and A.K. Miller, ed., ASME Applied Mechanics AMD-67, New York, pp. 1-31.
- DIANA, 1995, *DIANA User's Manual 6.0 ed.*, TNO Building and Construction Research, Delft, The Netherlands.
- Fey, R.H.B., 1992, "Steady-State Behaviour of Reduced Dynamic Systems with Local Nonlinearities," *PhD thesis*, Department of Mechanical Engineering, Eindhoven University of Technology, Eindhoven, The Netherlands.
- Fey, R.H.B., Van Campen, D.H., and De Kraker, A., April 1996, "Long Term Structural Dynamics of Mechanical Systems with Local Nonlinearities," ASME *Journal of Vibration and Acoustics*, (in press).

- Gunter, E. J., Humphris, R. H., and Springer H., 1983, "Influence of Unbalance on the Nonlinear Dynamical Response and Stability of Flexible Rotor-Bearing Systems," *Rotor Dynamical Instability*, Adams M.L., ed., Kluwer Academic Publishers, pp 37–58.
- Holmes, R., and Sykes, J.E.H., 1989, "Large-Amplitude Vibrations in Rotor Assemblies," *Journal of Sound and Vibration*, Vol. 133(2), pp. 377–351.
- Khonsari, M.M., and Chang, Y.J., 1993, "Stability Boundary of Non-Linear Orbits within Clearance Circle of Journal Bearings," ASME *Journal of Vibration and Acoustics*, Vol. 115, pp. 303–307.
- Moes, H., and Bosma, R., 1981, "Mobility and Impedance Definitions for Plain Journal Bearings," ASME Journal of Lubrication Technology, Vol. 103, pp. 468–470.
- Myers, C.J., 1984, "Bifurcation Theory Applied to Oil Whirl in Plain Cylindrical Journal Bearings," ASME *Journal of Applied Mechanics*, Vol. 51, pp. 244–250.
- Van de Vorst, E.L.B., Fey, R.H.B., De Kraker, A., and Van Campen, D.H., 1995, "Steady-State Behaviour of Nonlinear Flexible Rotor-Bearing Systems: Part I – An Efficient Numerical Analysis Method," *Machine Vibration*, Vol 3, pp 138–145.

158CHAPTER 9. STEADY-STATE BEHAVIOUR OF NONLINEAR FLEXIBLE ROTOR-BEARING ...



)

. .

.

160

# 10

## VIBRATION CONTROL OF PERIODICALLY EXCITED NONLINEAR DYNAMIC MULTI-DOF SYSTEMS.<sup>‡</sup>

MMMM

For nonlinear mechanical systems, which have stable subharmonic resonance peaks and one or more coexisting unstable harmonic solutions, a large reduction of maximum subharmonic, quasi-periodic or chaotic displacement can be established if the coexisting unstable harmonic solution could be made stable. The control effort to obtain this goal can be very small in that case. In this paper a method for controlling nonlinear multidegree-of-freedom (multi-DOF) systems to unstable periodic solutions is developed. This is established by putting a single control force somewhere on the system. Because the selected control method uses the full state of the system and since only measured displacements and accelerations of a very limited number of DOF's are assumed to be available, a reconstruction method has to be used for estimating the full state on-line. Simulations are done using a beam system supported by a one-sided spring which is controlled to the unstable harmonic solution. The robustness of the method with respect to model errors, system disturbance and measurement errors is examined. Furthermore, the performance of the method in case of a varying excitation frequency during the control is investigated.

## 10.1 Introduction.

This paper deals with the control of the long term behaviour of periodically excited nonlinear mechanical systems. The long term behaviour of a nonlinear dynamic system under periodic excitation can be periodic, quasi-periodic or chaotic. In case of periodic behaviour the period time of the system may be equal to the excitation period (harmonic solution) or n times the excitation period (1/n subharmonic solution). Subharmonic behaviour may lead to the occurrence of extra resonance peaks of the system. If quasiperiodic or chaotic behaviour occurs the response will have a frequency spectrum with

<sup>&</sup>lt;sup>‡</sup>Van de Vorst, E.L.B., Van Campen, D.H., Fey, R.H.B., De Kraker, A., and Kok, J.J., 1995, "Vibration Control of Periodically Excited Nonlinear Dynamic Multi-DOF Systems," *Journal of Vibration and Control*, Vol. 1 pp.75–92

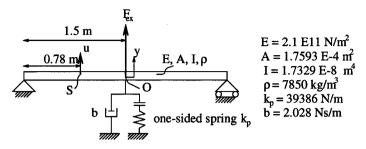


Figure 10.1 Beam system.

frequencies which are generated by the system itself. Also in case of stable quasi-periodic or chaotic solutions the maximum response of the system will increase in general. Often a harmonic solution coexists, which may be unstable. Usually the maximum displacement of this unstable harmonic solution is much lower than the maximum displacement (in absolute sense) of the stable subharmonic, quasi-periodic or chaotic solutions.

An example of a system showing subharmonic, quasi-periodic and chaotic behaviour is a two-dimensional beam system with periodic excitation and supported by a onesided spring (the nonlinearity) and a linear damper in its point of symmetry O (figure 10.1) (Fey, 1992). Periodic solutions of the beam are calculated for varying excitation frequency by solving two-point boundary value problems using the finite difference method in combination with a path-following method (Fey et al., 1996). The maximum displacements  $|y|_{max}$  of O occurring in the periodic solutions are shown in figure 10.2 for varying excitation frequency  $f_e$ . This figure shows in addition to the first harmonic peak also stable 1/2, 1/3, 1/5, 1/7 and 1/9 subharmonic peaks. The maximum displacements of the subharmonics are much larger than the maximum displacements of the coexisting harmonic solution, which is unstable below the stable branch with 1/2 subharmonics. Also quasi-periodic and chaotic behaviour (not visible in figure 10.2) is found in the frequency range  $f_e = 47-49$  Hz.

If the beam system is vibrating in the stable harmonic solution at  $f_e = 10$  Hz, and subsequently the excitation frequency is slowly increased to 50 Hz, the maximum response of the beam will increase when approaching the harmonic and subharmonic resonance peaks between 10 Hz and 50 Hz (figure 10.2). The growth of the response may lead to large strains and stresses which could cause damage to the structure. Therefore, it may happen that the resonance peaks should be avoided under operating circumstances and this can be realized using control. For reducing the maximum displacement of the harmonic resonance peak, a considerable control force has to be generated which will act as the necessary damping force. However, for reducing the maximum displacements of the subharmonic resonance peaks, the control effort eventually will be small (in theory even zero) if the system is controlled to the coexisting unstable harmonic solution.

This means for example that if the beam system mentioned previously is vibrating in the stable 1/2 subharmonic solution at  $f_e = 25$  Hz and subsequently is controlled to the coexisting unstable harmonic solution, the control forces will be large to start with but eventually become small or even tend to zero. This implies that a large reduction of the maximum response of the beam system is established by very little control effort,

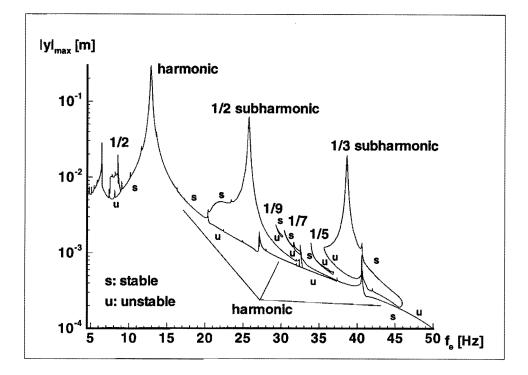


Figure 10.2 Maximum displacements of periodic solutions of point O of beam model without control.

because the maximum displacement of the unstable harmonic solution is much lower than that of the coexisting stable 1/2 subharmonic solution.

Using control also chaos can be avoided by forcing a nonlinear dynamic system to vibrate in an unstable periodic solution, because in a chaotic attractor always one or more unstable periodic solutions exist. A method for controlling chaos has been developed by Ott et al. (1990). This method uses the stable manifolds of the unstable periodic solution to control the system to that unstable periodic solution. A system, vibrating in a chaotic attractor, will, after some time, come close to the unstable periodic solution. Then the stable manifold is moved to the momentary state space position by slightly varying one system parameter. With the trajectory on the stable manifold, it will automatically approach the unstable periodic solution. In this method only one system parameter is slightly varied, which implies that in this method also the control effort will be very small. However, a disadvantage of this method is that the stable manifold and the periodic solution must be known beforehand. Since these depend on the system parameters, large changes of them during the control are not allowed. Furthermore this method is only useful for controlling chaos because if a system is vibrating in a subharmonic attractor as in our case, it will never come close to the coexisting unstable harmonic solution.

#### 164 CHAPTER 10. VIBRATION CONTROL OF PERIODICALLY EXCITED NONLINEAR...

In this paper a method is developed for controlling multi-degree-of-freedom (multi-DOF) systems to unstable periodic solutions by putting a control force somewhere on the system. In section 10.2 the theory is presented for controlling multi-DOF systems to a desired trajectory using the full state of the system. In section 10.3 a reconstruction method is presented, since only measured accelerations and displacements of some DOF's of the system will supposed to be available. In section 10.4 a method for calculation of the desired trajectory, which is the harmonic solution, under varying system parameters is presented. In section 10.5 an application is evaluated by numerical simulation: the beam supported by a one-sided spring mentioned above is controlled to the unstable harmonic solution. Using this beam system also the robustness of the controller-observer is investigated. Furthermore, the response of the beam system is evaluated for varying excitation frequency.

## 10.2 Control of multi-DOF nonlinear dynamic systems.

In this paper, a system is controlled by putting a single control force somewhere on the system. The equations of motion of a n-DOF nonlinear dynamic mechanical system with a constant mass matrix can be written as

$$\boldsymbol{M}\ddot{\boldsymbol{q}} + \boldsymbol{f_{nl}}(\dot{\boldsymbol{q}}, \boldsymbol{q}, t) = \boldsymbol{f_{ex}}(t) + \boldsymbol{u}$$
(10.1)

with M the constant mass matrix,  $f_{nl}$  the nonlinear internal forces,  $f_{ex}$  the external forces and

$$\boldsymbol{u} = \begin{bmatrix} 0 & \dots & 0 & u_k & 0 & \dots & 0 \end{bmatrix}^T.$$
(10.2)

In (10.2)  $u_k$  is the control force acting on DOF k. Equation (10.1) can be rewritten in first order form as

$$\dot{x} = f_{nl}^{*}(x,t) + f_{ex}^{*}(t) + u^{*}$$
(10.3)

where

$$\boldsymbol{x} = \begin{bmatrix} \boldsymbol{q} \\ \boldsymbol{\dot{q}} \end{bmatrix}, \quad \boldsymbol{f}_{nl}^* = \begin{bmatrix} \boldsymbol{\dot{q}} \\ -M^{-1}\boldsymbol{f}_{nl} \end{bmatrix}, \quad \boldsymbol{f}_{ex}^* = \begin{bmatrix} \boldsymbol{0} \\ M^{-1}\boldsymbol{f}_{ex} \end{bmatrix}, \quad \boldsymbol{u}^* = \begin{bmatrix} \boldsymbol{0} \\ M^{-1}\boldsymbol{u} \end{bmatrix}.$$
(10.4)

The system must be controlled to the desired trajectory  $q_d$ . For controlling the system sliding control (Slotine and Li, 1991) is used. Because the system is controlled by putting a control force on one DOF k, only one DOF is controlled to the desired trajectory. In the sliding control method a sliding variable  $s_k$  is used:

$$s_k = \dot{\epsilon}_k + \lambda \epsilon_k \tag{10.5}$$

with  $\lambda$  a positive user defined constant and  $\epsilon_k$  the tracking errors defined by

$$\epsilon_k = q_k - q_{d_k}.\tag{10.6}$$

Now it is assumed that if the sliding variable  $s_k$  approaches zero, the tracking errors  $\epsilon = q - q_d$  also approach zero.

For letting  $s_k$  approach to zero a sliding term is added to  $\dot{s}_k$ , resulting in the following equation

$$\dot{s}_k + \eta sgn(s_k) = 0 \tag{10.7}$$

with  $\eta$  a positive user defined control parameter. A Lyapunov function for this equation is

$$V = \frac{1}{2}s_k^2 \tag{10.8}$$

because V is positive definite and

$$\dot{V} = s_k \dot{s}_k = -s_k \eta sgn(s_k) = -\eta |s_k| \leqslant 0.$$
(10.9)

So  $\dot{V}$  is negative definite as long as  $s_k \neq 0$ . This means  $s_k = 0$  is a globally stable equilibrium point. Assume that  $s_k(t=0) > 0$  and let  $t_{reach}$  be the time required for  $s_k$  to become zero. Integrating equation (10.7) between t = 0 and  $t = t_{reach}$  leads to

$$s_k(t = t_{reach}) - s_k(t = 0) = 0 - s_k(t = 0) = -\eta(t_{reach} - 0)$$
(10.10)

which implies that

$$t_{reach} = s_k(t=0)/\eta \tag{10.11}$$

One would obtain a similar result starting with  $s_k(t = 0) < 0$ , and thus

$$t_{reach} = |s_k(t=0)|/\eta$$
 (10.12)

This means that  $s_k$  becomes zero in a *finite* time interval. Equation (10.5) implies that if  $s_k = 0$ , then  $\epsilon_k$  tends exponentially to zero with a time constant  $1/\lambda$ .

Equation (10.7) implies that during  $t < t_{reach}$  the sign of  $s_k$  does not change. However, in practice, model inaccuracies and model disturbances exist which can result in sign variations of  $s_k$  during the control time. This means that the control law is discontinuous across  $s_k = 0$ . Since the implementation of the associated control switching is imperfect, this leads to so-called chattering. Chattering is undesirable in practice because it involves high control activity and it may excite high frequency dynamics of the controlled system. To overcome this, a saturation function is used instead of a *sgn* function:

$$sat(s_k/\sigma) = \begin{cases} -1, & \text{if } s_k < -\sigma \\ s_k/\sigma, & \text{if } |s_k| \leq \sigma \\ 1, & \text{if } s_k > \sigma \end{cases}$$
(10.13)

If a saturation function is used, then (10.7) becomes

$$\dot{s}_k = -\eta sat(s_k/\sigma) \tag{10.14}$$

This implies that the time required for  $s_k$  to become  $\sigma$  is  $t_{\sigma} = |s_k(t=0) - \sigma|/\eta$  and for  $t \ge t_{\sigma}$ 

$$s_k = \sigma e^{-t/\sigma} \tag{10.15}$$

so  $s_k$  will again exponentially tend to zero.

Using (10.1) and (10.3), equation k of the system equations can be written as

$$\ddot{q}_k = [-M^{-1} f_{nl} + M^{-1} f_{ex}]_k + u_k^*$$
(10.16)

with  $u_k^* = [M^{-1}u]_k$ . Using (10.5), (10.6) and (10.16), (10.14) can be rewritten as

$$[-M^{-1}f_{nl} + M^{-1}f_{ex}]_k + u_k^* - \ddot{q}_{d_k} + \lambda \dot{\epsilon}_k + \eta sat(s_k/\sigma) = 0$$
(10.17)

This yields for the control force  $u_k^* = u_l + u_c$  with

$$u_l = -[-M^{-1}f_{nl} + M^{-1}f_{ex}]_k$$
(10.18)

where  $u_l$  is the co-called feedback linearization force (Slotine and Li, 1991), which linearizes equation k and

$$u_c = \ddot{q}_{d_k} - \lambda \dot{\epsilon}_k - \eta sat(s_k/\sigma) \tag{10.19}$$

where  $u_c$  is the sliding control force for controlling equation k.

Using (10.2), (10.4), (10.18) and (10.19), the total control force  $u_k$  can now be calculated:

$$[\boldsymbol{M}^{-1}\boldsymbol{u}]_{k} = u_{k}^{*} \to u_{k} = (u_{k}^{*})/[\boldsymbol{M}^{-1}]_{kk}$$
(10.20)

If  $[M^{-1}]_{kk}$  is zero another equation corresponding to DOF  $q_i$  must be controlled for which  $[M^{-1}]_{ki}$  is not zero.

This controller is stable if the so-called internal dynamics are stable (Slotine and Li, 1991). The internal dynamics of the system are all the system equations except the controlled equation. Stability of the internal dynamics can be calculated using zero-dynamics. In zero-dynamics the control force is chosen so that the output  $q_k$  and  $\dot{q}_k$  is zero. If the internal dynamics of the system is nonlinear, generally it is very difficult to calculate the stability of the internal dynamics.

# 10.3 Reconstruction of the full state using Kalman filtering.

The control method which is presented in section 10.2 needs the full state of the system. In this paper we assume that we only dispose of measured positions  $q_{m_i}$  and accelerations  $\ddot{q}_{m_i}$  for  $n_m$  DOF's ( $n_m \ll n$ ). Thus a reconstruction of the full state is necessary. The observer used in this paper is based on an observer model for estimating the full state:

$$\dot{\hat{x}} = \hat{f}_{nl}^{*}(\hat{x}, t) + \hat{f}_{ex}^{*}(t) + u^{*} + u_{o}^{*}$$
(10.21)

where  $\hat{f}_{nl}^*$  and  $\hat{f}_{ex}^*$  are approximations of  $f_{nl}^*$  and  $f_{ex}^*$  respectively,  $\hat{x}$  is the full state reconstruction and  $u_o^*$  the innovations. These innovations must be chosen in such way that the estimation errors  $\hat{x} - x$  are minimized for each moment in time.

In this paper Kalman filtering (Kalman, 1960, Kalman and Bucy, 1961) is used for the full state reconstruction. The estimated measured quantities can be filtered from the estimated state space:

$$\hat{\boldsymbol{x}}_{\boldsymbol{m}} = \hat{\boldsymbol{l}}(\hat{\boldsymbol{x}}, t) + \hat{\boldsymbol{H}}\boldsymbol{u}^* \tag{10.22}$$

where  $\hat{\boldsymbol{x}}_{m}$  is the column of  $2n_{m}$  estimated measured quantities

$$\hat{\boldsymbol{x}}_{\boldsymbol{m}} = \begin{bmatrix} \hat{q}_{m_1} & \dots & \hat{q}_{m_{n_m}} & \hat{\ddot{q}}_{m_1} & \dots & \hat{\ddot{q}}_{m_{n_m}} \end{bmatrix}^T$$
(10.23)

and

$$\hat{l}(\hat{\boldsymbol{x}},t) = \begin{bmatrix} T & 0 \\ 0 & T \end{bmatrix} \begin{bmatrix} \hat{\boldsymbol{q}} \\ -\hat{\boldsymbol{M}}^{-1} \hat{f}_{nl} + \hat{\boldsymbol{M}}^{-1} \hat{f}_{ex} \end{bmatrix}$$

$$\hat{\boldsymbol{H}} = \begin{bmatrix} T & 0 \\ 0 & T \end{bmatrix} \begin{bmatrix} 0 & 0 \\ 0 & \hat{\boldsymbol{M}}^{-1} \end{bmatrix}$$
(10.24)

In (10.24) T is a  $n_m \times n$ -matrix which filters the DOF's which are measured from the estimated displacement:

$$\hat{q}_m = T\hat{q} \tag{10.25}$$

The innovations  $\boldsymbol{u}_{o}^{*}$  are chosen to be:

$$\boldsymbol{u}_{o}^{*} = \boldsymbol{G}(\boldsymbol{x}_{m} - \hat{\boldsymbol{l}}(\hat{\boldsymbol{x}}, t) - \hat{\boldsymbol{H}}\boldsymbol{u}^{*})$$
(10.26)

with G the optimal Kalman filter matrix and  $x_m$  the measurement column.

Using (10.26) and (10.21) and assuming that the observer model is equal to the actual controlled model, for the estimation errors  $\hat{\epsilon} = x - \hat{x}$  holds:

$$\dot{\hat{\boldsymbol{\varepsilon}}} = \boldsymbol{f}_{\boldsymbol{n}\boldsymbol{l}}^{*}(\boldsymbol{x},t) - \boldsymbol{f}_{\boldsymbol{n}\boldsymbol{l}}^{*}(\hat{\boldsymbol{x}},t) - \boldsymbol{G}\left[\boldsymbol{l}(\boldsymbol{x},t) - \boldsymbol{l}(\hat{\boldsymbol{x}},t)\right] + \boldsymbol{w}(t) - \boldsymbol{G}\boldsymbol{v}(t) \quad (10.27)$$

if w(t) is the system disturbance and v(t) is the measurement noise.

Assuming that the estimation errors  $\hat{\epsilon}$  are small, equation (10.27) may be linearized around the state  $\boldsymbol{x}$  which results in:

$$\dot{\hat{\boldsymbol{\epsilon}}} = [\boldsymbol{F}_{nl}(\boldsymbol{x},t) - \boldsymbol{G}\boldsymbol{L}(\boldsymbol{x},t)]\hat{\boldsymbol{\epsilon}} + \boldsymbol{w}(t) - \boldsymbol{G}\boldsymbol{v}(t)$$
(10.28)

with

$$\boldsymbol{F}_{nl}(\boldsymbol{x},t) = \left. \frac{\partial \boldsymbol{f}_{nl}^*}{\partial \boldsymbol{x}} \right|_{\boldsymbol{x},t}$$
(10.29)

and

$$\boldsymbol{L}(\boldsymbol{x},t) = \left. \frac{\partial \boldsymbol{l}}{\partial \boldsymbol{x}} \right|_{\boldsymbol{x},t}$$
(10.30)

For determining the optimal Kalman filter G the Riccatti equation must be solved:

$$\dot{\boldsymbol{Q}} = [\boldsymbol{F}_{nl}(\boldsymbol{x},t) - \boldsymbol{GL}(\boldsymbol{x},t)]\boldsymbol{Q} + \boldsymbol{Q}[\boldsymbol{F}_{nl}(\boldsymbol{x},t) - \boldsymbol{GL}(\boldsymbol{x},t)]^{T} + \boldsymbol{V}_{\boldsymbol{w}} + \boldsymbol{GV}_{\boldsymbol{v}}\boldsymbol{G}^{T}$$
(10.31)

where Q is the Riccatti matrix,  $V_v$  and  $V_w$  are weight matrices for the measurement noise and system disturbance respectively, and the optimal Kalman filter G is

$$\boldsymbol{G} = \boldsymbol{Q} \boldsymbol{L}^T \boldsymbol{V}_n^{-1} \tag{10.32}$$

The initial conditions  $Q(t = 0) = Q_0$  should be chosen  $Q_0 > 0$ . Equations (10.31) and (10.32) show that the optimal Kalman filter depends on the state space x and time t which implies that the 2n \* 2n Riccatti equations should be integrated on-line. This makes it a very expensive reconstruction method.

In order to avoid very large computational times one can assume the linearized matrices  $F_{nl}$  and L to be constant, which yields also the optimal Kalman filter G to be constant. This is useful for systems with small nonlinearities. Another way to avoid the on-line integration of the Riccatti equation is assuming that the system is very close to the desired trajectory. The desired trajectory is periodic which means that the Kalman filter G(t) is also periodic. Using equations (10.31) and (10.32), the periodic Kalman filter can be calculated. A disadvantage of this approach is that although the Kalman filter is independent of the current state of the system, it certainly depends on the system parameters, for instance the excitation frequency. This means that in case of a varying excitation frequency during the control, the optimal Kalman filter must be recalculated during the control.

## 10.4 Computation of the desired trajectory.

For the reduction of the maximum response and minimization of the long term control effort, we choose the (possibly unstable) harmonic solution as the desired trajectory  $q_d$ . If all system parameters are known in advance, the desired trajectory can be calculated using the finite difference method, the shooting method (Ascher et al., 1988) or the incremental harmonic balance method (Fey et al., 1994). However, if one system parameter is changed during the control, the harmonic solution will change also and the desired trajectory must be updated.

One way to solve this problem is to calculate the harmonic solution for a grid of system parameters which may appear during the control time. This can be done using the shooting method, the finite difference method or the incremental harmonic balance method in combination with a path-following method. For reducing the amount of data, the harmonic solutions are written as truncated Fourier series:

$$q_{d} = \sum_{n=1}^{n_{h}} a_{n} \sin(2\pi f_{e} nt) + \sum_{n=1}^{n_{h}} b_{n} \cos(2\pi f_{e} nt) + c$$
(10.33)

with  $n_h$  the number of harmonic terms, which must be chosen large enough for describing the harmonic solution.

During the control the desired trajectory for one set of system parameters is calculated using equation (10.33) with constants  $a_n$ ,  $b_n$  and c which are interpolated linearly using the constants of the solutions on the grid points. Of course, the accuracy of the desired trajectory depends on the number of grid points and  $n_h$ . The advantage of this approach is that during the control no extra equations have to be integrated, only equation (10.33) has to be calculated.

## 10.5 Application: Beam supported by one-sided spring.

#### 10.5.1 Preliminaries.

In this section, some simulation results are presented for the two-dimensional pinnedpinned beam introduced in section 10.1. The beam is excited at O by a periodic force  $F_{ex} = 39.38cos(2\pi f_e t)$  ( $f_e \leq 50$  Hz). We assume small Rayleigh damping (damping matrix  $B = \beta K$ , with K the stiffness matrix of the linear beam and  $\beta = 10^{-6}$  s). The beam is supported in the point of symmetry O by a one-sided spring and a linear damper and is controlled by a single control force u in point S (figure 10.1), which has an upper bound of 20 N. Displacement and acceleration measurements are available for two points of the beam: the points O and S.

The beam is modelled using the finite element method and the number of DOF's of the linear part of the model (the beam) is reduced using a component mode synthesis method based on residual flexibility modes and free-interface eigenmodes up to a cutoff frequency of 400 Hz (Craig, 1985). Because nonlinear systems can generate higher frequencies than their excitation frequency, the cut-off frequency has been chosen higher than the maximum excitation frequency.

The beam model is reduced from 100 to 8 DOF's (2 residual flexibility modes for the DOF's corresponding to DOF's O and S, 6 free-interface eigenmodes with eigenfrequencies of 8.96 Hz, 35.83 Hz, 80.60 Hz, 143.2 Hz, 223.7 Hz, 321.9 Hz\*). Subsequently the reduced linear system is coupled with the nonlinear part, i.e. the one-sided spring, and the linear damper. In appendix 10.A the full system equations of motion are given for the reduced system.

Table 10.1 shows the values of the used control parameters. In the weight matrices,  $V_v$  for the measurement noise and  $V_w$  for the system disturbance, used to determine the optimal Kalman filter, the following parameters are taken:

<sup>\*</sup>Because the system without the control force is symmetric, for calculating figure 10.2 the asymmetric modes are not necessary and in that case the system can be reduced to 4 DOF's.

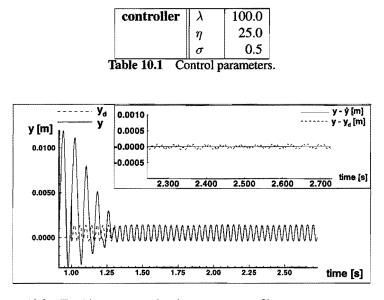
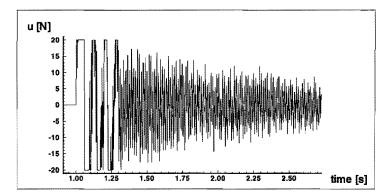
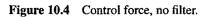


Figure 10.3 Tracking errors and estimate errors, no filter.





$$\boldsymbol{V_{v}} = \begin{bmatrix} 10^{-5} & 0 & 0 & 0\\ 0 & 10^{-5} & 0 & 0\\ 0 & 0 & 150 & 0\\ 0 & 0 & 0 & 150 \end{bmatrix}, \quad \boldsymbol{V_{w}} = 0.01\boldsymbol{I}.$$

Section 5.5 describes how the search of the parameters has been carried out.

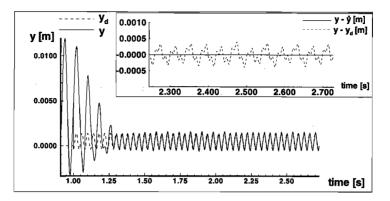


**Figure 10.5** Tracking errors and estimate errors,  $u_c$  filtered.

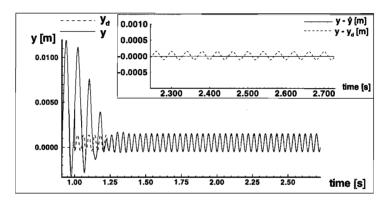


**Figure 10.6** Tracking errors and estimate errors,  $u_l$  filtered.

### 10.5.2 Control in case of exact system model.

In this subsection the system model used for the control force calculation and for the full state reconstruction is supposed to be equal to the actual system  $(\hat{f}_{nl}^* = f_{nl}^*, \hat{f}_{ex}^* = f_{ex}^*)$ . Moreover, it is assumed that system disturbance and measurement noise are absent, i.e.  $q_{m_i} = q_i$  and  $\ddot{q}_{m_i} = \ddot{q}_i$ . The excitation frequency  $f_e$  is equal to 25.0 Hz. Figure 10.2 shows a 1/2 subharmonic attractor (max amplitude approximately 8 mm) and an unstable harmonic solution (max amplitude approximately 1 mm) at this frequency.

A constant Kalman filter is used for reconstruction of the full state. For calculating the optimal Kalman filter the beam system is used for which the one-sided spring is replaced by a linear spring with the same stiffness constant as the one-sided spring. Notice that this is different from linearizing the system since a one-sided spring cannot be linearized. Because of this it is not trivial that the constant Kalman filter will work for this system.

For calculation of the desired trajectory the method described in section 10.4 is used with the number of harmonic terms  $n_h$  equal to 10.

Figure 10.3 shows the desired  $(y_d)$  and measured (y) responses as well as the final

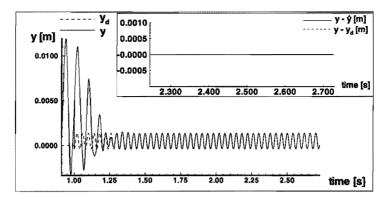
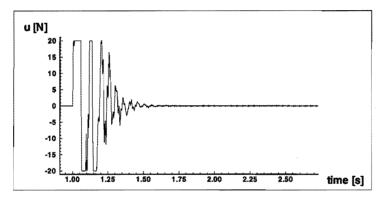


Figure 10.7 u filtered,  $f_c = 200$  Hz.



**Figure 10.8** Control effort, u filter  $f_c = 200$  Hz.

tracking errors  $y - y_d$  and estimate errors  $y - \hat{y}$  of the point of symmetry O of the beam. At t = 1 sec the control is switched on. Before t = 1 sec, the system is dominated by the 1/2 subharmonic attractor (the transient has not damped out completely yet). Figures 10.3–10.4 show that the constant Kalman filter works fine but that the tracking errors and control force do not converge to zero and that there are high frequencies in the control force.

As mentioned in section 10.2 the sliding term in the control force can cause high frequencies in this force, a phenomenon known as chattering. Here, although a saturation function is used instead of a sign function to overcome this problem, still high frequencies are found in the control force. For reducing the high frequencies in the control force digital filtering has been applied by a first order filter with a filter cut-off frequency  $f_c$  of 200 Hz, giving figures 10.5–10.8. In figure 10.5 the sliding control force  $u_c$  is filtered, which does not show any improvement. The tracking errors do not converge to zero. In figure 10.6 the feedback linearization control force  $u_l$  is filtered. This action has more effect, although the total control force and the tracking errors still do not converge to zero. In figures 10.7–10.8 the total control force is filtered. Now the tracking errors and the control force both converge to zero.

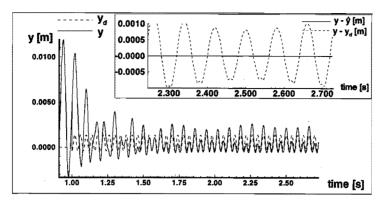


**Figure 10.9** u filtered,  $f_c = 25$  Hz.

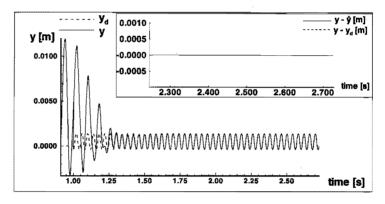


Figure 10.10 u filtered,  $f_c = 800$  Hz.

Figures 10.9 and 10.10 show the tracking errors if the control force u is filtered using filter bandwidths  $f_c$  of 25 Hz and 800 Hz, respectively. If  $f_c = 25$  Hz the control force and tracking errors do not converge to zero. If  $f_c = 800$  Hz the time for controlling the system to the unstable harmonic increases compared to the case  $f_c = 200$  Hz. The latter filter bandwidth seems to be a rather optimal one.

The results show that the high frequencies in the control force are not only caused by the sliding term. The control force limitation will also excite the high eigenmodes of the beam. This will result in high frequencies in the control forces because the beam is only weakly damped. However, the main reason for these high frequencies is the limitation to only one control force at one spot on the beam. This implies that if the system response contains eigenmodes which have little amplitude at the control DOF, it is very difficult to control these modes. This means that in general the digital filter bandwidth will depend on the DOF which is controlled.

In the next sections the filter bandwidth of the filter is set to  $f_c = 200$  Hz.

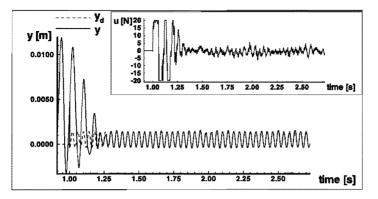


Figure 10.11 Displacement y and control force u, measurement noise and system disturbance, constant Kalman filter.

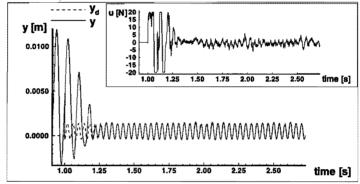


Figure 10.12 Displacement y and control force u, measurement noise and system disturbance, extended Kalman filter.

### 10.5.3 Robustness of controller-observer.

In the previous subsection the system model used for calculation of the control force is equal to the actual system  $(\hat{f}_{nl}^* = f_{nl}^*, \hat{f}_{ex}^* = f_{ex}^*)$ . Moreover, it is assumed that system disturbances and measurement noise are absent, so  $q_{m_i} = q_i$  and  $\ddot{q}_{m_i} = \ddot{q}_i$ . In practice model errors, system disturbances and measurement noise are unavoidable. In this section the robustness of the controller-observer is investigated. Noise is simulated by adding white noise with a normal distribution with zero mean and variance  $\sigma$  for ndiscrete points per period. Between these points linear interpolation is applied.

### Robustness to measurement noise and system disturbance.

Firstly the robustness to measurement noise and system disturbance is investigated. Figures 10.11 and 10.12 show the tracking errors and control force if the displacement measurement noise has a variance  $\sigma_d$  of 0.1 mm for 200 points per period (the maximum displacement  $y_d = 1.38$  mm), the acceleration measurement noise has a variance  $\sigma_a$  of 2 m/s<sup>2</sup> for 200 points per period (the maximum acceleration  $\ddot{y}_d = 41.4$  m/s<sup>2</sup>) and the excitation force noise has a variance  $\sigma_f$  of 2 N for 200 points per period (the maximum excitation force is 39.38 N). Again the excitation frequency is taken  $f_e = 25$  Hz.

In figure 10.11 the constant Kalman filter of section 10.5.2 is used. In figure 10.12 a varying Kalman filter is used (extended Kalman filtering); this optimal Kalman filter is periodic and is calculated using the desired trajectory (see section 10.3).

The figures show that Kalman filtering is robust for measurement noise and system disturbances. Further, the constant Kalman filter shows almost the same results as does the extended Kalman filter. The computational time for calculating the optimal constant Kalman filter was 0.15 CPU-sec on a Silicon Graphics Challenge (R4400, 150MHz processor). The computational time for calculating the optimal extended Kalman filter was 217 CPU-sec and is much higher because  $2n \times 2n$  Riccatti equations must be integrated over five periods before the Kalman filter is periodic. The computational time for simulation of figure 10.11 (constant Kalman filter) was 122 CPU-sec, whereas for figure 10.12 (extended Kalman filter) this mounted to 236 CPU-sec. This is due to the extended Kalman filter depends on the time. Therefore, the coefficients of the Kalman filter are written as truncated Fourier series with  $n_h = 10$ . Extra computational time is needed for calculation of the extended Kalman filter matrix G at each time step using the truncated Fourier series.

#### Robustness to model errors.

In this subsection the system model used for the reconstruction and for the calculation of the control force differs from the actual system. Firstly the actual system is made nonsymmetric by increasing the length on the right-hand side of the beam (figure 10.1) with 1 cm, whereas the system model remains symmetric. The consequence of this is that in this case also the asymmetric eigenmodes will be excited by the one-sided spring and external force, which was not the case until so far. Another consequence is that the eigenfrequencies of the undamped linear beam model used for reconstruction and control are 0.7% higher than the eigenfrequencies of the actual controlled system. Furthermore, the damper in the actual system has been assigned a damping constant b = 1.166 Ns/m, which is 50 % lower than the damping constant used in the system model. This is done because in practice it is difficult to determine the damping in the system.

Finally, the characteristic of the nonlinear spring is changed to

$$f_{spring} = k(y+e), \text{ with } k = \begin{cases} 0, & \text{if } y \leq -e \\ k_p, & \text{if } y > -e \end{cases}$$
(10.34)

The constant  $k_p$  is taken 43325 N/m, which is 10% higher than the stiffness of the one-sided spring used in the system model. The constant e is taken 0.1 mm (e = 0 mm in the system model).

Figures 10.13 and 10.14 show again that the constant Kalman filter gives almost the same results as the extended Kalman filter. However, using the extended Kalman filter the system goes faster to the desired trajectory. Nevertheless, comparison of the computational times, which are similar to the computational times in subsection 10.5.3.1, shows that extended Kalman filtering is much more expensive. Notice that, in absolute

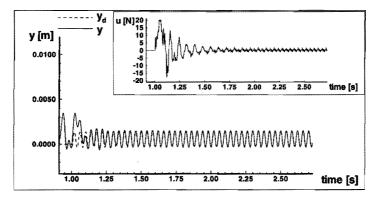


Figure 10.13 Displacement y and control force u, system errors, constant Kalman filter.

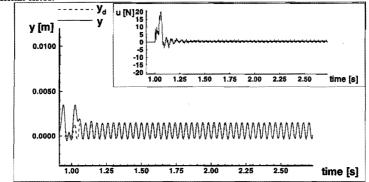


Figure 10.14 Displacement y and control force u, system errors, extended Kalman filter.

sense, the maximum displacement of the uncontrolled system is much lower than the maximum displacement of the uncontrolled system model (compare with figure 10.7 for t < 1 sec). The reason for this is that the model errors increase the frequency where the 1/2 subharmonic resonance peak occurs to a higher value.

The excitation frequency is a system parameter which has a large influence on the system behaviour. In practice the excitation frequency is not necessarily constant over a long time, so it has to be measured on-line. In figure 10.15 results are shown for the case that the excitation frequency  $f_e^*$  is assumed to be measured exactly and is modulated by a low-frequency component:

$$f_e^* = f_e(1 + A\cos(2\pi f_f t)). \tag{10.35}$$

where A = 0.01,  $f_f = 2$  Hz and a constant Kalman filter is used. The figure shows that the controller-observer is rather sensitive to the excitation frequency as expected. If the excitation frequency is not known exactly, the tracking errors will of course not converge to zero.

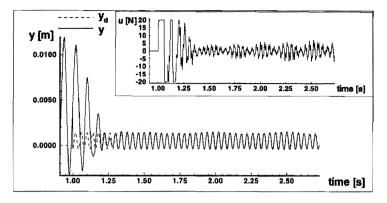


**Figure 10.15** Effect of  $f_e$  not constant.

### 10.5.4 Control of beam system for excitation frequency sweep.

In this subsection the beam system is controlled while increasing the excitation frequency  $f_e$  from 20 Hz to 50 Hz. The desired trajectory is calculated in advance (see section 10.4). The number of harmonic terms  $n_h$  was taken 10, whereas 415 periodic solutions, calculated beforehand, were used. In all figures presented in this subsection the actual controlled system is equal to the model again as described in section 10.5.2 and measurement noise and system disturbances are absent. The excitation frequency is incrementally increased. Each time after the excitation frequency is increased, it is kept constant over one excitation period, after which it is increased again. For reconstruction, the constant Kalman filter is used.

In figure 10.16a the response of the uncontrolled system is shown (the sweep takes 26.3 sec). Figure 10.16a shows that the maximum displacements of the system show bursts due to the subharmonic attractors. Figure 10.16c shows that if the system is controlled, the maximum displacements are reduced to a large extend although two very small resonance peaks remain. These are superharmonic resonance peaks at 27.1 Hz and 40.6 Hz (see figure 10.2) caused by higher eigenmodes, and are also visible in figure 10.16b which shows the desired trajectory  $y_d$  (the harmonic solution).

Figure 10.16d shows that in the beginning the control effort is large. This is because the system is not in its steady-state after 1.0 sec, and the observed full state  $\hat{x}$  is not equal to the full state x of the actual system. Furthermore, the control effort shows bursts near the two superharmonic peaks and also near some other (less high) peaks. Here, also superharmonic resonances can be seen although their maximum displacements are small. Also in the time interval between 16 and 24 seconds the control force is large over a long time. Here, the beam response does not converge to the desired trajectory. In section 10.5.2 it is stated that eigenmodes of the beam with small contribution to the control force DOF are difficult to control. This is the reason for filtering the control force, but apparently the filter bandwidth depends on the excitation frequency. Changing the filter bandwidth will help but one can also move the control force to another place on the beam. Moving the control force to another position results in other eigenmodes having nodes near the point where the control force acts, so other frequencies will be

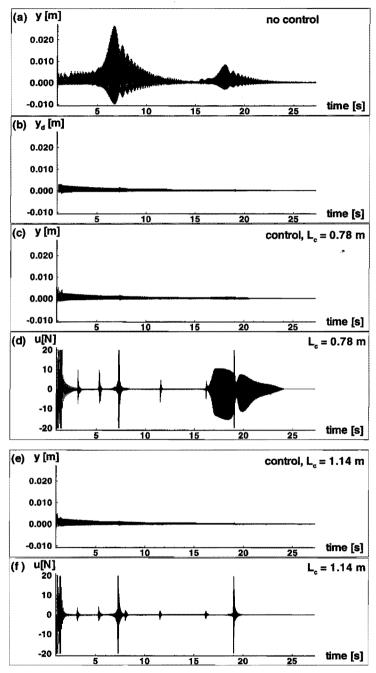


Figure 10.16 Frequency 'sweep' from 20 to 50 Hz in 26.3 sec (without measurement noise, system disturbance and model errors).

difficult to control.

Figures 10.16e-f show the response of the beam y and the control force u if the distance between the left-hand side of the beam and the point where the control force acts is increased from 0.78 m to 1.14 m. The figure shows that now the control force is large near the superharmonic resonance peaks only and between these resonance peaks the system does converge to the desired trajectory. Now the filter bandwidth  $f_c = 200$  Hz is sufficient for the whole excitation frequency range considered.

### 10.5.5 Choice of control parameters.

In this paper the final choice of the control parameters was found iteratively using a simulation for one excitation frequency. First the control parameters  $\lambda$ ,  $\eta$  and  $\sigma$  of the controller were determined assuming the knowledge of the full state of the system (no observer), and assuming that no model errors and no measurement noise are present. The observer parameters  $V_v$  and  $V_w$  were determined by estimating the state of the uncontrolled beam system, first without the one-sided spring, then with the one-sided spring. Subsequently the observer parameters where optimized by estimating the state of the controlled beam system. Finally the measurement noise, the system disturbance and model errors were added and again the control parameters and observer parameters were varied so that the tracking errors and the control force were minimized.

### 10.6 Conclusions and recommendations.

In this paper a method has been presented for controlling nonlinear dynamic multi-DOF systems to coexisting unstable periodic solutions in order to avoid resonances. This is established by putting a single control force somewhere on the system using sliding control and feedback linearization. After a short time this control force will tend to zero or become very small. Only measured displacements and accelerations of a limited number of DOF's are used in the observer.

Simulations of the beam problem showed that the control force can be filtered for a good convergence of the tracking errors and the control effort. The time for the control force and tracking errors to converge to zero depends on the filter bandwidth. If the bandwidth is chosen well, the control effort for keeping the beam vibrating in an unstable periodic solution is very small. Hence a large reduction of maximum displacement of the system is established by little long term control effort, although the stability of the beam system in combination with the controller-observer was not determined.

The simulations show that one system parameter may be varied during the control. In this case the control force will not become zero after some time, but if the parameter does not vary too fast, the control force still will be small. Only in the neighbourhood of superharmonic resonances can the control force become larger. Further, simulations using the beam problem shows that the controller-observer is very robust to model errors and measurement noise. For the investigated system the constant Kalman filter and extended Kalman filter show the same results. Because the constant Kalman filter is independent of the system parameters this observer is preferred for this system.

It is not clear yet how the stability of the controller-observer can be determined in advance. The stability of the controller can be calculated using zero-dynamics, although this is very difficult if the internal dynamics are nonlinear (as in our case). However, the reconstruction method can make the total controller-observer unstable even if the controller is stable.

A special problem is the choice of the control and observer parameters. It took a lot of trials to find the right parameters. The simulations show that the parameters do not seem to be very sensitive to the excitation frequency, in contrast with the system dynamics. The filter bandwidth has to be chosen much higher than the excitation frequency. If it is chosen too high, the convergence of the tracking errors is reduced. A low filter bandwidth, however, can result in not converging tracking errors. The results show that the filter bandwidth depends on the excitation frequency. By changing the position of the control force the dependence of the filter bandwidth can be reduced.

In the future, methods will be investigated for determining the controllability and observability of the system. These methods can help to choose the control and observer parameters and to determine the stability of the controller-observer. Furthermore, the filter of the control force will be further investigated and other control methods will be investigated in order to make the filter redundant.

### Acknowledgement

This work was supported by TNO Centre for Mechanical Engineering, Delft, The Netherlands. All calculations in this paper were done using a development release of the finite element package DIANA (1995) (module STRDYN for nonlinear dynamic analysis).

### 10.A Equations of motion of beam system.

The following equations of motion for the beam system can be obtained if the distance between the left hand side and the control force is 0.78 m. The system is modelled using finite elements and subsequently reduced using the Component mode synthesis method to 8 degrees of freedom.

The equations of motion of the beam system can be written as

$$\boldsymbol{M}\boldsymbol{\ddot{q}} + \boldsymbol{f}_{nl}(\boldsymbol{\dot{q}},\boldsymbol{q},t) = \boldsymbol{f}_{ex}(t) + \boldsymbol{u}$$
(10.36)

where

$ \left[ \begin{array}{cccccccccccccccccccccccccccccccccccc$										
$ \begin{bmatrix} 7.835E-3 & -2.007E-2 & 3.610E-4 & 7.940E-3 & -2.601E-2 & -5.766E-4 & 1.938E-2 & 5.174E-3 \\ 1.909E-1 & -4.356E-1 & 7.940E-3 & 1.753E-1 & -5.716E-1 & -2.204E-2 & 4.364E-1 & 1.384E-1 \\ -5.231E-1 & 1.346E+0 & -2.601E-2 & -5.716E-1 & 1.905E+0 & 3.818E-2 & -1.190E+0 & -3.450E-1 & (0.37) \\ -9.354E-2 & 2.872E-2 & -5.766E-4 & -2.204E-2 & 3.818E-2 & 1.007E+0 & -6.904E-2 & -6.266E-2 \\ 8.886E-1 & -1.569E+0 & 1.938E-2 & 4.364E-1 & -1.190E+0 & -8.904E-2 & 2.545E+0 & 5.925E-1 \end{bmatrix} $	ſ	1.165E+0	-3.941E - 1	7.835E-3	1.909E - 1	-5.231E - 1	-9.354E-2	8.886 E-1	7.816E-1	٦
$ \left\{ \begin{array}{cccccccccccccccccccccccccccccccccccc$		-3.941 E-1	1.985E+0	-2.007E-2	-4.356E - 1	1.346E+0	2.872E - 2	-1.569 E+0	-2.598E - 1	
$ \begin{bmatrix} -5.231E-1 & 1.346E+0 & -2.601E-2 & -5.716E-1 & 1.905E+0 & 3.818E-2 & -1.190E+0 & -3.450E-1 & (10.37) & -3.54E-2 & 2.872E-2 & -5.766E-4 & -2.204E-2 & 3.818E-2 & 1.007E+0 & -6.904E-2 & -3.626E-2 & 3.818E-2 & 1.007E+0 & -6.904E-2 & 2.545E+0 & 5.925E-1 & -1.599E+0 & -1.599E+0 & -1.599E+0 & -1.599E+0 & -5.925E-1 & -1.590E+0 & -6.904E-2 & 2.545E+0 & 5.925E-1 & -1.599E+0 & -1.5$		7.835E-3	-2.007E - 2	3.610E-4	7.940E-3	-2.601E - 2	-5.766E-4	1.938E-2	5.174E-3	
$\begin{array}{cccccccccccccccccccccccccccccccccccc$		1.909E - 1	-4.356E - 1	7.940 <i>E-</i> -3	1.753E - 1	-5.716E - 1	-2.204E-2	4.364E - 1	1.384E - 1	
8.886E - 1 - 1.569E + 0  1.938E - 2  4.364E - 1  -1.190E + 0  -6.904E - 2  2.545E + 0  5.925E - 1		-5.231E-1	1.346E+0	-2.601E-2	-5.716E - 1	1.905E+0	3.818E - 2	-1.190E+0	-3.450E - 1	(10.37)
		-9.354 E-2	2.872E-2	-5.766E - 4	-2.204E-2	3.818E - 2	1.007E+0	-6.904E-2	-6.266 E-2	
$\begin{bmatrix} 7.816E-1 & -2.598E-1 & 5.174E-3 & 1.384E-1 & -3.450E-1 & -6.266E-2 & 5.925E-1 & 1.524E+0 \end{bmatrix}$		8.886 <i>E</i> -1	-1.569E+0	1.938E-2	4.364E - 1	-1.190E+0	-6.904E - 2	2.545 <i>E</i> +0	5.925E - 1	
	L	7.816E-1	-2.598E - 1	5.174E-3	1.384E - 1	-3.450 E - 1	-6.266E-2	5.925E - 1	1.524E+0	1

and

$$f_{nl} = Kq + B\dot{q} + f_{os} \tag{10.38}$$

where

ĸ	=								
r	7.301E+4	-5.181E+4	0.000E+0	0.000E+0	0.000E+0	0.000E+0	0.000E+0	0.000 E+0	٦
	-5.181E+4	4.324 <i>E</i> +4	0.000E+0	0.000E+0	0.000E+0	0.000E+0	0.000E+0	0.000E+0	
	0.000E+0	0.000E+0	3.275E+1	6.777E+2	-2.207E+3	8.505E+1	2.089E+3	-6.659E+2	
	0.000E+0	0.000E+0	6.777E+2	1.559E+4	-4.735E+4	-4.404E+3	5.333E+4	3.448E+4	
	0.000E+0	0.000E+0	-2.207E+3	-4.735E+4	1.894E+5	-5.942E+3	7.509 E+4	4.652.E+4	(10.39)
	0.000E+0	0.000E+0	8.505E+1	-4.404E+3	-5.942E+3	8.093E+5	6.693E+3	4.327E+3	1 1
	0.000E+0	0.000E+0	2.089E+3	5.333E+4	7.509E+4	6.693E+3	1.891E+6	-5.240 E+4	
L	0.000E+0	0.000E+0	-6.659E+2	3.448 <i>E</i> +4	4.652E+4	4.327E+3	-5.240E+4	4.057E+6	
B									
в Г	7.301 E-2	-5.181 <i>E</i> -2	0.000 <i>E</i> +0	0.000 <i>E</i> +0	0.000 <i>E</i> +0	0.000 <i>E</i> +0	0.000 <i>E</i> +0	0.000 <i>E</i> +0	٦
<i>в</i> Г	7.301E-2 -5.181E-2	2.071 E+0	0.000E+0	0.000E+0	0.000E+0	0.000E+0	0.000E+0	0.000 E+0	1
<i>в</i> [	7.301E-2 -5.181E-2 0.000E+0	2.071 E+0 0.000 E+0	0.000E+0 3.275E-5	0.000E+0 6.777E-4	0.000E+0 -2.207E-3	0.000E+0 8.505E-5	0.000E+0 2.089E-3	0.000E+0 -6.659E-4	]
B	7.301 <i>E</i> -2 -5.181 <i>E</i> -2 0.000 <i>E</i> +0 0.000 <i>E</i> +0	2.071E+0 0.000E+0 0.000E+0	0.000 <i>E</i> +0 3.275 <i>E</i> -5 6.777 <i>E</i> -4	0.000 <i>E</i> +0 6.777 <i>E</i> -4 1.559 <i>E</i> -2	0.000E+0 -2.207E-3 -4.735E-2	0.000E+0 8.505E-5 -4.404E-3	0.000E+0 2.089E-3 5.333E-2	0.000 <i>E</i> +0 -6.659 <i>E</i> -4 3.448 <i>E</i> -2	]
B	$\begin{array}{c} 7.301 E-2 \\ -5.181 E-2 \\ 0.000 E+0 \\ 0.000 E+0 \\ 0.000 E+0 \end{array}$	2.071E+0 0.000E+0 0.000E+0 0.000E+0 0.000E+0	0.000 <i>E</i> +0 3.275 <i>E</i> -5 6.777 <i>E</i> -4 -2.207 <i>E</i> -3	0.000 <i>E</i> +0 6.777 <i>E</i> -4 1.559 <i>E</i> -2 -4.735 <i>E</i> -2	$\begin{array}{c} 0.000E\!+\!0\\ -2.207E\!-\!3\\ -4.735E\!-\!2\\ 1.894E\!-\!1 \end{array}$	$\begin{array}{c} 0.000  E + 0 \\ 8.505  E - 5 \\ -4.404  E - 3 \\ -5.942  E - 3 \end{array}$	0.000 <i>E</i> +0 2.089 <i>E</i> -3 5.333 <i>E</i> -2 7.509 <i>E</i> -2	0.000 <i>E</i> +0 -6.659 <i>E</i> -4 3.448 <i>E</i> -2 4.652 <i>E</i> -2	(10.40)
B	$\begin{array}{c} 7.301 \ E-2 \\ -5.181 \ E-2 \\ 0.000 \ E+0 \\ 0.000 \ E+0 \\ 0.000 \ E+0 \\ 0.000 \ E+0 \end{array}$	2.071E+0 0.000E+0 0.000E+0 0.000E+0 0.000E+0	$\begin{array}{c} 0.000E\!+\!0\\ 3.275E\!-\!5\\ 6.777E\!-\!4\\ -\!2.207E\!-\!3\\ 8.505E\!-\!5\end{array}$	0.000 <i>E</i> +0 6.777 <i>E</i> -4 1.559 <i>E</i> -2 -4.735 <i>E</i> -2 -4.404 <i>E</i> -3	$\begin{array}{c} 0.000 E+0 \\ -2.207 E-3 \\ -4.735 E-2 \\ 1.894 E-1 \\ -5.942 E-3 \end{array}$	$\begin{array}{c} 0.000 E + 0 \\ 8.505 E - 5 \\ -4.404 E - 3 \\ -5.942 E - 3 \\ 8.093 E - 1 \end{array}$	0.000 <i>E</i> +0 2.089 <i>E</i> -3 5.333 <i>E</i> -2 7.509 <i>E</i> -2 6.693 <i>E</i> -3	0.000 E+0 -6.659 E-4 3.448 E-2 4.652 E-2 4.327 E-3	(10.40)
B	$\begin{array}{c} 7.301 E-2 \\ -5.181 E-2 \\ 0.000 E+0 \\ 0.000 E+0 \\ 0.000 E+0 \end{array}$	2.071E+0 0.000E+0 0.000E+0 0.000E+0 0.000E+0	0.000 <i>E</i> +0 3.275 <i>E</i> -5 6.777 <i>E</i> -4 -2.207 <i>E</i> -3	0.000 <i>E</i> +0 6.777 <i>E</i> -4 1.559 <i>E</i> -2 -4.735 <i>E</i> -2	$\begin{array}{c} 0.000E\!+\!0\\ -2.207E\!-\!3\\ -4.735E\!-\!2\\ 1.894E\!-\!1 \end{array}$	$\begin{array}{c} 0.000  E + 0 \\ 8.505  E - 5 \\ -4.404  E - 3 \\ -5.942  E - 3 \end{array}$	0.000 <i>E</i> +0 2.089 <i>E</i> -3 5.333 <i>E</i> -2 7.509 <i>E</i> -2	0.000 <i>E</i> +0 -6.659 <i>E</i> -4 3.448 <i>E</i> -2 4.652 <i>E</i> -2	(10.40)

$$\boldsymbol{f_{os}} = \begin{bmatrix} 0 & 39386y_p & 0 & 0 & 0 & 0 & 0 \end{bmatrix}^T$$
(10.41)

with

$$y_p = \begin{cases} y, \quad y < 0\\ 0, \quad y \ge 0 \end{cases}$$
(10.42)

Furthermore, the external load force is

$$\boldsymbol{f_{ex}} = \begin{bmatrix} 0 & 39.38\cos(2\pi f_e t) & 0 & 0 & 0 & 0 & 0 \end{bmatrix}^T$$
(10.43)

and the control force is

The column with degrees of freedom can be written as

$$\boldsymbol{q} = \begin{bmatrix} y_{S} & y & \xi_{1} & \xi_{2} & \xi_{3} & \xi_{4} & \xi_{5} & \xi_{6} \end{bmatrix}^{T}$$
(10.45)

with  $y_s$  the displacement at point S and y the displacement at point O (figure 10.1).  $\xi_1 - \xi_6$  are the virtual degrees of freedom generated by the component mode synthesis method.

# References

- Ascher, U.M., Mattheij, R.M.M., and Russell, R.D., 1988, "Numerical Solution of Boundary Value Problems for Ordinary Differential Equations," Prentice-Hall, Inc..

### 182 CHAPTER 10. VIBRATION CONTROL OF PERIODICALLY EXCITED NONLINEAR...

- Craig Jr., R.R., 1985, "A Review of Time-Domain and Frequency-Domain Component Mode Synthesis Methods," *Combined Experimental/Analytical Modeling of Dynamic Structural Systems Using Substructure Synthesis*, D.R. Martinez and A.K. Miller, ed., ASME Applied Mechanics AMD-67, New York, pp. 1-31.
- DIANA, 1995, *DIANA User's Manual 6.0 ed.*, TNO Building and Construction Research, Delft, The Netherlands.
- Fey, R.H.B., 1992, "Steady-State Behaviour of Reduced Dynamic Systems with Local Nonlinearities," *PhD thesis*, Department of Mechanical Engineering, Eindhoven University of Technology, Eindhoven, The Netherlands.
- Fey, R.H.B., Van Campen, D.H., and De Kraker, A., April 1996, "Long Term Structural Dynamics of Mechanical Systems with Local Nonlinearities," ASME *Journal of Vibration and Acoustics*, (in press).
- Fey, R.H.B., Van de Vorst, E.L.B., Van Campen, D.H., De Kraker, A., Meijer, G.J., and Assinck, F.H., 1994, "Chaos and Bifurcations in a Multi-DOF Beam System with Nonlinear Support," Nonlinearity and Chaos in Engineering Dynamics, Proceedings IUTAM Symposium, London, 19-23 July 1993, J.M.T. Thompson and S.R. Bishop, ed., John Wiley & Sons, pp. 125-139.
- Kalman, R.E., 1960, "A New Approach to Linear Filtering and Prediction Problems," *Journal of Basic Engineering*, Vol. 82D, pp. 35–45.
- Kalman, R.E., and Bucy, R.S., 1961, "New Results in Linear Filtering and Prediction Theory," *Journal of Basic Engineering*, Vol. 83D, pp. 95-108.
- Ott, E., Grebogi, C., and Yorke, Y.A., 1990, "Controlling Chaos," *Physical Review Letters*, Vol 64, pp. 1196–1199.
- Slotine, J.-J.E., and Li, W., 1991, "Applied Nonlinear Control," Prentice-Hall Inc..

# 11

# STABILIZATION OF PERIODIC SOLUTIONS OF NONLINEAR MECHANICAL SYSTEMS: CONTROLLABILITY AND STABILITY.<sup>‡</sup>

MMMM

In nonlinear mechanical systems, which show stable (sub)harmonic, quasi-periodic and/or chaotic responses, together with coexisting (unstable) harmonic solutions, a large reduction of maximum subharmonic, quasi-periodic or chaotic displacement might be established if the coexisting unstable harmonic solution could be made stable. The control effort to obtain this goal can be very small. In this paper, a method is presented for determining the controllability of periodically excited nonlinear mechanical systems. This method determines if an unstable periodic solution can be stabilized using control. Furthermore, a method for calculating the local stability of an earlier developed control method, i.e. sliding computed torque control, for the above mentioned goal is presented. Simulation results are presented for a periodically excited beam system supported by a one-sided spring to demonstrate the capabilities of the above presented methods.

# 11.1 Introduction.

The long term behaviour of a nonlinear dynamic system under periodic excitation can be periodic, quasi-periodic or chaotic. In case of periodic behaviour the period time of the system response may be equal to the excitation period (harmonic solution) or n times the excitation period (1/n subharmonic solution). Subharmonic behaviour of the system may lead to the occurrence of extra resonance peaks. If quasi-periodic or chaotic behaviour occurs the response will have frequencies that are generated by the system itself. Also in case of stable quasi-periodic or chaotic solutions the maximum response of the system will increase in general compared to the harmonic response. Since large amplitudes usually give rise to large strains and stresses, damage to the system or structure is likely to occur. Thus resonance peaks, quasi-periodic and chaotic behaviour should be avoided under all operating circumstances. This can be achieved

<sup>&</sup>lt;sup>‡</sup>Van de Vorst, E.L.B., Kant, A.R., Van de Molengraft, M.J.G, Kok, J.J., and Van Campen, D.H., 1995, "Stabilization of Periodic Solutions of Nonlinear Mechanical Systems: Controllability and Stability," *Journal of Vibration and Control*, submitted

by using control.

In principle, active control can force the output of a system to any desired response if we are willing to supply the necessary control effort. From a practical point of view it is interesting if the control effort can be relatively low, while still meeting the control objectives. Often a low-amplitude harmonic solution coexists if subharmonic, quasiperiodic or chaotic motions occur. This is a natural solution of the system although it may be unstable. Because the harmonic solution is a natural solution of the system, the control effort to keep the system on the harmonic solution is expected to be very small (theoretically even zero). Then, the control effort which is needed to bring the system in this low-amplitude harmonic solution may be large initially, but probably only so during a short period.

In Van de Vorst et al. (1995) a control method is developed for controlling multidegree-of-freedom (multi-DOF) mechanical systems to unstable periodic solutions by putting a single control force somewhere on the system. The control method used in that paper is a sliding computed torque control method in combination with a first order low pass filter. This filter improves convergence of the tracking errors and the control force to zero.

In this paper a method is presented to determine whether an unstable periodic solution of a nonlinear mechanical system can be stabilized. Further, the high frequencies in the control force, which occur if no filter is used, are investigated. A method is presented for determining the local stability of the sliding computed torque controller (including the first order low pass filter). Some simulations are carried out to demonstrate the capabilities of the presented methods using a periodically excited beam system supported by a one-sided spring.

# 11.2 Controllability: Can an unstable periodic solution be stabilized?

### 11.2.1 Theory.

Before applying a control method, it is important to determine whether the unstable periodic solution can be stabilized. Most methods for determining the controllability of a system are developed for linear systems. However, we are dealing with nonlinear systems. The nonlinear system can easily be linearized with respect to the desired trajectory. Using the linearized (time-varying) system, the results on controllability for linear systems will be valid only locally, i.e. near the desired trajectory.

The equations of motion of an n-DOF nonlinear dynamic mechanical system with an assumed constant mass matrix can be written as

$$\boldsymbol{M}\boldsymbol{\ddot{q}} + \boldsymbol{f_{nl}}(\boldsymbol{\dot{q}}, \boldsymbol{q}, t) = \boldsymbol{f_{ex}}(t) + \boldsymbol{h}\boldsymbol{u}$$
(11.1)

with q the system degrees of freedom, M is the constant mass matrix,  $f_{nl}$  represents the nonlinear internal forces,  $f_{ex}$  are the time-dependent external forces, u is the control force acting on DOF k and

$$\boldsymbol{h} = \begin{bmatrix} 0_1 & \dots & 0_{k-1} & 1 & 0_{k+1} & \dots & 0_n \end{bmatrix}^T.$$
(11.2)

Equation (11.1) can be rewritten in state space form as

$$\dot{x} = f_{nl}^{*}(x,t) + f_{ex}^{*}(t) + bu$$
 (11.3)

where

$$\boldsymbol{x} = \begin{bmatrix} \boldsymbol{q} \\ \boldsymbol{\dot{q}} \end{bmatrix}, \quad \boldsymbol{f}_{nl}^* = \begin{bmatrix} \boldsymbol{\dot{q}} \\ -M^{-1}\boldsymbol{f}_{nl} \end{bmatrix}, \quad \boldsymbol{f}_{ex}^* = \begin{bmatrix} \boldsymbol{0} \\ M^{-1}\boldsymbol{f}_{ex} \end{bmatrix}, \quad \boldsymbol{b} = \begin{bmatrix} \boldsymbol{0} \\ M^{-1}\boldsymbol{h} \end{bmatrix}.$$
(11.4)

Linearizing (11.3) about the desired trajectory  $q_d$  yields

$$\delta \dot{\boldsymbol{x}} = \boldsymbol{A}(t)\delta \boldsymbol{x} + \boldsymbol{b}\boldsymbol{u} \tag{11.5}$$

where

$$\delta \boldsymbol{x} = \begin{bmatrix} \delta \boldsymbol{q} \\ \delta \dot{\boldsymbol{q}} \end{bmatrix}, \quad \boldsymbol{A} = \begin{bmatrix} \boldsymbol{0} & \boldsymbol{I} \\ -\boldsymbol{M}^{-1} \frac{\partial \boldsymbol{f}_{nl}}{\partial \boldsymbol{q}} \Big|_{\dot{\boldsymbol{q}}_{d}, \boldsymbol{q}_{d}, t} & -\boldsymbol{M}^{-1} \frac{\partial \boldsymbol{f}_{nl}}{\partial \dot{\boldsymbol{q}}} \Big|_{\dot{\boldsymbol{q}}_{d}, \boldsymbol{q}_{d}, t} \end{bmatrix}. \quad (11.6)$$

The solution of equation (11.5) can be written as

$$\boldsymbol{\delta x}(t) = \boldsymbol{\Phi}(t, t_0) \boldsymbol{\delta x}_0 + \int_{t_0}^t \boldsymbol{\Phi}(t, \tau) \boldsymbol{\delta u}(\tau) d\tau$$
(11.7)

with  $\delta x_0 = \delta x(t_0)$  and  $\Phi(t, t_0)$  the so-called fundamental matrix (cf. appendix 11.A). Because

$$\Phi(t_0, t_0) = I, \quad \Phi(t_2, t_0) = \Phi(t_2, t_1) \Phi(t_1, t_0), \quad \Phi^{-1}(t, t_0) = \Phi(t_0, t)$$
(11.8)

equation (11.7) can be rewritten as

$$\boldsymbol{\delta x_0} - \boldsymbol{\Phi}(t_0, t) \boldsymbol{\delta x}(t) = -\int_{t_0}^t \boldsymbol{\Phi}(t_0, \tau) \boldsymbol{\delta u}(\tau) d\tau$$
(11.9)

The standard practice for determining the controllability of a linear time-varying system is using a controllability gramian (Brockett, 1970)

$$\boldsymbol{W_{c}}(t_{0},t_{1}) = \int_{t_{0}}^{t_{1}} \boldsymbol{\Phi}(t_{0},\tau) \boldsymbol{b} \boldsymbol{b}^{T} \boldsymbol{\Phi}^{T}(t_{0},\tau) d\tau$$
(11.10)

When the control force u is chosen to be

$$u(t) = -\boldsymbol{b}^T \boldsymbol{\Phi}^T(t_0, t) \boldsymbol{\zeta}$$
(11.11)

with  $\boldsymbol{\zeta} \in \mathbb{R}^n$ , then the state  $\delta \boldsymbol{x}_1$  on  $t_1$  will be the solution of

$$\boldsymbol{\delta x_0} - \boldsymbol{\Phi}(t_0, t_1) \boldsymbol{\delta x_1} = \int_{t_0}^{t_1} \boldsymbol{\Phi}(t_0, \tau) \boldsymbol{\delta b}^T \boldsymbol{\Phi}^T(t_0, \tau) d\tau \boldsymbol{\zeta} = \boldsymbol{W_c}(t_0, t_1) \boldsymbol{\zeta} \quad (11.12)$$

The system is *completely* controllable on time  $t_1$  starting from  $t_0$ , i.e. every  $\delta x_1$  can be established using the control forces on  $t_0-t_1$  for arbitrary  $\delta x_0$ , if and only if the gramian  $W_c(t_0, t_1)$  is regular. After all, if  $W_c(t_0, t_1)$  is singular, at least one vector  $\gamma$  exists for which  $W_c(t_0, t_1)\gamma = 0$  and  $\gamma^T(\delta x_0 - \Phi(t_0, t_1)\delta x_1) \neq 0$ . In that case holds

$$\gamma^{T} \boldsymbol{W}_{c}(t_{0}, t_{1}) \gamma = \int_{t_{0}}^{t_{1}} \gamma^{T} \boldsymbol{\Phi}(t_{0}, \tau) \boldsymbol{b} \boldsymbol{b}^{T} \boldsymbol{\Phi}^{T}(t_{0}, \tau) \gamma d\tau = \int_{t_{0}}^{t_{1}} || \boldsymbol{b}^{T} \boldsymbol{\Phi}^{T}(t_{0}, \tau) \gamma ||^{2} d\tau = 0$$
(11.13)

which means that  $\boldsymbol{b}^T \boldsymbol{\Phi}^T(t_0, t) \boldsymbol{\gamma} = \boldsymbol{0}$ . Premultiplying equation (11.9) by  $\boldsymbol{\gamma}^T$  yields

$$\boldsymbol{\gamma}^{T}(\boldsymbol{\delta x_{0}} - \boldsymbol{\Phi}(t_{0}, t_{1})\boldsymbol{\delta x_{1}}) = -\int_{t_{0}}^{t_{1}} \boldsymbol{\gamma}^{T} \boldsymbol{\Phi}(t_{0}, \tau) \boldsymbol{b}\boldsymbol{u}(\tau) d\tau \neq 0$$
(11.14)

Because  $\boldsymbol{b}^T \boldsymbol{\Phi}^T(t_0, t) \boldsymbol{\gamma} = \boldsymbol{0}$  there is no control force  $\boldsymbol{u}(t)$  which can realize  $(\boldsymbol{\delta}\boldsymbol{x}_0 - \boldsymbol{\Phi}(t_0, t_1)\boldsymbol{\delta}\boldsymbol{x}_1)$  so the system is not completely controllable.

For stabilizing an unstable periodic solution, the system does not have to be *completely* controllable. The stability of a periodic solution can be determined using Floquet theory (see Appendix 11.A). Applying Floquet theory results in stable and unstable Floquet multipliers. The corresponding eigenvectors determine the stable and unstable directions in which the periodic solution attracts and repels trajectories in its near neighbourhood. These stable and unstable directions, also called the stable and unstable manifolds, are time-varying and periodic.

A state  $\delta x_0$  in the direct neighbourhood of an unstable periodic solution can be written as a linear combination of the stable and unstable eigenvectors

$$\delta \boldsymbol{x}_0 = \boldsymbol{\Psi}_s \boldsymbol{\alpha} + \boldsymbol{\Psi}_u \boldsymbol{\beta} \tag{11.15}$$

where  $\Psi_s(2n \times n_s)$  are the stable eigenvectors,  $\Psi_u(2n \times n_u)$  are the unstable eigenvectors,  $\alpha \in \mathbb{R}^{n_s}$  and  $\beta \in \mathbb{R}^{n_u}$   $(n_s + n_u = 2n)$ . Using this initial state, the state of the uncontrolled system will be

$$\delta \boldsymbol{x}(t) = \boldsymbol{\Phi}(t, t_0) \boldsymbol{\Psi}_{\boldsymbol{s}} \boldsymbol{\alpha} + \boldsymbol{\Phi}(t, t_0) \boldsymbol{\Psi}_{\boldsymbol{u}} \boldsymbol{\beta}$$
(11.16)

The first term on the right-hand side of equation (11.16) will approach asymptotically to zero if time proceeds, whereas the second term on the right-hand side will go to infinity. Because  $\delta \boldsymbol{x}(t)$  is a variation with respect to the desired trajectory  $\boldsymbol{x}_d(t)$  (the equations of motion were linearized about the desired trajectory),  $\delta \boldsymbol{x}(t) = 0$  is the desired trajectory for the linearized equations of motion. This means that if it is possible to control the system in such way that on time  $t_1$  the state will be

$$\boldsymbol{\delta x}(t_1) = \boldsymbol{\Phi}(t_1, t_0) \boldsymbol{\Psi_s} \boldsymbol{\theta} \tag{11.17}$$

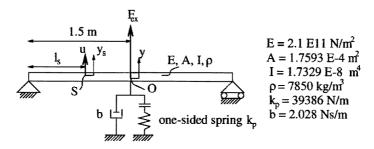


Figure 11.1 Beam system.

with  $\theta \in \mathbb{R}^{n_s}$ ,  $\delta x(t)$  will automatically tend to zero without any further control effort. In that case it is possible to stabilize the periodic solution.

Using equations (11.17), (11.15) and (11.11), (11.12) results in

$$\begin{aligned} \boldsymbol{W}_{\boldsymbol{c}}(t_0,t_1)\boldsymbol{\zeta} &= \boldsymbol{\delta}\boldsymbol{x}_0 - \boldsymbol{\Phi}(t_0,t_1)\boldsymbol{\delta}\boldsymbol{x}_1 \\ &= \boldsymbol{\Psi}_{\boldsymbol{s}}\boldsymbol{\alpha} + \boldsymbol{\Psi}_{\boldsymbol{u}}\boldsymbol{\beta} - \boldsymbol{\Phi}(t_0,t_1)\boldsymbol{\Phi}(t_1,t_0)\boldsymbol{\Psi}_{\boldsymbol{s}}\boldsymbol{\theta} \\ &= \boldsymbol{\Psi}_{\boldsymbol{s}}(\boldsymbol{\alpha}-\boldsymbol{\theta}) + \boldsymbol{\Psi}_{\boldsymbol{u}}\boldsymbol{\beta} \end{aligned}$$
(11.18)

and this can be rewritten as

$$-\Psi_s(\alpha - \theta) + W_c(t_0, t_1)\zeta = \Psi_u\beta$$
(11.19)

If a solution of equation (11.19) exists for arbitrary  $\alpha$  and  $\beta$ , then the periodic solution can be stabilized using the control force. Because

$$\operatorname{rank}\left[ \begin{array}{cc} \Psi_{s} & \Psi_{u} \end{array} \right] = 2n \tag{11.20}$$

it is easy to see that this condition is satisfied if the following condition holds

$$\operatorname{rank}\left[ \Psi_{s} \quad W_{c}(t_{0}, t_{1}) \right] = 2n \tag{11.21}$$

### 11.2.2 Simulations.

In this section some simulation results are presented for a two-dimensional pinnedpinned beam shown in figure 11.1. The beam is excited at the point of symmetry O by a periodic force  $F_{ex} = 39.38cos(2\pi f_e t)$  ( $f_e \leq 50$  Hz). We assume small Rayleigh damping (damping matrix  $C = \chi K$ , with K the stiffness matrix of the linear beam and  $\chi = 10^{-6}$  s). The beam is supported in its point of symmetry O by a one-sided spring and a linear damper and is controlled by a single control force u in point S (figure 11.1).

The beam is modelled using the finite element method and the number of DOF's of the linear part of the model (the beam) is reduced using a component mode synthesis method based on residual flexibility modes and free-interface eigenmodes up to a cutoff frequency of 400 Hz (Craig, 1985). Because nonlinear systems can generate higher frequencies than their excitation frequency, the cut-off frequency has been chosen higher

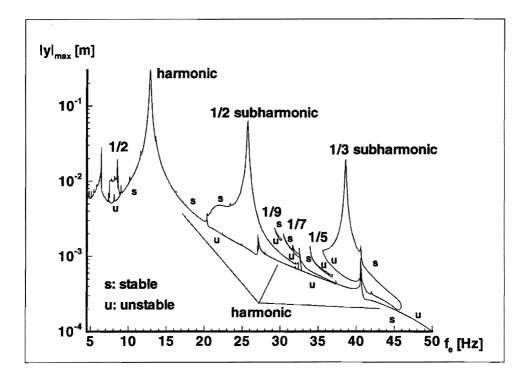


Figure 11.2 Maximum displacements of periodic solutions of point O of beam model without control.

than the maximum excitation frequency. The beam model is reduced from 100 to 8 DOF's (2 residual flexibility modes for the DOF's in points O and S, 6 free-interface eigenmodes with eigenfrequencies of 8.96 Hz, 35.83 Hz, 80.60 Hz, 143.2 Hz, 223.7 Hz, 321.9 Hz). Subsequently the reduced linear system is coupled with the nonlinear part, i.e. the one-sided spring, and the linear damper.

Periodic solutions of the uncontrolled beam system are calculated for varying excitation frequency by solving two-point boundary value problems using the finite difference method in combination with a path-following method (Fey et al., 1996). The maximum displacements  $|y|_{max}$  of O occurring in the periodic solutions are shown in figure 11.2 for varying excitation frequency  $f_e$ . This figure shows in addition to the first harmonic peak also stable 1/2, 1/3, 1/5, 1/7 and 1/9 subharmonic peaks. The maximum displacements of the subharmonics are much larger than the maximum displacements of the coexisting harmonic solution, which is unstable below the stable branch with 1/2 subharmonics. Also quasi-periodic and chaotic behaviour (not visible in figure 11.2) is found in the frequency range  $f_e = 47-49$  Hz. Figure 11.2 was calculated using a development release of the finite element package DIANA (1995).

The rank of the left-hand side of equation (11.21) has to be calculated to determine if the unstable harmonic solutions in the frequency range  $f_e = 20-50$  Hz can be stabilized.

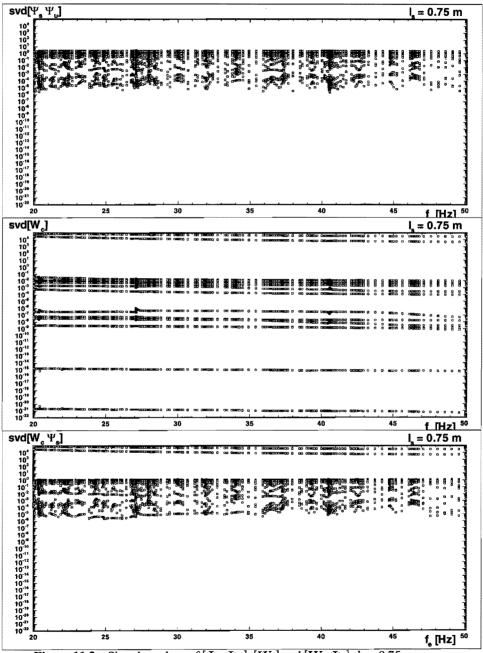


Figure 11.3 Singular values of  $[\Psi_s \Psi_u]$ ,  $[W_c]$  and  $[W_c \Psi_s]$ ;  $l_s = 0.75$  m.

For determining the rank of a matrix, the singular values of this matrix are calculated and the number of nonzero singular values yields the rank of the matrix. In practice, it is difficult to distinguish between singular values which are really zero and singular values which are not zero. Because the monodromy matrix, partitioned according to the left-hand side of (equation (11.20)), has rank 2n, the singular values of equation (11.20) can be used to assess the singular values of the controllability gramian  $W_c$ .

For calculating the singular values of the matrix whose columns are the eigenvectors of the monodromy matrix, the singular values are calculated of a matrix with columns consisting of the real and imaginary parts of the complex conjugate eigenvectors. All columns of this matrix are normalized at length one. Analysing the singular values of the controllability gramian  $W_c(t_0, t_1)$  showed that the singular values remain constant if the integration time  $t_1 - t_0$  is more than one period  $T_p$ . Because of this in the next results the controllability gramian  $W_c$  is calculated by integration of equation (11.10) over one period  $T_p$  so  $W_c = W_c(0, T_p)$ .

Figure 11.3 shows the singular values of the above partitioned monodromy matrix  $\begin{bmatrix} \Psi_s & \Psi_u \end{bmatrix}$  as well as the singular values of the gramian  $\begin{bmatrix} W_c \end{bmatrix}$  and of  $\begin{bmatrix} W_c & \Psi_s \end{bmatrix}$  in the frequency range  $f_e = 20-50$  Hz of the beam system. The distance between the left-hand side of the beam and the control force is taken  $l_s = 0.75$  m (of course the singular values of  $\begin{bmatrix} \Psi_s & \Psi_u \end{bmatrix}$  are independent on the position of the control force).

The results in figure 11.3 indicate that the beam system (with a control force at  $l_s = 0.75 \text{ m}$ ) is not completely controllable because some singular values of the controllability gramian are very small. However, using the control force the unstable harmonic solutions can locally be stabilized since the singular values of  $\begin{bmatrix} W_c & \Psi_s \end{bmatrix}$  lie in the same range as the singular values of  $\begin{bmatrix} \Psi_s & \Psi_u \end{bmatrix}$ .

Figure 11.4 shows the singular values of  $\begin{bmatrix} W_c & \Psi_s \end{bmatrix}$  for varying position  $l_s$  of the control force. The figure shows that the harmonic solutions cannot be stabilized if the control force is very close ( $l_s = 0.01$  m) to the left-hand side of the beam. In that case some singular values are very small. Only in the frequency ranges 38–40 Hz and 41–47 Hz the smallest singular values are larger but in these frequency ranges the harmonic solution is stable without control. For the other positions of the control force, the harmonic solutions can be stabilized in the whole frequency range.

# 11.3 Sliding computed torque control: Stability analysis.

### 11.3.1 Filtering the control force.

In Van de Vorst et al. (1995) sliding computed torque control (Slotine and Li, 1991) in combination with a first order low pass filter is used. In this control method, one DOF is controlled to its desired trajectory assuming that, as a result, the other DOF's will go to their desired trajectory too.

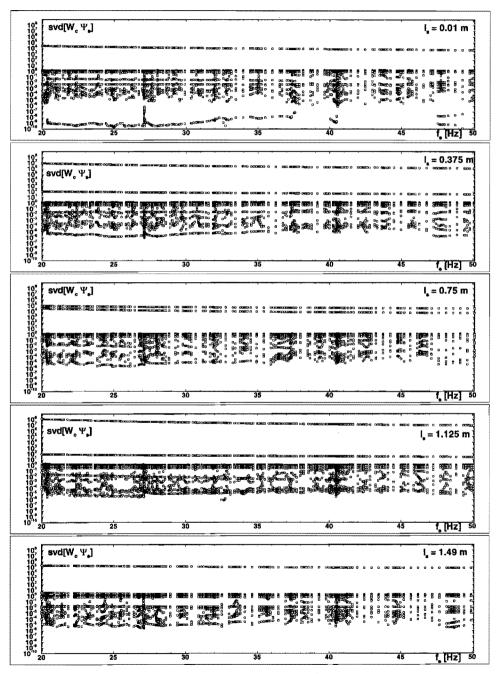
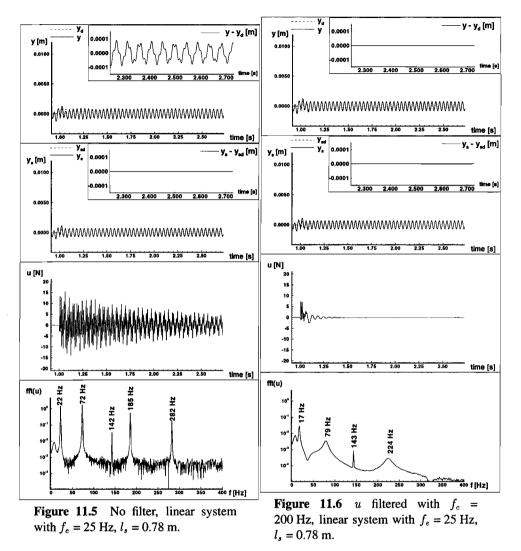


Figure 11.4 Singular values of  $[W_c \Psi_s]$  for varying  $l_s$ 



The control force u acting on DOF k can be calculated as follows

$$u_{k} = \left(\boldsymbol{h}^{T}\boldsymbol{M}^{-1}\boldsymbol{h}\right)^{-1} \left(\boldsymbol{h}^{T}\boldsymbol{M}^{-1}\boldsymbol{f}_{nl} - \boldsymbol{h}^{T}\boldsymbol{M}^{-1}\boldsymbol{f}_{ex} + \boldsymbol{h}^{T}\boldsymbol{\ddot{q}}_{d} - \lambda\boldsymbol{h}^{T}\boldsymbol{\dot{\epsilon}} - \eta sat(\boldsymbol{h}^{T}\boldsymbol{s}/\sigma)\right)$$
(11.22)

where

$$\mathbf{s} = \dot{\boldsymbol{\epsilon}} + \lambda \boldsymbol{\epsilon} \tag{11.23}$$

with  $\epsilon = q - q_d$  and

$$sat(\mathbf{h}^{T}\mathbf{s}/\sigma) = \begin{cases} -1, & \text{if } \mathbf{h}^{T}\mathbf{s} < -\sigma \\ \mathbf{h}^{T}\mathbf{s}/\sigma, & \text{if } |\mathbf{h}^{T}\mathbf{s}| \leq \sigma \\ 1, & \text{if } \mathbf{h}^{T}\mathbf{s} > \sigma \end{cases}$$
(11.24)

 $u_k$  is filtered by a first order low pass filter with bandwidth  $f_c$ :

$$\dot{u} = 2\pi f_c (u_k - u) \tag{11.25}$$

In Van de Vorst et al. (1995) it has been shown that if the beam system with onesided spring (section 11.2.2) is controlled without filtering, the control force shows high frequencies, yielding a slow convergence of the tracking errors. Figures 11.5 and 11.6 show the results of controlling the beam system *without* the one-sided spring for  $f_e =$ 25 Hz and  $l_s = 0.78$  m. The one-sided spring is taken out because in a linear system it is easier to detect the eigenfrequencies. The control parameters are taken  $\lambda = 100.0$ ,  $\eta =$ 25.0 and  $\sigma = 0.5$ . In figure 11.5 the control force is not filtered whereas in figure 11.6 the control force is filtered with a first order filter with bandwidth  $f_c = 200$  Hz.

At t = 1 s the beam is controlled to its steady-state solution (which is stable because the system is linear). Because at t = 1 s the beam is not in its steady-state, control effort is needed to bring it there. The figures show that in both cases the tracking errors of the displacement  $y_s$  of the beam at the control force converge quickly to zero. If the control force is not filtered, the tracking errors of the displacement y of the middle of the beam converge very slowly to zero and because of this high frequencies occur in the control force. The frequencies occurring in the control force correspond with the eigenfrequencies of the linear beam if it is supported at the position of the control force (the eigenfrequencies of the linear beam supported in  $y_s$ -direction at the control force are  $f_1 = 21.88$  Hz,  $f_2 = 72.39$  Hz,  $f_3 = 142.4$  Hz,  $f_4 = 185.1$  Hz,  $f_5 = 282.1$  Hz). Apparently one position of the beam is controlled so fast to its desired trajectory that the system starts vibrating in eigenmodes corresponding to the system supported at the control position. This can be avoided by correcting the control parameters in the way that the position at the control force is more slowly controlled to its desired trajectory. However, this will result in a slower convergence of all the tracking errors. Figure 11.6 shows that using a first order low pass filter yields a large improvement of the convergence of the tracking errors and control force. Except for the frequency at 17 Hz, the frequencies occurring in the control force are similar to the eigenfrequencies of the uncontrolled system.

#### 11.3.2 Stability analysis.

For determining the stability of the controlled system, the equations of motion are rewritten as

$$\dot{x}^* = f^*(x^*, t)$$
 (11.26)

where  $\boldsymbol{x^*} = \begin{bmatrix} \boldsymbol{q}^T & \dot{\boldsymbol{q}}^T & \boldsymbol{u} \end{bmatrix}^T$  and

$$\begin{aligned} \boldsymbol{f}^{*}(\boldsymbol{x}^{*},t) &= \\ \begin{bmatrix} \dot{\boldsymbol{q}} \\ -\boldsymbol{M}^{-1}\boldsymbol{f}_{nl} + \boldsymbol{M}^{-1}\boldsymbol{f}_{ex} + \boldsymbol{M}^{-1}\boldsymbol{h}\boldsymbol{u} \\ 2\pi\boldsymbol{f}_{c}\left\{ \left(\boldsymbol{h}^{T}\boldsymbol{M}^{-1}\boldsymbol{h}\right)^{-1}\boldsymbol{h}^{T}\left(\boldsymbol{M}^{-1}\boldsymbol{f}_{nl} - \boldsymbol{M}^{-1}\boldsymbol{f}_{ex} + \ddot{\boldsymbol{q}}_{d} - \lambda\dot{\boldsymbol{\epsilon}} - \eta \boldsymbol{sat}(\boldsymbol{s}/\sigma)\right) - \boldsymbol{u}_{j}^{(\text{full},27)} \end{aligned} \right]^{7} \end{aligned}$$

Linearizing equation (11.27) with respect to the desired trajectory  $\boldsymbol{x}_{\boldsymbol{d}}^{*}(t) = \begin{bmatrix} \boldsymbol{q}_{\boldsymbol{d}}^{T} & \boldsymbol{\dot{q}}_{\boldsymbol{d}}^{T} & 0 \end{bmatrix}^{T}$  yields

$$\boldsymbol{\delta} \dot{\boldsymbol{x}}^* = \boldsymbol{A}^*(t) \boldsymbol{\delta} \boldsymbol{x}^* \tag{11.28}$$

where

$$\delta \boldsymbol{x}^{*} = \begin{bmatrix} \delta \boldsymbol{q} \\ \delta \dot{\boldsymbol{q}} \\ \delta \boldsymbol{u} \end{bmatrix}, \quad \boldsymbol{A}^{*} = \begin{bmatrix} 0 & \boldsymbol{I} & \boldsymbol{0} \\ -M^{-1} \frac{\partial \boldsymbol{f}_{nl}}{\partial \boldsymbol{q}} \Big|_{\boldsymbol{\dot{q}}_{d}, \boldsymbol{q}_{d}, t} & -M^{-1} \frac{\partial \boldsymbol{f}_{nl}}{\partial \boldsymbol{\dot{q}}} \Big|_{\boldsymbol{\dot{q}}_{d}, \boldsymbol{q}_{d}, t} & M^{-1}\boldsymbol{h} \\ \boldsymbol{u}_{\boldsymbol{q}}^{T} & \boldsymbol{u}_{\boldsymbol{\dot{q}}}^{T} & -2\pi f_{c}^{(1)} \end{bmatrix}.29$$

In (11.29)  $u_q$  and  $u_{\dot{q}}$  can be calculated as

$$\boldsymbol{u}_{\boldsymbol{q}}^{T} = 2\pi f_{c} \left( \boldsymbol{h}^{T} \boldsymbol{M}^{-1} \boldsymbol{h} \right)^{-1} \left\{ \boldsymbol{h}^{T} \boldsymbol{M}^{-1} \left. \frac{\partial \boldsymbol{f}_{\boldsymbol{n}\boldsymbol{l}}}{\partial \boldsymbol{q}} \right|_{\boldsymbol{\dot{q}}_{\boldsymbol{d}}, \boldsymbol{q}_{\boldsymbol{d}}, \boldsymbol{t}} - \boldsymbol{h}^{T} \left( \frac{\eta \lambda}{\sigma} \right) \right\}$$
(11.30)

$$\boldsymbol{u}_{\dot{\boldsymbol{q}}}^{T} = 2\pi f_{c} \left( \boldsymbol{h}^{T} \boldsymbol{M}^{-1} \boldsymbol{h} \right)^{-1} \left\{ \boldsymbol{h}^{T} \boldsymbol{M}^{-1} \left. \frac{\partial \boldsymbol{f}_{\boldsymbol{n}l}}{\partial \dot{\boldsymbol{q}}} \right|_{\dot{\boldsymbol{q}}_{\boldsymbol{d}}, \boldsymbol{q}_{\boldsymbol{d}}, t} - \boldsymbol{h}^{T} \left( \frac{\eta}{\sigma} + \lambda \right) \right\} \quad (11.31)$$

Notice that  $q_d(t)$  as well as the matrix  $A^*(t)$  is periodic:  $A^*(t) = A^*(t + T_p)$ . Using Floquet-theory (see Appendix 11.A) the local stability of the periodic solution  $q_d(t)$ can now be determined. Applying Floquet theory results in Floquet multipliers which can be recalculated as characteristic exponents  $\rho$ . The real parts of these characteristic exponents determine the local stability of the periodic solution: if all real parts are smaller than zero the periodic solution (and hence the controlled system) is locally stable near the desired trajectory. If one or more real parts are larger than zero, the controlled system is unstable near the desired trajectory. Notice that this does not necessarily mean that the trajectories of the system become unbounded since the system is nonlinear and the characteristic exponents are only meaningful if the system is in the neighbourhood of the desired trajectory.

### 11.3.3 Simulations

In this section some simulation results are presented for the nonlinear beam system of section 11.2.2. The control parameters are taken  $\lambda = 100.0$ ,  $\eta = 25.0$  and  $\sigma = 0.5$ . The maximum absolute control force is taken  $|u|_{max} = 20$  N.

Figure 11.7 shows the response of the system if the excitation frequency is linearly increased from 20 Hz to 50 Hz in 26.3 sec (see also Van de Vorst et al. (1995)). If the system is not controlled (figure 11.7a), the maximum displacements increase because of the subharmonic resonance peaks. Using small control effort, the maximum displacements are reduced (figures 11.7b–c). The position  $l_s$  of the control force is taken 0.78 m and the filter bandwidth is  $f_c = 200$  Hz.

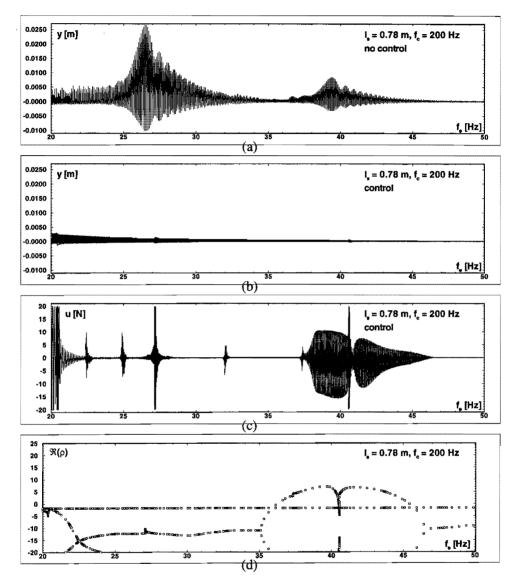


Figure 11.7 Frequency sweep from 20 to 50 Hz in 26.3 s: (a) y of uncontrolled system, (b) y of controlled system, (c) control force u, (d) real parts of characteristic exponents of controlled system

At the beginning the control force is high because the system not being in its steadystate. In small frequency ranges near 22.5 Hz, 25 Hz, 27 Hz, 32 Hz and 37 Hz, the control force increases for a short while after which it converges to small values again. In these frequency ranges superharmonic resonances occur due to the high-frequency symmetric eigenmodes of the system (see also figure 11.2). In the frequency range 37-46 Hz the control effort is high over a larger frequency interval. In figure 11.7d the real parts of the characteristic exponents  $\rho$  of the controlled system are shown resulting from Floquet theory. This figure shows that in the frequency range 35.5–45.5 Hz the controlled system is locally unstable (one of the real parts of  $\rho$  is larger than zero in that frequency range). Investigation of the Floquet multipliers of the controlled system learns that this unstable interval is marked by two flip bifurcations. This indicates that period doubling occurs in this frequency range: the controlled system has a 1/2 subharmonic solution as its steady-state for which of course the control force is not zero. Figure 11.7b indicates that the response corresponding to the maximum amplitude of this 1/2 subharmonic solution is almost equal to the desired trajectory (the harmonic solution of the uncontrolled system) because the maximum response of the system does not increase much in the unstable frequency range.

Because it takes some time before the control force increases if the controlled system is unstable and the excitation frequency is linearly increased during the control sweep, the control force does not increase immediately in the unstable frequency range. It also takes some time before the control force converges to zero if the frequency is increased to the stable frequency range again. From figure 11.7 it can be concluded that, although the stability analysis is only locally valid, here reliable results are obtained for the global system (if the system moves into the stable frequency range, the control force converges to zero again).

Figure 11.8 shows the real parts of the characteristic exponents of the controlled system resulting from Floquet theory for varying excitation frequency and bandwidth of the filter. The position  $l_s$  of the control force is taken 0.78 m again. The harmonic solutions of the uncontrolled system are unstable in the frequency ranges 20.2–37.5 Hz and 47.5–49.5 Hz.

In figure 11.7 it was already shown that the controller is not stable over the whole frequency range. Figure 11.8 shows that using the filter the unstable part can be moved and decreased but the filter cannot make the controlled system stable over the entire frequency range. Also by changing the control parameters it was not possible to get better results. Notice that for some filter bandwidths stable harmonic solutions of the uncontrolled system become unstable if the system is controlled. This is remarkable because if the controlled system is vibrating in the harmonic solution, the control force is zero (in theory). Apparently, little disturbances on the system result in a nonzero control force which makes the harmonic solution unstable.

The largest real part of the characteristic exponents gives an indication about how quickly the controlled system converges to its desired trajectory. The more negative this real part, the faster the system converges. Figure 11.8 shows that the optimal filter bandwidth for the system with  $l_s = 0.78$  m is  $f_c = 600$  Hz. For  $f_c = 600$  Hz, the largest real part of the characteristic exponents takes the lowest value except of course for the unstable parts.

Figure 11.9 shows the real part of the characteristic exponents for varying excitation frequency and varying position  $l_s$  of the control force. The control parameters are taken the same as in figure 11.8. Further, the filter bandwidth is taken  $f_c = 200$  Hz. The figure shows that if the control force is moved to the middle of the beam, the frequency range where the controlled system is unstable decreases and disappears for  $l_s = 1.125$  m and

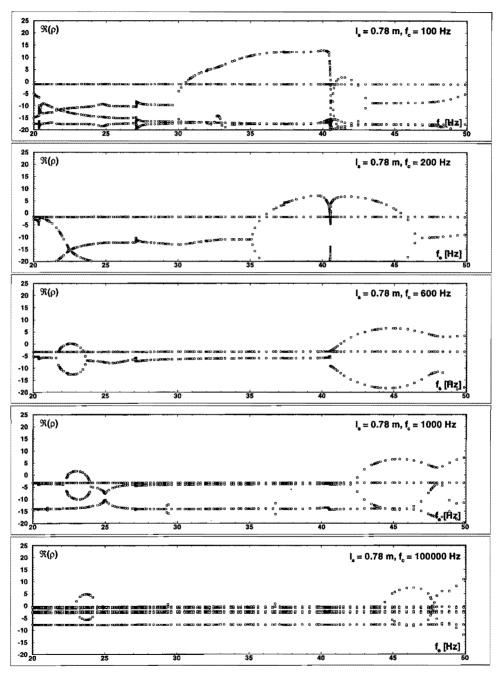


Figure 11.8 Real parts of characteristic exponents of controlled system for varying filter bandwidth  $f_c$ ;  $l_s = 0.78$  m.

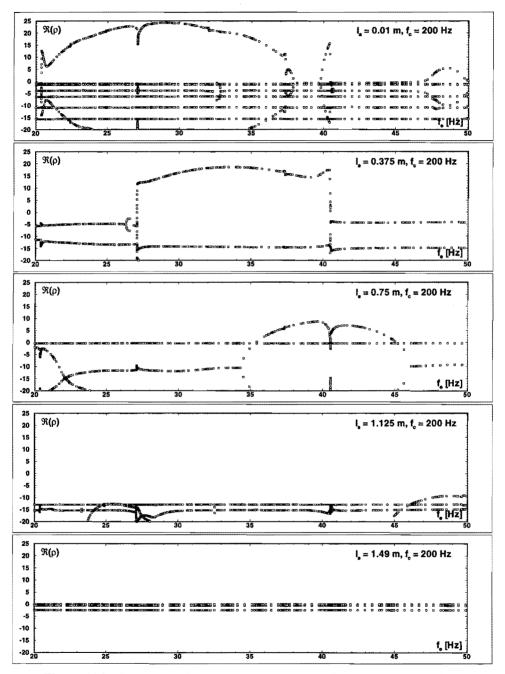


Figure 11.9 Real parts of characteristic exponents of controlled system for varying control position  $l_s$ ;  $f_c = 200$  Hz.

1.49 m. For  $l_s = 0.01$  m the unstable frequency intervals of the controlled system are the same as the unstable frequency intervals of the uncontrolled system. This means that for  $l_s = 0.01$  m the harmonic solutions cannot be stabilized and this was already concluded from the controllability analysis.

By looking at the largest real parts of the characteristic exponents, it could be concluded that  $l_s = 1.125$  m seems to be the optimal position for the control force. This is, however, not necessarily true. Comparing the case  $l_s = 0.75$  m to  $l_s = 0.78$  m in figure 11.8 shows that for  $l_s = 0.75$  m the largest characteristic exponent is higher and lies near zero, although the difference between the two positions is small. The eigenmode corresponding to this characteristic exponent is asymmetric and has a node at  $l_s = 0.75$ m. This means that this eigenmode cannot be controlled by the control force. However, because this eigenmode has also a node at the middle of the beam, the eigenmode will not be activated during the control. This means that this eigenmode does not have to be controlled and does not have a negative effect on the convergence of the tracking errors. Even if the eigenmode has a node at the position of the control force and a node at the position of the nonlinearity. In that case, the control force will be very small while the tracking errors can be relatively large, slowly converging to zero.

If the control force is near the middle of the beam, i.e.  $l_s = 1.49$  m, all asymmetric eigenmodes will be uncontrollable. However, similar to  $l_s = 0.75$  m, these asymmetric eigenmodes are not activated during the control. From this, it can be concluded that the middle of the beam is the optimal position for controlling the beam to the unstable harmonic solution.

Notice that if the control force is positioned at a node of an eigenmode, not always good results (control force converging to zero) will be obtained. If the eigenmode, that has a node at the position of the control force, has no node at the middle of the beam, this eigenmode will be activated by the one-sided spring. In that case the beam system will not track in the desired trajectory  $y_d$  at the middle of the beam. Because the one-sided spring is nonlinear, also other eigenmodes (which have no node at the position of the control force) will be activated and, as a result, the control force will not converge to zero as long as the eigenmode has not damped out.

In figures 11.10 and 11.11 this is demonstrated by putting the control force on a node of the third symmetric eigenmode ( $f_3 = 80.60$  Hz,  $l_s = 1.0$  m). The linear damper in the middle of the beam is removed in these simulations, because this damper damps the symmetric eigenmodes too quickly. Figure 11.10 shows that the tracking errors and control force indeed do not quickly converge to zero. Figure 11.11 shows results for the system without one-sided spring. Now, although the tracking error at the middle of the beam is not zero, the control force still converges to zero. This is due to the fact that in contrast with the nonlinear system, the eigenmodes in the linear system are decoupled.

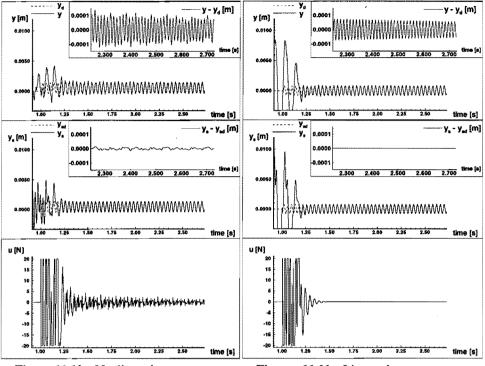


Figure 11.10 Nonlinear beam system without linear damper with  $f_e = 25$  Hz,  $l_s = 1.0$  m,  $f_c = 200$  Hz.

Figure 11.11 Linear beam system without damper with  $f_e = 25$  Hz,  $l_s = 1.0$  m,  $f_c = 200$  Hz.

# 11.4 Conclusions.

In this paper a method is presented for determining whether an unstable periodic solution of a periodically excited nonlinear mechanical system can be stabilized using a single control force. Simulations with a periodically excited beam supported by an one-sided spring show that using this method it is possible to determine the controllability of the system.

Furthermore, a method is presented for determining the local stability of a sliding computed torque controller in combination with a first order low pass filter. Simulations with the beam system show that the first order filter avoids high frequencies corresponding to high system eigenfrequencies in the control force and that the tracking errors quickly converge to zero. Using Floquet theory it is possible to assess the local stability of the controlled system. By examining the characteristic exponents resulting from Floquet theory it is possible to choose the optimal values of the filter bandwidth, the control parameters and the control position. Although the stability analysis is only valid near the desired trajectory, the simulations indicate that the results can also be useful to some extent to assess the global stability of the system.

### Acknowledgement.

This work was supported by the Centre for Mechanical Engineering of TNO Building and Construction Research, Delft, The Netherlands.

# 11.A Stability analysis: Floquet theory

The local stability of a periodic solution q(t) is investigated by linearizing the equations of motion (11.3) of the uncontrolled system around that solution and examining the evolution in time of an infinitesimally small perturbation  $\delta q(t)$ . Using a first order formulation and neglecting higher order terms, substitution of the perturbed solution  $q(t) + \delta q(t)$  in (11.3) gives:

$$\delta \dot{\boldsymbol{x}} = \boldsymbol{A}(t) \delta \boldsymbol{x}, \quad \boldsymbol{A}(t) = \begin{bmatrix} \mathbf{0} & \boldsymbol{I} \\ -\boldsymbol{M}^{-1} \left( \frac{\delta \boldsymbol{f}_{nl}(t)}{\delta \boldsymbol{q}} \right) & -\boldsymbol{M}^{-1} \left( \frac{\delta \boldsymbol{f}_{nl}(t)}{\delta \dot{\boldsymbol{q}}} \right) \end{bmatrix}$$
(11.32)

where  $\delta \boldsymbol{x} = \begin{bmatrix} \delta \boldsymbol{q}^T & \delta \dot{\boldsymbol{q}}^T \end{bmatrix}^T$  and with initial conditions  $\delta \boldsymbol{x}(t_0) = \delta \boldsymbol{x}_0$ . The general solution of (11.32) is:

$$\delta \boldsymbol{x}(t) = \boldsymbol{\Phi}(t, t_0) \delta \boldsymbol{x}_0, \quad \boldsymbol{\Phi}(t_0, t_0) = \boldsymbol{I}$$
(11.33)

where  $\Phi(t, t_0)$  is the so-called fundamental matrix. If the solution q(t) is periodic with period time  $T_p$  (and hence  $A(t) = A(t + T_p)$ ), Floquet theory (see for example Seydel (1988)) shows that the fundamental matrix  $\Phi(t, t_0)$  satisfies:

$$\mathbf{\Phi}(t+T_p,t_0) = \mathbf{\Phi}(t,t_0)\mathbf{\Phi}(t_0+T_p,t_0) = \mathbf{\Phi}(t,t_0)\mathbf{\Phi}_{\lambda}$$
(11.34)

where  $\Phi_{\lambda}$  is the so-called monodromy matrix, which is assumed to have a spectral decomposition:

$$\boldsymbol{\Phi}_{\boldsymbol{\lambda}} = \boldsymbol{\Psi}^{\boldsymbol{\Gamma}} \boldsymbol{\lambda}_i \lrcorner \boldsymbol{\Psi}^{-1} \tag{11.35}$$

where  $\Psi$  is the decomposition matrix and  $\lambda_i$  are the eigenvalues of  $\Theta_{\lambda}$ . Using (11.34) it can easily be shown that  $(t^* = t - t_0 - \kappa T_p, 0 \le t^* < T_p, \kappa \in \mathbb{Z})$ :

$$\Theta(t, t_0) = \Theta(t_0 + t^*, t_0) \Psi^{\Gamma} \lambda_i \lrcorner^{\kappa} \Psi^{-1}$$
(11.36)

So, if the solution q(t) is periodic, the long term behaviour of  $\delta \boldsymbol{x}(t)$  is predestinated by the eigenvalues  $\lambda_i$  of  $\boldsymbol{\Phi}_{\boldsymbol{\lambda}}(|\lambda_{i+1}| \leq |\lambda_i|)$ , the so-called Floquet multipliers.

Sometimes the fundamental matrix is written in the form

$$\boldsymbol{\Phi}(t,t_0) = \boldsymbol{\Theta}(t)e^{\boldsymbol{\Phi}_{\boldsymbol{\rho}}T_{\boldsymbol{p}}(t-t_0)}, \quad \boldsymbol{\Theta}(t_0) = \boldsymbol{I}$$
(11.37)

where  $\Theta(t) = \Theta(t + T_p)$ . The monodromy matrix follows now from

$$\mathbf{\Phi}_{\lambda} = e^{\mathbf{\Phi}_{\rho}T_{p}} = e^{\mathbf{\Psi}_{\rho} \Gamma_{\rho_{i}} \cdot \mathbf{\Psi}_{\rho}^{-1}T_{p}}$$
(11.38)

where  $\rho_i$  are the *characteristic exponents* defined by

$$\lambda_i = e^{\rho_i T_p} \tag{11.39}$$

The following stability conditions result:

- (asymptotically) stable periodic solution, periodic attractor, if:  $|\lambda_i| < 1$ , or  $\Re(\rho_1) < 0, \forall i$
- marginally stable periodic solution, if:  $|\lambda_1| = 1$ , or  $\Re(\rho_1) = 0$
- unstable periodic solution, periodic repellor, if:  $|\lambda_1| > 1$  or  $\Re(\rho_1) > 0$

The eigenvectors  $\Psi$  corresponding to the Floquet multipliers can also be divided into stable and unstable eigenvectors,  $\Psi_s$  and  $\Psi_u$ . These eigenvectors are the initial stable and unstable directions in the state space at  $t = t_0 + kT_p$ ,  $k \in \mathbb{N}$ . Trajectories starting at the stable (unstable) directions will approach the periodic solution when time increases (decreases).

More details about Floquet theory can be found in Seydel (1988).

## References

- Brockett, R.W., 1970, Finite Dimensional Linear Systems, John Wiley & Sons, Inc..
- Craig Jr., R.R., 1985, "A Review of Time-Domain and Frequency-Domain Component Mode Synthesis Methods," *Combined Experimental/Analytical Modeling of Dynamic Structural Systems Using Substructure Synthesis*, D.R. Martinez and A.K. Miller, ed., ASME Applied Mechanics AMD-67, New York, pp. 1-31.
- DIANA, 1995, *DIANA User's Manual 6.0 ed.*, TNO Building and Construction Research, Delft, The Netherlands.
- Fey, R.H.B., Van Campen, D.H., and De Kraker, A., April 1996, "Long Term Structural Dynamics of Mechanical Systems with Local Nonlinearities," ASME *Journal of Vibration and Acoustics*, (in press).
- Seydel, R., 1988, "From Equilibrium to Chaos, Practical Bifurcation and Stability Analysis," Elsevier Science Publishing Co. Inc..
- Slotine, J.-J.E., and Li, W., 1991, "Applied Nonlinear Control," Prentice-Hall Inc..
- Van de Vorst, E.L.B., Van Campen, D.H., Fey, R.H.B., De Kraker, A. and Kok, J.J., 1995, "Vibration Control of Periodically Excited Nonlinear Dynamic Multi-DOF Systems," *Journal of Vibration and Control*, Vol 1, pp. 75–92.



12

# **CONCLUSIONS AND RECOMMENDATIONS.**

In this thesis the long term dynamics of nonlinear mechanical systems is analysed. It is shown that systems consisting of large linear parts and local nonlinearities can be analysed very efficiently if a component mode synthesis method is applied for reducing the number of degrees of freedom of the linear parts which are modelled using finite elements.

In this thesis, three methods were used to solve the two-point boundary value problems for calculating the periodic solutions; finite differences, multiple shooting and incremental harmonic balance. The first method is the most efficient one from a computational point of view if an equidistant time mesh can be used. A disadvantage of this method is that it cannot be used for "hard" discontinuities, i.e. discontinuities which cause a large change of the state of the system in a small time interval (dry friction, rigid stops). Improving the finite difference method in the way that a variable time mesh can be used should solve this problem. The computational time, however, will increase very much in this case. Therefore, it is not useful to improve the finite difference method. For systems with no "hard" discontinuities, the method gives accurate results and is very efficient.

As an example of the above, a rotor-bearing system with 44 degrees of freedom and seven local nonlinearities (oil journal bearings) was investigated successfully using finite differences (Hendrikx, 1994). This system cannot be analysed using the shooting method due to the large computational times which are then involved.

For systems with "hard" discontinuities, the multiple shooting method is useful as long as a time integration method is used with a variable time step size. This time integration method is responsible for the large computational times if the number of degrees of freedom of the investigated system is large. Of course, the multiple shooting method would be less computational time consuming if an integration method with a steady step size is used. However, then the method cannot be used for "hard" discontinuities. At this moment, systems up to eight degrees of freedom (with similar nonlinearities as used in this thesis) can be analysed using the (multiple) shooting method with reasonable computational times.

The incremental harmonic balance method is very efficient for weakly nonlinear systems. In that case the number of harmonic terms in the incremental harmonic balance method can be taken low, resulting in very low computational times even for systems with many degrees of freedom. The method is also useful for getting quickly a global view of a system response. Then, the calculated system response will not be very accurate but accurate enough to determine, for instance, at which frequency resonances in the nonlinear system occur.

The total computational time for analyzing a nonlinear system depends on its number of degrees of freedom and on the kind of nonlinearities which are involved. For example, the four-DOF system in chapter 2 (beam with at its middle a one-sided spring) can be analyzed using finite differences. Calculating one harmonic solution of this system takes less than 1 CPU-sec on a Hewlett-Packard/9000 (fourth order central difference scheme and 400 discretization points). The total time for calculating the response of this system (figure 2.5), including finding subharmonic solutions and calculating a total of approximately 4200 periodic solutions takes about five hours. The six-DOF system in chapter 5 (beam with Hertzian contact with  $\xi_m = 0.015$ ) has to be analyzed using the multiple shooting method due to the stiff elastic stop. Calculating one harmonic solution of this system takes approximately 25 CPU-sec (Adams variable step/order integration method with accuracy of 9 significant digits). The total time for calculating the response of this system (42000 periodic solutions, figure 5.3) takes more than a month. Also the amount of damping in the system strongly influences the total computational time. In weakly damped systems the high frequency eigenmodes will stronger influence the low frequency response. This results in more superharmonic resonance peaks in the low frequency response. For calculating the response not only more eigenmodes have to be included in the reduced system resulting in more degrees of freedom, also more periodic solutions have to be calculated near the extra superharmonic resonance peaks. For example, for the system response of the six-DOF system in chapter 5 with  $\xi_m$  = 0.003 instead of  $\xi_m = 0.015$ , 71000 periodic solutions have to be calculated instead of 42000, making the total computational time much larger.

It is shown that local nonlinearities in a large linear system can change the dynamic behaviour of the system drastically. Furthermore, the results indicate that the high eigenfrequencies of the linear parts of the system may have a large influence on the low frequency steady-state behaviour of the nonlinear system, especially if the system is lightly damped. The eigenfrequencies of the linear parts play an key role in the system response. The frequencies for which the nonlinear system resonates harmonically, have higher or lower values than the eigenfrequencies of the linear system. How much they differ depends on the type and severity of the nonlinearities. In the systems investigated in this thesis, especially the first harmonic resonance frequency changes (to a higher value) whereas the other harmonic resonance frequencies remain approximately the same.

Because the frequencies which occur in a periodic solution of a nonlinear system are a multiple of the basis frequency (i.e. the lowest frequency occurring in the periodic solution) of that periodic solution, often extra (superharmonic) resonance peaks occur if one of the resonance frequencies of the nonlinear system equals a multiple of the excitation frequency. Often 1/n subharmonic behaviour occurs if at 1/n times the excitation frequency a (superharmonic) resonance peak exists. Knowing this, it becomes possible to predict the response of the system once the resonance frequencies of the nonlinear system are known.

In parts I and II it was shown that it is possible to predict the existence of subharmonic branches in this way. The size of these subharmonic branches depends on the damping level in the system and the type and strongness of local nonlinearities involved. The more damping is present in the system, the smaller the subharmonic branches become. The stronger the nonlinearities are, the larger (amplitude and width) the subharmonic branches become.

In part I a comparison between experimental and numerical results indicates that a one-sided leaf spring with much higher eigenfrequencies than the maximum excitation frequency which is investigated, can be modelled using a one-sided massless spring. Furthermore, it may be concluded that an elastic stop in a dynamic system can be modelled accurately using the Hertzian contact force law despite the fact that this theory is developed for static analysis.

By calculating the stable and unstable manifolds of unstable periodic solutions, it is possible to determine the global stability of attractors of single-DOF systems. If the single-DOF system is already a good approximation of the system (like the beam supported by the one-sided spring), in part II experiments show that it is possible to use the single-DOF system for analyzing the global stability of the attractors of the system. If the single-DOF system is not a good approximation of the multi-DOF system or if the system cannot be reduced to a single-DOF system (like a rotordynamic system), manifolds cannot be used to assess the global stability of coexisting attractors. In that case another method like the cell-mapping method (Hsu, 1987, Van der Spek, 1994) can be used. However, the cell-mapping method is a very expensive method from a computational point of view, especially for multi-DOF systems. Furthermore, the cellmapping method is not very useful for detecting fractal basin boundaries and weakly damped systems.

For multi-DOF systems, still the one-dimensional unstable manifolds can be calculated. From their shape, it can be assessed whether the boundaries of the basins of attraction are fractal or not. Attractors with a low global stability often occur if the basin boundaries are fractal. So using the unstable manifolds, often an assessment of the global stability can be made. Nevertheless, in the future, research should be done to develop methods for quickly analyzing the global stability of attractors of multi-DOF systems.

In part III rotor systems with oil journal bearings were analysed successfully. Oil journal bearings are a very different class of nonlinearities compared to a one-sided spring or an elastic stop. Oil journal bearings have a large damping level. Because of this no superharmonic resonances where found in the systems which were investigated in part III. However, 1/2 subharmonic and quasi-periodic behaviour was found for high angular rotor speeds. The quasi-periodic behaviour was dominated by the first resonance frequency of the shaft so again the linear eigenmodes play an important key role in the

system response. Because of this the quasi-periodic behaviour showed a much higher response than the coexisting harmonic solutions. Analysis showed that by adding a mass unbalance to a moderate level these harmonic solutions can be made stable, resulting in a much lower system response. However, still high amplitude quasi-periodic solutions can coexist. Using a nonlinear analysis, the mass unbalance needed for stabilizing the harmonic solutions can be determined. This cannot be done using linear analysis. In Van Liempt (1995) the coexistence of stable harmonic solutions and quasi-periodic solutions was shown in an experiment. However, in this experiment, in which the same system is analysed as in part III of this thesis, it was difficult to determine the exact actual mass unbalance because the shaft was not straight. Because of this it was impossible to determine the mass unbalance which is necessary for stabilizing the system. In the future, this experiment should be improved by using a more straight and balanced shaft. Using this experiment the numerical results in part III can be verified more accurately.

Not only in rotor-bearing systems coexisting (unstable) low amplitude harmonic solutions were found together with stable high amplitude subharmonic or quasi-periodic behaviour. Also in the beam systems with one-sided spring or elastic contact this phenomenon occurs. In part IV a method was developed to control nonlinear dynamic systems in the way that the unstable harmonic solutions become stable. Because these harmonic solutions are natural solutions of the system, the control force will be theoretically zero if the system vibrates in an unstable harmonic solution. Because of this, a large amplitude reduction can be established using very small control effort. In part IV it was shown that using only one control force it is possible to stabilize unstable harmonic solutions of the beam with one-sided spring. Also if the excitation frequency is varied during the control, it is possible to reduce the maximum system response by using very small control effort. Methods were developed for analyzing the stability of the controlled system and the controllability of the system.

In the future, other nonlinearities like dry friction and rigid stops should be analysed both numerically and experimentally. Since the characteristics of the local nonlinearities have a very large influence on the system response, it is important to be sure that the nonlinearity is modelled well. Before analyzing a complex system with local nonlinearities, first simple systems with similar nonlinearities should be investigated both numerically and experimentally in order to check whether the nonlinearities are modelled well and to learn which phenomena take place. Eventually, identification methods can be used to arrive at a good model for the nonlinearity (Verbeek, 1993, Van de Molengraft, 1990). The current numerical methods may need to be improved for numerical analysis of systems with dry friction and rigid stops.

In this thesis, systems are investigated with periodic or constant loads. For linear systems, generally frequency responses and eigenfrequencies are used to predict the system behaviour for other (not periodic) loads like shock loads or stochastic loads. It is interesting to investigate if the response of a nonlinear system with aperiodical or nearly periodical loads can be predicted using the response of the system with periodic loads which is investigated for various excitation frequencies and/or load amplitudes by calculating periodic solutions. This is not obvious because the superposition principle does not hold for nonlinear systems.

Also the presented control method can be improved. The control method does not guarantee stability of the controlled system. Furthermore, the need for the filter in the control method should be further investigated. It is interesting to investigate if the filter does also work for other control concepts. In the thesis, it was stated that because of measurement noise, model disturbances and model errors the control force will not tend exactly to zero if the system approaches the calculated (unstable) harmonic solution. Because of the model errors and disturbances, this calculated harmonic solution will not be the harmonic solution of the actual system. The presented control method controls the system to the calculated harmonic solution not taking into account the required control effort. In some cases, the control effort can be smaller if the system is controlled not exactly to the calculated harmonic solution. In that case, approximately the same reduction of the maximum response is established with smaller control effort. The presented control method can be improved in such way that not only the tracking errors are minimized but also the control effort.

The presented control method uses a single control force for controlling the system. In some cases, one control force will not be sufficient to stabilize an unstable harmonic solution. Think, for instance of a rotor-bearing system where the degrees of freedom are only coupled by the gyroscopic effects and the bearings. This coupling may not be enough to control a rotor-bearing system to an unstable harmonic solution using only a single control force. In this case, one wants to control the system using two control forces. So the control method should be expanded in such a way that multiple control forces can be applied.

#### References

- Hendrikx, R.T.W.M., 1994, "The Dynamic Behaviour of HR.MS. Witte de With," *Master's thesis*, WFW-report 94.062, TNO-report 94-CMC-R0532, Department of Mechanical Engineering, Eindhoven University of Technology, Eindhoven, The Netherlands (in Dutch).
- Hsu, C.S., 1987, "Cell to Cell Mapping; A Method of Global Analysis for Nonlinear Systems," Springer-Verslag of Applied Mechanics.
- Van Liempt, F.P.H., 1995, "Experimental Investigation of a Rotor Dynamic System," WFWreport 95.182, Department of Mechanical Engineering, Eindhoven University of Technology, Eindhoven, The Netherlands (in Dutch).
- Van de Molengraft, M.J.G., 1990, "Identification of Nonlinear Mechanical Systems for Control Application," *PhD thesis*, Department of Mechanical Engineering, Eindhoven University of Technology, Eindhoven, The Netherlands.
- Van der Spek, J.A.W., 1994, "Cell Mapping Methods: Modifications and Extensions," *PhD thesis*, Department of Mechanical Engineering, Eindhoven University of Technology, Eindhoven, The Netherlands.
- Verbeek, G., 1993, "Nonlinear Parametric Identification using Periodic Equilibrium States with Application to an Aircraft Landing Gear Damper," *PhD thesis*, Department of Mechanical Engineering, Eindhoven University of Technology, Eindhoven, The Netherlands.



A

# **COMPONENT MODE SYNTHESIS.**

In this appendix the Component mode synthesis method which is used in this thesis is described shortly. For a more detailed describtion the reader is referred to Craig (1985), Van de Vorst (1991), and Fey (1992).

We consider a nonlinear dynamic system consisting of linear components and local nonlinearities. Firstly, the nonlinear system is divided into linear and nonlinear components. The linear components are assumed to be slightly damped or proportionally damped. This implies that discrete dampers and/or disks with gyroscopy have to be added to the reduced linear components after the reduction. The  $n_x$ -column of degrees of freedom (DOF's)  $\boldsymbol{x} = \begin{bmatrix} \boldsymbol{x}_b^T & \boldsymbol{x}_i^T \end{bmatrix}^T$  of a linear component is divided into a  $n_b$ -column  $\boldsymbol{x}_b$  with interface DOF's (i.e. externally loaded DOF's and DOF's loaded by adjacent linear components or local nonlinearities), and a  $n_i$ -column  $\boldsymbol{x}_i$  ( $n_i = n_x - n_b$ ) with unloaded internal DOF's.

As an example, we consider the rotordynamic system shown in figure 1. The system consists of a rotor (rigid disk) and a flexible shaft supported on one side by an oil journal bearing and pinned (simply supported) on the other side. Only the gyroscopic effects of the rotor are taken into account; the gyroscopic effects of the shaft are neglected. The shaft is assumed to be modally damped with modal damping coefficients  $\xi = 0.01$  for all eigenmodes. The shaft is modelled using the finite element method. If this system is divided into linear and nonlinear components, one single modally damped linear component exists, which is the shaft without rotor and oil journal bearing (figure 2). The 6 interface DOF's of the linear component are two displacements and two rotations for coupling the disk to the shaft (DOF's  $y_r$ ,  $z_r$ ,  $\phi_{y_r}$ ,  $\phi_{z_r}$ ) and the displacements for coupling the oil journal bearing (DOF's  $y_b$ ,  $z_b$ ).

The equations of motions of the linear component are denoted as:

$$\boldsymbol{M_c} \ddot{\boldsymbol{x}} + \boldsymbol{C_c} \dot{\boldsymbol{x}} + \boldsymbol{K_c} \boldsymbol{x} = \boldsymbol{f_c} \tag{A.1}$$

where  $M_c$ ,  $C_c$  and  $K_c$  are the mass matrix, the damping matrix and the stiffness matrix, respectively, all of size  $(n_x, n_x)$ . The frequency-response function  $H_c(\omega)$  of the

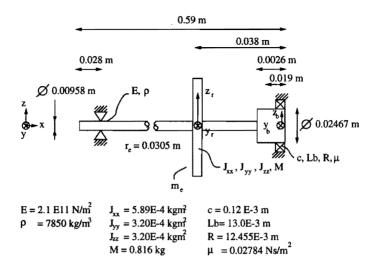


Figure A.1 Rotordynamic system.

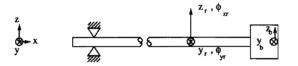


Figure A.2 Linear component with interface DOF's.

undamped component can be written as:

$$\boldsymbol{H_c}(\omega) = \sum_{k=1}^{n_x} \frac{\boldsymbol{u_k} \boldsymbol{u_k}^T}{(\omega_k^2 - \omega^2)}$$
(A.2)

where

•  $\omega_k$ : k-th eigenfrequency of undamped linear component ( $\omega_1 < \omega_2 < \ldots < \omega_{n_x}$ ).

•  $u_k$ : mass normalized k-th eigenmode of undamped linear component:  $u_k^T M_c u_k = 1$ .

For sufficiently small excitation frequencies  $\omega$  the contribution of the eigenmodes with frequency larger than  $\omega_{n_k}$  is approximately constant. So the frequency-response function can be approximated by

$$\boldsymbol{H}_{c}(\omega) \approx \sum_{k=1}^{n_{k}} \frac{\boldsymbol{u}_{k} \boldsymbol{u}_{k}^{T}}{(\omega_{k}^{2} - \omega^{2})} + \sum_{k=n_{k}+1}^{n_{x}} \frac{\boldsymbol{u}_{k} \boldsymbol{u}_{k}^{T}}{(\omega_{k}^{2})}$$
(A.3)

In general this approximation will be accurate for excitation frequencies  $\omega < \omega_{n_k}$ . Using equation (A.3) the response of the linear component can be approximated by

$$\boldsymbol{x} = \boldsymbol{H}_{\boldsymbol{c}}(\omega)\boldsymbol{f}_{\boldsymbol{c}} \approx \sum_{k=1}^{n_{k}} \frac{\boldsymbol{u}_{k} \boldsymbol{u}_{k}^{T}}{(\omega_{k}^{2} - \omega^{2})} \boldsymbol{f}_{\boldsymbol{c}} + \sum_{k=n_{k}+1}^{n_{x}} \frac{\boldsymbol{u}_{k} \boldsymbol{u}_{k}^{T}}{(\omega_{k}^{2})} \boldsymbol{f}_{\boldsymbol{c}}$$
(A.4)

where  $f_c$  is the column with forces. Since only forces are acting on the interface DOF's of the linear component due to external loads and/or adjacent linear components and/or local nonlinearities, the force on the linear component can be written as

$$\boldsymbol{f_c} = \left[ \begin{array}{cc} \boldsymbol{f_b}^T & \boldsymbol{0_i}^T \end{array} \right] \tag{A.5}$$

with  $f_b$  the column with forces on the interface DOF's.

Because

$$\boldsymbol{u_k}^T \boldsymbol{K_c} \boldsymbol{u_k} = \omega_k^2 \tag{A.6}$$

which implies that

$$\boldsymbol{K_c}^{-1} = \sum_{k=n_1}^{n_x} \frac{\boldsymbol{u_k} \boldsymbol{u_k}^T}{(\omega_k^2)} = \sum_{k=1}^{n_k} \frac{\boldsymbol{u_k} \boldsymbol{u_k}^T}{(\omega_k^2)} + \sum_{k=n_k+1}^{n_x} \frac{\boldsymbol{u_k} \boldsymbol{u_k}^T}{(\omega_k^2)}$$
(A.7)

it is easy to see that the response of the linear component for excitation frequencies  $\omega < \omega_{n_k}$  can be approximated by a linear combination of the  $n_k$  eigenmodes of the component:

$$\boldsymbol{U}_{\boldsymbol{k}} = \left[ \begin{array}{cccc} \boldsymbol{u}_1 & \boldsymbol{u}_2 & \dots & \boldsymbol{u}_{n_{\boldsymbol{k}}} \end{array} \right] \tag{A.8}$$

and the  $n_b$  so-called residual flexibility modes:

$$\boldsymbol{\Phi}_{\boldsymbol{b}} = \left(\boldsymbol{K}_{\boldsymbol{c}}^{-1} - \sum_{k=1}^{n_{k}} \frac{\boldsymbol{u}_{\boldsymbol{k}} \boldsymbol{u}_{\boldsymbol{k}}^{T}}{(\omega_{\boldsymbol{k}}^{2})}\right) \boldsymbol{F}_{\boldsymbol{b}}$$
(A.9)

with  $F_b = \begin{bmatrix} I_{bb} & 0_{ib}^T \end{bmatrix}^T$  where  $I_{bb}$  is  $(n_b, n_b)$ -identity matrix. The above holds for a statically determinate component. If the

The above holds for a statically determinate component. If the component can move as a rigid body, also the rigid body modes of the component have to be included, and since  $K_c^{-1}$  does not exist for these components, an alternative algorithm has to be applied for calculating the residual flexibility modes:

$$\boldsymbol{\Phi}_{\boldsymbol{b}} = \left(\boldsymbol{G}_{\boldsymbol{e}} - \sum_{k=n_r+1}^{n_k} \frac{\boldsymbol{u}_k \boldsymbol{u}_k^T}{(\omega_k^2)}\right) \boldsymbol{F}_{\boldsymbol{b}}$$
(A.10)

where  $n_r$  is the number of rigid body modes and  $G_e$  is the elastic flexibility matrix:

$$\boldsymbol{G}_{\boldsymbol{e}} = \sum_{k=n_r+1}^{n_x} \frac{\boldsymbol{u}_k \boldsymbol{u}_k^T}{(\omega_k^2)} = \boldsymbol{P}^T \boldsymbol{G} \boldsymbol{P}$$
(A.11)

In (A.11) the matrix  $\boldsymbol{P}$  is defined by:

$$\boldsymbol{P} = \boldsymbol{I} - \boldsymbol{M}_c \boldsymbol{U}_r \boldsymbol{U}_r^T \tag{A.12}$$

where  $U_r = \begin{bmatrix} u_1 & \dots & u_{n_r} \end{bmatrix}$  are the rigid body modes, while the matrix G is defined by:

$$\boldsymbol{G} = \begin{bmatrix} \boldsymbol{K}^{\star - 1} & \boldsymbol{0} \\ \boldsymbol{0} & \boldsymbol{0} \end{bmatrix}$$
(A.13)

where  $K^*$  is the  $(n_x - n_r, n_x - n_r)$ -stiffness matrix of the reduced component if  $n_r$  DOF's are supported in such way that  $K^{*-1}$  exists. For the proof of the correctness of this algorithm the reader is referred to Craig (1985).

Using the  $n_k$  columns of  $U_k$  and the  $n_b$  columns of  $\Phi_b$  in the reduction matrix  $T_1 = \begin{bmatrix} \Phi_b & U_k \end{bmatrix}$ , the following Ritz approximation of the component displacement field can now be applied:

$$\boldsymbol{x} = \boldsymbol{T_1}\boldsymbol{p}', \quad \rightarrow \quad \begin{bmatrix} \boldsymbol{x_b} \\ \boldsymbol{x_i} \end{bmatrix} = \begin{bmatrix} \boldsymbol{\Phi_{bb}} & \boldsymbol{U_{bk}} \\ \boldsymbol{\Phi_{ib}} & \boldsymbol{U_{ik}} \end{bmatrix} \begin{bmatrix} \boldsymbol{p_b} \\ \boldsymbol{p_k} \end{bmatrix}$$
(A.14)

Starting from (A.14), the DOF's  $p_b$  are replaced by the interface DOF  $x_b$  using a coordinate transformation matrix  $T_2$  to permit simple coupling of the reduced component equations:

$$\begin{bmatrix} p_b \\ p_k \end{bmatrix} = \begin{bmatrix} \Phi_{bb}^{-1} & -\Phi_{bb}^{-1}U_{bk} \\ 0_{kb} & I_{kk} \end{bmatrix} \begin{bmatrix} x_b \\ p_k \end{bmatrix}, \quad \rightarrow \quad p' = T_2 p \qquad (A.15)$$

This results in the following total transformation:

$$\boldsymbol{x} = \boldsymbol{T}\boldsymbol{p}, \quad \boldsymbol{T} = \boldsymbol{T}_1 \boldsymbol{T}_2 \tag{A.16}$$

Applying the transformation (A.16) to the unreduced equations of motion (A.1), the  $(n_k + n_b)$  reduced component equations become:

$$\boldsymbol{T}^{T}\boldsymbol{M}_{c}\boldsymbol{T}\boldsymbol{\ddot{p}} + \boldsymbol{T}^{T}\boldsymbol{C}_{c}\boldsymbol{T}\boldsymbol{\dot{p}} + \boldsymbol{T}^{T}\boldsymbol{K}_{c}\boldsymbol{T}\boldsymbol{p} = \boldsymbol{T}^{T}\boldsymbol{f}_{c}$$
(A.17)

Notice that the order of the reduction depends on the sum of the number of interface DOF and the number of kept eigenmodes. The latter determines the frequency domain in which the reduced component can be used with sufficient accuracy.

After reduction the local nonlinearities are added to the reduced linear components. This can be done easily since the interface DOF's are available in the reduced components. The  $n_q$ -column with independent system DOF's q of the reduced nonlinear system contains the modal DOF's  $p_k^{(i)}$  of all reduced linear components i ( $i = 1, ..., N_c$ ) and a column y, containing all interface DOF's  $x_b^{(i)}$  of the system. Local nonlinearities  $f_{ny}$ , which for simplicity are assumed to be only a function of y and  $\dot{y}$ , are added by means of the  $n_q$ -column with internal loads  $f_{nl}$ , whereas external loads  $f_y$  are collected in  $f_{ex}$ . The equations of motion of the reduced system are given by:

$$M\ddot{q} + f_{nl} = f_{ex} \tag{A.18}$$

with:

$$\boldsymbol{q} = \left[\boldsymbol{p}_{\boldsymbol{k}}^{(1)T}, \dots, \boldsymbol{p}_{\boldsymbol{k}}^{(N_c)T}, \boldsymbol{y}^T\right]^T, \quad \boldsymbol{y} = \left[\boldsymbol{x}_{\boldsymbol{b}}^{(1)T}, \dots, \boldsymbol{x}_{\boldsymbol{b}}^{(N_c)T}\right]^T \quad (A.19)$$

$$\boldsymbol{f}_{nl} = \boldsymbol{C}\boldsymbol{\dot{q}} + \boldsymbol{K}\boldsymbol{q} + \left[\boldsymbol{0}_{\boldsymbol{k}}^{(1)T}, \dots, \boldsymbol{0}_{\boldsymbol{k}}^{(N_c)T}, \boldsymbol{f}_{n\boldsymbol{y}}^T(\boldsymbol{\dot{y}}, \boldsymbol{y})\right]^T$$
(A.20)

$$\boldsymbol{f_{ex}} = \left[\boldsymbol{0_k}^{(1)T}, \dots, \boldsymbol{0_k}^{(N_c)T}, \boldsymbol{f_y}^T\right]^T$$
(A.21)

As mentioned before, the eigenfrequencies  $\omega \leq \omega_c$  of (A.18) for the case  $f_{ny} = f_{ex} = 0$  are very accurate, with  $\omega_c$  the cut-off frequency for mode selection. In general, higher eigenfrequencies will be inaccurate. Because nonlinear systems can generate higher frequencies than their excitation frequency, in general  $\omega_c$  has to be chosen higher than the maximum excitation frequency (Aarts, 1993).

#### References

- Aarts, J.W., 1993, "Component Mode Synthesis for Nonlinear Dynamical Systems," Master's thesis, WFW-report 93.048, TNO-report 93-CMC-R0546, Department of Mechanical Engineering, Eindhoven University of Technology, Eindhoven, The Netherlands (in Dutch).
- Craig Jr., R.R., 1985, "A Review of Time-Domain and Frequency-Domain Component Mode Synthesis Methods," *Combined Experimental/Analytical Modeling of Dynamic Structural Systems Using Substructure Synthesis*, D.R. Martinez and A.K. Miller, ed., ASME Applied Mechanics AMD-67, New York, pp. 1-31.
- Fey, R.H.B., 1992, "Steady-State Behaviour of Reduced Dynamic Systems with Local Nonlinearities," *PhD thesis*, Department of Mechanical Engineering, Eindhoven University of Technology, Eindhoven, The Netherlands.
- Van de Vorst, E.L.B., 1991, "Component Mode Synthesis," *Master's thesis*, TNO-report BI-91-146\*, Department of Mechanical Engineering, Eindhoven University of Technology, Eindhoven, The Netherlands (in Dutch).



B

# PERIODIC SOLUTION SOLVERS.

Periodic solutions are calculated by solving a two-point boundary value problem, which is defined by

$$\begin{cases} f_p^2 \boldsymbol{M}(r) \boldsymbol{q''} + \boldsymbol{f_{nl}}(f_p \boldsymbol{q'}, \boldsymbol{q}, \tau/f_p, r) = \boldsymbol{f_{ex}}(\tau/f_p, r) \\ \boldsymbol{q}(\tau) = \boldsymbol{q}(\tau+1) \\ \boldsymbol{q'}(\tau) = \boldsymbol{q'}(\tau+1) \end{cases}$$
(B.1)

with  $\tau = t/T_p = f_p t$  the dimensionless time,  $T_p = 1/f_p$  the period time of the periodic solution, an accent represents a derivative to  $\tau$  and r represents a system parameter, for example the excitation frequency. In the following sections three methods are described for solving this two-point boundary value problem: the finite difference method, the multiple shooting method and the incremental harmonic balance method.

#### **B.1** Finite Difference Method.

Approximations of periodic solutions can be obtained efficiently by using a finite difference technique. In this section the finite difference method is described shortly. For a more detailed description the reader is referred to Fey (1992).

The dimensionless time  $\tau$  is discretized by  $n_{\tau}$  equidistant points  $\tau_i = i/n_t =: i\Delta \tau$ ,  $i = 0, \ldots, n_{\tau} - 1$ , in one period  $T_p$ . By applying a central difference scheme, the following approximations  $\tilde{q'}_i$  and  $\tilde{q''}_i$  are obtained for the velocities  $q'_i$  and accelerations  $q''_i$ , respectively, for  $i = 0, \ldots, n_{\tau} - 1$  ( $O(\Delta \tau^2)$ );  $Q_i$  is an abbreviation for quantity  $Q(\tau_i)$ ):

$$\tilde{q'}_{i} = (\tilde{q}_{i+1} - \tilde{q}_{i-1})/(2\Delta\tau), \quad \tilde{q''}_{i} = (\tilde{q}_{i+1} - 2\tilde{q}_{i} + \tilde{q}_{i-1})/(\Delta\tau^{2})$$
 (B.2)

Of course one can use also other discretization schemes like a  $O(\Delta \tau^4)$  central difference scheme. Substitution of (B.2) in the two-point boundary value problem (B.1) leads to a

set of  $n_q \times n_\tau$  nonlinear algebraic equations, which is formally denoted as:

$$\boldsymbol{h}_{\boldsymbol{f}}(\boldsymbol{z}_{\boldsymbol{f}},r) = \boldsymbol{0}, \quad \boldsymbol{z}_{\boldsymbol{f}} = [\boldsymbol{\tilde{q}}_0^T, \dots, \boldsymbol{\tilde{q}}_{\boldsymbol{n}_{\tau}-1}^T]^T$$
 (B.3)

with

$$h_{f} = \begin{bmatrix} f_{p}^{2}M(r)\tilde{q''}_{0} + f_{nl_{0}} - f_{ex_{0}} \\ f_{p}^{2}M(r)\tilde{q''}_{1} + f_{nl_{1}} - f_{ex_{1}} \\ \vdots \\ f_{p}^{2}M(r)\tilde{q''}_{n_{\tau}-1} + f_{nl_{n_{\tau}-1}} - f_{ex_{n_{\tau}-1}} \end{bmatrix}$$
(B.4)

If r is given a value  $r_{s,1}$ , the corresponding discretized periodic solution  $z_{f_{s,1}}$  can be solved from (B.3) using the iterative (damped) Newton process. The Jacobian can be written as

$$\partial h / \partial z_{f} = \begin{bmatrix} A_{0} & C_{0} & & & B_{0} \\ B_{1} & A_{1} & C_{1} & & & \\ & B_{2} & A_{2} & C_{2} & & \\ & & \ddots & & \\ & & & B_{n_{\tau}-2} & A_{n_{\tau}-2} & C_{n_{\tau}-2} \\ & & & B_{n_{\tau}-1} & A_{n_{\tau}-1} \end{bmatrix}$$
(B.5)

where

$$A_{i} = -2f_{p}^{2}\frac{M(r_{s,1})}{\Delta\tau^{2}} + \frac{\partial f_{nl_{i}}}{\partial q}$$

$$B_{i} = f_{p}^{2}\frac{M(r_{s,1})}{\Delta\tau^{2}} - f_{p}\frac{(\partial f_{nl_{i}}/\partial\dot{q})}{2\Delta\tau}$$

$$C_{i} = f_{p}^{2}\frac{M(r_{s,1})}{\Delta\tau^{2}} + f_{p}\frac{(\partial f_{nl_{i}}/\partial\dot{q})}{2\Delta\tau}$$
(B.6)

Because the Jacobian  $\partial h/\partial z_f$  has a special structure (the upper left part has a band structure), the decomposition of the Jacobian can be carried out very efficiently which makes the finite difference method a very efficient method for calculating periodic solutions. Naturally, the solution, which will be found, depends on the initial estimate  $z_0$ .

In case of autonomous systems, the period time  $T_p$  of the periodic solution is unknown and has to be calculated too. In this case an extra equation has to be added to make the set of equations solvable. Because the periodic solution of an autonomous system can be shifted over an arbitrary time interval, an equation can be formulated, which fixes the phase. This can be achieved by setting one of the components of  $\tilde{q'}$  equal to zero at a certain time  $\tau_i$ . For solving the set of  $(n_q \times n_\tau) + 1$  nonlinear equations the derivative

#### B.2. MULTIPLE SHOOTING METHOD.

 $(\partial h_f / \partial f_p)$  is needed and can be obtained with

$$\partial \boldsymbol{h}_{f} / \partial f_{p} = \begin{bmatrix} 2f_{p}\boldsymbol{M}(r)\tilde{\boldsymbol{q}''}_{0} + \left(\frac{\partial \boldsymbol{f}_{nl_{0}}}{\partial \dot{\boldsymbol{q}}}\right)\tilde{\boldsymbol{q}'}_{0} \\ \vdots \\ 2f_{p}\boldsymbol{M}(r)\tilde{\boldsymbol{q}''}_{n_{\tau}-1} + \left(\frac{\partial \boldsymbol{f}_{nl_{n_{\tau}-1}}}{\partial \dot{\boldsymbol{q}}}\right)\tilde{\boldsymbol{q}'}_{n_{\tau}-1} \end{bmatrix}$$
(B.7)

For path-following (see appendix C) also the derivative  $\partial h_f / \partial r$  is needed. If r is the excitation frequency  $(r = f_p)$  then the derivative becomes

$$\frac{\partial h_{f}}{\partial r} = \left[ \begin{cases} 2rM + r^{2}\frac{\partial M}{\partial r} \\ i \end{cases} \tilde{q}''_{0} + \left(\frac{\partial f_{nl_{0}}}{\partial \dot{q}}\right) \tilde{q}'_{0} + \frac{\partial f_{nl_{0}}}{\partial r} - \frac{\partial f_{ex_{0}}}{\partial r} \\ \vdots \\ \left\{ 2rM + r^{2}\frac{\partial M}{\partial r} \right\} \tilde{q}''_{n\tau-1} + \left(\frac{f_{nl_{n\tau-1}}}{\partial \dot{q}}\right) \tilde{q}'_{n\tau-1} + \frac{\partial f_{nl_{n\tau-1}}}{\partial r} - \frac{\partial f_{ex_{n\tau-1}}}{\partial r} \end{cases} \right]$$
(B.8)

else the derivative becomes

$$\partial \boldsymbol{h}_{f} / \partial r = \begin{bmatrix} r^{2} \frac{\partial M}{\partial r} \tilde{\boldsymbol{q}''}_{0} + \frac{\partial \boldsymbol{f}_{nl_{0}}}{\partial r} - \frac{\partial \boldsymbol{f}_{e\boldsymbol{x}_{0}}}{\partial r} \\ \vdots \\ r^{2} \frac{\partial M}{\partial r} \tilde{\boldsymbol{q}''}_{n\tau-1} + \frac{\partial \boldsymbol{f}_{nl_{n\tau-1}}}{\partial r} - \frac{\partial \boldsymbol{f}_{e\boldsymbol{x}_{n\tau-1}}}{\partial r} \end{bmatrix}$$
(B.9)

#### **B.2** Multiple Shooting Method.

In this section the multiple shooting method is described shortly. For a more detailed description the reader is referred to Ascher et al. (1988).

In the multiple shooting method, the two-point boundary value problem (B.1) is rewritten in first order form:

$$\begin{cases} s' = f(s, \tau/f_p, r) \\ s(\tau) = s(\tau + 1) \end{cases}$$
(B.10)

with

$$\boldsymbol{s} = \begin{bmatrix} \boldsymbol{q} \\ f_p \boldsymbol{q'} \end{bmatrix}$$
(B.11)

and where

$$\boldsymbol{f}(\boldsymbol{s},\tau/f_p,r) = \left[\begin{array}{c} \boldsymbol{q'} \\ \frac{1}{f_p} \boldsymbol{M^{-1}}(r) \left\{-\boldsymbol{f_{nl}}(f_p \boldsymbol{q'},\boldsymbol{q},\tau/f_p,r) + \boldsymbol{f_{ex}}(\tau/f_p,r)\right\}\end{array}\right] (B.12)$$

In the multiple shooting method the period time is discretized by  $n_s$  equidistant points  $\tau_i = i/n_s =: i\Delta\tau, i = 0, ..., n_s - 1$ . Equation (B.10) is integrated by means of a numerical time integration method over the time intervals and a periodic solution is found if the following criterium is satisfied:

$$\boldsymbol{h}_{\boldsymbol{s}}(\boldsymbol{z}_{\boldsymbol{s}},r) = \boldsymbol{0} \tag{B.13}$$

with

$$\boldsymbol{z}_{\boldsymbol{s}} = \begin{bmatrix} \boldsymbol{s}_{0} \\ \vdots \\ \boldsymbol{s}_{n_{s}-1} \end{bmatrix}, \quad \boldsymbol{h}_{\boldsymbol{s}} = \begin{bmatrix} \boldsymbol{s}_{0}(\tau_{0} + \Delta \tau) - \boldsymbol{s}_{0}(\tau_{0}) \\ \boldsymbol{s}_{1}(\tau_{1} + \Delta \tau) - \boldsymbol{s}_{1}(\tau_{1}) \\ \vdots \\ \boldsymbol{s}_{n_{s}-1}(\tau_{n_{s}-1} + \Delta \tau) - \boldsymbol{s}_{n_{s}-1}(\tau_{n_{s}-1}) \end{bmatrix}$$
(B.14)

Again, for a given  $r = r_{s,1}$  the corresponding solution  $z_{s_{s,1}}$  can be solved from (B.13) using the iterative (damped) Newton process. The Jacobian can be obtained as

where  $J_i$  is calculated by numerical time integration of equation (B.10) linearized about the trajectory  $s_i(\tau_i + \tau)$ :

$$\delta \mathbf{S}' = \left(\frac{\partial \mathbf{f}}{\partial s}\right) \delta \mathbf{S}, \quad \frac{\partial \mathbf{f}}{\partial s} = \begin{bmatrix} \mathbf{0} & \frac{1}{f_p}\mathbf{I} \\ -\frac{1}{f_p}\mathbf{M}^{-1}\left(\frac{\partial \mathbf{f}_{nl}}{\partial q}\right) & -\frac{1}{f_p}\mathbf{M}^{-1}\left(\frac{\partial \mathbf{f}_{nl}}{\partial \dot{q}}\right) \end{bmatrix} (B.16)$$

with  $\delta S(\tau_i) = I$  and  $\delta S(\tau_i + \Delta \tau) = J_i$ . Although, again the upper left part of the Jacobian  $\partial h/\partial z_s$  has a band structure, the shooting method is not very efficient because for the calculation of  $J_i$  4 ×  $n_q$  ×  $n_q$  equations have to be integrated over one time interval. If  $n_s = 1$ , the Jacobian becomes

$$\partial \boldsymbol{h} / \partial \boldsymbol{z}_{\boldsymbol{s}} = \boldsymbol{J}_{\boldsymbol{0}} - \boldsymbol{I} \tag{B.17}$$

and this is called *simple* shooting method.

In case of autonomous systems one component of  $\dot{q}$  has to be made zero to make the set of equations solvable. The derivative  $(\partial h_s/\partial f_p)$  can now be obtained as

$$\partial \boldsymbol{h}_{s} / \partial f_{p} = \begin{bmatrix} \partial \boldsymbol{s}_{0}(\tau_{0} + \Delta \tau) / \partial f_{p} \\ \vdots \\ \partial \boldsymbol{s}_{n_{s}-1}(\tau_{n_{s}-1} + \Delta \tau) / \partial f_{p} \end{bmatrix}$$
(B.18)

where  $\partial \boldsymbol{s_i}(\tau_i + \Delta \tau) / \partial f_p$  can be calculated by integration of

$$\delta \boldsymbol{s_r'} = \left(\frac{\partial \boldsymbol{f}}{\partial \boldsymbol{s}}\right) \delta \boldsymbol{s_r} + \left(\frac{\partial \boldsymbol{f}}{\partial f_p}\right) \delta f_p \tag{B.19}$$

with  $\delta s_r(\tau_i) = 0$ ,  $\delta f_p = 1$ ,  $\delta s_r(\tau_i + \Delta \tau) = \partial s_i(\tau_i + \Delta \tau) / \partial f_p$  and

$$\frac{\partial \boldsymbol{f}}{\partial f_p} = -\boldsymbol{f}/f_p \tag{B.20}$$

For path-following (see appendix C) also the derivative  $\partial h_s / \partial r$  is needed:

$$\partial \boldsymbol{h}_{\boldsymbol{s}} / \partial r = \begin{bmatrix} \partial \boldsymbol{s}_{\boldsymbol{0}}(\tau_{\boldsymbol{0}} + \Delta \tau) / \partial r \\ \vdots \\ \partial \boldsymbol{s}_{\boldsymbol{n}_{\boldsymbol{s}}-1}(\tau_{\boldsymbol{n}_{\boldsymbol{s}}-1} + \Delta \tau) / \partial r \end{bmatrix}$$
(B.21)

where  $\partial s_i(\tau_i + \Delta \tau) / \partial r$  can be calculated by integration of

$$\delta \boldsymbol{s}_{\boldsymbol{r}}^{\prime} = \left(\frac{\partial \boldsymbol{f}}{\partial \boldsymbol{s}}\right) \delta \boldsymbol{s}_{\boldsymbol{r}} + \left(\frac{\partial \boldsymbol{f}}{\partial r}\right) \delta r \tag{B.22}$$

with  $\delta s_r(\tau_i) = 0$ ,  $\delta r = 1$ ,  $\delta s_r(\tau_i + \Delta \tau) = \partial s_i(\tau_i + \Delta \tau)/\partial r$  and if r is the excitation frequency  $(r = f_p)$ , then

$$\frac{\partial \boldsymbol{f}}{\partial r} = -\frac{\boldsymbol{f}}{r} + \left[ \frac{1}{r} \left\{ \frac{\partial (\boldsymbol{M}^{-1})}{\partial r} \left\{ -\boldsymbol{f}_{nl} + \boldsymbol{f}_{ex} \right\} - \boldsymbol{M}^{-1} \left\{ \frac{\partial \boldsymbol{f}_{nl}}{\partial r} - \frac{\partial \boldsymbol{f}_{ex}}{\partial r} \right\} \right] \right] (B.23)$$

else

$$\frac{\partial \boldsymbol{f}}{\partial r} = \left[ \begin{array}{c} \boldsymbol{0} \\ \frac{1}{f_p} \left\{ \frac{\partial \left( \boldsymbol{M}^{-1} \right)}{\partial r} \left\{ -\boldsymbol{f}_{\boldsymbol{nl}} + \boldsymbol{f}_{\boldsymbol{ex}} \right\} - \boldsymbol{M}^{-1} \left\{ \frac{\partial \boldsymbol{f}_{\boldsymbol{nl}}}{\partial r} - \frac{\partial \boldsymbol{f}_{\boldsymbol{ex}}}{\partial r} \right\} \right\} \end{array} \right] \quad (B.24)$$

#### **B.3** Incremental Harmonic Balance method.

In this section the incremental harmonic balance method is described shortly. For a more detailed description the reader is referred to Lau and Yuen (1991).

In the incremental harmonic balance method the periodic solutions are approximated using truncated Fourier series:

$$\tilde{q} = Y z_h \tag{B.25}$$

where  $z_h$  is a  $(2 \times n_h) + 1$ -column with constants, while

$$Y = \begin{bmatrix} T_h & & \\ & T_h & \\ & & \ddots & \\ & & & T_h \end{bmatrix}$$
(B.26)

where

$$\boldsymbol{T_h} = \begin{bmatrix} 1 & \cos(\tau) & \cos(2\tau) & \dots & \cos(n_h\tau) & \sin(\tau) & \sin(2\tau) & \dots & \sin(n_h\tau) \end{bmatrix}$$
(B.27)

By applying a Galerkin procedure a periodic solution is found if the following criterion is satisfied:

$$\boldsymbol{h_h}(\boldsymbol{z_h}, r) = \boldsymbol{0} \tag{B.28}$$

with

$$\boldsymbol{h}_{\boldsymbol{h}} = \int_{0}^{2\pi} \boldsymbol{Y}^{T} \left\{ f_{p}^{2} \boldsymbol{M}(r) \boldsymbol{Y}^{\prime\prime} \boldsymbol{z}_{\boldsymbol{h}} + \boldsymbol{f}_{nl}(f_{p} \boldsymbol{Y}^{\prime} \boldsymbol{z}_{\boldsymbol{h}}, \boldsymbol{Y} \boldsymbol{z}_{\boldsymbol{h}}, \tau/f_{p}, r) - \boldsymbol{f}_{\boldsymbol{ex}}(\tau/f_{p}, r) \right\} \partial \tau$$
(B.29)

Again, for a given value  $r = r_{s,1}$  the corresponding solution  $z_{h_{s,1}}$  can be solved from the  $(2n_h + 1) \times n_q$  nonlinear equations in (B.28) using the iterative (damped) Newton process. The Jacobian can be obtained as

$$\partial \boldsymbol{h}_{\boldsymbol{h}} / \partial \boldsymbol{z}_{\boldsymbol{h}} = \int_{0}^{2\pi} \boldsymbol{Y}^{T} \left\{ f_{p}^{2} \boldsymbol{M}(r_{s,1}) \boldsymbol{Y}^{\prime\prime} + f_{p} \frac{\partial \boldsymbol{f}_{nl}}{\partial \dot{\boldsymbol{q}}} \boldsymbol{Y}^{\prime} + \frac{\partial \boldsymbol{f}_{nl}}{\partial \boldsymbol{q}} \boldsymbol{Y} \right\} \partial \tau \qquad (B.30)$$

Notice that the Jacobian is a full matrix, so the incremental harmonic balance method is not efficient for large  $n_h$ -values.

In case of autonomous systems one component of  $Y'z_h$  has to be made zero to make the set of equations solvable. The derivative  $(\partial h_h/\partial f_p)$  can now be obtained as

$$\partial \boldsymbol{h}_{\boldsymbol{h}} / \partial f_{\boldsymbol{p}} = \int_{0}^{2\pi} \boldsymbol{Y}^{T} \left\{ 2f_{\boldsymbol{p}} \boldsymbol{M}(\boldsymbol{r}) \boldsymbol{Y}^{\prime\prime} + \frac{\partial \boldsymbol{f}_{\boldsymbol{n}\boldsymbol{l}}}{\partial \dot{\boldsymbol{q}}} \boldsymbol{Y}^{\prime} \right\} \partial \tau$$
(B.31)

For path-following (see appendix C) also the derivative  $\partial h_h / \partial r$  is needed. If r is the excitation frequency  $(r = f_p)$ , then the derivative becomes

$$\partial \boldsymbol{h}_{\boldsymbol{h}}/\partial r = \int_{0}^{2\pi} \boldsymbol{Y}^{T} \left\{ \left\{ 2r\boldsymbol{M} + r^{2} \frac{\partial \boldsymbol{M}}{\partial r} \right\} \boldsymbol{Y}'' + \frac{\partial \boldsymbol{f}_{\boldsymbol{n}\boldsymbol{l}}}{\partial \dot{\boldsymbol{q}}} \boldsymbol{Y}' + \frac{\partial \boldsymbol{f}_{\boldsymbol{n}\boldsymbol{l}}}{\partial r} - \frac{\partial \boldsymbol{f}_{\boldsymbol{e}\boldsymbol{x}}}{\partial r} \right\} \frac{\partial \tau}{(B.32)}$$

else the derivative becomes

$$\partial \boldsymbol{h}_{\boldsymbol{h}} / \partial r = \int_{0}^{2\pi} \boldsymbol{Y}^{T} \left\{ r^{2} \frac{\partial \boldsymbol{M}}{\partial r} \boldsymbol{Y}^{\prime \prime} + \frac{\partial \boldsymbol{f}_{\boldsymbol{n}l}}{\partial r} - \frac{\partial \boldsymbol{f}_{\boldsymbol{ex}}}{\partial r} \right\} \partial \tau$$
(B.33)

#### References

- Ascher, U.M., Mattheij, R.M.M., and Russell, R.D., 1988, "Numerical Solution of Boundary Value Problems for Ordinary Differential Equations," Prentice-Hall Inc..
- Fey, R.H.B., 1992, "Steady-State Behaviour of Reduced Dynamic Systems with Local Nonlinearities," *PhD thesis*, Department of Mechanical Engineering, Eindhoven University of Technology, Eindhoven, The Netherlands.
- Lau, S.L. and Yuen, S.W., 1991, "The Hopf Bifurcation and Limit Cycle by the Incremental Harmonic Balance Method," *Computer Methods in Applied Mechanics and Engineering*, Vol. 91, pp. 1109–1121.

220



# PERIODIC

# PATH-FOLLOWING OF PERIODIC SOLUTIONS.

By applying a path-following (pf) technique the designer of a dynamic system is able to investigate how a periodic solution is influenced by a change in r. In essence the technique consists of a predictor-corrector mechanism. Starting from a known solution  $z_{s,k}, r_{s,k}$  the prediction  $z_{p,k}, r_{p,k}$  of pf-step k is chosen on the tangent to the solution branch at the point  $z_{s,k}, r_{s,k}$  ( $h_{(Q)} := \partial h / \partial Q$ ):

$$\begin{bmatrix} \boldsymbol{z}_{\boldsymbol{p},\boldsymbol{k}}^T & r_{\boldsymbol{p},\boldsymbol{k}} \end{bmatrix}^T = \begin{bmatrix} \boldsymbol{z}_{\boldsymbol{s},\boldsymbol{k}}^T & r_{\boldsymbol{s},\boldsymbol{k}} \end{bmatrix}^T + \sigma_{\boldsymbol{p},\boldsymbol{k}} \begin{bmatrix} (-\boldsymbol{h}_{(\boldsymbol{z})}^{-1}\boldsymbol{h}_{(\boldsymbol{r})})^T & 1 \end{bmatrix}^T$$
(C.1)

where  $\sigma_{p,k}$  is a well-chosen step size. Subsequently this prediction is corrected iteratively using the orthogonal trajectory method of Fried (1984) ( $z_{c,k,1} = z_{p,k}, r_{c,k,1} = r_{p,k}$ ):

$$\begin{bmatrix} \boldsymbol{z}_{c,k,m+1} \\ \boldsymbol{r}_{c,k,m+1} \end{bmatrix} = \begin{bmatrix} \boldsymbol{z}_{c,k,m} \\ \boldsymbol{r}_{c,k,m} \end{bmatrix} - \begin{bmatrix} (\boldsymbol{h}_{(z)} + \boldsymbol{h}_{(r)}(\boldsymbol{h}_{(z)}^{-1}\boldsymbol{h}_{(r)})^T)^{-1}\boldsymbol{h} \\ (\boldsymbol{h}_{(z)}^{-1}\boldsymbol{h}_{(r)})^T (\boldsymbol{h}_{(z)} + \boldsymbol{h}_{(r)}(\boldsymbol{h}_{(z)}^{-1}\boldsymbol{h}_{(r)})^T)^{-1}\boldsymbol{h} \end{bmatrix}$$
(C.2)

In (C.2) the correction is orthogonal to the solution space of  $h(z, r) = h(z_{c,k,m}, r_{c,k,m})$ . The correction process is stopped if some convergence criterion is satisfied. During the iterative correction process it is required that the norm of the residue is decreased monotonically:

$$||h(z_{c,k,m+1}, r_{c,k,m+1})|| < ||h(z_{c,k,m}, r_{c,k,m})||$$
 (C.3)

If (C.3) is not satisfied then a new prediction is calculated using a smaller stepsize  $\sigma_{p,k}$ .

If the step size is too large, the pf-process may return to the part of the solution curve already passed through. Often this will occur in areas, where the solution branch is heavily curved. The phenomenon can be prevented by requiring that the angle  $\beta_1$ between the scaled tangent in pf-step k and the line pointing form the solution of pf-step k to the solution of pf-step k + 1 is smaller than a user defined angle  $\beta_{1\text{max}}$ :

$$\beta_{1} = \arccos \frac{\begin{bmatrix} \boldsymbol{z}_{\boldsymbol{p},\boldsymbol{k}}^{T} & r_{\boldsymbol{p},\boldsymbol{k}} \end{bmatrix} \begin{bmatrix} (\boldsymbol{z}_{\boldsymbol{s},\boldsymbol{k+1}} - \boldsymbol{z}_{\boldsymbol{s},\boldsymbol{k}})^{T} & (r_{\boldsymbol{s},\boldsymbol{k+1}} - r_{\boldsymbol{s},\boldsymbol{k}}) \end{bmatrix}^{T}}{|| \begin{bmatrix} \boldsymbol{z}_{\boldsymbol{p},\boldsymbol{k}}^{T} & r_{\boldsymbol{p},\boldsymbol{k}} \end{bmatrix} || || \begin{bmatrix} (\boldsymbol{z}_{\boldsymbol{s},\boldsymbol{k+1}} - \boldsymbol{z}_{\boldsymbol{s},\boldsymbol{k}})^{T} & (r_{\boldsymbol{s},\boldsymbol{k+1}} - r_{\boldsymbol{s},\boldsymbol{k}}) \end{bmatrix} ||} \leqslant \beta_{1\max}$$
(C.4)

Furthermore it is possible that the pf-process accidentally jumps over to another branch or a remote part of the same branch if the step size is too large. Usually this can be prevented by requiring that the shape of the increment in the predictor step does not differ much from the shape of the difference of the two succesive solutions  $z_{s,k}$  and  $z_{s,k+1}$ :

$$\beta_{2} = \arccos \frac{\boldsymbol{z}_{\boldsymbol{p},\boldsymbol{k}}^{T} (\boldsymbol{z}_{\boldsymbol{s},\boldsymbol{k+1}} - \boldsymbol{z}_{\boldsymbol{s},\boldsymbol{k}})}{||\boldsymbol{z}_{\boldsymbol{p},\boldsymbol{k}}||| || (\boldsymbol{z}_{\boldsymbol{s},\boldsymbol{k+1}} - \boldsymbol{z}_{\boldsymbol{s},\boldsymbol{k}})||} \leqslant \beta_{2\max}$$
(C.5)

If condition (C.4) or (C.5) is not fulfiled, a new prediction will be calculated using a smaller stepsize  $\sigma_{p,k}$ .

More details about the path-following method can be found in Fey (1992).

#### References

- Fey, R.H.B., 1992, "Steady-State Behaviour of Reduced Dynamic Systems with Local Nonlinearities," *PhD thesis*, Department of Mechanical Engineering, Eindhoven University of Technology, Eindhoven, The Netherlands.
- Fried, I., 1984, "Orthogonal Trajectory Accession to the Nonlinear Equilibrium Curve," Computer Methods in Applied Mechanics and Engineering, Vol. 47, pp. 283–297.

# SUMMARY

In engineering practice, an increasing necessity can be observed for taking into account the influence of nonlinearities in the description of the dynamic behaviour of complex mechanical systems for several reasons. Firstly, quite often characteristic dynamic behaviour can be observed in complex mechanical systems which cannot be explained from analysis of linear models of such systems (often containing many degrees of freedom). Secondly, it appears that in a number of cases nonlinearities in a design effectively can be used for vibration control or vibration minimization. Besides the fundamental need for a better understanding of the dynamic behaviour, also the wide availability of digital computers with rapidly increasing powerfulness is a very stimulating factor for nonlinear analyses of dynamical systems.

A typical orbit of a dissipative linear or nonlinear mechanical system driven by a periodic excitation or a constant force consists of a transient, whereafter the system will settle in a post-transient set, the long term behaviour of the system, also called the steady-state behaviour. The long term behaviour of nonlinear systems is much more complex than the long term behaviour of linear systems. Solutions of the equations of motion for linear systems will always have the same character as the excitation forces; if the excitation is sinusoidal, the long term behaviour will also be sinusoidal and will be unique. Because this is not the case in nonlinear systems, the analysis of the long term behaviour of such systems is much more complex and time consuming.

The long term solutions of the equations of motion for nonlinear mechanical system can be computed in a direct way by solving two-point boundary value problems obtained by supplementing the equations of motion with periodicity conditions for the solutions. In this thesis three methods are used to solve the two-point boundary value problems: the finite difference method, the multiple shooting method and incremental harmonic balance method. Which method can be used the best depends on the type and strongness of nonlinearity in the system under consideration.

Frequently, in mechanical systems from a spatial or geometrical point of view, nonlinearities have a local character. This means that from a spatial point of view,

these local nonlinearities constitute only a restricted part of the mechanical system under consideration. However, their presence in general has important consequences for the overall dynamic behaviour. Important examples of local nonlinearities in mechanical systems are: fluid-film bearings in rotating machinery, dry friction and backlash phenomena in certain connections of mechanical systems, nonlinear spring and damper supports in piping or vehicle systems, etc..

This thesis contains a collection of papers, published in various journals and books and is focused on nonlinear mechanical systems with local nonlinearities. The advantage of this kind of systems is that they can be divided into linear and nonlinear components, where the linear components (modelled using finite elements) have much more degrees-of-freedom (DOF's). Then, the DOF's of the linear components can be reduced using a component mode synthesis method. The dynamic behaviour of a reduced linear component is an approximation to that of the corresponding unreduced linear component and is valid in a certain frequency range. After reduction, the reduced linear parts are coupled with the local nonlinearities and a reduced nonlinear system is created, the behaviour of which is an approximation to that of the unreduced nonlinear system. Using the reduced system again periodic solutions can be calculated, now very efficiently. In this way, flexible systems with local nonlinearities can be analysed very efficiently. The reduction method and periodic solution solvers are implemented in the finite element package DIANA.

Using these numerical tools, in this thesis multi-DOF systems with discontinuities and rotor-bearing systems are investigated. Discontinuous systems constitute an important class of nonlinear mechanical systems. In many practical engineering applications, discontinuities occur. The equations of motion of a system with discontinuities cannot be linearized, so it is very difficult to predict the system response without a nonlinear analysis. The system which is investigated is a beam system which is periodically excited in the middle. In one case the beam is supported in the middle by a one-sided spring. In another case the beam system has at its middle an elastic stop, which is modelled using the contact law of Hertz. In this way an impact problem is created. Comparison of the numerical and experimental results showed that a one-sided leaf spring with much higher eigenfrequencies than the maximum excitation frequency which is investigated, can be modelled using a one-sided massless spring. Furthermore, it may be concluded that an elastic stop in a dynamic system can be modelled accurately using the Hertzian contact force law despite the fact that this theory is developed for static analysis.

Nonlinear dynamic systems can settle in different attractors for one set of system parameters. From a practical point of view, it is important to determine which attractor is approached, because the maximum response of the different attractors can be very different and also the frequencies occurring in the attractors can be very different. High system responses may lead to large strains and stresses which could cause damage to the structure. Which attractor will be approached by the system depends on the initial state of the system and the global stability of the attractors (how large are the basins of attraction of the attractors). If the global stability is low, small perturbations on the system will easily result in a jump to another attractor. In this thesis, a method for calculating manifolds is described and it is shown how the global stability of attractors can be determined using these manifolds. Experiments are presented that indicate that if the single-DOF system is already a good approximation of the system, it is possible to use the single-DOF system for analyzing the global stability of the attractors of the system.

Journal bearings are an essential feature of all rotating machinery and provide the vital load-carrying capacity to support rotors against static and dynamic loads. The standard practice for dynamic imbalance response and stability analysis of rotorbearing systems is to determine the linearized bearing stiffness and damping coefficients about a stationary equilibrium position. In this mathematical assumption, the synchronous motion about the stationary equilibrium position is described by ellipses in case of low values of the unbalance. However, when the unbalance level becomes moderate to large, the rotor orbits are not necessarily elliptical, due to the nonlinear characteristics of the bearings. Furthermore, in a linear system, operating above the threshold angular rotor speed, the amplitude of motion grows exponentially with time and the orbits become unbounded. In an actual system this is not necessarily the case, because the nonlinear effects can cause the motion to be bounded by limit cycles. Moreover, under some circumstances a lower total response can be obtained by having a moderate level of rotor unbalance in the system. In this thesis, a simple rotor-bearing system is investigated consisting of a flexible shaft with disk, supported on one side by an oil journal bearing and pinned on the other side. This system is analysed for different bearing models and unbalances. The results show that because oil journal bearings have a large damping level, no superharmonic resonances where found. However, 1/2 subharmonic and quasi-periodic behaviour was found for high angular rotor speeds. The guasi-periodic behaviour was dominated by the first resonance frequency of the shaft. Because of this the quasi-periodic behaviour showed a much higher response than the coexisting harmonic solutions. Analysis showed that by adding a mass unbalance these harmonic solutions can be made stable resulting in a much lower system response. However, still high amplitude quasi-periodic solutions can coexist.

Finally, a method is developed for stabilizing unstable harmonic solutions in order to reduce high system response with low control effort. Because of the local nonlinearities the system behaviour can change drastically, resulting in system responses with undesirable frequencies and enlargement of the maximum system response by subharmonic resonance peaks. Generically, a low amplitude harmonic solution coexists which may be unstable or may have a low global stability. A control method is developed which provides that using one single control force on one position of the system, the system can be controlled to that harmonic solution, unstable or stable. Because the harmonic solution is a natural solution of the system, the control force will become very small, theoretically even zero, if the system settles in the harmonic solution. It is shown that using only one control force it is possible to stabilize unstable harmonic solutions of the beam with one-sided spring. Also if the excitation frequency is varied during the control, it is possible to reduce the maximum system response by using very small control effort. Methods are developed for analyzing the stability of the controlled system and the controllability of the system.

# SAMENVATTING

In de werktuigkundige praktijk valt om verschillende redenen een toenemende vraag waar te nemen naar het meenemen van de invloed van niet-lineariteiten in de beschrijving van het dynamisch gedrag van mechanische systemen. Ten eerste treedt er in complexe mechanische systemen vaak karakteristiek gedrag op dat niet verklaard kan worden met de analyse van lineaire modellen (vaak met veel vrijheidsgraden) van die systemen. Ten tweede blijkt het zo te zijn dat in sommige gevallen de niet-lineariteiten gebruikt kunnen worden voor het regelen en/of reduceren van de trillingen die optreden. Afgezien van de fundamentele noodzaak van het beter begrijpen van het dynamische gedrag is ook de beschikbaarheid van digitale computers met snel groeiende rekencapaciteit een stimulerende factor voor het uitvoeren van niet-lineaire analyses van dynamische systemen.

Een typische trajectorie van een dissipatief lineair of niet-lineair systeem, aangestoten door een periodieke excitatie of door een constante kracht, bestaat uit een inschakelverschijnsel waarna het systeem naar zijn lange termijn gedrag zal gaan. Het lange termijn gedrag van een niet-lineair systeem is veel complexer dan het lange termijn gedrag van een lineair systeem. Lange termijn oplossingen van lineaire systemen hebben altijd hetzelfde karakter als de excitatie krachten: wanneer de excitatie sinusvormig is zal het lange termijn gedrag ook sinusvormig zijn en bovendien uniek. Omdat dit niet het geval is bij niet-lineaire systemen, is de analyse van het lange termijn gedrag van niet-lineaire systemen veel complexer en tijdrovender.

Het lange termijn gedrag van een mechanisch systeem kan berekend worden op een directe manier door twee-punts randvoorwaarde-problemen op te lossen die verkregen worden door de bewegingsvergelijkingen te combineren met de randvoorwaarden voor periodiciteit. In dit proefschrift zijn drie methoden gebruikt voor het berekenen van twee-punts randvoorwaarden-problemen: de eindige-differentiemethode, de "shooting"-methode en de "incremental harmonic balance"-methode. Welke methode het best gebruikt kan worden hangt af van het type en de sterkte van de niet-lineairiteit van het systeem dat wordt onderzocht.

In mechanische systemen hebben de niet-lineariteiten vaak een lokaal karak-

ter. Dit betekent ruimtelijk bekeken dat de lokale niet-lineariteiten een klein deel vormen van het mechanische systeem dat wordt onderzocht. Echter, hun aanwezigheid is van grote invloed op het totale dynamisch gedrag van het systeem. Belangrijke voorbeelden van lokale niet-lineariteiten in mechanische systemen zijn: nietlineaire lagers in roterende machines, droge wrijving en speling in bepaalde verbindingen van mechanische systemen, niet-lineaire veren en dempers in pijpleiding- en voertuig-systemen, etc..

Dit proefschrift is een verzamelijk van wetenschappelijke artikelen, gepubliceerd in verschillende tijdschriften en boeken. In dit proefschrift ligt het accent op nietlineaire systemen met lokale niet-lineariteiten. De prettige eigenschap van deze soort systemen is dat ze verdeeld kunnen worden in lineaire en niet-lineaire componenten, waarbij de lineaire componenten (gemodelleerd met de eindige-elementenmethode) veel meer vrijheidsgraden hebben. Daarna wordt het aantal vrijheidsgraden van de lineaire componenten gereduceerd met behulp van een "component mode synthese"-methode. Het dynamische gedrag van een gereduceerde lineaire component is een benadering van het dynamisch gedrag van de oorspronkelijke ongereduceerde component en is geldig in een bepaald frequentie-gebied. Na reductie worden de gereduceerde lineaire componenten gekoppeld met de lokale nietlineariteiten, resulterend in een gereduceerd niet-lineaire systeem dat een benadering is van het ongereduceerde niet-lineaire systeem. Met dit gereduceerde systeem kunnen heel efficient periodieke oplossingen bepaald worden. Op deze manier kunnen flexible systemen met lokale niet-lineariteiten zeer efficient geanalyseerd worden. De reductiemethode en de methodes voor het bepalen van periodieke oplossingen zijn geïmplementeerd in het eindige elementen pakket DIANA.

Met deze numerieke "tools" zijn in dit proefschrift systemen met meerdere vrijheidsgraden en discontinuiteiten alsmede rotor-lager-systemen onderzocht. Discontinue systemen zijn een belangrijke soort niet-lineaire mechanische systemen. In veel praktische mechanische toepassingen treden discontinuiteiten op. Een systeem met discontinuiteiten kan niet gelineariseerd worden en daardoor is het erg moeilijk om het systeem-gedrag te voorspellen zonder een niet-lineaire analyse. Het systeem dat onderzocht is, is een balk die in het midden periodiek wordt aangestoten. In één geval is de balk in het midden ondersteund door een eenzijdige veer. In een ander geval is de balk ondersteund door een elastische stop waardoor een impact-probleem is gecreëerd. Vergelijking van experimentele en numerieke resultaten duidt erop dat een eenzijdige bladveer met veel hogere eigenfrequenties dan het frequentiegebied dat wordt onderzocht, gemodelleerd kan worden als een massaloze eenzijdige veer. Verder kan geconcludeerd worden dat een elastische stop nauwkeurig gemodelleerd kan worden met de kontaktkracht-regel van Hertz hoewel deze theorie oorspronkelijk is ontwikkeld voor statische analyses.

Niet-lineaire dynamische systemen kunnen in verschillende attractoren terechtkomen voor een "set" van systeemparameters. Uit praktisch oogpunt is het belangrijk te weten welke attractor bereikt wordt omdat de maximale responsie en de frequenties die optreden in de verschillende attractoren erg verschillend kunnen zijn. Grote systeemresponsies kunnen leiden tot grote rekken en spanningen en zouden schade kunnen veroorzaken aan het systeem. Welke attractor bereikt wordt door het systeem hangt af van de begincondities van het systeem en de globale stabiliteit van de attractoren (hoe groot zijn de attractie-gebieden van de attractoren). Als de globale stabiliteit laag is kunnen kleine verstoringen op het systeem gemakkelijk resulteren in een sprong naar een andere attractor. In dit proefschrift wordt een methode beschreven voor het berekenen van zogenaamde manifolds en er wordt getoond hoe de globale stabiliteit bepaald kan worden gebruikmakend van deze manifolds. Met experimenten wordt aangetoond dat wanneer een systeem met één vrijheidsgraad al een goede benadering is van het werkelijke systeem, het mogelijk is om met het één-vrijheidsgraad systeem de globale stabiliteit van de attractoren te bepalen.

(Glij)lagers zijn essentiele onderdelen voor alle roterende machines en geven de mogelijkheid tot het ondersteunen van rotoren die belast worden door statische en dynamische krachten. In standaard numerieke analyses voor dynamische onbalans-reponsies en stabiliteits-analyses van rotor-lager systemen worden de gelineariseerde lager-stijfheids- en -dempings-coefficienten rond een stationaire positie bepaald. Bij deze mathematische aanname wordt de beweging rond de stationaire positie beschreven door ellipsen in het geval van lage waarden van de onbalans. Echter, wanneer het onbalans-niveau te groot wordt hoeven de rotorbanen niet meer elliptisch te zijn door de niet-lineaire karakteristieken van de lagers. Verder zal een lineair systeem, dat boven de kritische rotor-snelheid draait, rotorbanen hebben die exponentieel groeien in de tijd en naar oneindig gaan. In een werkelijk systeem zal dit niet het geval zijn omdat de niet-lineaire effecten begrensde rotorbanen tot gevolg zullen hebben. In dit proefschrift is een eenvoudig rotor-lager-systeem onderzocht dat bestaat uit een flexibele as met rotor die aan één kant ondersteund wordt door een olie-glijlager en opgelegd is aan de andere kant. Het systeem is geanalyseerd voor verschillende lagermodellen en onbalansen. De resultaten laten zien dat olie-lagers een grote demping veroorzaken en daardoor worden geen superharmonische resonanties gevonden. Wel zijn 1/2 subharmonische en quasi-periodieke oplossingen gevonden voor hoge assnelheden. Het guasi-periodiek gedrag wordt gedomineerd door de eerste resonantie-frequentie van de as. Daardoor heeft het quasi-periodiek gedrag een veel hogere responsie dan de tegelijk bestaande harmonische oplossingen. Analyses laten verder zien dat door het toevoegen van massaonbalans instabiele harmonische oplossingen stabiel kunnen worden en dit resulteert in lagere systeem-responsies. Echter, naast die stabiele harmonische oplossingen kunnen dan nog steeds guasi-periodieke oplossingen bestaan met hoge amplitudes.

Tot slot is er een methode ontwikkeld voor het stabiliseren van instabiele harmonische oplossingen om hoge systeem-responsies te reduceren met geringe regelinspanning. Door de niet-lineariteiten kan het systeemgedrag sterk veranderen en dit resulteert vaak in systeemgedrag met ongewenste frequenties en in een vergroting van de maximale systeem-responsie bij subharmonische resonantie-pieken. Meestal bestaat er tegelijkertijd ook een harmonische oplossing met een lage amplitude welke instabiel kan zijn of een lage globale stabiliteit kan hebben. Een regelmethode is ontwikkeld die ervoor zorgt dat met behulp van één regelkracht op een positie van het systeem, het systeem geregeld kan worden naar de harmonische oplossing, stabiel of niet stabiel. Omdat een harmonische oplossing een natuurlijke oplossing is van het systeem zal de regelkracht heel klein, theoretisch zelfs nul, worden als het systeem zich in de harmonische oplossing bevindt. In dit proefschrift wordt aangetoond dat het mogelijk is om met behulp van één regelkracht instabiele harmonische oplossingen van het balksysteem met eenzijdige veer te stabiliseren. Ook als de excitatiefrequentie wordt gevarieerd gedurende de regeltijd is het mogelijk de maximale responsie van het systeem te reduceren met behulp van weinig regelinspanning. Methodes zijn ontwikkeld voor het bepalen van de stabiliteit van het geregelde systeem en de regelbaarheid van het systeem.

#### ACKNOWLEDGEMENTS

The author wishes to acknowledge his appreciation to the **Centre for Mechanical Engineering of TNO Building and Construction Research** for the financial support of this research.

Furthermore, the author wants to thank the people who supported him at TNO Building and Construction Research, in particular R.H.B. Fey of the Centre for Mechanical Engineering and P. Nauta of Numerical Mechanics. Moreover, he wants to acknowledge his appreciation to the staff who supported him at Eindhoven University of Technology, in particular D.H. van Campen, A. de Kraker, L. Kodde, M.J.G van de Molengraft, J.J. Kok, J.P.A. Banens, E.A. Muiderman, H. van Leeuwen and W. van de Water. He wants to thank all the mechanical engineering students who contributed in some way to this thesis, viz. J.W. Aarts, F.H. Assinck, A.T.J. te Baerts, P.A. den Dikken, M. de Goeij, M.F. Heertjes, R.W.T.M. Hendrikx, A.R. Kant, F.P.H. van Liempt, L.T.A. Sanders, A.F. de Vries and M.W.J.E. Wijckmans.

Finally, he thanks all the anonymous reviewers of various journals for their valuable comments regarding the submitted manuscripts.

#### 232 Long Term Dynamics and Stabilization of Nonlinear Mechanical Systems.

### **CURRICULUM VITAE**

07-04-1968	Geboren te Steensel (NBr.)
08–1980 – 06–1985	HAVO aan het Rythovius College in Eersel.
08-1985 - 06-1987	HTS Werktuigbouwkunde aan de Hogeschool Eindhoven.
09–1987 – 08–1991	Studie Werktuigbouwkunde aan de Technische Universiteit
	Eindhoven.
11-1991 - 12-1995	Assistent in Opleiding aan de Technische Universiteit
	Eindhoven.

Edward van de Vorst werd geboren op 7 april 1968 te Steensel. Van 1980 tot en met 1985 volgde hij met succes HAVO onderwijs aan het Rythovius College in Eersel. Hierna volgde hij twee jaar een studie HTS Werktuigbouwkunde aan de Hogeschool Eindhoven.

In september 1987 begon hij met de studie Werktuigbouwkunde aan de Technische Universiteit Eindhoven (TUE) die werd afgerond, cum laude, in augustus 1991. Het afstudeerwerk werd tussen januari 1991 en augustus 1991 uitgevoerd bij de afdeling Numerieke Mechanica van TNO-Bouw in Rijswijk onder begeleiding van P. Nauta (TNO), A. de Kraker en D.H. van Campen (beide TUE). Dit werk resulteerde in de module *SUBSTR* in het eindige-elementen-pakket *DIANA* voor het reduceren van vrijheidsgraden van lineaire componenten met behulp van een component mode synthese methode.

Van november 1991 tot en met december 1995 was hij als Assistent in Opleiding in dienst van de vakgroep Fundamentele Werktuigkunde (WFW) van de faculteit Werktuigbouwkunde aan de TUE. Onder verantwoordelijkheid van de promotoren D.H. van Campen en J.J. Kok en mede begeleid door R.H.B. Fey (TNO), A. de Kraker, en M.J.G. van de Molengraft (beide TUE), verrichte hij onderzoek naar de lange-termijn-dynamica en stabilisatie van niet-lineaire mechanische systemen. Dit onderzoek werd uitgevoerd bij en gefinancieerd door de afdeling Centrum voor Mechanische Constructies van TNO-Bouw in Delft. Dit werk resulteerde in de module *STRDYN* in het eindige-elementen-pakket *DIANA* voor het analyseren

#### 234 Long Term Dynamics and Stabilization of Nonlinear Mechanical Systems.

van niet-lineaire dynamische systemen, een aantal wetenschappelijke artikelen en verscheidene conferentiebijdragen.

## Stellingen

#### behorend bij het proefschrift

#### Long Term Dynamics and Stabilization of Nonlinear Mechanical Systems.

- 1. Wanneer in een niet-lineair periodiek aangestoten systeem met één graad van vrijheid de harmonische resonantiefrequentie bekend is, kan de ligging van bijna alle subharmonische oplossingen voorspeld worden.
  - Dit proefschrift, deel 1 en 2.
- 2. In veel niet-lineaire dynamische analyses van rotor-lager-systemen worden lagertheorieën gebruikt waarin de invloed van de as-snelheid op het cavitatie-gebied in het lager wordt verwaarloosd. Dit is meestal niet correct, zie Van de Vorst et al. (1995).
  - Van de Vorst, E.L.B., Fey, R.H.B., De Kraker, A., and Van Campen, D.H., 1995, "Steady-State Behaviour of Nonlinear Flexible Rotor-Bearing Systems: Part II – Application: Influence of Cavitation Modelling," *Machine Vibration*, Vol 3 pp. 146-155 (dit proefschrift, hoofdstuk 9).
- 3. Wanneer er een 1/n subharmonische zadelpunt-oplossing, een 1/m subharmonische attractor en een 1/m subharmonische zadelpunt-oplossing coëxisteren, met n > m en n/m is irrationeel, dan bestaan er altijd heterokliene punten wanneer de instabiele manifolds van de 1/n subharmonische zadelpunt-oplossing worden aangetrokken door de 1/m subharmonische attractor, zie Van de Vorst et al. (1993).
  - Van de Vorst, E.L.B., Fey, R.H.B., Van Campen, D.H., and De Kraker, A., 1993, "Manifolds of Nonlinear Dynamic Single-DOF Systems," *Topics in Applied Mechanics, Integration of Theory & Applications in Applied Mechanics, J.F. Dijksman and F.T.M.* Nieuwstadt, ed., Kluwer Academic Publishers, pp. 293–303 (dit proefschrift, hoofdstuk 6).
- 4. "Cell mapping," een methode voor het bepalen van attractie-gebieden van nietlineaire dynamische systemen, is minder geschikt voor het detecteren van fractale attractie-gebieden. Dit komt doordat de cellen in de "cell mapping"-methode een eindige afmeting hebben.
- 5. In Thompson (1994) wordt gesteld dat er n systeemparameters gevarieerd moeten worden om structurele stabiliteit te krijgen wanneer een systeem op een codimensie n bifurcatie zit. Dit is niet correct: het variëren van één systeemparameter is voldoende om weer structurele stabiliteit te verkrijgen.
  - Thompson, J.M.T., 1994, "Basic Concepts of Nonlinear Dynamics," Nonlinearity and Chaos in Engineering Dynamics, Proceedings IUTAM Symposium, London, 19-23 July 1993, J.M.T. Thompson and S.R. Bishop, ed., John Wiley & Sons, pp. 1–21.
- 6. Het komt nog te vaak voor dat wetenschappelijke artikelen op het gebied van nietlineaire dynamica uitsluitend worden gepubliceerd omdat in een bepaald systeem chaotisch gedrag is gevonden tijdens simulaties. Aan het feit dat dit gedrag vaak optreedt bij onrealistische waarden van de systeemparameters wordt voorbijgegaan.

- 7. MATLAB is een computerprogramma waarmee zeer effectief numerieke problemen geprogrammeerd kunnen worden. Echter, omdat een MATLAB-programma 20 tot 25 keer langzamer is en veel meer computergeheugen vraagt dan een FORTRANof C-programma, zou het alleen voor *kleine* numerieke problemen gebruikt moeten worden en niet bijvoorbeeld als "tool" voor berekeningen volgens de eindigeelementen-methode met een behoorlijk aantal vrijheidsgraden. Voor dit soort toepassingen is MATLAB dan ook niet ontworpen.
- 8. Uit het oogpunt van vermindering van CO<sub>2</sub>-gas in de atmosfeer is het theoretisch beter om alle regenwouden te kappen en opnieuw in te planten. Bewezen is namelijk dat een jong regenwoud meer CO<sub>2</sub>-gas opneemt dan een oud regenwoud. Voorwaarde is wel dat het hout dat vrijkomt bij het kappen niet verbrand wordt of gaat rotten, omdat er dan extra CO<sub>2</sub>-gas in de atmosfeer komt.
- 9. De groeiende invloed van Greenpeace op de media en dus de bevolking kan gevaarlijk zijn als men zich realiseert dat het milieu voor Greenpeace vaak meer een soort "religie" is, waardoor de wetenschappelijke feiten over het hoofd worden gezien. Verder kan Greenpeace het verwijt worden gemaakt dat ze wel milieu-problemen onder de aandacht brengt maar geen oplossingen aandraagt.
- 10. Wanneer men de VI-editor in UNIX eenmaal goed onder de knie heeft, is deze editor in het gebruik het meest efficiënt van alle.
- 11. De computerberekeningen van dit proefschrift hebben gezamelijk meer dan vier jaar CPU-tijd gekost.

Eindhoven, maart 1996

Edward van de Vorst